Antonio Luque
Viacheslav Andreev
Editors

SPRINGER SERIES IN OPTICAL SCIENCES 130

Concentrator Photovoltaics

Springer

Springer Series in
OPTICAL SCIENCES 130

founded by H.K.V. Lotsch

Springer Series in

OPTICAL SCIENCES

The Springer Series in Optical Sciences, under the leadership of Editor-in-Chief *William T. Rhodes*, Georgia Institute of Technology, USA, provides an expanding selection of research monographs in all major areas of optics: lasers and quantum optics, ultrafast phenomena, optical spectroscopy techniques, optoelectronics, quantum information, information optics, applied laser technology, industrial applications, and other topics of contemporary interest.
With this broad coverage of topics, the series is of use to all research scientists and engineers who need up-to-date reference books.

The editors encourage prospective authors to correspond with them in advance of submitting a manuscript. Submission of manuscripts should be made to the Editor-in-Chief or one of the Editors. See also www.springeronline.com/series/624

Antonio L. Luque Viacheslav M. Andreev

Concentrator Photovoltaics

With 250 Figures and 6 Tables

Springer

Antonio L. Luque

Universidad Politécnica de Madrid
Instituto de Energía Solar
E.T.S.I. Telecomunicación
28040 Madrid, Spain
Email: luque@ies-def.upm.es

Professor Viacheslav M. Andreev

Ioffe Physico-Technical Institute
Polytekhnicheskaya str. 26
194021 St. Petersburg, Russia
Email: vmandreev@mail.ioffe.ru

Library of Congress Control Number: 2007923072

ISSN 0342-4111

ISBN 978-3-540-68796-2 Springer Berlin Heidelberg New York

Typesetting: Digital data supplied by editors
Production: LE-TEX Jelonek, Schmidt & Vöckler GbR, Leipzig
Cover: eStudio Calamar S.L., F. Steinen-Bro, Girona, Spain

SPIN 11554271 57/3180/YL - 5 4 3 2 1 0 Printed on acid-free paper

Preface

Although the discovery of the photovoltaic effect is attributed to Alexandre Edmond Becquerel, who in 1839 presented to the Academy of Sciences of Paris a study on the effects of the light on the electric currents going through an electrolyte with a separating membrane, Prof. William G. Adams and his student, Richard E. Day, presented to the Royal Society of London in 1877 the experiments that led them to unequivocally conclude 'a current could be started in the selenium by the action of the light alone'. These experiments had already been carried out under concentrated light.

After the oil crisis of 1973, when photovoltaics was considered as the best chance to get inexhaustible energy form the sun, the option of using concentrators was examined. Important technological developments took place then, but the subsequent assimilation of the oil-crisis effects reduced the interest in photovoltaics in general and, more acutely, in concentrated photovoltaics. The driving force of photovoltaic development has been, since then, the wish of sustainability. This has been a powerful driving force that has led the photovoltaic industry to be one of the fastest-growing industries – 33.4% per year as compared with the 6.2% of the semiconductor industry between 1996 and 2004 – and a much more appropriate one for the rhythm of the development that this new technology can withstand.

This scenario has been inappropriate, however, to promote concentrator solutions. It has been based on home applications, often attributed to the aesthetics of the building, or other small and isolated applications where concentrated photovoltaics is not practical.

Despite the tremendous potential of the present photovoltaic solutions, however, it is doubtful if they can reach the coveted exploitation of the sun's resources in a massive form. Prices in photovoltaics are decreasing too slowly. That is why researchers are looking for a breakthrough that will permit prices to decrease faster. According to Sharp, the biggest silicon solar cells producer that manufactures 25% of all the cells in the world, this breakthrough has already arrived. It is the novel super-high-efficiency solar cells which have reached an efficiency of 39% and are attempting to go further. Publicly funded programs to develop other super-high-efficiency concepts are starting to flourish.

Under these circumstances a number of companies, both established and start-ups, are declaring that they are ready to put their products on the market. A large-scale (16.2 million Euros) demonstration program is being funded by one Spanish public administration (Region of Castilla La Mancha) in order to install photovoltaic concentrator plants.

At this challenging moment the editors, who in 1979 presented simultaneously, but independently, two pioneering books on photovoltaic concentration (in English and Russian), are revisiting the subject but are giving the floor to various authors who have contributed to the development of our present knowledge on concentrated photovoltaics, and to those who are getting involved in the challenging endeavour of industrializing and commercializing it.

For this purpose, the book is therefore organized as follows:

The book consists of three sections: 'Introduction', 'Concentrator Foundation' and 'Commercial Concentrator Systems and Components'. The section 'Introduction' presents a historical survey of PV concentrator developments together with the recent situation in this field and the reasonable future of the PV concentrator technology. An unambiguous answer to the question 'Why CPV?' is also given. Despite feasible new discoveries and inventions, the authors give a detailed analysis of the material availability and manufacturing potential for extending the present technologies for mass production of solar cells and arrays.

In the second section, the chapter 'Silicon Concentrator Solar Cells' is the only chapter in the book which deals with Si solar cells. Requirements for obtaining high-efficiency cells and their use in point-focus and linear-concentration systems are discussed. The feasibility of applying such cells in a multijunction cell stack together with III-V solar cells is also considered. A comparative analysis of Si and III-V multijunction cells is presented.

In the chapter 'Multijunction Concentrator Solar Cells' the authors show that the efficiency of a concentrator III-V solar cell can be drastically increased by the use of tandem heterostructures. They present an overview of development of such multijunction cells and describe their manufacture and characterization. New solar cell concepts are discussed as well.

The chapter 'Very-High-Concentration Challenges of III-V Multijunction Solar Cells' focuses on the problems which III-V multijunction solar cells encounter when operating at very high sunlight concentrations under real conditions, and how those problems can be circumvented. An approach to develop III-V multijunction cells capable of operating at least at 1000× concentration and a cost analysis of PV installations are presented.

In the chapter 'Concentrator Optics' consideration is given to design and performance of different types of optical sunlight concentrators aimed to obtain high-flux PV systems. Problems of commercialization are considered as well.

The chapter 'Solar Cell Cooling' deals with the ways of heat removal from a cell which has resulted from excess solar energy, and which is not converted into electricity, including their performance, cost and reliability.

In the chapter 'Terrestrial PV Concentrator Systems' concentrator module design, indoor characterization of the modules and sun trackers are described. Data on indoor and outdoor measurements of concentrator modules are presented as well.

Chapter 'Solar Thermophotovoltaics' concerns solar thermophotovoltaic system research and development. Detailed consideration is given to solar concentrators, emitters and TPV cells for such systems. Efficiency potentialities of solar TPV systems are discussed.

The chapters of the section 'Commercial Concentrator Systems and Components' present detailed description and discussion of R&D of concentrator photovoltaic systems and sun tracking carried out in the firms and research institutions in the United States (Spectrolab Inc., Amonix Inc.), Spain (Inspira SL, Instituto de Energia Solar), Germany (Concentrix Solar, GmbH) and Japan (Toyota Technological Institute, Daido Steel Corp., Sharp Corp.).

Madrid — Antonio Luque
St. Petersburg — Viacheslav Andreev

Contents

List of Contributors

Zh.I. Alferov
Ioffe Physico-Technical Institute
26 Polytechnicheskaya str.
194021 St. Petersburg
Russia
E-mail: Zhores.Alferov@mail.ioffe.ru

C. Algora
Instituto de Energía Solar
Universidad Politécnica de Madrid
E.T.S.I. Telecomunicación
Avda. Complutense 38
28040 Madrid
Spain
E-mail: algora@ies-def.upm.es

V. Andreev
Ioffe Physico-Technical Insitute
26 Polytechnicheskaya
St. Petersburg 194021
Russia
E-mail: vmandreev@mail.ioffe.ru

I. Antón
Instituto de Energía Solar
Universidad Politécnica de Madrid
ETSI Telecomunicación
Ciudad Universitaria
28040 Madrid
Spain
E-mail: nacho@ies-def.upm.es

K. Araki
Daido Steel Corporation
Daido-cho, Minami,
Nagoya 457–8645
Japan
E-mail:k-araki@ac.daido.co.jp

A.W. Bett
Fraunhofer Institute
for Solar Energy Systems (ISE)
Heidenhofstrasse 2
79110 Freiburg
Germany
E-mail: andreas.bett@ise.fraunhofer.de

A. Blakers
Centre for Sustainable Energy Systems
Australian National University
Canberra 0200
Australia
E-mail: andrew.blakers@anu.edu.au

R. Cervantes
Inspira, SL
C/Vivero, 5
28040 Madrid
Spain
E-mail: rcervantes@inspira.es

F. Dimroth
Fraunhofer Institute
for Solar Energy Systems (ISE)
Heidenhofstrasse 2
79110 Freiburg
Germany
E-mail:
frank.dimroth@ise.fraunhofer.de

V. Garboushian
Amonix, Inc.
3425 Fujita St.
Torrance, CA 90505
USA
E-Mail: vahan@amonix.com

J.M. Gordon
Department of Solar Energy
and Environmental Physics
Jacob Blaustein Institutes
for Desert Research
Ben-Gurion University of the Negev,
Sede Boqer Campus 84990
Israel
E-mail: jeff@bgu.ac.il

N.H. Karam
Spectrolab, Inc.
12500 Gladstone Avenue
Sylmar, CA 91342
USA
E-mail: nasser.karam@boeing.com

V. Khvostikov
Ioffe Physico-Technical Insitute
26 Polytechnicheskaya
St. Petersburg 194021
Russia
E-mail: vlasov@scell.ioffe.ru

R.R. King
Spectrolab, Inc.
12500 Gladstone Avenue
Sylmar, CA 91342
USA
E-mail: rking@spectrolab.com

O. Laurent
Inspira, SL
C/Vivero, 5
28040 Madrid
Spain
E-mail: olaurent@inspira.es

H. Lerchenmüller
Concentrix Solar GmbH,
Solar Info Center
79072 Freiburg
Germany
E-mail: hansjoerg.lerchenmueller@
concentrix-solar.de

A. Luque
Instituto de Energía Solar
Universidad Politécnica de Madrid
28040 Madrid
Spain
E-mail: luque@ies-def.upm.es

I. Luque-Heredia
Inspira, SL
C/Vivero, 5
28040 Madrid
Spain
E-mail: iluque@inspira.es

P.H. Magalhães
Inspira, SL
C/Vivero, 5
28040 Madrid
E-mail: phmagalhaes@inspira.es

G. Martinelli
Universita degli Studi di Ferrara
via Saragat 1/c
44100 Ferrara
Italy
E-mail: martinelli@fe.infn.it

J.M. Moreno
Inspira, SL
C/Vivero, 5
28040 Madrid
E-mail: jmmoreno@inspira.es

G. Quéméré
Inspira, SL
C/Vivero, 5
28040 Madrid
Spain
E-mail: gquemere@inspira.es

V.D. Rumyantsev
Ioffe Physico-Technical Institute
26 Polytechnicheskaya str.
St. Petersburg 194021
Russia
E-mail: rumyan@scell.ioffe.rssi.ru

G. Sala
Instituto de Energía Solar
Universidad Politécnica de Madrid
ETSI Telecomunicación
Ciudad Universitaria
28040 Madrid
Spain
E-mail: sala@ies-def.upm.es

R.A. Sherif
Spectrolab, Inc.
12500 Gladstone Avenue
Sylmar, CA 91342
USA

G. Siefer
Fraunhofer Institute for Solar Energy Systems (ISE)
Heidenhofstrasse 2
79110 Freiburg
Germany
E-mail: gerald.siefer@ise.fraunhofer.de

A. Slade
Amonix, Inc.
3425 Fujita St.
Torrance, CA 90505
USA
E-Mail: alex@amonix.com

K. W. Stone
Amonix, Inc.
3425 Fujita St.
Torrance, CA 90505
USA
E-Mail: ken@amonix.com

T. Takamoto
Sharp Corporation
282–1 Hajikami, Shinjo
Nara 639–2198
Japan
E-mail: takamoto.tatsuya@sharp.co.jp

A. Vlasov
Ioffe Physico-Technical Insitute
26 Polytechnicheskaya
St. Petersburg 194021
Russia
E-mail: vlasov@scell.ioffe.ru

M. Yamaguchi
Toyota Technological Institute
2–12–1 Hisakata, Tempaku
Nagoya 468–8511
Japan
E-mail: masafumi@toyota-ti.ac.jp

1 Past Experiences and New Challenges of PV Concentrators

G. Sala and A. Luque

1.1 Introduction

The general idea of a photovoltaic (PV) concentrator is to use optics to focus sunlight on a small receiving solar cell (Fig. 1.1); thus, the cell area in the focus of the concentrator can be reduced by the concentration ratio. At the same time the light intensity on the cell is increased by the same ratio. In other words, cell surface is replaced by lens or mirror surface in PV concentrators and the efficiency and price of both determine the optimum configuration.

Medium- and high-concentration systems require accurate tracking to maintain the focus of the light on the solar cells as the sun moves throughout the day. This adds extra costs and complexity to the system and also increases the maintenance burden during operation. For systems with small solar cells, or using low concentration, passive cooling (interchange of heat with the surrounding air) is feasible.

After 30 years of concentrator development and practically no industrial or commercial activities, the photovoltaic concentration market seems ready to take off and grow rapidly because of feed-in tariff laws approved in several sunny countries and the availability of a sufficient amount of very efficient, up to almost 40%, III-V multijunction cells.

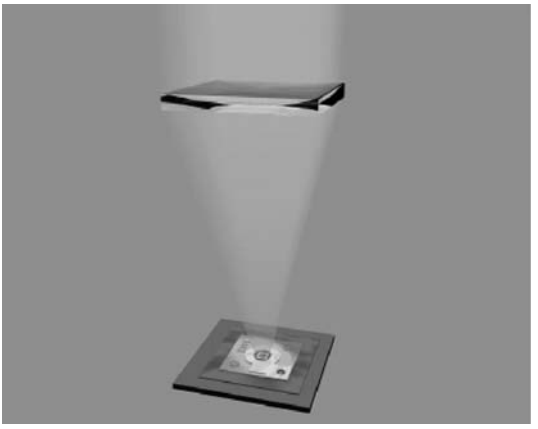

Fig. 1.1. The principle of PV concentration, using Fresnel lens optics. (Courtesy of FhG/ISE, Freiburg, Germany)

Fig. 1.2. The SANDIA-II array, the first modern PV concentrator made at Sandia National Laboratories, Albuquerque, New Mexico, in 1977. It consist of 5-cm-diameter Si cells operating on two axes under cast acrylic Fresnel lenses at 32 suns, with passive cooling

The lack of official qualification regulations may restrict the commercialization of unproven technologies until manufacturers define the minimum requirements before contracting and installing new power plants. Great strides are being made in this direction.

In this chapter a brief summary of the history of photovoltaic concentration is combined with an overview of the present and future of this technology, including an outline of the present situation as well as comments on the material availability and manufacturing challenges if photovoltaic concentration has to supply a significant portion of the world's electricity.

1.2 Past Experience

The development of PV concentrator technology started effectively in 1976 at National Sandia Laboratories with the construction of 1 kW peak array, later called Sandia I and Sandia II (Fig. 1.3) [1]. This early work identified and tried to solve the majority of the problems linked to concentration systems and gave satisfactory answers to many of them.

Fresnel lenses, two-axis tracking, concentrator silicon cells at 40× and analogue closed-loop tracking control systems were the characteristics of this pioneering prototype. Several reproductions, in some cases accompanied by component improvements, were soon made in France, Italy and Spain, with prototypes ranging from 500 W to 1 kW (Fig. 1.4) [2–4].

A pre-industrial, but not yet commercial, action was carried out in 1981 by Martin Marietta with version III of Sandia Technology, who installed

Fig. 1.3. The 1-kWp Ramon Areces Array was developed at 'Universidad Politécnica de Madrid', Spain, in 1980. It followed the Sandia Labs concept, but all components were locally made. Curiously, the Fresnel lenses were made of a thin film of silicone stuck on glass, an idea that has recently been taken up again and might be of interest in the future

Fig. 1.4. The 350-kWp SOLERAS project power plant was the world's first and largest concentration plant. It was built and deployed in Saudi Arabia, using the evolution of Sandia Labs (technology by Martin Marietta)

a 350-kWp demonstration plant in Saudi Arabia, called SOLERAS (Figs. 1.5, 1.6) [5]. Although there was no market pressure, Nasby and co-workers at Sandia Labs developed 20% efficient Si concentrator cells in 1980 [6] which allowed the expectations of both cost reduction of concentrators and conventional PV modules to be increased. Six years later, the man responsible for the SOLERAS project wrote the following:

This PVPS has been operating very well in the hot desert environment since its inception, however the net permanent power is degraded by 20% due to ceramic substrates solder joint delamination problem by the daily thermal cycling and fatigue, short circuit problems, and water penetration/condensation inside the modules. The temperature of the cells was found to be excessively higher than the original designed value, and the heat sink assembly was not enough to cool down the cells.

Fig. 1.5. Martin Marietta PV concentrator assembly line built for the SOLERAS project

Fig. 1.6. Checking the bifacial cells of a 4.5× fully static concentrator prototype before filling the module with transparent dielectric (Madrid 1986)

These are practically the same words that have been used to explain the results of more recent concentrator photovoltaic (CPV) demonstrations; Despite these problems, the Soleras plant continued in operation for 18 years.

So clear was the understanding that efficiency was a key factor in this technology that Swanson et al., after the experiences of R.J. Schwartz, developed the point contact (PC) solar cells – the best Si cell ever made – to be used at a high concentration level ($> 150\times$) [7].

Although there were several concentration cells developed in the world, with efficiencies ranging from 19.6% at the UPM to 27% by Swanson et al., the production capacity was poor and concentrator cells were difficult to find for 25 years. The rare investors that were interested in the PV concentration 'miracle' were discouraged when they discovered that concentration cells were not available, or that the cost ratio with flat-module cells was larger than the concentrator gain.

An alternative to the idea of high concentration that requires specialized cells and tracking was the concept of static concentration based on concentrators developed for Cerenkov radiation by Winston and Hinterberger [8] which was improved with the bifacial cell (Fig. 1.7) [9]. Once the bifacial cell came into in production in Isofotón – a spin-off of the UPM in 1981 – several prototypes were developed by these two partners (Fig. 1.8). This was a product with none of the supposed drawbacks associated with concentrator: it was static, modular like a flat panel, 12-V nominal and able to collect and concentrate (to a large extent) diffuse radiation. But the commercialization never started in reality, perhaps because the introduction of a new product was uncertain and expensive; The investment required to make this product was really small, but the margin of cost reduction was probably not sufficient to justify the effort.

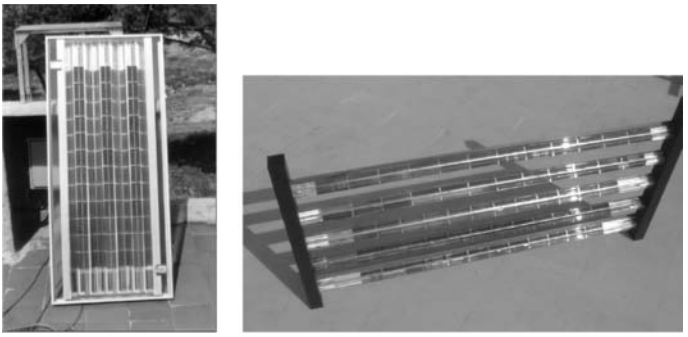

Fig. 1.7. Isofotón and the UPM developed several static concentrators with bifacial cells. The good technical performance was not followed up by their industrialization. *Left*: 1988; *right*: 1998. (From [10])

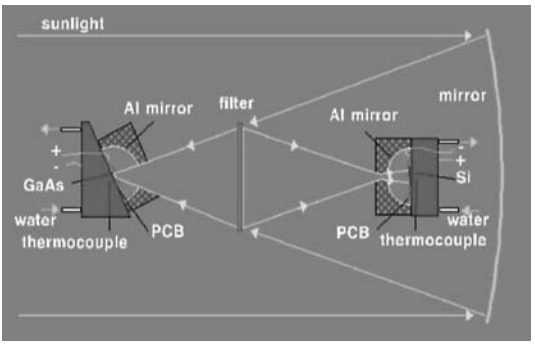

Fig. 1.8. The PV-EYE device combined light spectrum splitting and gap matching (AsGa and Si concentrator cells) with angular confining cavities which redirected cell surface reflected light to the cell again. A European record of 29.6% was achieved with this arrangement in 1990

Neither the ideas of spectrum splitting from 1980 at Varian, nor the realization with an European efficiency record (29.7%) from PV-EYE, using with two cells (AsGa and Si) inside angular confining cavities [11] at levels near 800× in 1991 [12], resulted in any attempt to industrialize concentrators (Fig. 1.9).

In the 1990s the most significant industrialization action was carried out by Entech who installed several hundreds of kilowatts using 20× curved Fresnel lenses (Fig. 1.10) [13].

With flat-panel cells whose price tended to decrease continuously due to mass production, one industrialization opportunity was linked to the Laser Grooved Buried Contact (LGBG) Cell [14] technology, an industrial approach

Fig. 1.9. A two-axis tracking 100-kW ENTECH power plant in Texas. System efficiency of up to 14% was demonstrated with this technology at 20 suns: curved Fresnel lenses showed optical efficiency of over 85%. Different cells were used to make the receivers

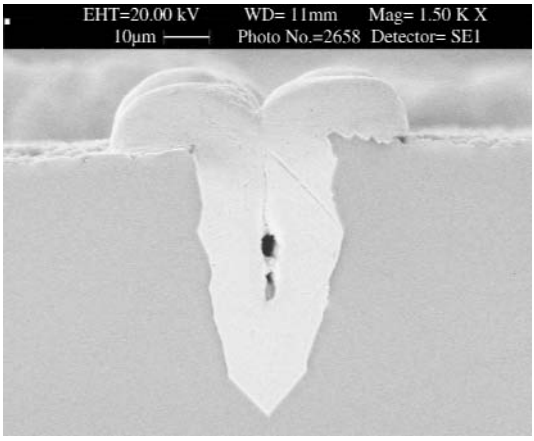

Fig. 1.10. Metal finger cross section of the BP Solar SATURN cell. The low grid resistance was key operating these cells in concentration very efficiently, despite their being made on the same production line as the 1-sun SATURN cell

following the outstanding progress of the University of New South Wales on crystalline silicon cells.

Concentrator LGBG cells (also called SATURN after the name of the industrialization project by BP Solar) shows near-uniform voltage in its metal grid (Fig. 1.11) and low recombination surface which allows it to reach 18.5% efficiency at 30× and up to 20% in small cells (1 cm^2) at 100× [15].

These cells were very convenient for use in concentrator systems because their 1-sun version is probably more expensive than the conventional cells from the competitors per watt peak but used as $125 \times 125 - mm^2$ concentrator cells, and designed for 30×, they could be sold at 10 – 12 € each, which would be very attractive to the manufacturer (BP Solar).

An opportunity for this technology opened up in 1995 with the EUCLIDES prototype developed by IES/UPM and BP Solar which was installed in Madrid. It proved up to 14% power efficiency and 10% yearly energy conversion ratio at a lower cost than the flat-plate power plant at that time [16].

Following the Madrid prototype, a planed 480-kWp EUCLIDES demonstration plant was built in Tenerife under the joint effort of BP Solar, the Instituto de Tecnología y Energías Renovables (ITER) on Tenerife and the IES/UPM (Fig. 1.12). Several problems associated with receiver manufacturing and some overestimation of the concentrator benefits pushed BP Solar to abandon the project instead of solving its manufacturing defects. During the merge with Amoco (and its subsidiary Solarex) concentrator plans were practically abandoned, although they continue to manufacture short series of concentrator SATURN cells for R&D projects [17]. These cells were also occasionally used by Entech in their lineal concentrators.

Fig. 1.11. The EUCLIDES demonstration power plant in Tenerife (1998) subsidized by the EU to industrialize the Madrid Prototype (1995). The mirrors were shaped aluminium plates covered with silvered acrylic film which cast 3.2 W/cm^2 on receivers including SATURN cells. The partners were ITER, BP Solar and UPM

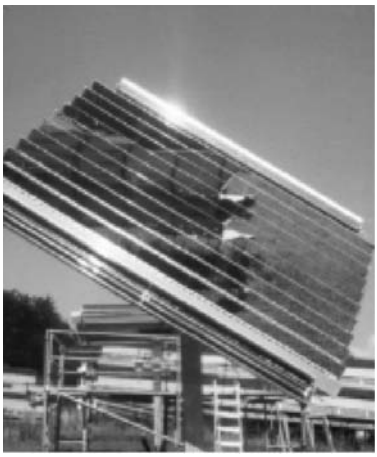

Fig. 1.12. ZSW (Stuttgart) developed very low concentration systems (2 and 10×) with the ARCHIMEDES concept, which includes one-axis passive-tracking hydraulic drivers. The picture shows a one-axis tracking 2× concentrator

The substantial European Commission investment in the EUCLIDES concentrator technology created a wave of activity in this field, many centred on the use of SATURN cells, such as ZSW with the ARCHIMEDES system (Fig. 1.13), but also others adopting the spacecraft Si cells technology (ASE; LETI, DEMOCRITOS and still others based on PC cells (Ferrara University).

The silicon PC solar cells, sized about 1 cm^2, have given rise to a set of concentrators of which the most successful version is the one by Amonix [18] leading to a product that is technically ready, probably, with the cell and receiver manufacture well tested and reliable (Fig. 1.14).

The PC cells are much more expensive than ordinary cells but, unlike ordinary solar cells, which, because the base resistance cannot operate above

Fig. 1.13. Two-axes tracking arrays from AMONIX, installed at Arizona Public Service, Scottsdale. They use 27% efficient BPC solar cells operating at 250× under point focusing laminated Fresnel lenses: the nominal array power is 25 kW. This technology was licensed to GUASCOR-FOTON (Spain) in 2005 and is currently being commercialized

Fig. 1.14. Field of PV parabolic dishes manufactured by Solar Systems in White Clifts, NSW (Australia). Each dish focuses the light on a compact actively cooled receiver, whose surface is a parquet of BPC cells. Each disk is rated 25 kWp nominal

about 100 suns, they can operate at much higher concentrations, in the range of 300 suns, because they are not traversed from up to down by any current [19].

The large parabolic dishes from the Australian company Solar Systems (Fig. 1.15) have been also equipped with these Si-PC cells in their focus area to produce about 25 kW per dish. The newest trends, however, are associated with III-V multijunction solar cells, which have achieved incredibly high efficiencies [20], approaching 40%, and the concentrators associated with them. Spectrolab and Emcore in the United States, and RWE in Germany, are cell producers and willing to sell these cells to system manufacturers. Sharp, the biggest Si cells manufacturers, is also a cell producer, but it is also planning to manufacture concentrator systems.

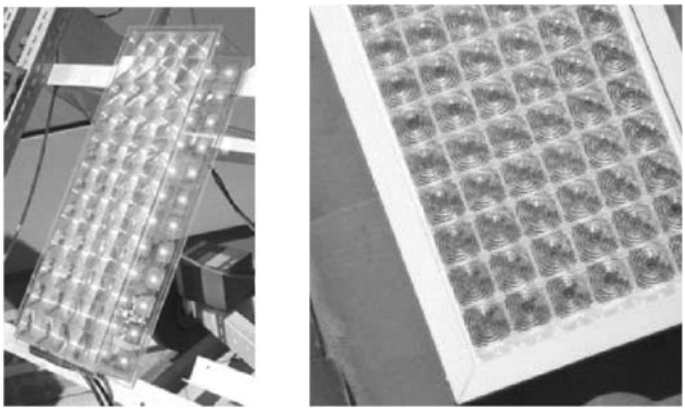

Fig. 1.15. CONCENTRIX (*left*) and ISOFOTON (*right*) have developed compact concentrator systems using 2- and 1-mm-diameter multijunction micro-cells operating at about 400 and 1000×, respectively

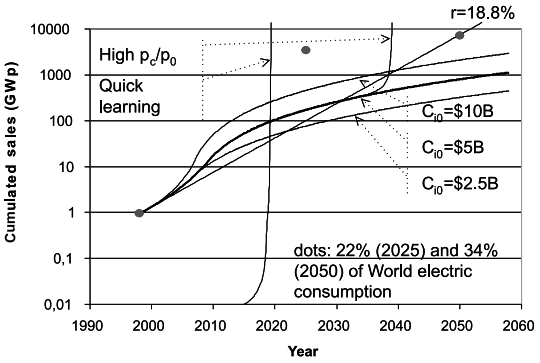

Fig. 1.16. Accumulated PV installations for different capital availability. Labels C_{i0} = \$ 10 B, 5 B and 2.5 B represent 0.1, 0.05 and 0.025% of the GDP of the industrialized countries. The cureve labelled *High* p_c/p_0 represents the case in which the competition with the prevailing electricity is produced for module prices of \$ 0.7/Wp (in the rest of the cases it is \$ 0.35/Wp). The case for high learning has a learning factor of 0.68 (for the rest of the cases the learning factor is 0.8253)

Research centres, such as the IES/UPM, the Fraunhofer Institute for Solar Energy (FhG/ISE) and the Ioffe Institute, are deeply involved in this new type of concentrator development. Isofotón, in cooperation with IES/UMP, is certainly the oldest company working in this new concept concentrator [21]. Other new venture-capital fed small companies spun-off from research groups are starting to work including Concentrix, a spin-off of FhG/ISE (Fig. 1.16) [22].

1.3 An Interpretation of the Past

When, after the first oil shock, the1974 Cherry Hill Conference in the United States took place, it appeared reasonable that a quick path to the mass production of solar electricity, taking into account that the available solar cells were too expensive, was to use concentrators. Accordingly the first industrializing trials and analyses, such as those of Martin Marietta in Saudi Arabia, were directed towards this end. However, the urgent problem posed by the oil shocks was solved before a cost-effective solar converter was in place; therefore, the interest waned and, for more than a decade, PV specialists were forced to find their own way. This path was ploughed along the land of sustainability.

The urgency of this motivation, however, is very different. It requires a large degree of intergenerational solidarity, and this is a feeling only recently added to our moral stock; thus, for many years it was assumed that the non-professional PV market would only fullfil developing-country applications, or the houses of individuals or institutions that wanted to contribute

to sustainability goals through their involvements but even more so, by their example. Commercial effort was therefore made in these directions. Architectural integration to make the clean, but expensive, new PV technology attractive was necessary and, taking into account that the short-term forecasts for concentrators concluded that it did not reduce costs sufficiently to make it competitive with conventional electricity, all applications remained of a modest size and were not deemed appropriate to be satisfied by concentrators.

Under these circumstances, dedicated high-efficiency concentrator cells ceased to be manufactured or, if they were, it was in such small amounts that the indirect costs meant a cell price that offset the cost reduction per cell area reduction, with the few exceptions already described.

The CPV does not currently have a single line of their own in the PV market breakdown by technology. Despite this apparent failure, however, the more-or-less intermittent maintenance of R&D lines has permitted CPV to remain a subject at an academic level (e.g. concentrators are regularly researched in the doctorate program of the IES/UPM) and to create a small, but effective, group of specialists ready for the next step, which we described later. Among them, the group at the IES/UPM was the first to publish a book on this topic in English in 1989 [23]. In the same year scientists at the Ioffe Institute published another book on CPV in Russian that was translated into English in 1997 [24]. The latter book was oriented more towards heterostructure solar cells, whereas the former concentrated more on the non-imaging optics.

1.4 The Need for CPV

In 2001 one of us published [25] a forecasting model of the markets and prices for PV technology in the first half of this century. The model has been especially accurate in the short-term forecasting (from 1998 onwards). The model couples the learning curve, that characterizes the reduction of costs every time the cumulated production is doubled, with the elasticity of demand - which is the logarithmic derivative of the market with respect to the price, changed of sign. The results are detailed in Fig. 1.16. Vertical asymptotes tells us that the cost of PV electricity equals that of the prevailing electricity, but the vertical growth is an artefact of the model that is not intended for this situation (it assumes infinite potential demand); however, the asymptotes show when this competitive situation is reached. This model tells us that, while present PV technology will lead to very large markets, its penetration will not be enough to contribute substantially to sustainability. The reason is the slow PV learning curve. On the other hand, the same model predicts that if the learning curve is faster, like the one for semiconductor memories, in few years from the entrance into the market, prices in competition with the prevailing electricity could be reached.

What prevents the learning curve from being faster? In our opinion, it is the fact that the efficiency of the present solar cells is bound by theoretical fundamental reasons (essentially Shockley and Queiser [26]) to a value of 40% [27]. This makes any practical increase of efficiency very difficult and therefore reduces the learning speed. The fundamental theoretical reasons are based on the fact that a solar cell is a two-level device that only converts effectively the photons with energy close to the energy separation of these levels (the band gap). The photons with less energy are totally lost and for those of higher energy the energy separation between levels (the band gap) is an upper limit of the energy at which the electrons are delivered. The limit derived from the two-level nature of solar cells is referred to as the SQ limit.

Multijunction cells escape this limitation. In fact, their limiting efficiency is about 86% [27] under the same conditions that resulted in a 40% limitation for the cells made of a single semiconductor; thus, multijunction cells, or in general, some kind of solar converters not bound by the SQ limit, may, in principle, increase the efficiency much more than the single semiconductor cells. This should lead to a faster learning curve and, if they are able to reach the market, they may reduce prices faster than present solar cells and thus accelerate the penetration of solar electricity. One problem lies in the gaining of the small portion of market that would allow self-learning through experience and therefore trigger a faster learning curve.

Not only are MJ solar cells in this situation, but also a number of concepts have been developed that may fulfil these requirements. They are often called third-generation [28] or new-generation [29] solar cells. The FULL-SPECTRUM Integrated project [30], with 19 R&D centres involved, has been launched by the European Union in order to fund R&D in innovative concepts (including multijunction solar cells) able to develop under this faster learning curve.

A common feature of these novel cells is their high cost. In fact, MJ solar cells developed for space applications have very different requirements. But MJ solar cells and many other sophisticated concepts may be adapted to terrestrial uses assuming that they are used in concentrators. In this way, concentrators are necessary to make use of the new opportunities that are offered by the latest developments in the science and the technology of solar cells. The consequence is that concentrators must be developed, and a bigger institutional effort should be devoted to this endeavour.

1.5 New Challenges in CPV

The present situation seems to replicate the one existing when the concentrators started in the mid-1970s, but now there are some important differences:

1. The non-concentrator option in MJ solar cells is only devoted to space. No large amounts of cells are expected for this market, and therefore

the reduction in price through the learning curve will not suffocate the development of terrestrial concentrator options.
2. Very high concentrations are needed to make these cells cost-effective, but unlike silicon cells, the concentration of which can hardly go above 300 suns, MJ solar cells can probably operate very efficiency at about 1000 suns. The optics and the tracking are also challenging subjects, but as we see later, all of them seem to have a solution.

Efficiency is an important aspect of the new scenario. It will decrease the very important BOS costs. The concentration factor is also important at least at the start, because it will avoid the cell cost from becoming a barrier to cost reduction. This requires new approaches to the cell itself, the optics, the automated module assembly and tracking development. Of these aspects, the development of the cell is the one to which more attention has been devoted. By 2004 the race towards 40% efficient MJ solar cells was already in progress. The leading results in the United States [31] and Japan, which have reached the world's top efficiencies, but also in Europe, show the way to others. University groups, research institutes and companies mostly in Spain [32], Russia and Germany soon envisaged a business model based on tiny MJ solar cells operating in integrated concentrators operating at over 400×.

Attempts to operate at higher concentrations were undertaken in 2001 at IES/UPM with GaAs single-junction solar cells with an efficiency of 26.2% at 1000× [32]. Later at FhG/ISE, 3 J solar cells of 35.2% at 700× were achieved [33]. This is possible because the MJ cells, usually of III-V materials are very thin, because they are made with direct-gap semiconductors. The substrate is inactive, and therefore it can be made with very low resistivity without compromising lifetime. Nevertheless, these high concentrations are only possible if the cells are very small, about 1 mm^2, so that the extraction of the current becomes easy. Again, such a small size is not possible in silicon because of its high diffusion length, which makes the cells very sensitive to perimeter recombination.

Cell efficiency for CPV has to be high for several reasons. Firstly, concentrators only collect direct radiation. Secondly, the concentrator itself has a less-than-one efficiency. If we assume that the direct normal radiation/global normal radiation ratio is 80%, as it corresponds to a good climate, and we assume that the optic efficiency is 80%, then we can conclude that only 64% of total available light is cast on the concentrator cell. Assuming that conventional modules are 15% efficient, we must conclude that the minimum efficiency allowed in concentrator cells is 23.4% in order to equal the energy production of flat module arrays with same collector area; thus, the efficiency of concentrator cells must be at least 24% (under standard test conditions) in order to be cost competitive with flat panels. Although it can be argued that a reduction in the cell area could be a factor in cost reduction, this is uncertain (concentrator cells are more expensive), and the commercial

success for lower efficiency will be problematic. If this argument is true, only PC silicon cells, such as those used by Amonix in the United States, Guascor Photon in Spain and Solar Systems in Australia, have only a marginal chance of leading to a cost-competitive product. On the other hand, most MJ solar cell-based products, if operating at sufficiently high concentration, may be cost-effective with respect to a flat-module PV.

Concerning the optics, there are fundamental limitations that reduce the angular acceptance with the level of concentration [34]. The angular acceptance is the angle at which the rays entering the optics reach the cell. It must at least cover the apparent sun's semi-diameter of 0.26°, but it is good if it is larger because this will allow the requirements for manufacturing and tracking to be eased. Non-imaging optics attempt to enlarge this angle as much as possible, and this discipline has developed since 1978 (when Winston et al. published their first book on the topic [35]). In this development the IES/UPM staff has participated in a leading way [36]. An important topic for concentrators with a large angular acceptance is achieving a homogeneous illumination on the cell at the same time.

It has been said that high-concentration cells, operating at or near 1000 suns, must be small, in part, for the reasons stated (to reduce ohmic losses), and in part, to facilitate the spreading of the heat produced by the energy cast by the sun and not converted into electricity. In this way the cells are very much of the size of an LED, and novel concentrators may benefit very much from the development in LED manufacture [31]. (It is noteworthy that the heat dissipation in power LED's is higher that the one of a solar cells at 1000×.)

Finally, the remaining challenge is associated with the tracking. The tracking structure constitutes an important part of the CPV cost, and in the past it has been treated as a trivial part of the CPV system. Things have recently changed, and the Spanish company Inspira has made a significant effort in this direction, as explained elsewhere in this book.

The challenge is not associated with the lack of reliability, as is often said without any data to support it. In Spain several tens of MW in the so-called solar farms have been installed, and this market continues to grow fast, so it has to be assumed that the customers are satisfied. But the tracking structures for flat modules are designed to withstand gravity and wind stresses safely, whereas in concentration they are designed to flex, that is, the structure must not, under the operational designed conditions, have a flexure higher than that permitted by the optics and the tracking mechanisms, including the control electronics.

The safe design of the tracking structure must consider the high winds recommended under the local building codes, but the occurrence of these winds is very uneven. Operation of the trackers must be assured only for the winds usually present in the area by putting the tracker in a stowing position when they are exceeded [38].

Concerning the control electronics, in the past it was based on closed-loop solutions in which a sensing device assured a good alignment of the sun with the sensor. The aiming of the sensor with the modules was left to a purely mechanical procedure, completed in some cases with a unclearly defined output-based trial an error. Modern trackers tend to be built using control based on ephemeris calculations with an error model of the mechanical structure along the lines first developed by Penzias and presently followed routinely (T-Point tracking) in astronomical instruments [39]. Accurate measurements (to 1000th of a degree) of the tracking aiming error have been carried out [40] and for the moment an accuracy of less than 0.1° for 98% of the operation time has been reported, but it has also been reported that the use of less accurate error models brings the tracking error to more than 0.3°.

For the final design of the tracker the flexure of the modules has to be adjusted [41] in such way that the angular acceptance of the modules correlated with the sun's semi-diameter (between 0.3 and 0.7° in existing modules) must allow for the loss resulting from the tracking mechanism and its control (0.1° in good control systems) and for the flexure. This leaves to the

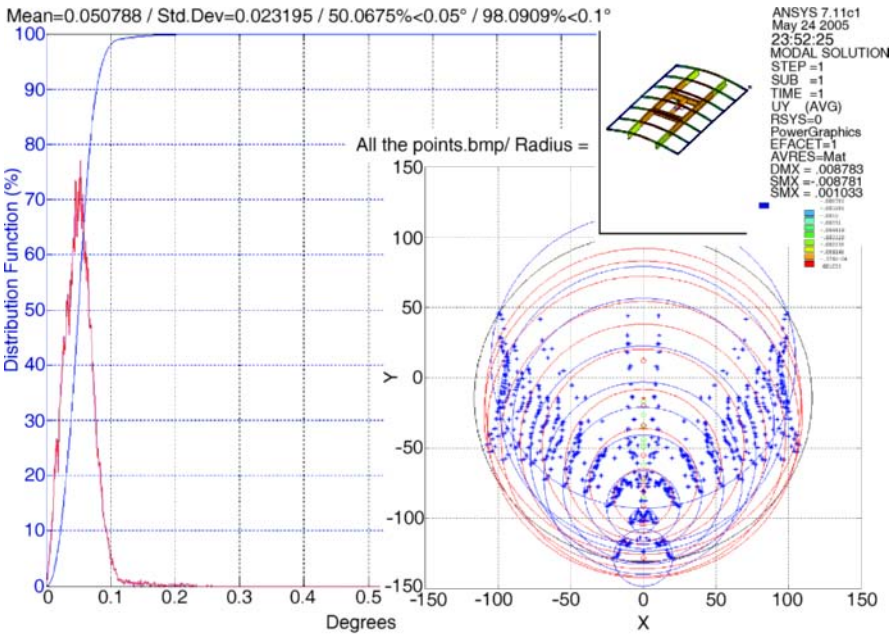

Fig. 1.17. *Left*: Distribution function of the misaiming angle. *Right*: Pointing vectors and minimum encircling circles (MEC) at different elevations with maximum service wind speed windward and leeward to the module's active surface. Tracking accuracy has to be higher than the MEC at any elevation

flexure an angle that is larger ($0.2 - 0.6°$) when the optics are more tolerant; however, more tolerant optics sometimes means less efficient and maybe more expensive ones, and all these factors must be taken into account in the optimal design of CPV systems. We are presently at the very beginning of understanding all these systemic approaches and, in reality, no system has thus far been designed following all of these principles.

There is very little experience of inverter operation with concentrators. On the one hand, they operate mostly at high power level, which is positive, but on the other hand, the variations in direct light intensity on cells as the result of clouds, limited acceptance angle, wind loads inducing tracking inaccuracies, etc., are fast and require the DC/DC maximum power point tracking to be fast as well. Several protections against inverter instabilities can make the control system too slow, wasting too much energy. Alternatively, the high efficiency of the inverter at low irradiance levels is not an advantage in CPV applications because the power level is usually high.

The PV concentrator modules will be asked to pass similar accelerated tests as flat modules, mainly because they are the closest references, but the variability of concentrator design options demand more complex regulatory documents and it is risky to extrapolate, without enough validated experience, the tests and valuation of results. Although this reserve exists between the manufacturers and regulation makers, it is generally accepted that tests on the following are required to demonstrate minimum module performance characteristics: (a) electrical insulation test, wet and dry; (b) thermal cycling plus damp heat test; (c) hail-impact test; (d) humidity freeze, water spray tests; (e) By-pass diode thermal, hot-spot test; and (f) off-axis damage tests.

1.6 Other Challenges Specific to Mass Production

In this section we depict the material availability and manufacturing potential for extending present technologies to a mass-production scenario. (We caution the reader that it is very likely that many new discoveries and inventions will appear that will make this analysis obsolete, but we still think the exercise has some value.)

The penetration of PV to supply about 20% of the world's electricity by 2025 should be about 100 GW per year. A production rate of 100 GW/year – 40% efficient (module efficiency) – will stress the steel market by approximately 2% and the glass market by about 10%, but should the lenses be made, like today, on a thick PMMA substrate, it would need 1.5 times the total current world production of acrylic. If we take into account that acrylic comes from oil, the perspectives are not too good for this material; thus, alternatives should be taken into account. Thin-film polymer on glass is already being used by some manufacturers. This might reduce the reliance on the oil product by more than one order of magnitude.

The 100-GW annual production rate will require an area of cells equivalent to 100 MW at 1 sun if the cells are to operate at 1000× under the concentrator optics. For multijunction cells based on germanium substrates 25 million wafers of 100 cm^2 are required. which is equivalent to 3.75 times the present annual production of electronic-grade germanium. Extraction from coal ash ensures total resources equal to 130 times the current yearly availability [42, 43]; however, if a migration of MJ solar cells to the abundant silicon substrates is successful, the stress on this material would be negligible.

The production of gallium metal is about 210 metric tons per year. With the previous hypothesis and assuming an active layer of about 10 µm, it is possible to produce about 1000 GW per year so that this material does not appear to be a drastic limitation to the PV growth.

Another challenge to high-level concentrator technology is given by the number of wafers and cells to be managed. The MJ solar cells are grown in a Metalorganic Chemical Vapor Epitaxy reactor. Assuming that a reactor can accommodate 12 wafers of the said size (presently they are somewhat smaller), and that including maintenance they may have 7 runs per day, 815 reactors will be necessary to grow the multilayer in the aforementioned 25 million wafers.

Regarding assembly, if we assume that cells are 1 mm^2 for the 1000× level, then the number of cells to be processed and interconnected is about 250 billion (250×10^9 per year. Current equipment used for the electronic chip market is limited to about three chips per second, which comes to (taking four cells per second to include tome for maintenance) 1982 the number of bonding machines to be built for cell assembly. Other manufacturing equipment will indeed be necessary for other tasks, but this paragraph, like the preceding one, aims at giving an order of magnitude of equipment that will be necessary for the manufacture of the cells and the concentrator modules.

We now consider the trackers. Assuming trackers of 50 m^2 (20 kW at 40% efficiency), the number of trackers required would be around 5 million per year.

All the preceding figures may be compared with those of the automobile industry. This industry manufactures more than 60 million cars per year and each car has 30 – 60 thousand parts; therefore, this industry is handling in the range of 1800 – 3600 billion (3600×10^9) parts per year. A concentrator PV module of 0.1 kW (with 250 cells) will probably not have more than 1500 parts in total; thus, we are talking about 1500 billion parts to be assembled; The PV industry, therefore, if based on concentrators for mass production, will be of a size not very different to the present size of the automobile industry.

1.7 Present Opportunities

The biggest opportunity probably comes from the rising awareness that CPV is necessary. One cannot witness the advances in MJ solar cells for space pro-

grams and remain unaltered. The immediate conclusion is that the only way of adapting these advances to the much bigger, terrestrial market is through the use of CPV. A number of programs (FULLSPCTRUM, DARPA, etc.) are also supporting the development of novel concepts based on sophisticated cells that will certainly have to be based on CPV.

A prominent example of this new interest is the presentation that Takashi Tomita, Corporate Director and Group General Manager of the Solar Systems Group of the Sharp Corporation – the biggest silicon solar cells producer in the World – presented at the special invited session organized on 8 May 2006 in the framework of the WCPEC-4 (the PV world conference) to deal with the transition to a world market. His talk was entitled 'Blazing A New Path to the Future' [44] and concluded:
I have explained in the above the current situations of photovoltaic industries and concentrator photovoltaic system towards next generation phase, not only silicon-based technology but also other technologies development including III-V compound cells is essential.

And then continued: *Concentrator type photovoltaic system will make a key role especially in the areas where direct sun irradiation is abundant. Technological breakthrough to overcome some of obstacles in dissemination of concentrator type photovoltaic system until now is getting ready and further electricity generation cost reduction by concentrator photovoltaic system is expected.*

This is not the only company, however, that has declared their interest in CPV. Other companies are probably more ready to enter the market. Among them, Isofotón, one of the top ten cell producers in the world (and a spin-off from the IES/UPM), which has a long standing R&D activity in this sector (in cooperation with IES/UPM) with the latest generation of optics and MJ cells, has made numerous declarations on their commitment to concentrators. For example, the magazine 'Energías Renovables', issued on the Internet on 22 July 2006, had an article entitled 'ISOFOTON to produce 5 MW of concentration cells for 2007'.

Newcomers are also entering the field. Jackie Jones wrote in Renewable Energy World (Internet issue of 2 September 2005):
The Guascor Group is investing in new manufacturing plant for CPV for the Spanish market, following an arrangement made with Amonix earlier this year (2005). Guascor Fotón is constructing a factory near Bilbao, Spain, to assemble the systems, apparently using solar cell assemblies shipped from Amonix's California plant. It is understood that Guascor plans to manufacture and install 10 MW *of CPV in Spain during 2006, and the capacity of the factory is expected to expand the following year.*

The expectations have not yet been totally fulfilled, but they say that they have already sold 1 MW, although nothing has yet been delivered. Assembly work is proceeding in their factory in Bilbao. To our knowledge, this is thus far the largest commercial activity in the world in CPV.

As a new venture-capital operation of Good Energies (who succeeded in launching Q-cells) and as a spin-off from the Fraunhofer Institute for Solar Energy (FhG/ISE), the company Concentrix, has been established. In a press release of 27 February 2006 they declared:
Concentrix will begin operating its first production line in midyear 2006 to manufacture concentrator modules. The company has already begun delivering demonstration plants to strategic partners. Commercial availability of concentrator photovoltaic power plants is scheduled for early 2007.

Furthermore, The Energy Blog published the on 19 February 2006 states:
SolFocus Inc., a spinoff from H2Go in 2004, and Xerox's Palo Alto Research Center (PARC) on 16 February announced a research collaboration to develop solar Concentrator PV (CPV) systems. The broad agreement is to jointly develop CPV systems that can deliver low-cost, reliable solar energy... Up to 2 MW *(megawatts) of the Gen 1 design will be installed in 2006-2007 at pilot sites in California, Hawaii, and Shanghai, China.*

According to these press releases, it looks like that 2007 will be the year in which PV concentration will unambiguously enter the market. Even if things go more slowly, there are enough participants who believe that this time concentrators will actually come into their own.

Despite that the American, German and Japanese markets that will not be absent, a good opportunity for CPV commercialization launching is linked to the feed-in tariffs in force in Spain, and more recently established in Italy, the two sunniest countries in the EU. Feed-in tariff opened the way to the 'power plant grid-connected market': the one dreamt of by concentrator makers over the past two decades.

Silicon feedstock shortage, consequence of fast market growth, is also giving an unexpected opportunity to concentrators to enter the market at prices similar to flat-plate power plants. In particular, the Spanish investors are anxious to install PV to profit from the good conditions brought in by the feed-in tariff and are disappointed by the lack of silicon cells on the market. They would be, in principle, most willing to accept concentrators.

Their enthusiasm decreases, however, when they learn that there is currently hardly any field experience in this technology. To amend this situation, a new initiative has been launched in Spain following plans developed by the IES/UPM. Below we reproduce some excerpts from the official presentation of this plan, which was presented on 8 March 2006:
Photovoltaic concentration technology has been the subject of investigation in Spain since 1976 and the country has attained an outstanding and well-regarded position for this work. For example, it was in Spain where the first monograph on the subject, published in Bristol in 1989, was authored and where, in Tenerife in 1998, the one of biggest photovoltaic concentration plants in the World was deployed. Nonetheless, this technology is not yet being manufactured. But we believe that the level achieved by prototypes is already ripe enough as to make its industrialisation imminent. The above-

mentioned Centre aims at being the global catalyst for this industrialisation.

In Spain we have climatic conditions well suited for concentration – that is to say, considerable direct radiation – that, combined with the economic conditions offered through Plan for the Promotion of Renewable Energies, is attracting a general interest to install such systems. Spanish companies are among the most advanced in the industrial development of this technology.

But the continuing lack of commercial applications means that approved norms suitable for photovoltaic concentration do not exist yet, nor have sufficient experiments been carried out on the precise prediction of the production of such systems, nor is it known for certain the costs of their installation and maintenance, etc.

The Centre will cover these aspects. In various places in Castilla La Mancha, plants of photovoltaic concentration with a total of 2.7 MW *using three or four concentration technologies that are now in development, in Spain and elsewhere in the World, will be set up. There is no precedent for such an operation.*

These plants will allow the selected companies to be able to move from the current state of prototypes-in-development to the manufacturing pilot line and to know the problems and costs of installation in the field, all of which is necessary for the commercial deployment of these technologies.

It is hoped that these actions will contribute to the achievement that photovoltaic solar energy begins a new path that should bring down prices sufficiently within the medium term to allow a massive penetration of solar energy.

The international call for tenders has already been issued and the deadline for bidding is 8 September 2006.If the call is satisfactorily resolved, we are sure that the reader will have more news on this.

1.8 Conclusion

During the 1970s photovoltaic concentrators looked like a promising solution to the stresses caused by the oil shock of 1973. The realization that the cost will not be as low as felt necessary in the short term aborted its deployment and held back the normal development of this technology for more than 30 years. Things clearly seem to have changed drastically. This is a special moment for PVC technology, because many positive factors have come together to promote the launching of industrial and commercial activity. Concentrator solar cell efficiency has almost reached 40%. Several companies are already entering the market and others have announced their forthcoming presence. Companies such as Sharp, which produces 25% of the world's solar cells (mostly silicon), strongly base their strategy on the new super-high-efficiency concentrators.

More than 1 MW has been already sold (but not yet delivered) in Spain. Other companies have already announced their products on the market.

These pioneering industrial and commercial activities must be helped as much as possible in order to avoid any significant problem at the beginning. A good guarantee for technical success is to qualify the system components before their deployment and to test the field performance of new products as soon as possible.

The new Spanish Institute of CPV Systems of Puertollano (Castilla La Mancha) will help in this process, guiding the companies and customers as much as possible to reach reasonable agreements that allow both, business to be carried out and their products to be improved as quickly as possible.

References

1. E.L. Burgess, DA Pritchard. Proc 13th Photovoltaic Specialists Conference (IEEE New York, 1978), 1121
2. G. Sala, G.L. Araújo, A. Luque, J. Ruiz, M.A. Coello, E. Lorenzo, F. Chenlo, J. Sanz, A. Alonso. Proc ISES International Solar Energy Society Silver Jubilee Congress (Pergamon, New York 1979), 1737
3. M. Claverie, A. Dupas, D. Esteve (CNRS, France). Proc 3rd E.C. Photovoltaic Solar Energy Conference (Reidel, Dordrecht, 1980), 381
4. M. Giuffrida, G.P. Tornielli, S. Pidatella, A. Repetto, E. Bellafronte, P.E. Zani. Proc 3rd E.C. Photovoltaic Solar Energy Conference (Reidel, Dordrecht, 1980), 391
5. A. Salim, N. Eugenio. Solar Cells 29:1 (1990)
6. R Nasby, C.M. Gardner, H.T. Weaver, F.W. Sexton, J.L. Rodriguez. Proc 15th IEEE Photovoltaic Specialist Conference, (IEEE, New York, 1981), 132
7. Sinton, Y. Kwark, R.M. Swanson. IEEE Trans Electron Dev 32:2553 (1985)
8. R. Winston, H. Hinterberger. Rev Sci Instrum 37:1094 (1966)
9. A. Luque, J.M. Ruiz, A. Cuevas, J. Eguren, J.M. Gómez Agost. Records of the 1st European Communities Photovoltaic Solar Energy Conference, 269–277, Luxemburg, 1977)
10. P. Benitez, M. Hrnandez, R. Mohedano, F. Muñoz. Proc SPIE 3781:22 (1999)
11. I. Tobías, A. Luque, J.C. Miñano. Int J Solar Energy 10:185 (1991)
12. A. Luque, J.C. Miñano, P.A. Davies, M.J. Terrón, I. Tobías, G. Sala, J. Alonso. Proc IEEE PV Specialists Conference (IEEE New York, 1991), 99
13. M. O'Neill, A. McDanal, R. Walters, J. Perry. Proc 22nd Photovoltaic Specialists Conference (IEEE, New York, 1991), 523
14. M.A. Green, A.W. Blakers, S.R. Wenham, S. Naranayan, M.R. Willison, M. Taouk, T. Szpitalak. Proc 18th Photovoltaic Specialists Conference (IEEE, New York, 1985), 39
15. T.M. Bruton, K.C. Heasman, J.P. Nagle. Proc 12th EC Photovoltaic Solar Energy Conference. (Stephens, Belford, 1994), 531
16. A. Luque, G. Sala, J.C. Arboiro, T. Bruton, D. Cunningham, N. Mason. Progr Photovoltaics 5:195 (1997)
17. G. Sala, I. Antón, J.C. Arboiro, A. Luque, E. Camblor, E. Mera, M. Gasson, M. Cendagorta, P. Valera, M.P. Friend, J. Monedero, S. González, F. Dobón, I. Luque. Proc 16th EC Photovoltaic Solar Energy Conference (James and James, London 2000), 2072

18. V. Garboushian, D. Roubideaux, S. Yoon. Proc 25th Photovoltaic Specialists Conference (IEEE, New York, 1996), 1373
19. A.W. Bett, B. Burger, F, Dimroth, G. Siefer, H. Lerchenmüller. High concentration PV using III-V solar cells. Proc 2006 IEEE 4th World Conf Photov Energy Conv
20. R.R. King, D.C. Law, C.M. Fetzer, R.A. Sherif, K.M. Edmondson, S. Kurtz, G.S. Kinsey, H.L. Cotal, J.H. Ermer, R.A. Sherif, N.H. Karam. Proc 20th European Photovoltaic Solar Energy Conf and Exhibition (WIP Munich 2005), 118
21. V. Diaz, L.L. Alvarez, J. Alonso, A. Luque, C. Mateos. Proc European PV Solar Conference (WIP, Munich, 2004), 2086
22. A.W. Bett, F. Dimroth, S.W. Gluntz et al. Proc 19th European PV Solar Conference (WIP, Munich 2004), 2488
23. Luque A. Solar cells and optics for photovoltaic concentration. Adam Hilger, Bristol, 1989
24. V.M. Andreev, V.A. Grilikhes, V.D. Rumyantsev. Photovoltaic conversion of concentrated sunlight. Wiley, Chichester, 1997
25. A. Luque. Progr Photovoltaics 9:303 (2001)
26. W. Shockley, H. Queisser. J Appl Phys 32:510 (1961)
27. K. Emery, M. Meusel, R. Beckert, F. Dimroth, A.W. Bett, W. Warta. Procedures for evaluating multijunction concentrators. Proc 28th IEEE Photovoltaic Specialists Conference, Anchorage, Alaska, 2000, 1126–1130
28. M.A. Green. Third generation photovoltaics. Advanced solar energy conversion. Springer, Berlin, Heidelberg New York, 2004
29. A. Marti, A. Luque (Eds.). Next generation photovoltaics: high efficiency through full spectrum utilization. Institute of Physics, Bristol, 2004
30. A. Luque, A. Martí, A. Bett, V.M. Andreev, C. Jaussaud, J.A.M. van Roosmalen, J. Alonso, A. Raüber, G. Strobl, W. Stolz, C. Algora, B. Bitnar, A. Gombert, C. Stanley, P. Wahnón, J.C. Conesa, W.G.J.H.H. van Sark, A. Meijerink, G.P.M. can Klink, K. Barnham, R. Danz, T. Meyer, I. Luque, R. Kenny, C. Christophides, G. Sala, P. Benitez. Solar Energy Mater Solar Cells 87:467 (2005)
31. C. Algora, V. Diaz. Fourteenth EC Photovoltaic Solar Energy Conference (Stephens, Belford, 1997), 1724
32. C. Algora, E. Ortiz, V. Díaz, R. Peña, V.M. Andreev, V.P. Khvostikov, V.D. Rumyantsev. IEEE Trans Electron Dev 48 840 (2001)
33. F. Dimroth, M. Meusel, C. Baur, A.W. Bett, G. Strobl. Proc 31st IEEE Photovoltaic Specialists Conference (IEEE, New York, 2005)
34. A. Luque. Solar Cells 3:355 (1981)
35. R. Winston, W.T. Welford. Optics of nonimaging concentrators: light and solar energy. Academic Press, San Diego, 1978
36. R. Winston, J.C. Miñano, P. Benítez. Non-imaging optics. Elsevier, San Diego, 2005
37. C. Algora, V. Diaz. Fourteenth EC photovoltaic solar energy conference (Stephens, Belford, 1997), 1724
38. I. Luque-Heredia, C. Martín, M.T. Mañanes, J.M. Moreno, J.L. Auger, J.L. Bodin, J. Alonso, V. Díaz, G. Sala. Proc 3rd World Conference on Photovoltaic Energy Conversion (Arisumi Printing, Osaka, 2003), 857

39. I. Luque-Heredia, J.M. Moreno, G. Quéméré, R. Cervantes, P.H. Magalhães. Proc 20th European Photovoltaic Solar Energy Conference (WIP, Munich, 2005), 2047
40. I. Luque-Heredia, R. Cervantes, G. Quéméré. A sun tracking error monitor for photovoltaic concentrators. Proc 3rd World Conference on Photovoltaic Energy Conversion, Hawaii, 2006
41. I. Luque-Heredia, G. Quéméré, P.H. Magalhães, L. Hermanns, A. Fraile de Lerma, A. Luque. Modelling structural flexure effects in CPV sun trackers. Proc 21st European Photovoltaic Solar Energy Conference, Dresden, 2006
42. PV FAQs, Does the world have enough materials for PV to help to address climate change? DOE/GO-102005–2113, June 2005
43. P.N. Gabby, U.S. Geological Survey, Mineral Commodity Summaries, (703), 648–4957, pbabby@usgs.gov, January 2006
44. T. Tomita. Blazing a new path to the future. Proc WCPEC-4, (IEEE, New York, 2006)

2 III-V Heterostructures in Photovoltaics

Zh.I. Alferov, V.M. Andreev, and V.D. Rumyantsev

2.1 Introduction

The sun is a huge, inexhaustible, absolutely safe energy source. There is a growing conviction that the power industry of the future has to be based on the large-scale use of solar energy. Reliance on the solar-powered industry must be considered not only as a sure choice but also as the only alternative for mankind as a long-term prospect. The cost of developing a new energy basis is never small. Fortunately, a scientific and technological basis exists as a result of the advancements of electronics, laser techniques and electric power engineering for spacecrafts, which may serve as the starting point for the development of the terrestrial solar electric power industry based on application of semiconductors.

Edmond Becquerel first observed the photovoltaic (PV) effect in a liquid-solid interface in 1839. W.G. Adams and R.E. Day carried out the first experiments with solid-state photocells based on selenium in 1876 [1]. It took more than a half a century for the creation of the first solar cells with an efficiency barely exceeding 1%. These were thallium sulfide photocells with a rectifying region [2]. The investigations were carried out under the leadership of Academician A.F. Ioffe, who in 1938 submitted a programme for the use of solar photovoltaic roofs for consideration by the USSR government. A decisive event was the creation in 1954 of silicon-based photocells with a p-n junctions that were characterized by an efficiency of 6% [3]. The first practical use of silicon solar arrays took place not on the Earth, but in near-Earth space: in 1958, satellites equipped with such arrays were launched – Russian 'Sputnik-3' and American 'Vanguard-1'.

For a long time semiconductor devices were applied mainly as converters of electricity into electricity of a different kind (alternating currents into direct ones, HF generation, switching, etc.) or in electronic circuits for information processing and translation (radio, communication, etc.). In addition to the "classical" semiconductor materials – germanium and silicon – III-V semiconductors were synthesized – first of them indium antimonide in 1950 [4]. The first solar cells with a p-n junction based on gallium arsenide were fabricated in the early 1960s. These cells were capable of operating even when being significantly heated. The first practical application of improved GaAs solar arrays to supply energy was even more exotic than in the case of silicon ones.

They provided the electricity supply for the Russian space probes 'Venera-2' and 'Venera-3' operated in the vicinity of Venus (1965), as well as for the moon cars 'Lunokhod-1' (1970) and 'Lunokhod-2' (1972).

The further progress of the solar cells was associated with the development of the semiconductor heterostructures, which have now become the basic approach in fabrication of the cells for both space and terrestrial applications. We discuss the history as well as the future prospects of solar energy conversion by modern photovoltaic cells based on III-V materials. These devices have now matured scientifically and technologically to such an extent that they may be regarded as a technical basis for large-scale solar power engineering in the future.

2.2 Early History of III-V Heterostructures

The idea of using heterojunctions in semiconductor electronics was put forward at the very dawn of electronics. In the first patent concerning the p-n junction transistors, W. Shockley [5] proposed a wide-gap emitter to obtain unidirectional injection. A.I. Gubanov first theoretically analyzed I-V characteristics of isotype and anisotype heterojunctions [6]. The important theoretical considerations at this early stage of heterostructure research, however, were done by H. Kroemer, who introduced the concept of quasi-electric and quasi-magnetic fields in a graded-band gap heterojunction and made an assumption that heterojunctions might exhibit extremely high injection efficiencies in comparison with homojunctions [7].

Initially, the theoretical progress was much faster than experimental realization. In 1966, it was predicted [8] that the density of injected carriers, could by several orders of magnitude, exceed the carrier density in the wide-gap emitter ("superjunction" effect). The most important peculiarities of semiconductor heterostructures were underlined at that time: superinjection of carriers; optical confinement; and electron confinement.

The realization of the wide-gap window effect was very important for photodetectors, solar cells and LEDs. It permitted considerably broadening and precise control of the spectral region for solar cells and photodetectors, and improving drastically the efficiency of LEDs. The main physical phenomena in double and single classical heterostructures are shown in Fig. 2.1.

It was necessary to find heterostructures where these phenomena could be realized. At that time general scepticism existed with respect to the possibility of creating an "ideal" heterojunction with a defect-free interface and, primarily, with theoretical injection properties. Even a very pioneering study of the first lattice-matched epitaxial grown single-crystal Ge−GaAs heterojunctions by R.L. Anderson [9] did not give any proof of the injection of carriers in heterostructures. Mostly due to this general scepticism, there existed only a few groups trying to discover an "ideal couple", which was, naturally,

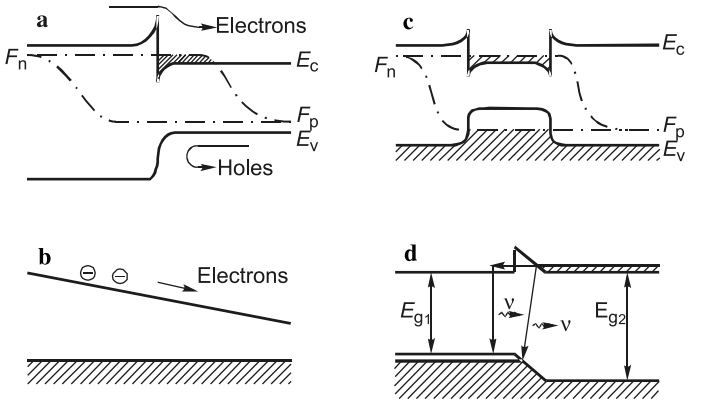

Fig. 2.1. Main physical phenomena in classical heterostructures. **a** One-side injection and superinjection; **b** diffusion in built-in quasi-electric field; **c** electron and optical confinement; **d** diagonal tunneling through a heterostructure interface

a difficult problem. There are many conditions that should be met in determining compatibility of thermal, electrical and crystallochemical properties, and for the crystalline and band structures of the contacting materials.

A fortuitous combination of a number of properties, i.e. a small electron effective mass and wide energy gap, effective radiative recombination and a sharp optical absorption edge due to the "direct" band structure, as well as a high electron mobility at the absolute minimum of the conduction band, ensured for GaAs, even at that time, a place of honour in semiconductor physics and electronics. Since the maximum effect is obtained by using heterojunctions between the semiconductor serving as the active region and more wide band material, the most promising systems explored in that time were GaP−GaAs and AlAs−GaAs. To be "compatible", materials of the "couple" should have, as the first and most important condition, close values of the lattice constants Fig. 2.2; therefore, heterojunctions in the AlAs−GaAs system were preferable.

Studies of phase diagrams and the growth kinetics in this system, and development of the liquid epitaxy (LPE) technique especially for heterostructure growth, soon resulted in fabricating the first lattice-matched AlGaAs heterostructures. When we published the first paper [10] on this subject, we were lucky to be the first to find out a unique – practically an ideal – lattice-matched system for GaAs, but as frequently happened, simultaneously and independently the same results were achieved by H. Rupprecht and J. Woodall at T. Watson IBM Research Center [11].

The progress in the semiconductor heterostructure field was subsequently very rapid. First of all, we proved experimentally the unique injection properties of the wide-gap emitters and superinjection effect [12], and the stimulated emission [13]. We also established the band diagram of the AlGaAs−GaAs

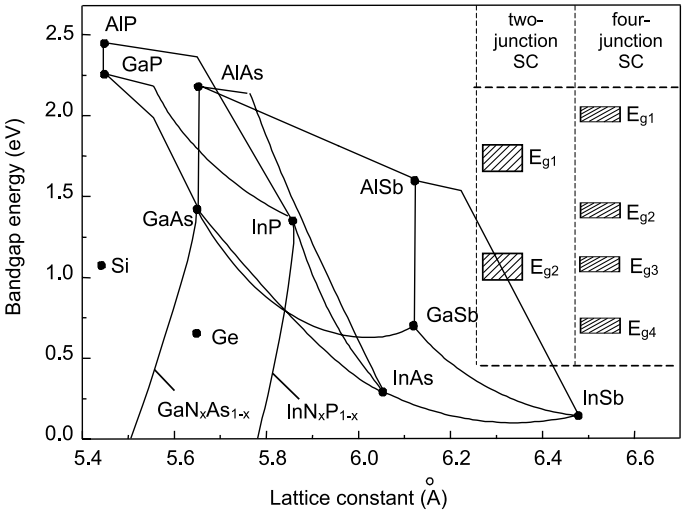

Fig. 2.2. Band gap Eg as a function of the lattice constant for Si,Ge, and III-V compounds and their solid solutions. Hatched rectangles correspond to Eg ranges for various materials that provide the highest efficiency of solar cells with two and four p-n junctions

heterojunction and carefully studied luminescence properties [14] and diffusion of carriers in a graded-band gap heterostructure. At the same time, the majority of the most important devices with realization of the main advantages of the heterostructure concepts were created: low threshold at room temperature heterolasers [15–18]; high effective LED [11, 19]; heterostructure solar cells [20]; heterostructure bipolar transistors [21]; and heterostructure p-n-p-n switching devices [22]. One of the first successful applications in industrial scale production was that of heterostructure solar cells in space research. AlGaAs solar cells have been installed on many Russian sputniks. Our space station "Mir" has been using them for 15 years.

At this early stage of the development of heterostructure physics and technology, it became clear that we needed to look for new lattice-matched heterostructures in order to cover a broad area of the energy spectrum. The first important step was taken in the works [23, 24], in which the various lattice-matched heterojunctions based on quaternary III-V solid solutions were proposed, which permitted independent variation of the lattice constant and the band gap. Soon, InGaAsP compositions were recognized as being among the most important ones for many different practical applications, especially lasers in the infra-red regions for fibre-optic communications [25] and in the visible regions [26].

In the early 1970s, ideal lattice-matched heterostructures were limited by the mentioned materials only. Later, this "world map" of III-V heterostructure

was drastically expanded (Fig. 2.2). Now it is necessary to add wide-band gap-III nitrides.

2.3 Photovoltaic and Related Phenomena in III-V Heterostructures

2.3.1 Sunlight Concentration: Both Effectiveness and Economy

Conversion of concentrated sunlight gives additional possibility for increasing the efficiency of solar cells. The generated photocurrent increases linearly with light intensity and the output voltage increases, in turn, with the logarithmic law; thus, light intensity following the generated power rises superlinearly with concentrating the radiation, so that the efficiency of photovoltaic conversion increases. The maximum calculated concentration ratio at the distance from the sun corresponding to the Earth's orbit is 46,200. This concentration ratio is usually set in the estimations of thermodynamically limited efficiency for different types of solar cells. Also, an assumption concerning ideal parameters of the cell material is relevant: only radiative channel of minority carriers' recombination should be valid. Specifically, for multijunction cells comprising several tens of cascades, the limiting efficiency is about 87%, which is very close to the Carnot cycle efficiency; thus, multijunction photocells, in addition to demonstrating the highest efficiency values to date and a good outlook for their rise in the nearest future, also have the best "fundamental" prospects.

The fact that GaAs-based heterostructure solar cells can operate efficiently at a significant (several hundred or even several thousand times) concentration of sunlight [27–30], and in this respect differ favourably from silicon cells, was pointed out as far back as the late 1970s and early 1980s. The first experiments to create concentrator-based photovoltaic modules with high-power AlGaAs/GaAs cells relate to that time [28]. Increase in photovoltaic conversion efficiency can be realized in practice, if a higher current does not produce a noticeable voltage drop across the internal resistance of a photocell. That is why a radical reduction in internal ohmic losses is a key problem in the development of concentrator solar cells. The prospects for an efficiency rise by operating with concentrators look tempting; however, the main motivating force in creating concentrator modules is the possibility of reducing the consumption of semiconductor materials for the generation of the required electric power proportional to the sunlight concentration ratio. In this case semiconductor photocells of relatively small area receive power from the sun in the focal plane of the concentrators (mirrors or lenses). These concentrators can be fabricated from relatively cheap materials. The contribution of the photocell cost to the solar module cost begins to be insignificant, whereas concentrator module efficiency depends directly on the efficiency of the employed photocells; thus, the prerequisites for economically justified ap-

plication of the most effective – even if expensive – photocells based on III-V compounds are being created.

2.3.2 Radiative Recombination Limitations

All semiconductor materials have a property, to a greater or lesser extent, to generate luminescence. Two very valuable ways of luminescence initiation exist. The first way is photoexcitation. Radiative recombination of electron–hole pairs photogenerated in a semiconductor is referred to as photoluminescence (PL). The internal quantum yield of PL may increase with increasing the intensity of illumination due to a tendency to saturation of possible non-radiative bulk and surface channels until the fundamental recombination mechanism of interband electron transitions becomes dominant. Starting from this illumination level, internal (and, correspondingly, external) quantum yield of PL is characterized by a constant value up to the range of "very high" illumination levels, when it may increase owing to generation of stimulated emission, or it may decrease due to activation of Auger recombination process.

The second way of the luminescence initiation is applicable to semiconductor samples having a p-n junction. In flowing the forward current, charge carriers are injected into the opposite region and recombine there. Radiative recombination of carriers injected under action of the external power source is referred to as the electroluminescence (EL). As a rule, the internal quantum yield of EL increases with increasing the current density through the p-n junction, owing to a tendency of both leakage, and non-radiative channel saturation, until the fundamental diffusion mechanism becomes dominant. Both factors – intense illumination and the current of high density flowing through the p-n junction – are the characteristic features of operation of solar cells converting the concentrated sunlight. It is clear that the luminescent radiation must play a noticeable role in operation of concentrator cells fabricated on the basis of direct-gap materials, such as GaInP and GaAs, in which the radiative recombination efficiency can be close to 100%. This is particularly related to the open circuit regime, when there is no photocurrent drain from a cell to an external electric load. Accounting for the luminescent phenomena permits understanding of some features of operation of solar cells on the basis of multilayer heterostructures, in particular of monolithic cascade solar cells. The detailed analysis of the luminescent phenomena in the solar cell structures is of prime importance and has allowed us to propose and realize in practice a set of effective luminescent methods for cell quality testing and efficiency evaluation [29].

The ability of a converting system to operate reversibly is, in general, a characteristic feature of a potentially very highly efficient system. In the case of photoelectrical converters, the reversibility principle implies a possibility to convert the sunlight into electricity, and vice versa, by means of one and the same device. Such a consideration is justified for a photocell, if its p-n

junction(s) is formed in a semiconductor material characterized by highly radiative recombination efficiency. This property is inherent in direct-gap III-V semiconductors. In particular, effective photon-assisted carrier transport may take place both within and between photoactive regions of the III-V-based solar cells. (It is noted that manifestation of this property was carried out by means of a comprehensive study of the experimental samples, heterostructures which played a very important role.)

2.3.3 Heterostructure As a Tool for Investigation of Semiconductor Properties

The most convincing evidence of an important role of the photon-assisted carrier transport is presented by the results of investigations of the solar cell heterostructures with intermediate conversion of radiation (Fig. 2.3) [29,30]. In such structures, the sunlight, after passing through a wide-gap "window" layer 1, is absorbed in the narrow-gap layer 2 and generates electron–hole pairs. The minority carriers are confined within this layer due to the existence of the interface potential barriers and recombine there producing secondary narrow-band PL radiation with quantum energy $h\nu_2$. In turn, PL radiation propagates into the cell structure and is absorbed in the vicinity of the p-n junction, creating minority carriers for photocurrent generation. If one considers the photoresponse spectrum of such a structure starting from the low-energy side, the p-n junction sensitivity can be estimated, because the incident light penetrates the p-n junction region without absorption in the narrow-gap layer. After "self-calibration" of the p-n junction, the absorption/re-emission mechanism in the narrow-gap layer is initiated that becomes apparent as a step down on the photoresponse curve. The ratio of the photoresponse signals after re-emission (P_2) and before it (P_0) is determined by the internal quantum efficiency of luminescence η_i. The value of η_i is then a result of calculation involving self-absorption coefficient of the

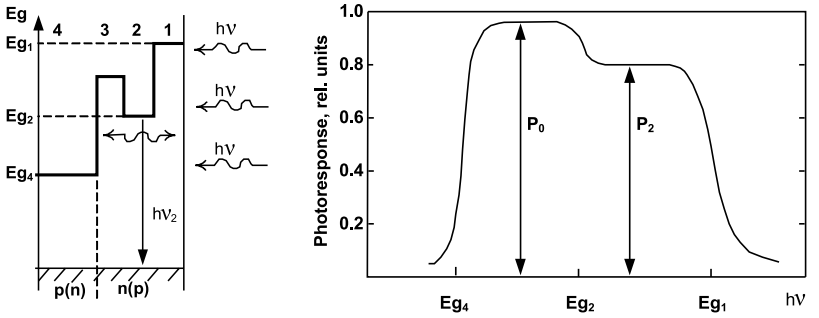

Fig. 2.3. Schematic of a heterostructure with intermediate conversion of radiation [43, 44], and photoresponse spectrum of a photocell based on such a heterostructure

isotropic luminescent light and refraction index of the semiconductor material. In the middle of 1970s, the method for η_i evaluation described above had been applied to investigations of the direct band-gap AlGaAs layers of the AlGaAs−GaAs heterostructures giving η_i values as high as $\eta_i = 95\%$ at the illumination intensity level of $10^{-5}\,\mathrm{W\,cm^{-2}}$ and $\eta_i = 97\%$ at $1\,\mathrm{W\,cm^{-2}}$ and room temperature [30].

At the same time, the first multilayer heterostructures of a new material – InGaP−InGaAsP lattice-matched with GaAs and GaAsP substrates – grown by liquid-phase epitaxy with the aim of visible laser development – had been studied. In particular, the internal quantum efficiency of 60% had been measured inInGaAsP photoactive layers at the illumination level of $10^{-4}\,\mathrm{W\,cm^{-2}}$ and 300 K [31]. The measured value increased up to $\eta = 80\%$ at $300\,\mathrm{W\,cm^{-2}}$. It is noted that difference in energy gaps between active layer and wide-gap $In_{0.5}Ga_{0.5}P$ emitters was only 120 meV, so that a significant rejection of the photogenerated carriers from the InGaAsP layer took place under estimating η_i values. Later [32], a possibility for higher η_i values (approximately 90%) at higher illumination intensities was demonstrated, as well as a tendency for further increase in it at larger energy-gap differences between the active layer and emitters.

Another method for η_i evaluation under photoexcitation consists of recording the PL spectra of a multilayer heterostructure (see Fig. 2.4). The short-wavelength incident light generates a luminescent line $h\nu_1$ in layer 1, which is nearest to the surface. Owing to the high refraction index of the structure and the isotropic character of the spontaneous luminescence, the main part of this luminescence ($> 95\%$) cannot leave the structure and is absorbed in the narrower-gap layer 3 generating a luminescent line $h\nu_3$. Withdrawal conditions for luminescence generated in layer 3 are similar to those in layer 1, if an additional absorbing layer (layer 5 in Fig. 2.4 which may be absorbing substrate) exists in the heterostructures. If η_i value in layer 3 is

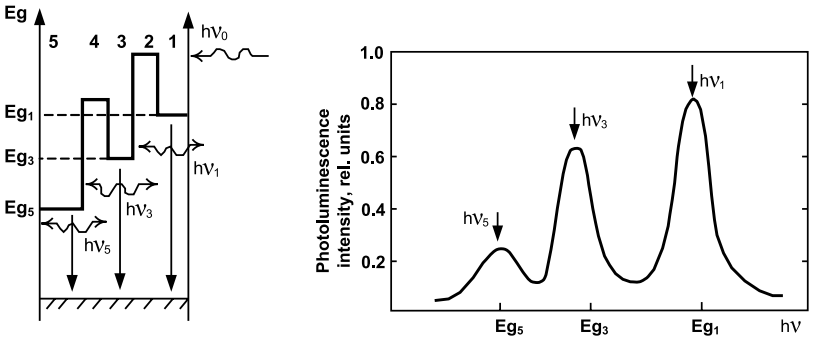

Fig. 2.4. Schematic of a heterostructure for η_i evaluation in the layer 3 by photoexitation, and the photoluminescence spectrum of such a heterostructure

100%, an amount of light of photon energy $h\nu_3$ going out from the sample is almost the same as of $h\nu_1$ – an amount of the light generated in layer 1; therefore, direct comparison of the areas under spectral contours of the lines, $h\nu_1$ and $h\nu_3$, is a good estimation for η_i value in layer 3 being made more accurate by accounting for self-absorption and some other factors.

In the middle of 1970s the method for η_i evaluation described above was applied to investigation of the AlGaAs/GaAs heterostructures giving η_i values of about 100% at room temperature [33]. Somewhat later, at direct photoexcitation of the luminescent region in double heterostructures without any additional absorbing layers (the samples realizing multipass effects for the luminescent light inside the structure), external quantum efficiency of photoluminescence as high as 75% was measured [34]. Also, η_i value in the range of $97.2\% + / - 0.2\%$ at room temperature had been confirmed. As for the LPE grown InGaP/GaAs heterostructures, in varying the thickness of the luminescent region in them in the range of $1.5 - 0.01\,\mu\text{m}$, interface recombination velocity as low as $5\,\text{cm}\,\text{s}^{-1}$ was demonstrated [35].

It would be interesting to renew corresponding investigations for the case of the modern metal-organic chemical vapor deposition (MOCVD)-grown (Al)InGaP/InGaAsP heterostructures optimized for conversion of concentrated solar energy. In fact, importance of accounting for photon-assisted carrier transport between sub–cells in the heterostructure of a multijunction cell begins to be obvious at high-enough η_i values. Corresponding investigations would be especially important for promotion of such a new concept of solar energy conversion as thermophotonics [36]. Indeed, for realizing the benefits of this approach a very high external electroluminescent quantum efficiency is required. Achievements in the field of MOCVD growth could yield gain in quality of the heterostructures exceeding that obtained recently for GaAs-based photoactive regions [37].

2.4 Concentrator III-V Heterostructure Solar Cells

2.4.1 AlGaAs/GaAs Single-Junction Cells

The design of AlGaAs/GaAs heterostructure solar cells [20] opened up new fields in solar energy conversion. The aforementioned studies were performed in the fabrication and investigation of "ideal" heterojunctions in the AlAs/GaAs system, which were aimed at improving solar cells, among other things. One of the results of these studies was the technical implementation of the idea of a wide-gap window for solar cells. The aim was to protect the photoactive region of a cell against the influence of surface recombination. Defect-free heterojunctions between AlGaAs (wide-gap window) and p-n GaAs (photoactive region) were successfully formed, which provided ideal conditions for the photogeneration of electron–hole pairs and their collection by the p-n junction. Since photocells with a GaAs photoactive region turned

out to be even more radiation resistant, they quickly found an application in space arrays, despite their significantly higher cost compared with silicon cells. An example of a large-scale application of AlGaAs/GaAs solar cells was the solar array installed in 1986 on the Russian space station 'Mir' (Fig. 2.5).

Silicon and GaAs largely meet the requirements for solar cell fabrication as perfect semiconductor materials. If these materials are compared in terms of their suitability for fabricating solar cells with a single p-n junction, the maximum possible efficiencies of photovoltaic conversion are nearly alike and are close to the absolute maximum for a single-junction photocell. Clearly, the undoubted advantages of silicon are its wide natural abundance, non-toxicity and relatively low price. All these factors and the intensive development of the industry of semiconductor electronic devices have determined the extremely important role of silicon photocells in the formation of solar photovoltaics. Despite the considerable efforts applied to the development of various types of thin-film solar arrays, crystalline silicon (both in single- and polycrystalline modifications) still makes the greatest contribution to the world's production of solar arrays for terrestrial applications.

Until the mid-1980s, the development of solar cells, both silicon and GaAs, was based on relatively simple structures and technologies. A planar structure with a shallow p-n junction produced by diffusion was used in silicon photocells. Epitaxial technologies were necessary for the formation of an AlGaAs wide-gap window on GaAs photocells. The relatively simple LPE technique was applied, which was derived earlier for the fabrication of the first generation of heterolaser structures. In the case of photocells, only one wide-gap p−AlGaAs layer had to be grown, whereas the p-n junction was formed by

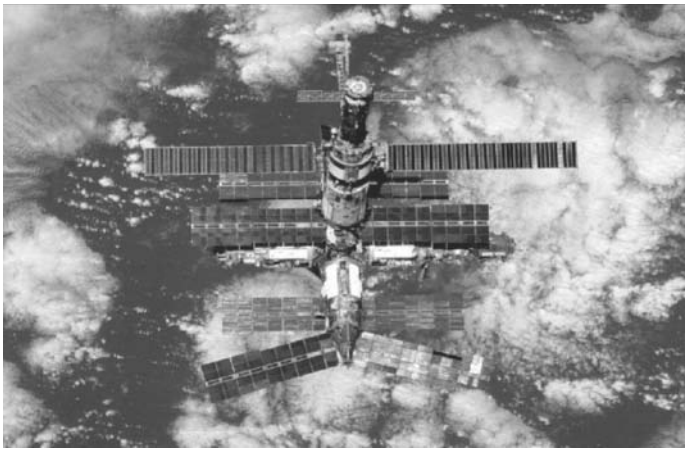

Fig. 2.5. Space station 'Mir' equipped with an AlGaAs/GaAs heterostructure solar cell array

the diffusion of a p-type impurity from the melt into the base material of n−GaAs (Fig. 2.6a).

The further progress in the field of GaAs-based solar cells was stimulated by the both improvement of LPE technology [38] and the application of new epitaxial techniques for heterostructure growth. The main achievement here was the MOCVD technique. This method was derived in the course of the development and improvement of injection lasers, LEDs and second-generation photocells based on III-V compounds.

The following improvements were introduced into the structure of solar cells. Firstly, the wide-gap AlGaAs window was optimized, and its thickness became comparable with that of the nano-sized active regions in heterolasers. The AlGaAs layer served also as the third component in the triple-layered antireflection coating of a photocell (ARC; Fig. 2.7a). A heavily doped narrow-gap contact layer was grown on the top of the wide-gap AlGaAs window, and it was removed during the post-growth treatment in the areas between the contact stripes. Secondly, a back (behind the p-n junction) wide-gap layer was introduced, which ensured, along with the front wide-gap layer, a double-sided confinement of photogenerated carriers within the region of light absorption (Fig. 2.6d). The recombination losses of carriers before their collection by the p-n junction were reduced. At this stage of the optimization of single-junction AlGaAs/GaAs photocell heterostructures, the newly developed MOCVD technique was still competing with the modified low-temperature LPE technique.

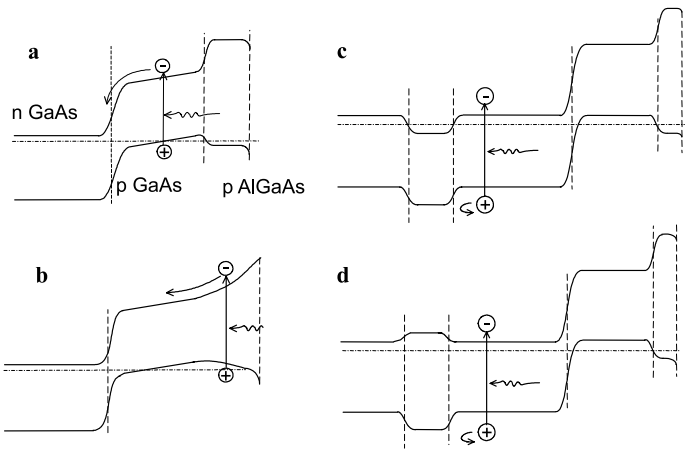

Fig. 2.6. Band diagrams of p−AlGaAs−p−n−GaAs heterojunction solar cells: **a** a structure in which a p−GaAs layer with a built-in electric field is produced by Zn diffusion into an n−GaAs base during the growth of a wide-gap p−AlGaAs layer; **b** graded band gap structure with a high built-in electric field; **c** a structure with a back potential barrier formed by a heavily-doped n^+−GaAs layer; **d** a structure with a back wide-gap layer

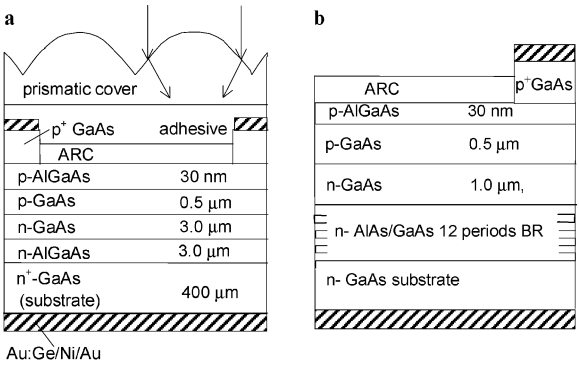

Fig. 2.7. Schematic diagrams of AlGaAs/GaAs single-junction multilayer solar cells. **a** LPE grown structure with a back potential barrier and thin wide-gap p−AlGaAs window. **b** MOCVD-grown solar cell structure with an embedded Bragg mirror. The Bragg mirror comprises 12 pairs of AlAs(72 nm)/GaAs(59 nm) layers; it is tuned to wavelength $\lambda = 850$ nm with a reflectance of 96%. As a result, a double pass of the long-wavelength light through the structure is attained,which allows the base n-layer thickness to be reduced to $1 - 1.5\,\mu$m

For these structures the record efficiency of 27.6% for illumination with the concentrated AM1.5 sunlight was measured in MOCVD-grown solar cells (this value is an absolute record for photocells with a single p-n junction) [39]. At the same time, the record efficiency of 24.6% for single-junction cells at illumination with a 100× concentration of AM0 sunlight still belongs to LPE-grown solar cells [40, 41]. Also, the highest efficiencies for high concentration ratios in the range of $1000 - 2000$ suns (AM1.5d) were measured in the LPE-grown AlGaAs/GaAs cells (Fig. 2.8): 26.2% (1000×) and 25.0% (2000×) [42]. These cells can operate under ultra-high sunlight concentration with efficiency as high as 23% at 5800 suns (AM1.5d) [43].

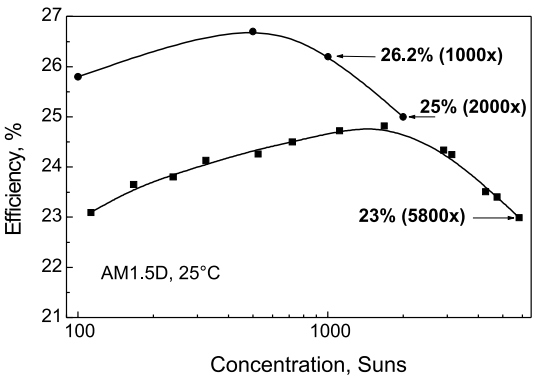

Fig. 2.8. Efficiency as a function of sunlight concentration in the LPE grown AlGaAs/GaAs single-junction solar cells [42, 43]

In MOCVD-grown AlGaAs/GaAs solar cell structures, a single wide-gap AlGaAs layer, which forms the back potential barrier, can be replaced by a system of alternating pairs of AlAs/GaAs layers making up a Bragg mirror (Fig. 2.7b). The wavelength of the reflection peak for such a mirror is chosen in the vicinity of the absorption edge of the photoactive range, so that the long-wavelength light that was not absorbed in this region during one passage can be absorbed during the second passage after reflection from the mirror [44]. At the same time, the wide-gap mirror layers continue to serve as the back barrier for photogenerated carriers. In these conditions, the thickness of the photoactive region can be reduced by half without loss of current as compared with the thickness of structures without a mirror. This factor led to a significant increase in the radiation resistance of such a type of photocells, because the amount of lattice defects generated under irradiation by high-energy particles decreased proportionally to the thickness of the photoactive region.

Apart from implementing the scientific and technological achievements in the development of heterolaser structures in the structures of solar photocells, the application of new epitaxial techniques made it possible to resolve several strictly "photoelectric" problems. The use of the non-equilibrium epitaxial conditions and the superlattice approach made it possible to grow perfect GaAs based heterostructures on a germanium substrate. From this point onwards, heterophotocells on germanium become the main candidates for applications on the majority of spacecrafts. The decisive factor here is mechanical strength of germanium, which is higher than that of GaAs previously used for substrates; therefore, the arrays composed of GaAs-based photocells on germanium are comparable in weight and strength with silicon ones but outperform them in efficiency and radiation resistance.

2.4.2 Tandem solar cells

The idea of tandem solar cells began to be discussed in the early 1960s and was considered to be promising; however, increasing the efficiency seemed a long way away. The situation started to change in the late 1980s, when many research groups concentrated their efforts on developing different types of dual-junction solar cells (Figs. 2.2, 2.9).

In the first stage, the best results on efficiency were obtained in mechanically stacked photocells; however, everyone understood that the really promising cells would be those with a monolithic structure. Researchers from the National Renewable Energy Laboratory (USA) were the first to develop such structures [45]. Using germanium substrates and MOCVD technique, they grew multilayer structures matched by their lattice constant, in which the upper photocell had a p-n junction in the $In_{0.5}Ga_{0.5}P$ solid solution and the lower one was in GaAs. The cells were electrically connected in series by means of a tunnel p-n junction specially formed between the cascades. Efficiency of 30.2% (AM1.5d,180×) was obtained in these cells.

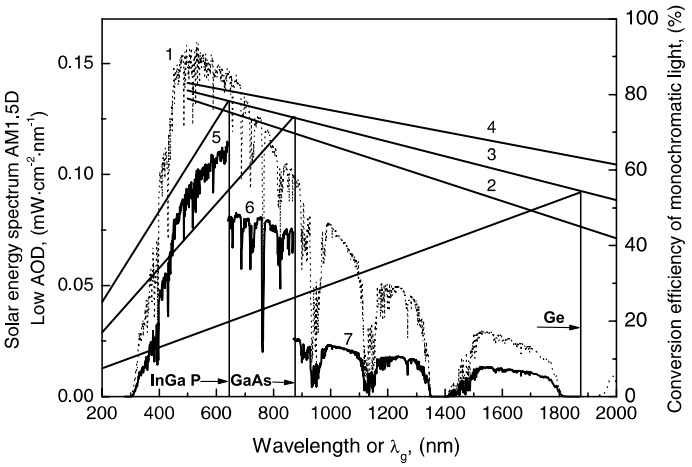

Fig. 2.9. Curve 1, the AM1.5D low AOD energy spectrum for the non-concentrated sunlight. Straight lines 2, 3, and 4 are the maximum "monochromatic" efficiencies of an ideal solar cell for photocurrent densities $j_{\rm ph} = 0.1$, 1.0, and 1.0 A/cm^2, respectively; they depend on the cutoff wavelengths of the semiconductor materials. Slanting lines on the left represent the dependences of the conversion efficency in ideal solar cells based on $In_{0.5}Ga0.5P$, GaAs and Ge materials at $j_{\rm ph} = 1.0$ A/cm^2. Curves 5, 6, and 7 show the fraction of solar energy converted to electric power in the corresponding cascades that make up a solar cell with three p-n junctions

At the same time, the interest to triple-junction cells was growing. As a consequence of well-directed efforts, efficiency as high as 39% (AM1.5D,low AOD,236×) has been demonstrated in GaInP/(In)GaAs/Ge cells [46]. Despite such impressive results in the monolithic tandem cells' development, several research groups have been continuing to direct their efforts towards evolution of the mechanically stacked multijunction cell concept started in 1989 by Fraas and Avery with the demonstration of a 32.6% (AM1.5D,100×) efficient concentrator GaAs/GaSb mechanically stacked dual junction cell [47]. Later, the monolithic concept was combined with mechanical approach for the GaInP/GaAs−GaSb cells; however, the main motivating force in creating concentrator modules was the possibility of reducing the consumption of semiconductor materials in proportion to the sunlight concentration ratio in generating the required electrical power. In this case, mirrors or lenses fabricated from relatively inexpensive materials could concentrate sunlight onto semiconductor photocells of a relatively small area, located in the focal plane of the concentrators. The contribution of the cost of the photocell to that of the solar module became insignificant, although the efficiency of the module depended directly on the efficiency of the photocells employed. This is an essential prerequisite for an economically justified application of the most effective, though expensive, photocells based on III-V compounds.

The Ioffe Institute has started the activity in the multijunction concept in the early 1990s with developing the top GaAs cell by the low-temperature liquid-phase epitaxy technique and a bottom InGaAs or GaSb cell by LPE and Zn diffusion techniques [48]. Efficiency as high as 28.2% (AM0,70×)was obtained in these mechanically stacked tandems. Putting into operation the modern AIX 200/4 reactor equipped with EpiRas 2000TT unit (real time in-situ epitaxy monitoring tool) has stimulated the development of high-efficiency monolithic GaInP/GaAs dual-junction cells (Figs. 2.10, 2.11, 2.12), which also can be used in mechanical stacks with the bottom GaSb cells. It is noteworthy that the EpiRas system provides simultaneous measurements of the different characteristic parameters by the following three methods: normalized reflection spectroscopy; reflection anisotropy spectroscopy (RAS); and emissive pyrometry. This allows obtaining data concerning the real temperature of the growth surface, growth rate, thickness of the layers, composition of ternary alloys, doping levels, surface reconstruction and interface quality. Permanent recording the RAS signal during wafer-heating process makes it possible to measure the wafer deoxidation temperature. The surface

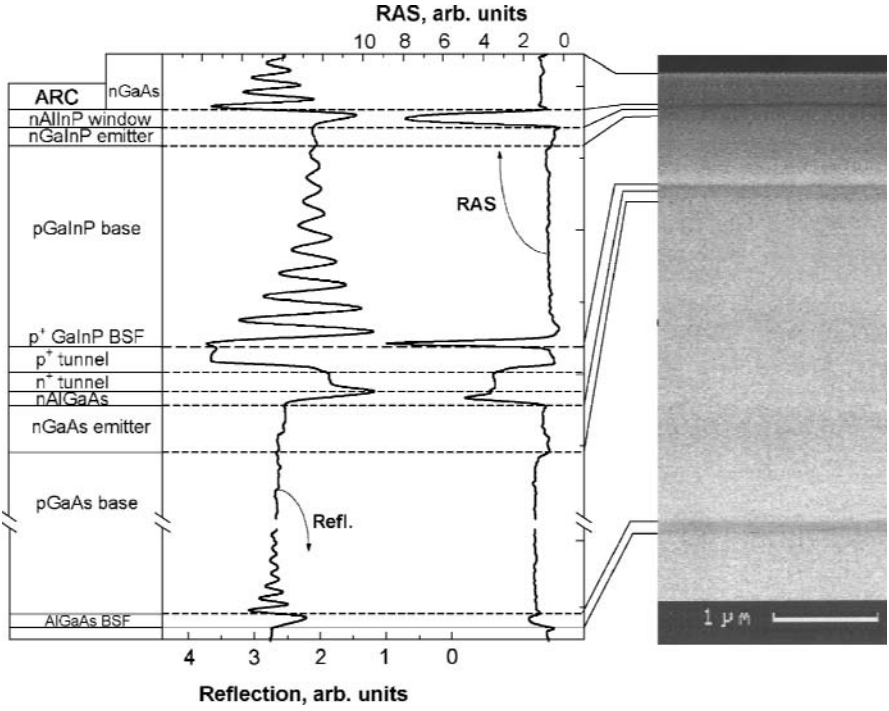

Fig. 2.10. GaInP/GaAs monolithic dual-junction cell structure: cross-sectional diagram *left*; time resolved curves of light reflection (at $h\nu = 2\,\mathrm{eV}$) and RAS (at $h\nu = 3.5\,\mathrm{eV}$) recorded during the structure growth (in the middle); scanning electron microscope image of the structure *right*

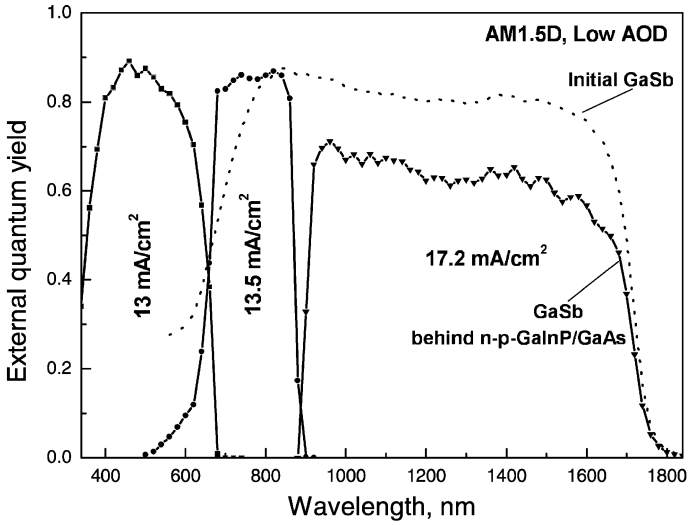

Fig. 2.11. Spectral response of a hybrid GaInP/GaAs (monolithic) / GaSb mechanically stacked triple-junction cell

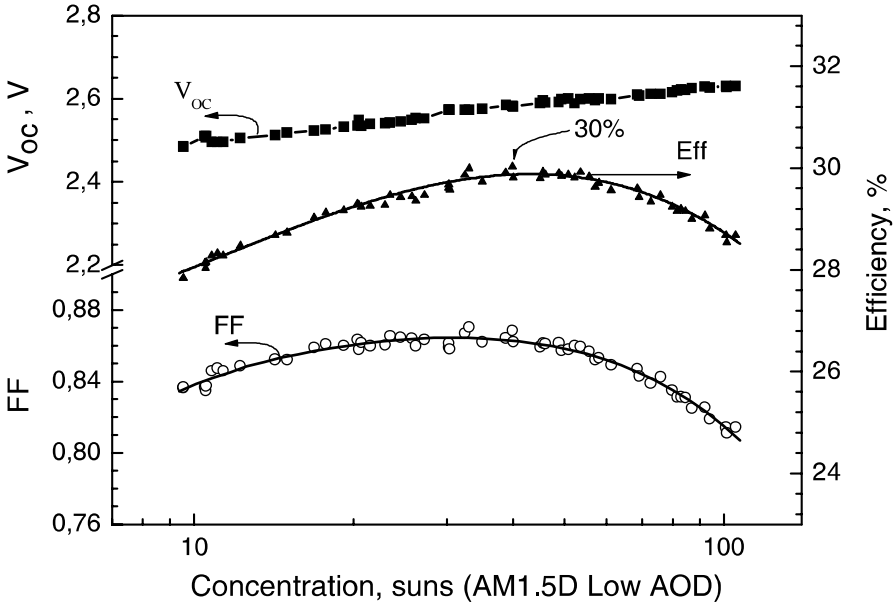

Fig. 2.12. Efficiency, V_{OC} and FF versus sunlight concentration for a GaInP/GaAs dual-junction cell

and interface roughness can be estimated as well. Due to difference in refraction indices of the growing materials, oscillations arise on the time-resolved light reflection curve. Attenuation of these oscillations due to increase in absorption in the growing layer is used for determining the composition in the case of the ternary alloys, whereas period of oscillations is used for growth rate and layer thickness calculations. Examples of data obtained from EpiRas system are shown in Fig. 2.8. Layer parameters calculated with the help of these data are in good agreement with those measured by means of the scanning electron microscopy, secondary ion mass spectroscopy and X-ray diffractometry.

The maximum efficiency is above 30% at a concentration ratio of $30-50\times$ (Fig. 2.12) in the developed dual-junction cells [49]. Gradually decreasing the absorption losses in InGaP/GaAs top cell with thinning GaAs or with lowering its doping level gradually increases transmittance, which allows obtaining higher values of the photocurrent density in the bottom GaSb cell in mechanical stacks (Fig. 2.11). The GaSb cell efficiency of 5.0–5.9% (50 – 400 suns) has been measured behind a GaInP/GaAs dual-junction cell based on a 100 μm GaAs substrate. The efficiency of hybrid (monolithic/mechanically stacked) GaInP/GaAs−GaSb cells is 35% at 50 – 100 suns (AM1.5D) [49]. (More detailed description of multijunction solar cells is presented elsewhere in this book.)

It may appear that we have paid too much attention to the development of complicated and expensive photocells formed from III-V compounds. Being developed for use in a relatively narrow and specific field of energy supply, i.e. space, do they hold any promise for use in the large-scale photovoltaics of the future? We believe that the answer is positive, and that there exist strong arguments for this conclusion.

The structure of a triple-junction solar cell is complex, and it will become even more complicated after the development, for example, of four- and even five-junction photocells; however, the epitaxial growth of such structures is a completely automated process, the success of which is totally dependent on the progress made in the base technology. The consumption of the initial materials (gases in the MOCVD technique) depends only slightly on the number of cascades. Since all photoactive regions are, as a rule, made of direct-band materials, the total thickness of the epitaxial structure grown is only a few micrometers.

The cost of an epitaxial structure is largely determined by its substrate. As mentioned previously, the use of a germanium substrate, which was foreign to III-V materials, enabled us to improve the operational parameters of space solar arrays. In fact, this has resulted in the "second birth" of the technology of germanium, which was the first classical material in semiconductor electronics but was later superceded by silicon. The cost of germanium as a substrate material is lower than that of GaAs used for this purpose, to say nothing of its technological merits (mechanical stability in post growth treatment)

and the fact that it can be included in the process of photovoltaic conversion in a cascade structure; however, looking back at the successes achieved in nanoheterostructure technologies, one may suppose that germanium, now a substrate material, will probably be superseded again by silicon, which is an even cheaper and technologically more convenient material. Research in this area is already under way; thus, the application of high-tech methods in the production of photocells based on III-V compounds may result not only in a radical increase in efficiency (in multijunction structures), but also a radical decrease in the cost of heterostructure photocells.

We now consider the prospects for increasing efficiency in tandem solar cells. The experience to date in the development of triple-junction photocells gives a reason to hope for achieving higher efficiency in four-, five- and maybe even more multiple-junction structures. There are no scientific or theoretical doubts that these hopes will be justified when suitable materials for intermediate cascades are found and grown to the appropriate quality. The search for these materials is underway, and here several areas may be singled out.

A 'traditional' direction is 'merely' the synthesis of new materials. Among III-V materials, these are semiconductor nitrides and borides, which have still found little or no commercial application. There is already considerable technological experience of wide-gap nitrides (grown by the MOCVD technique), motivated by the bright prospects of revolution in lighting technology. It is quite likely that we will witness the general replacement of hot mercury and incandescent tungsten in lighting devices by "cold" structures based on III-V materials of micrometer thickness; however, more favourable for tandem photocells are narrow-gap materials, which are better lattice-matched (in lattice type and lattice constant) with the materials currently used in triple-junction structures. These may be, for example, GaInNAs solid solutions (Fig. 2.2), which are currently being intensively studied. It is noteworthy that complication of the photocell structure, namely, the transition to multijunction structures, reduces the requirements for the bulk properties of the materials used. Indeed, the larger the number of junctions, the thinner the photoactive region in each junction and the weaker the effect of such parameters as the minority carrier diffusion length on the efficiency of the device. The method of compensating insufficiently good bulk properties of a material by technologically perfecting the cascade structure has also begun to be used in the development of new types of thin-film solar arrays.

We now discuss some other possible ways of improving solar cells. We refer to earlier experience in the development of semiconductor electronics, in particular, III-V lasers (Fig. 2.13). Until now, two stages could be distinguished in this development. The first stage is associated with the creation of heterostructures; the second, with the creation of nanostructures. In both cases, the main initial ideas were directed toward improving injection lasers and developing technologies for their fabrication. In the 1970s a tradition was even established according to which the parameters of injection heterolasers

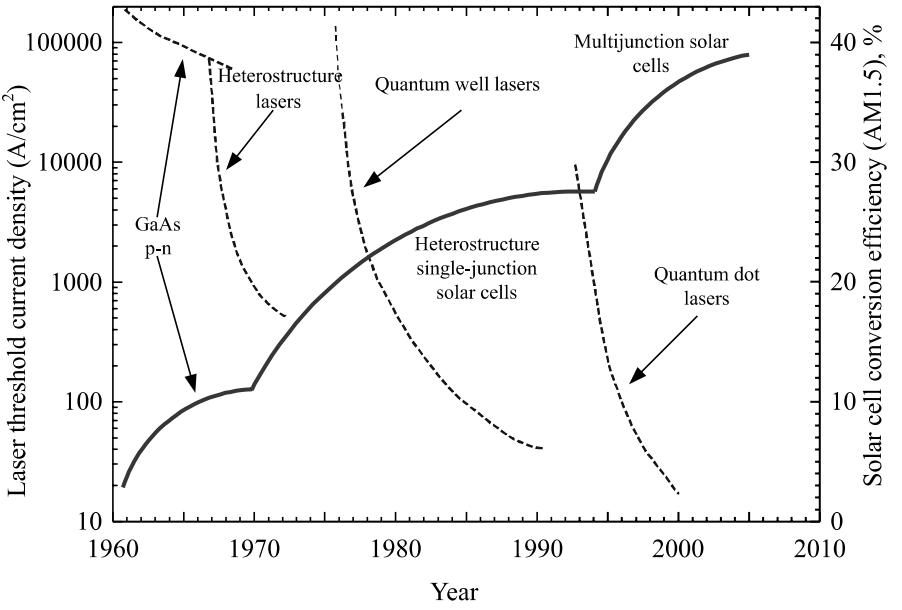

Fig. 2.13. Evolution of parameters of injection lasers and solar cells based on III-V heterostructures. Dashed lines *left axis*, the evolution of threshold current for three generations of injection lasers. Solid lines *right axis*, the evolution of efficiency in solar cells based on different structures

produced by a particular technique always served as a criterion of perfection for this technique. The definition a "laser-quality material" implied that, owing to high crystal perfection, a given heterostructure would be capable of operating at the super-high excitation densities necessary for lasing. Analyzing current trends in the design of third-generation injection lasers, we find primarily a transition to quantum dot (QD) structures [50].

In the structure of multijunction solar cell, in addition to the use of newly created materials with the desired absorption spectrum, it would probably be possible to improve the characteristics of commutating tunnel diodes (increase the peak current) by introducing superlattices created from vertically correlated QDs between the n^+ and p^+ layers. Additionally, other proposals, including old ones, for the enhancement of photovoltaic converter efficiency, the realization of which necessitates 'newly constructed' materials, also exist.

2.4.3 Approaches Alternative to Tandem

A new approach involving the use of materials with QDs has been proposed for solar cell development: the creation of a photoactive medium with an "intermediate band" [51]. Semiconductor material for such cells should have an intermediate half-filled (or metallic) band close to the centre of the for-

bidden gap. In addition to the conventional abandoning electrons from the valence to the conduction band by absorption of high-energy photons, abandoning to/from intermediate band to the conduction band can be realized by absorption of low-energy photons. This three-photon effect ensures a better utilization of the solar spectrum. Voltage degradation is expected to be prevented by the existence of three separated quasi-Fermi levels, each one related to each of the existing bands. The maximum efficiency of 63% was calculated for a cell of the band gap of 1.95 eV with the intermediate band Fermi level located at 0.71 eV from one of the bands. The generalization of this concept to more than two intermediate band gaps (multiband solar cells) gives the maximum theoretical efficiency of 86.8% that is identical to the efficiency of a large stack of tandem cells. Low-dimensional structures can constitute a way for engineering the intermediate-band concept. In addition, quantum mechanical calculations have shown that, in principle, it is possible to arrange atoms of a bulk material in such a way that it can exhibit the required intermediate band.

Solar thermophotovoltaics (TPV) [52] is based on the principle of intermediate conversion of highly concentrated solar radiation into radiation of a heated (up to 1200 – 2000 °C) selective emitter with following photovoltaic conversion of this radiation by a low-band gap ($Eg = 0.5 - 0.8$ eV) photocell. Significant reserves for increase in solar TPV efficiency lie in possibilities for secondary action of photoconverter on radiation source (emitter of photons), that is, the non-used photons can be reflected back to the radiator keeping it hot. Such a possibility is completely absent in solar power systems; therefore, the TPV generator is a complex and more closed system which should be more effective if the principle of radiation recirculation is used. An interesting way for TPV converter efficiency increase is the development of selective emitters matched to the PV cells. Such a selective emitter should radiate strongly at $h\nu > Eg$ and weakly at longer wavelengths. A similar role is played by an optical filter. This component is usefully included in the TPV system to return sub-bandgap-energy photons back to the emitter to re-heat it. This optical element can be made as a dielectric stack (deposited on the cell or emitter surface, or arranged as a separate component) or as a metallic reflector on the back surface of the cells. In other words, combining the filters, metal reflectors on the cell back and selective emitters, we have considerable room for shaping the spectrum of the energy used by a cell. The theoretical conversion efficiency of the TPV concept is 84.5% and the expected one in practice is around 40%. The possibility of high efficient PV conversion of selective radiation has been confirmed by experiments with conversion of the monochromatic radiation with photon energy just a little higher than the cell band gap. An efficiency of 56% was measured in GaAs-based cells under monochromatic illumination at wavelength of 850 nm and $ETA = 49\%$ was detected in a GaSb cell at 1680 nm wavelength [53].

Photocells with graded band gap in photoactive region give an additional possibility for the efficiency increase at a high excitation level, at which the quantity of generated electron–hole pairs is higher than quantity of majority carriers, through the conservation of carrier energy. If a cell heterostructure has a gradient (ΔEg) of the band gap with Eg reduced from the front surface, the additional voltage arises owing to separation of electrons and holes generated by photons of different energies in the different parts of the graded band gap layer. In the case of a very high excitation level, the value of this additional voltage can be close to $\Delta Eg/q$ [54]. The theoretical efficiency limit of this approach is the same as for an infinite tandem cell stack; however, to utilize this effect, new semiconductor materials with special properties should be developed. Low-dimensional quantum well/dot structures open the room for preparation of such materials and cells. A short period of superlattices were grown by MBE for fabrication of the graded band gap layers in the laser structure [55]. In this way, both an excellent heterointerface smoothness and a high internal quantum efficiency were obtained. The lowest threshold current was, for a long time, a world record for semiconductor injection lasers and a good demonstration of the superlattice application for fabrication of graded band gap layers of high quality.

Hot carrier cells should utilize the energy of photogenerated carries before their thermalization and collection by a p-n junction. The limiting efficiency of this approach is the same as for tandem cells. However, to realize this approach, carrier cooling rates would have to have been sufficiently reduced, or radiative recombination rates sufficiently accelerated; thus, the special materials with particular band structures should be developed for these cells.

Multiple electron-hole pair cells with the quantum efficiency higher than unity also allow increased efficiency. The theoretical efficiency for an idealized cell of such a type is the same as for an infinite tandem cell stack. Many electron–hole pairs should be generated by each incident photon in this case. The higher-than-one quantum efficiency behaviour was actually found, although very close to one, for high-energy visible photons and for UV photons; however, competitive processes of the carrier energy relaxation are so efficient that they have not allowed noticeable improvement in solar cell performance until now.

All of the foregoing proposals are related to the quest to increase (first theoretically and then in practice) the efficiency of solar photovoltaic conversion to the thermodynamic limit of 93%, which is determined by the Carnot cycle.

2.5 Conclusion

It is impossible to imagine modern solid-state physics without semiconductor heterostructures. Heterostructures and, particularly, double heterostructures, including Quantum Wells, Wires and Dots, are the subject of research

in two-thirds of the semiconductor physics community. If the possibility of controlling the conductivity type of a semiconductor material by doping with various impurities, and if the idea of injecting non-equilibrium charge carriers was to inject the seeds themselves, from which semiconductor electronics was developed, heterostructures could make it possible to solve the considerably more general problem of controlling the fundamental parameters of semiconductor crystals and devices: band gaps; effective masses of charge carriers and their mobilities; refractive indices; electron energy spectrum; etc.

The advancements of the physics and technology of semiconductor heterostructures has resulted in remarkable changes in everyday life. Heterostructure electronics is widely used in many areas of human activity. It is hardly possible to imagine our present age without telecommunication heterolaser-based systems, light-emitting diodes, heterostructure bipolar transistors and low-noise HEMTs for high-frequency applications. Heterostructure lasers are in the majority of homes, in the form of CD and DVD players. In the very near future regular lighting will be carried out by heterostructure light-emitting diodes of 'high-brightness' design.

At present, III-V heterostructure solar cells are already widely used for space applications. Further progress of terrestrial application of III-V solar cells is associated with the development of cells with efficiencies exceeding 45% at concentrated sunlight. These devices can form a technical basis for large-scale solar power engineering in the future. In this case considerable amounts of electrical energy supplying our homes will be generated in heterostructure solar cells illuminated by the sun through the concentrators.

References

1. W.G. Adams, R.E. Day. Philos Trans R Soc Lond 167, 313 (1877)
2. A.F. Ioffe, A.V. Ioffe. Phys Z Sowjetunion 7, 343 (1935)
3. D.M. Chapin, C.S. Fueller,G.L. Pearson. J Appl Phys 25, 676 (1954)
4. N.A. Goryunova, Dissertation, Leningrad State University, Physicotechnical Institute, Leningrad (1951)
5. W. Shockley. Circuit Element Utilizing Semiconductor Material. U.S. Patent 2269347, 25 September 1951
6. A.I. Gubanov. Theory of the contact between two semiconductors with different types of conduction. Zh Tekh Fiz 20, p. 1287 (1950)
7. H. Kroemer. Theory of a wide-gap emitter for transistors. Proc IRE 45, p. 1535 (1957)
8. Zh.I. Alferov,V.B. Khalfin, R.F. Kazarinov. A characteristic feature of injection into heterojunctions. Fiz Tverd Tela, 8, pp 3102–3105, 1966 [Sov Phys Solid State, 8, p. 2480, 1967]
9. R.L. Anderson. Gemanium-gallium arsenide heterojunctions. IBM J Res Dev 4, p. 283 (1960)
10. Zh.I. Alferov, V.M. Andreev, V.I. Korol'kov, D.N. Tret'yakov, V.M. Tuchkevich. High-voltage p-n junctions in $Ga_xAl_{1-x}As$ crystalls. Fiz Tekh

Poluprovodn 1, pp. 1579–1581, 1967 [Sov Phys Semicond 1, pp. 1313–1314, 1968]
11. H.S. Rupprecht, J.M. Woodall, G.D. Pettit. Efficient visible electroluminescence at 300 K from $Ga_{1-x}Al_xAs$ p-n junctions grown by liquid-phase epitaxy. Appl Phys Lett 11, p. 81 (1967)
12. Zh.I. Alferov,V.M. Andreev, V.I. Korol'kov, E.L. Portnoi, D.N. Tret'yakov. Injection properties of n−$Al_xGa_{1-x}As$−p−GaAs heterojunctions. Fiz Tekh Poluprovodn 2, pp. 1016–1017 (1968) [Sov Phys Semicond 2, pp. 843–844, 1969]
13. Zh.I. Alferov, V.M. Andreev, V.I. Korol'kov, E.L. Portnoy, D.N. Tret'yakov. Coherent radiation of epitaxial heterojunction structures in the AlAs−GaAs system. Fiz Tekh Poluprovodn 2, pp. 1545–1547 (1968) [Sov Phys Semicond 2, pp. 1289–1291, 1969]
14. Zh.I. Alferov, V.M. Andreev, V.I. Korol'kov, E.L. Portnoi, D.N. Tret'yakov. Recombination radiation in epitaxial structures in the AlAs−GaAs system. In Proc IX Int Conf on the Physics of Semiconductors, Moscow, 1968, 1 ("Nauka", Leningrad, 1968), pp. 504–510
15. Zh.I. Alferov,V.M. Andreev, E.L. Portnoy, M.K. Trukan. AlAs−GaAs heterojunctions injection lasers with a low room-temperature threshold. Fiz Tekh Poluprovodn 3, pp. 1328–1332 (1969)[Sov Phys Semicond 3, pp.1107–1110, 1970]
16. I. Hayashi. Heterostructure lasers. IEEE Trans Electron Devices, ED-31, pp. 1630–1645 (1984)
17. Zh.I. Alferov,V.M. Andreev, D.Z. Garbuzov,Yu.V. Zhilyaev, E.P. Morozov, E.L. Portnoi, V.G. Trofim. Investigation of the influence of the AlAs−GaAs heterostructure parameters on the laser threshold current and the realization of continuous emission at the room temperature. Fiz Tekh Poluprovodn 4, pp. 1826–1829 (1970) [Sov Phys Semicond 4, pp. 1573–1575, 1971]
18. I. Hayashi, M.B. Panish, P.W. Foy, S. Sumski. Junction lasers which operate continuously at room temperature. Appl Phys Lett 17, pp. 109–111 (1970)
19. Zh.I. Alferov, V.M. Andreev, V.I. Korol'kov, E.L. Portnoi, A.A. Yakovenko. Spontaneous radiation sources based on structures with AlAs−GaAs heterojunctions. Fiz Tekh Poluprovodn 3, pp. 930–933 (1969) [Sov Phys Semicond 3, pp. 785–787, 1970]
20. Zh.I. Alferov, V.M. Andreev, M.B. Kagan, I.I. Protasov, V.G. Trofim. Solar-energy converters based on p-n $Al_xGa_{1-x}As$−GaAs heterojunctions. Fiz Tekh Poluprovodn 4, pp. 2378–2379, (1970) [Sov Phys Semicond 4, pp. 2047–2048, 1971]
21. Zh.I. Alferov, F.A. Ahmedov, V.I. Korol'kov, V.G. Nikitin. Phototransistor utilizing a GaAs−AlAs heterojunction. Fiz Tekn Poluprovodn 7, pp. 1159–1163 (1973) [Sov Phys Semicond 7, pp. 780–782, 1973]
22. Zh.I. Alferov, V.M. Andreev, V.I. Korol'kov, V.G. Nikitin, A.A. Yakovenko. p-n/p-n structures based on GaAs and on $Al_xGa_{1-x}As$ solid solutions. Fiz Tekn Poluprovodn 4, pp. 578–581 (1970) [Sov Phys Semicond 4, pp. 481–483, 1971]
23. Zh.I. Alferov, V.M. Andreev, S.G. Konnikov, V.G. Nikitin, D.N. Tret'yakov. Heterojunctions on the base of III-V semiconducting and of their solid solutions. In: Proc Int Conf Phys Chem Semicond Heterojunctions and Layer Structures, Budapest, 1970, 1. Ed. G. Szigeti (Academiai Kiado, Budapest, 1971), pp. 93–106
24. G.A. Antipas, R.L. Moon, L.W. James, J. Edgecumbe, R.L. Bell. In: Gallium arsenide and related compounds. Conf Ser IOP, 17, p. 48 (1973)

25. A.P. Bogatov, L.M. Dolginov, L.V. Druzhinina, P.G. Eliseev, L.N. Sverdlova, E.G. Shevchenko. Heterolasers on the base of solid solutions $Ga_xIn_{1-x}As_yP_{1-y}$ and $Al_xGa_{1-x}Sb_yAs_{1-y}$. Kvantovaya Electron 1, p. 2294 (1974) [Sov J Quantum Electron, 1, p. 1281, 1974]
26. Zh.I. Alferov, I.N. Arsent'ev, D.Z. Garbuzov, S.G. Konnikov, V.D. Rumyantsev. Generation of coherent radiation in $nGa_{0.5}In_{0.5}P-pGa_{x\sim0.55}In_{1-x}As_{y\sim0.10}P_{1-y}-nGa_{0.5}In_{0.5}P$. Pisma Zh Tech Fiz 1, pp. 305–310 (1975) [Sov Phys Tech Phys Lett 1, pp. 147–148, 1975]
27. L.W. James, R.L. Moon. GaAs concentrator solar cells. Appl Phys Lett 26, pp. 467–470 (1975)
28. Zh.I. Alferov, V.M. Andreev, Kh.K. Aripov, V.R. Larionov, V.D. Rumyantsev. Solar photovoltaic installation with output power of 200 W based on AlGaAs-heterophotocells and mirror concentrators. Geliotekhnika 6, p. 3 (1981)
29. V.M. Andreev, V.A. Grilikhes, V.D. Rumyantsev. Photovoltaic conversion of concentrated sunlight. Wiley, Chichester (1997)
30. Zh.I. Alferov, V.M. Andreev, D.Z. Garbuzov, V.R. Larionov, V.D. Rumyantsev, V.B. Khalfin. Heterophotocells with intermediate conversion of radiation. Fiz Tekh Poluprovodn 11, pp. 1765–1770 (1977) [Sov Phys Semicond 11, 1977]
31. I.N. Arsent'ev, D.Z. Garbuzov, V.D. Rumyantsev. Internal quantum efficiency of radiative recombination in heterostructures based on wide-gap InGaAsP solid alloys. Proc Second All-USSR Conference on Physical Processed in Semiconductor Heterostructures, vol. II, pp. 107–109, Ashkhabad, 1978 (in Russian)
32. E.V. Tulashvili, L.S. Vavilova, D.Z. Garbuzov, I.N. Arsent'ev, V.B. Khalfin. Influence of recombination in emitters on photoluminescence characteristics of the double heterostructures $In_{0.5}Ga_{0.5}P$-InGaAsP. Fiz Tekh Poluprovodn 16, pp. 1645–1649 (1982) [Sov Phys Semicond 16, 1982]
33. Zh.I. Alferov, V.M. Andreev, D.Z. Garbuzov, V.D. Rumyantsev. 100% internal quantum efficiency of radiative recombination in light-emitting diodes based on AlAs−GaAs. Fiz Tekh Poluprovodn 9, pp. 462–469 (1975) [Sov Phys Semicond 9, 1975]
34. Zh.I. Alferov, V.G. Agafonov, D.Z. Garbuzov, N.Yu. Davidyuk, V.R. Larionov, V.B. Khalfin. Multipass heterostructures. External quantum efficiency of radiation. Fiz Tekh Poluprovodn 10, pp. 1497–1506 (1976) [Sov Phys Semicond 10, 1976]
35. N.Yu. Antonishkis, I.N. Arsent'ev, D.Z. Garbuzov, V.P. Evtichiev, V.V. Krasovskii, A.V. Chudinov, A.E. Svelokuzov. Efficiency of the luminescence and interface recombination velocity in heterostructures based on Al−Ga−As and In−Ga−As−P systems. Fiz Tekh Poluprovodn 20, pp. 708–712 (1986)[Sov Phys Semicond 20, 1986]
36. M.A. Green. Third generation photovoltaics: ultrahigh conversion efficiency at low cost. Progr Photovoltaics Res Appl 9, pp. 123–135 (2001)
37. K. Lin, K.R. Catchpole, T. Trupke, P. Campbell, M. Green, A.G. Aberle,R. Corkish, A.W. Bett, F. Dimroth. High external quantum efficiency from double heterostructures layers as selective emitters in thermophotonic systems. Proc 3rd World Conference on Photovoltaic Energy Conversion, Osaka, 2003
38. V.M. Andreev, B.V. Egorov, V.M. Lantratov, V.D. Rumyantsev, S.I. Troshkov. Solar heterophotocells with increased p-n junction depth. Sov Phys Techn Phys 28 (8), pp. 1022–1023 (1984)

39. M.E. Green, K. Emery, D.L. King, S. Igari, W. Warta. Solar cell efficiency tables (version 20). Prog Photovoltaics Res Appl 10, 355 (2002)
40. V.M. Andreev, A.B. Kazantsev, V.P. Khvostikov, E.V. Paleeva, V.D. Rumyantsev, M.Z. Shvarts. High-efficiency (24.6%, AM0) LPE grown AlGaAs/GaAs concentrator solar cells and modules. Proc 1st World Conference on Photovoltaic Energy Conversion, Hawaii, 1994, pp. 2096–2099
41. S.G. Balei, D.J. Flood. Space photovoltaics. Progr Photovoltaics Res Appl 6, pp. 1–14 (1998)
42. C. Algora, E. Ortiz, I. Rey-Stolle, V. Diaz, P. Pena, V.M. Andreev, V.P. Khvostikov, V.D. Rumyantsev. A GaAs solar cell with efficiency of 26.2% at 1000 suns and 25.0% at 2000 suns.IEEE Trans Electron Dev 48 (5), pp. 840–844 (2001)
43. V.M. Andreev, V.P. Khvostikov, V.R. Larionov, V.D. Rumyantsev, E.V. Paleeva, M.Z. Shvarts, C. Algora. 5800 Suns AlGaAs/GaAs concentrator solar cells. Technical Digest of the International Photovoltaic Science and Engineering Conference, Sapporo, Japan, 1999, pp. 147–148
44. M.Z. Shvarts, O.I. Chosta, I.V. Kochnev, V.M. Lantratov, V.M. Andreev. Radiation resistant AlGaAs/GaAs concentrator solar cells with internal Bragg reflector. Solar Energy Mater Solar Cells 68, pp. 105–122 (2001)
45. K.A. Bertness, S.R. Kurtz, D.J. Friedman, A.E. Kibber, C. Kramer, J.M. Olson. High efficiency GaInP/GaAs tandem solar cells for space and terrestrial applications. Proc 1st World Conference on Photovoltaic Energy Conversion, Hawaii, 1994, pp. 1671–1678
46. R.R. King, D.C. Law, C.M. Fetzer, R.A. Sherif, K.M. Edmondson, S. Kurtz, G.S. Kinsey, H.L. Cotal, D.D. Krut, J.H. Ermer, N.H. Karam. Pathways to 40%-efficient concentration photovoltaics. Proc 20th European PVSEC, Barcelona, Spain, 2005, pp. 6–10
47. M. Green, K. Emery, D. King, Y. Hisikawa, W. Warta. Solar cell efficiency tables (version 27). Prog Photovoltaics 14, p. 45 (2006)
48. V.M. Andreev, L.B. Karlina, A.B. Kazantsev, V.P. Khvostkov, V.D. Rumyantsev, S.V. Sorokina, M.Z. Shvarts. Concentrator tandem solar cells based on AlGaAs/GaAs−InP/InGaAs (or GaSb) structures. Proc 1st World Conference on Photovoltaic Energy Conversion, Hawaii, 1994, pp. 1721–1724
49. M.Z. Shvarts, P.Y. Gazaryan, V.P. Khvostikov, V.M. Lantratov, N.K. Timoshina. InGaP/GaAs−GaSb and InGaP/GaAs/Ge−InGaAsSb hybrid monolithic/stacked tandem concentrator solar cells. Proc 21st European Photovoltaic Solar Energy Conference, Dresden, 2006
50. Zh.I. Alferov, N.A. Bert, A.Yu. Egorov, A.E. Zhukov, P.S. Kop'ev, A.O. Kosogov, I.L. Krestnikov, N.N. Ledentsov, A.V. Lunev, M.V. Maksimov, A.V. Sakharov, V.M. Ustinov, A.F. Tsatsul'nikov, Yu.M. Shernyakov, D. Bimberg. An injection heterojunction laser based on arrays of vertically coupled InAs quantum dots in a GaAs matrix. Fiz Tekh Poluprovodn 30, pp. 351–356 (1996) [Semiconductors 30, pp 194–196, 1996]
51. A. Marti, L. Guadra, A. Luque. Intermediate-band solar cells. In: Next generation photovoltaics. High efficiency through full spectrum utilization. A. Marti, A. Luque (Eds). Institute of Physics Publishing, pp. 140–164 (2004)
52. P.A. Davies, A. Luque. Solar thermophotovoltaics: brief review and a new look. Solar Energy Mater Solar Cells 33, pp. 11–22 (1994)

53. V.M. Andreev, V.A. Grilikhes, V.P. Khvostikov, O.A. Khvostikova, V.D. Rumyantsev, N.A. Sadchikov, M.Z. Shvarts. Concentrator PV modules and solar cells for TPV systems. J Solar Energy Mater Solar Cells 84, pp. 3–17 (2004)
54. Zh.I. Alferov, V.M. Andreev, Yu.M. Zadiranov, V.I. Korol'kov, N. Rahimov, T.S. Tabarov. Photo-emf in $Al_xGa_{1-x}As$ graded band-gap heterostructures. Pisma Zh Tech Fiz 4, pp. 369–372 (1978) [Sov Tech Phys Lett 4 (4), 149–150, 1978]
55. Zh.I. Alferov, A.M. Vasiliev, S.V. Ivanov, P.S. Kop'ev, N.N. Ledentsov, M.E. Lutsenko, B.Yu. Melser, V.M. Ustinov. Reducing the threshold in GaAs−AlGaAs DHS SCH quantum well lasers ($j_{th} = 52\,\mathrm{A\,cm^2}$,$T = 300\,\mathrm{K}$) with quantum well restriction by short period superlattice of variable period. Pisma Zh Techn Fiz 14, 1803–1806 (1988) [Sov Tech Phys Lett 14, 782, 1988]

3 Silicon concentrator solar cells

A. Blakers

3.1 Introduction

Solar photovoltaic (PV) concentrator systems can be divided into two broad categories: point-focus systems typically utilizing square Fresnel lenses, parabolic dishes and central receivers; and line-focus systems typically utilizing linear Fresnel lenses and parabolic troughs. The illumination intensity is typically $10-50\,\mathrm{Wcm}^2$ for the point-focus category and $1-5\,\mathrm{Wcm}^2$ for the line-focus category, compared with $0.1\,\mathrm{W\,cm}^2$ for non-concentrated sunlight.

This chapter summarizes the design of silicon solar cells for use in point-focus and line-focus solar concentrator systems. The differences between solar cells designed for high and moderate concentration are described, along with the conflicting requirements for operation under concentration. Cell design is related to the design of other parts of the optical concentrator where the latter places particular constraints on the former.

The cost of a point-focus solar concentration system per square metre of collection area is larger than the cost of a line-focus system, which in turn is larger than the area-related balance-of-systems costs of a non-concentrating photovoltaic system. It therefore makes economic sense to use highly efficient solar cells in point-focus concentrator systems, even though the solar cell cost per square centimetre is high.

In a line-focus concentrator system, the requirement for high efficiency is relaxed in favour of reduced cost, since the concentration ratio is about ten times smaller and the area of solar cell required is therefore ten times larger. Even modified 1-sun solar cells can be considered for use at the lower end of the concentration range; however, the economically optimum efficiency and cost per square centimetre of solar cell is considerably larger than for non-concentrator systems.

3.2 Requirements for Highly Efficient Silicon Solar Cells

Specialized silicon solar cells used in solar concentrator systems are fabricated using techniques capable of delivering high cell efficiency. The key requirements for such cells are:

1. High material quality with long minority carrier lifetimes
2. Good design of diffusions in order to minimize resistance and recombination losses
3. Excellent surface passivation
4. Good passivation of cell edges (particularly for small cells)
5. Excellent reflection control and light trapping
6. Good design of metallizations in order to minimize optical and resistance losses

3.2.1 High Minority Carrier Lifetimes

Concentrator silicon solar cells are preferably fabricated using wafers that have large minority carrier lifetime (hundreds to thousands of microseconds). This means that the diffusion length is considerably larger than the wafer thickness, leading to high internal quantum efficiency. In addition, recombination in the base region of the solar cell is suppressed. Silicon wafers that meet this requirement include those fabricated using the float-zone technique or Czochralski wafers that have either low boron doping (i.e. high-resistivity wafers) or low oxygen levels (such as magnetic Cz). The avoidance of high levels of both boron and oxygen suppresses the formation of boron-oxygen complexes that can reduce minority carrier lifetime.

During the mid-1980s to the mid-1990s the efficiency of non-concentrator silicon cells rose by half to 24%, primarily due to work at Stanford University and the University of New South Wales. An important component of this rapid improvement was the introduction of processed techniques that allowed the preservation of the large minority carrier lifetime present in unprocessed float-zone grown silicon wafers. Before this time, both the need and the technical requirements for high lifetime cell processing were poorly understood.

Reliance can be placed on aluminium gettering to segregate metallic impurities that enter the silicon wafer during high-temperature processing to the rear surface. While this is an effective technique, a drawback is that the aluminium-silicon layer on the rear surface of the wafer has a high effective surface recombination rate. Nevertheless, relatively efficient solar cells can be fabricated using cell designs that sacrifice light absorbed near the rear surface of the solar cell. Cells made on heavily doped wafers, with resistivities in the range $0.1-0.5\,\Omega$cm, maximize open-circuit voltage and fill factor at the cost of red response, and can achieve efficiencies above 24% under concentration [1].

Pioneering work at Stanford University in the 1980s [2] demonstrated that clean processing could readily preserve the high starting minority carrier lifetime of the silicon wafer. The key is to ensure that wafers are cleaned before high-temperature processing, and that the furnace tubes are clean. The use of a furnace ambient containing a few percent of chlorine is extremely effective in preventing metallic impurities from diffusing into the silicon wafers. The

chlorine is typically delivered using trichloroethane (which is being phased out due to its deleterious effect on the ozone layer) or Trans 1,2-Dichloroethylene. Furnace tubes and quartzware can be cleaned in an oxygen-chlorine ambient in advance of a particular process at a temperature higher than the desired process temperature, which eliminates the need to run chlorine during the actual process.

The ability to maintain the high minority carrier lifetime of the starting wafer throughout processing eliminates the need for the gettering of impurities by means of aluminium, phosphorus doping and other techniques. This increases process latitude in independently choosing surface doping, oxidation, metallization and other parameters.

3.2.2 Doping and Electrical Contacts

Most conventional solar cells are fabricated on p-type substrates. One reason for this is that electron mobility is about three times larger than hole mobility, which means that transport of electrons in the base of the solar cell as minority carriers to the collecting junction is easier than for holes. Another reason is that most solar cells are sheet-diffused on the sunward surface with dopants of the opposite polarity to the substrate doping. It is considerably easier to obtain high-quality phosphorus diffusions than high-quality boron diffusions. Set against these advantages is the formation of boron-oxygen complexes in p-type Cz silicon that reduce minority carrier lifetime.

In the case of back-contact solar cells under concentration, high-resistivity wafers are used. The cells operate in high injection. Lightly doped wafers have the highest available diffusion length, which helps minimize losses associated with the transport of both electrons and holes to the rear surface of the cell.

Sheet phosphorous diffusions on the sunward surface of conventional cells ("the emitter") need to be relatively heavy in order to minimize resistance losses in the lateral transport of electrons to the metal grid. This resistance loss is proportional to the sheet resistance and the square of the spacing between gridlines; however, excessive doping causes loss of blue response, because holes created by short-wavelength photons absorbed very close to the surface recombine without being collected by the junction (i.e. the effective hole diffusion length in the emitter is less than the junction depth).

Heavy doping is associated with excess recombination within the doped layer, caused by Auger recombination, band-gap narrowing and other heavy doping effects. This can be minimized by driving-in the doping atoms at a high temperature in order to create a deeper junction ($\sim 1\,\mu m$) with a reduced surface concentration. The average hole diffusivity is also improved by this process. A sheet resistance after drive-in in the range $70-120\,\Omega$ per square is consistent with good blue response and acceptable lateral resistance losses.

Electrical contacts are required to extract current from a solar cell. These contacts are typically metal-silicon contacts and are associated with large surface recombination currents per unit area of contact. Fortunately, straightforward methods exist to suppress this recombination. Heavy doping of phosphorus and boron beneath negative and positive contacts, respectively, largely excludes minority carriers from the vicinity of the metal-silicon contact. The heavy doping also suppresses contact resistance. This allows the contact area to the small regions, which reduces recombination at the electrical contacts and the associated heavily doped regions. Sheet resistances in the range $5-25\,\Omega$ per square after drive-in are typically employed at the electrical contacts to the cell.

3.2.3 Surface Passivation

Surface recombination, and recombination in heavily doped regions of the surface, account for the majority of recombination in many solar cells. It is well known that the growth of a layer of silicon dioxide on the silicon surface is extremely effective in suppressing surface recombination. Oxidation at a temperature of $900-1100\,^{\circ}\mathrm{C}$ in oxygen, followed by in-situ annealing in nitrogen or argon, is a reliable method of surface passivation. Typically the oxidation is followed by annealing in forming gas (5% hydrogen in nitrogen or argon) to hydrogenate the silicon-oxide interface.

Silicon nitride deposited by plasma enhanced chemical vapour deposition at $400\,^{\circ}\mathrm{C}$ has excellent surface passivation properties, as well as being a good antireflection coating [3]. Open-circuit voltages of around 720 mV have been observed [4]. Suitable thermal annealing allows large improvements in the performance of these films, pointing to the role of hydrogen in surface passivation.

Surface passivation using a heterojunction of amorphous silicon has yielded open-circuit voltages as high as 730 mV under non-concentrated sunlight [5]. An advantage of this technique is that process temperatures of only $200\,^{\circ}\mathrm{C}$ are required. A disadvantage of this technique is absorption of light in the amorphous silicon and the overlying transparent conducting oxide. Replacement of amorphous silicon with wide band-gap amorphous silicon carbide, and improved transparent conducting oxides, could pave the way for a substantial improvement in concentrator cell performance.

Heterojunctions could have an important role in reducing recombination at electrical contacts without the need to include heavy doping beneath the contact. Silicon solar cell efficiency has saturated in recent years, limited primarily by surface recombination.

3.2.4 Edge Recombination

Solar cells are usually cut from a host wafer at the end of solar cell processing using a dicing saw, diamond scriber or laser. The cut edges are completely unpassivated and often have sustained substantial crystal damage including micro-cracks. In the case of a square 1 cm^2 solar cell that is 250 µm thick, the unpassivated edges have a surface area of 0.1 cm^2, which is 5% of the total surface area of the cell. This significantly limits the potential cell efficiency. The ideality factor associated with edge recombination is typically larger than unity, which means that the fill factor of the solar cell is more affected than the open-circuit voltage.

Recombination at the edges of solar cells can be suppressed in a number of ways. The area of the edges is proportional to the wafer thickness, and so thin solar cells have reduced edge recombination. The larger area ($\sim 20\,cm^2$) solar cells typically used in linear concentrator systems have a correspondingly smaller ratio of the edge area to the surface area of the solar cell, which usually means that the effect of edge recombination is small.

Avoidance of cutting through the p-n junction of the solar cell substantially reduces junction recombination, which typically dominates edge recombination; thus, the cell can be designed so that the p-n junction does not extend to the region of the cut edges. If a wide border of undoped silicon is left around the outside of the active area of the solar cell, typically several times wider than the cell is thick, then the effect of the cut edges can be minimized. This is viable for cells designed to be used singly at the focus of a Fresnel lens, but is not the solution for solar cells designed to be used in a dense array at the focus of a dish concentrator.

Passivation of the cell edges is possible by performing a large fraction of the edge cuts prior to passivation steps in the cell-fabrication process. At the end of the cell process only a relatively small fraction of the cell edges require cutting or fracturing to extract the completed solar cell. This method considerably increases the complexity of cell processing and increases the risk of wafer breakage.

3.2.5 Reflection Control and Light Trapping

About one-third of the sunlight striking a bare polished silicon wafer is reflected. Reflection losses can be controlled by incorporating antireflection coatings on the cell surface or by roughening the cell surface, or preferably both.

Antireflection coatings provide a graded refractive index between that of silicon and that of the air or transparent pottant media surrounding the cell. Silicon dioxide, which is often used as a passivation layer, can be used as an antireflection coating; however, the refractive index (1.46) is well below optimum (1.9 – 2.4), leading to excessive reflection losses.

Common antireflection layer materials include silicon nitride and titanium dioxide. The former, when deposited using plasma enhanced chemical vapour deposition, has excellent surface passivation properties which eliminates the need for an underlying oxide surface passivation layer. The latter has high transparency and an ideal refractive index (2.4) for use in encapsulated solar cells.

The layers of a multilayer antireflection scheme are preferably arranged in order of refractive index, with the highest index material next to the silicon. This means that a silicon dioxide layer with thickness greater than a few tens of nanometres significantly degrades the optical performance of an overlying antireflection coating such as TiO_2 ($n = 2.4$). Fortunately, a few tens of nanometres of silicon dioxide is sufficient to yield high-quality surface passivation.

Roughening the silicon surface (texturing) can reduce reflection losses by causing reflected light to strike a neighbouring part of the silicon surface, and thus have a second chance of absorption. Only a crude antireflection coating is necessary to reduce reflection from a textured surface to very low levels.

The ease with which roughening can be achieved by the use of anisotropic etches has led to the near-universal use of (100) oriented silicon wafers for high-efficiency solar cells. Texturing in alkaline etches such as potassium hydroxide or tetramethyl ammonium hydroxide can easily produce upright pyramids with (111) oriented faces and with a height of a few microns. This is widely used in the solar cell industry. An isotropic etch, consisting of a mixture of hydrofluoric acid and nitric acid, can be used to round sharp features, thus reducing recombination rates without unduly increasing reflection losses. An alternative texturing method that is often used in highly efficient solar cells is to selectively mask the surface of a wafer with silicon dioxide to create an array of square windows separated by a mesh of narrow orthogonal oxide stripes. Alkaline etching then creates inverted pyramids with (111) faces that lack sharp edges and points.

Texturing most of the surface of a wafer changes the predominant surface orientation from (100) to (111). This leads to an increase in surface recombination rates, both because of the increased surface area and the fact that (111) oriented silicon has an intrinsically higher recombination rate than (100) silicon; however, the reduction in optical losses heavily outweighs the small reduction in voltage from the cell.

Another reason for texturing the surface of solar cells is light trapping. Although three-quarters of the solar spectrum is absorbed in the first 20 μm of a silicon solar cell, several millimetres of silicon are required to absorb most of the remaining photons. Thin silicon wafers suffer from slightly reduced absorption of sunlight; however, it is possible to trap weakly absorbed infrared photons in the silicon by roughening one or both surfaces of the wafer. Light within the silicon (which has a refractive index n_2 of about 3.6 for long wavelength light) is totally internally reflected if it strikes the surface at an

angle larger than arcsin (n_1/n_2) to the normal; 16° in air ($n_1 = 1.0$) and 25° in an encapsulated ($n_1 \sim 1.5$) package.

Many types of texturing provide excellent light trapping, with a performance that approaches the limit for a randomizing (Lambertian) light trapping scheme of $4{n_2}^2 W$ or about $50W$ [6], where W is the wafer thickness. Geometrical light trapping schemes, such as inverted pyramids, can match or sometimes exceed the performance of Lambertian light trapping [7].

In tracking concentrator systems the range of angles that the incoming light makes to the normal to the silicon surface is restricted. If the cell is designed so that it will only accept light within an angle θ of the normal to the cell surface, then it is possible to restrict the escape of light. The average path length of light in the silicon in this case can in principle be as high as $4{n_2}^2 W/\sin^2\theta$ [8]. This allows for the use of very thin substrates ($< 10\,\mu\text{m}$) without significant loss of short circuit current; however, other factors, such as the fact that surface recombination restricts the obtainable open-circuit voltage in silicon solar cells even if recombination in the cell volume is suppressed by the use of thin substrates, and the design and the wafer-handling complications associated with very thin solar cells, means that practical concentrator cells have thicknesses of many tens to a few hundred micrometres.

3.2.6 Reflection Losses from Cell Metallization

Most solar cells have a metal grid on the front surface for the negative electrical contact and a sheet of metal on the rear surface for the positive electrical contact. Some solar cell designs, such as back-contact solar cells and Sliver solar cells, do not have metal on the sunward surface.

The metal grid design of a conventional solar cell is a trade–off between resistance losses and reflection losses. Smaller solar cells have smaller currents and smaller fractional shading by the metal grid, but at the cost of larger edge recombination and handling requirements.

Various methods are available to reduce the effective optical width of metal gridlines. Perhaps the simplest method is to take advantage of the fact that gridlines produced by the silver electroplating of thin and narrow initial deposited gridlines have a cross-sectional shape that is approximately a half circle (Fig. 3.1). The silver surface is highly reflective. Approximately one-third of the light that strikes such a gridline in an encapsulated solar cell will be reflected downwards to strike the silicon between the gridlines. Another one-third of the light is reflected upwards, but at such an angle that it is totally internally reflected at the interface between the air and the transparent packaging material and is eventually absorbed by the silicon; thus, the effective optical width of such a gridline is only about one-third of the geometrical width [9]. For solar cells designed for linear concentrators, with illumination intensities of $1-5\,\text{W/cm}^2$, the combined reflection and resistance losses from such gridlines are small [10].

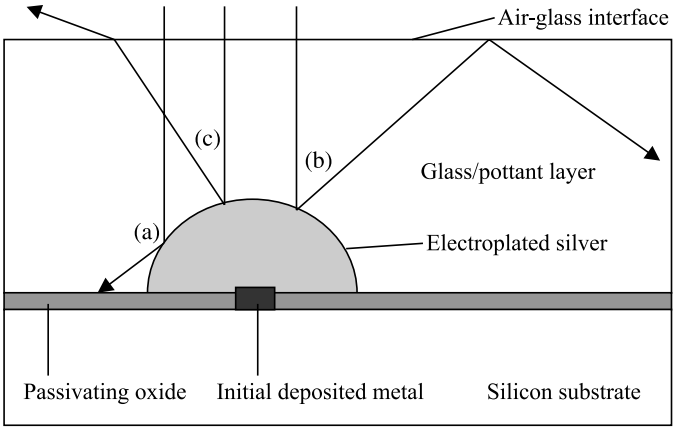

Fig. 3.1. The optical width of an encapsulated metal finger with a semicircular cross section is about one-third of the geometrical width for a wide range of incident angles. Ray **a** is reflected downwards onto the silicon and ray **b** is totally internally reflected at the air-glass interface after reflection from the metal finger. Only ray **c** escapes

3.3 Silicon Solar Cells for Point-Focus Concentrator Systems

The designs of cells for use in point-focus concentrator systems (Fig. 3.2), with typical illumination intensities in the range $10-50\,\mathrm{W/cm^2}$, fall into two categories: a conventional $n^+/p/p^+$ structure and a back contact structure. Efficiencies above 24% under concentration have been achieved with conventional designs; however, the conventional structure has the major disadvantage of substantial resistive and reflective losses from the gridlines on the illuminated surface. Economic analysis shows that high efficiency is more important than reduced solar cell cost at these high illumination intensities; therefore, back-contact solar cells are favoured even if they have a somewhat greater cost per square centimetre than conventional solar cells.

Back-contact cells (Fig. 3.3) have both positive and negative electrical contacts on the rear of the cell in an interdigitated pattern [11, 12]. This eliminates reflective losses from the metallization, and allows sufficient metal to be used to reduce resistive losses to small values. It also allows simplification of cell interconnection since there is no need to access the front surface of the cell with interconnects. This design requires that both electrons and holes, which are mostly created near the front surface, be transported to the rear surface for collection without substantial loss. For this reason diffusion lengths should be many times larger than the cell thickness. Thin ($80-150\,\mu\mathrm{m}$) high-resistivity float zone wafers are typically used.

Excellent front-surface passivation is required to minimize surface recombination losses due to the elevated electron and hole concentrations

Fig. 3.2. Hermannsburg, Australia, 190 kW power station, with SunPower back contact solar cells in the receiver at the focus. (Courtesy Solar Systems)

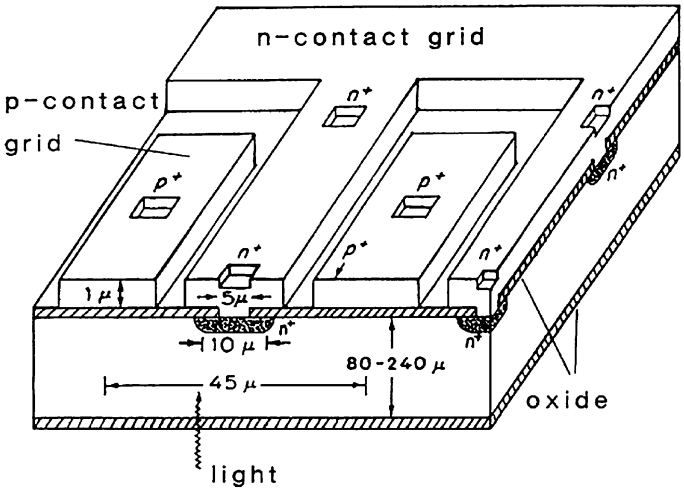

Fig. 3.3. Back contact solar cell, illustrating the advantage of placing both contacts on the rear surface (From [2])

present under concentrated sunlight at the maximum power point. The enhanced sensitivity of the back contact cell to front surface recombination can lead to enhanced susceptibility to UV induced degradation of surface passivation. Measures to ameliorate this problem include incorporating a light phosphorus diffusion, stabilizing surface passivation by a variety of means and incorporating UV absorbing materials in the transparent cover materials.

The back-contact cell proved to be the best design for high-concentration silicon solar cell applications, and stable cell efficiencies around 27% have been achieved [13, 14]; however, the very small market for such cells means that prices remain high per square centimetre.

Before the 1990s, the technical requirements for high-lifetime cell processing were poorly understood, leading to a mistaken perception that the back-contact cell would necessarily be substantially more difficult and costly to produce than conventional structures. Rather than focus on the tiny concentrator cell market, Sunpower [15] has entered the non-concentrator market with a premium efficiency product.

Recently, triple-junction III-V solar cells, with efficiencies above 40%, have been developed. It seems that silicon solar cells for high concentration systems are unlikely to be economically competitive, although silicon cells could form part of a multijunction cell stack.

3.4 Silicon Solar Cells for Line-Focus Concentrator Systems

A variety of solar cell designs can be used for linear concentrator systems operating at typical illumination intensities of $1-5\,\mathrm{W/cm^2}$. The cells must be considerably cheaper per square centimetre than point-focus concentrator cells operating at $10-50\,\mathrm{W/cm^2}$. The low cost per square centimetre of silicon solar cells compared with triple-junction III-V solar cells means that there is an attractive market for silicon cells in linear concentrator systems in the short to medium term.

3.4.1 High-Efficiency Silicon Solar Cells

Conventional line-focus silicon solar cells designed to operate at an intensity of $1-5\,\mathrm{W/cm^2}$ at the focal line of a trough concentrator have typical dimensions of $40 \times 50\,\mathrm{mm^2}$. Busbars run down two opposite edges, and metal fingers spaced about $300\,\mu\mathrm{m}$ run between the two busbars (Fig. 3.4).

The advantage of shifting both metal contacts to the rear, as in the back-contact design, is considerably reduced in linear concentrator systems because the smaller current density means that less metal is required on the sunward surface. In principle, metal resistance losses can be made arbitrarily small in back-contact cells. In practice, however, there is a maximum thickness for the metallization beyond which metal peeling becomes a problem.

Both conventional and back-contact solar cells can take full advantage of high lifetime processing, excellent surface passivation, good reflection control and good light trapping, and can achieve efficiencies above 24%.

The market for PV linear concentrator systems is small. For this reason there is no large-scale manufacturing of highly efficient (>24%) specialist

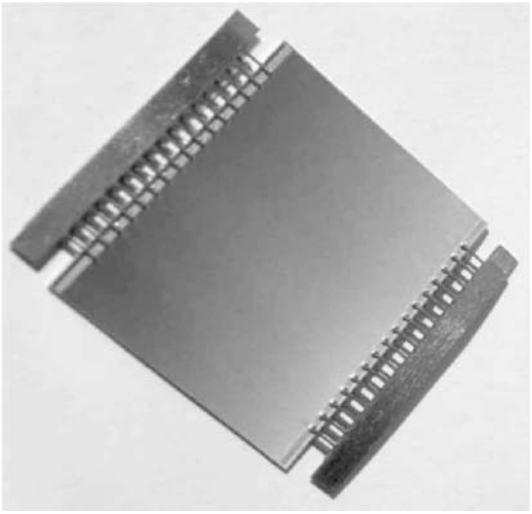

Fig. 3.4. Tabbed linear $5 \times 4\,\mathrm{cm}^2$ conventional linear concentrator solar cell fabricated at ANU

solar cells for linear concentrator systems. This means that the cost of specialist high-efficiency cells for linear concentrators is high, which in turn limits growth of the market for linear PV concentrators.

3.4.2 Upgraded 1-Sun Solar Cells

Solar cells from factories that produce tens of millions of cells per year for the non-concentrator photovoltaic market have far lower costs per square centimetre than high-efficiency silicon solar cells produced for the concentrator market in small quantities by specialist manufacturers. There may be considerable commercial advantage if reasonable efficiencies can be obtained from non-concentrator solar cells when used in line-focus concentrator systems.

A typical non-concentrator solar cell will experience an increase in open-circuit voltage of about 10% when illuminated under 10 suns; however, resistive losses will normally rise faster than the increase in open-circuit voltage, leading to an overall reduction in cell efficiency under concentration.

Screen printed solar cells lack many of the high-efficiency features present in specialized concentrator solar cells, including large diffusion lengths and good surface passivation. The metal grid requires modification in order to handle the currents arising from concentrated sunlight. One method of doing this is to print additional metal to reduce resistive losses, which causes additional shading of the top surface of the cell. Shading losses can be ameliorated through the use of prism covers [16], which refract light away from the metal fingers and hence cause the optical width of the fingers to be less than the geometrical width; however, the inherently low efficiency of screen-printed solar cells militates against the economical viability of this option.

Buried contact solar cells [17] have several high-efficiency features, including relatively light emitter diffusion (which enhances the blue response) and relatively good surface passivation (which enhances the blue response and the open circuit voltage). Buried contact solar cells have metal fingers that are created with the assistance of laser scribing. It is easy to program the laser to produce a larger number of more closely spaced fingers. In this way, good cell efficiencies ($\sim 18\%$) can be maintained under moderate concentration ($1-5\,\mathrm{W/cm^2}$) with relatively small departures from conventional processing [18].

Sunpower Corporation has commercialized the back-contact solar cell for non-concentrator applications [15]. The cells have efficiencies under 1 sun illumination in the range of 21%. Reinforcement of the positive and negative metal conductors on the rear surface to handle increased current under concentration does not lead to additional shading losses. By this means, efficiencies above 17% are readily obtainable under illumination of $1-3\,\mathrm{W/cm^2}$. It would be relatively straightforward for Sunpower to produce very good ($\sim 22\%$) linear concentrator cells were the market sufficiently large to justify the change that is required in the standard cell fabrication process.

3.4.3 Linear Concentrator Receivers

There is a close relationship between solar cell design and the design of the receivers on which the cells are mounted at the focal line of the linear concentrator.

Moving shadows are common in linear concentrators (Fig. 3.5) arising from structural elements, gaps between mirrors, shading from neighbouring collectors and from the fact that in single-axis tracking systems an end of a receiver is not illuminated for substantial parts of the year because sunlight enters the collector at a low angle. Since the cells in a receiver are typically connected in series in order to build voltage, special care needs to be taken with bypass diodes in order to avoid damage to shaded cells or the loss of output from an entire receiver in which only one or two cells are shaded. The bypass diodes need to be heat sunk, and there is a substantial performance loss when bypass diodes switch on in response to reduced illumination.

Linear concentrators typically produce a Gaussian illumination profile. The width of the solar cell needs to be sufficient to capture more than 90% of the concentrator sunlight, with an additional margin to take account of the fact that sun tracking is generally intermittent rather than continuous. This means that the centre of the solar cell is much more strongly illuminated than the edges of the solar cell, leading to enhanced resistive losses compared with the uniform illumination normally used to measure and sort the solar cells. In addition, the cell temperature in the centre is higher than at the edges. Flux modification can be used to create uniform illumination, at additional cost.

Fig. 3.5. Parabolic trough concentrator, illustrating the shadows cast on receivers by gaps between the mirrors and structural elements

Fig. 3.6. Slivers, each 1 mm wide and 50 µm thick

Another significant issue is thermal expansion mismatch between cell and receiver. This is a particular problem for the larger cells typically used in linear concentrator systems.

3.4.4 Sliver Solar Cells

Sliver solar cells (Fig. 3.6) have attractive applications in both non-concentrator and concentrator photovoltaic systems [19,20]. Sliver solar cells fabricated for non-concentrator applications are also suitable for linear concentrator applications, in the range $1-3\,\mathrm{W/cm^2}$. This offers the prospect of low costs per square centimetre due to high-volume cell production for non-concentrator applications.

Sliver cells are long (5 – 10 cm), thin (40 – 80 μm) and narrow (0.7 – 2 mm), and have efficiencies above 20% at 1 sun. Standard silicon wafers ($\sim 0.7-2$ mm thick) are used as the starting material for the fabrication process. Thousands of narrow grooves are etched that extend through the wafer (Fig. 3.7). The grooves lead to the creation of a series of thin silicon strips ("Slivers").

The host wafer is processed using standard techniques. The slivers are then cut out of the wafer frame to form individual Sliver cells. Each 15 cm diameter wafer can yield hundreds to thousands of Sliver cells with a combined surface area that is $10-30\times$ the surface area of the host wafer. The positive and negative contacts of each cell are located on the two edges, rather than the faces, of the cells. This eliminates shading of the cell by metal fingers, ensures perfect bifacial response and allows easy series interconnection of the cells.

The rotation of each sliver through 90° generates a large gain in the active surface area – "area multiplication" – compared with the starting wafer. In a conventional solar cell process, processing takes place on the wafer surfaces – essentially a 2D process. In the Sliver cell process, cells are formed in the wafer volume – essentially a 3D process, which produces a large increase in the active surface area of solar cells per unit volume of silicon consumed and per wafer that is processed.

Individual Sliver cells can be connected in series to build voltage rapidly, at a rate of 7 – 10 V per linear centimetre. A typical solar cell designed for use in a trough concentrator has an area of $40\times 50\,\mathrm{mm^2}$, and a maximum power voltage of about 0.7 V. Groups of 70 Sliver cells, each 0.7 mm wide and 40 mm long, can be connected in series to mimic the dimensions of such a cell. The main difference is that the voltage will be $70\times$ larger (50 V) and the current $70\times$ smaller. These groups can be connected in parallel. This greatly reduces the effect of partial shading on receiver output, and the protective diode arrangements can be simplified.

Sliver cells are naturally perfectly bifacial, which allows their use in a variety of novel linear concentrator systems, in particular in microconcentrators, where the narrowness of the cell matches the small width of the concentrator optics. Sliver cells are flexible because they are thin, allowing them to be wrapped around curved surfaces.

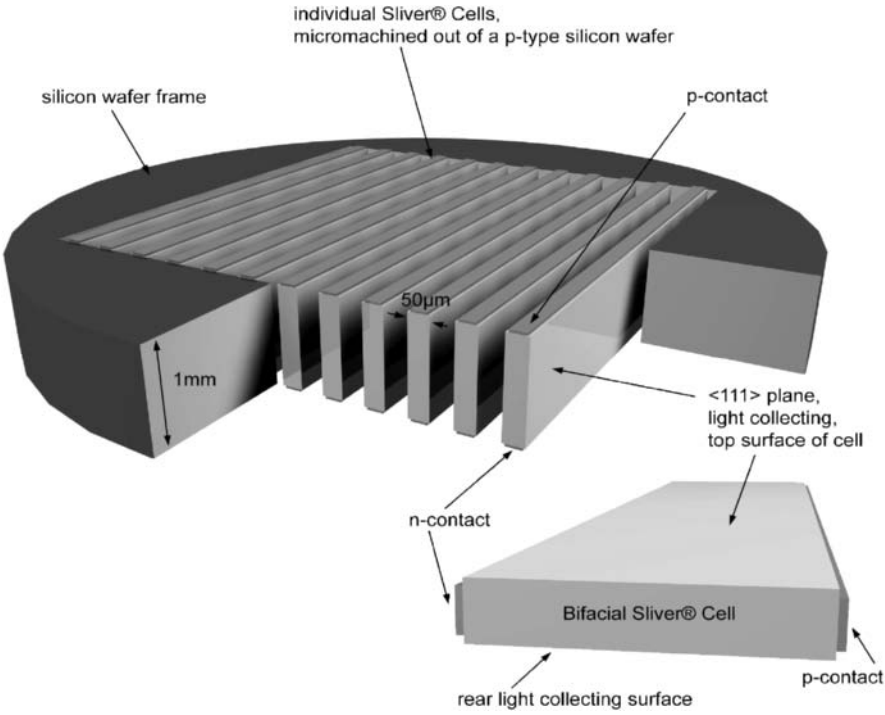

Fig. 3.7. The Sliver cell process. Each processed wafer contains hundreds or thousands of individual Sliver solar cells

3.5 Conclusion

Silicon solar cell efficiency has saturated in recent years, limited primarily by surface recombination. Recently triple junction III-V solar cells, with efficiencies above 40%, have been developed. It seems that silicon solar cells for high-concentration systems ($> 10\,\mathrm{W/cm^2}$) are unlikely to be economically competitive, although silicon cells could form part of a multijunction cell stack.

Silicon solar cells for linear concentrators ($1-5\,\mathrm{W/cm^2}$)are likely to be competitive with the higher efficiency but much higher cost of multijunction cells for a considerable time to come. Such cells can take full advantage of high-efficiency cell processing techniques to reach efficiencies well above 20%.

The market for PV linear concentrator systems is small. For this reason there is no large-scale manufacturing of highly efficient ($> 24\%$) specialist solar cells for linear concentrator systems. This means that the cost of specialist high-efficiency cells for linear concentrators is high, which in turn limits growth of the market for linear PV concentrators.

The availability of upgraded 1 sun cells suitable for moderate concentration, such as back contact, buried contact and Sliver cells, provides an oppor-

tunity to build a viable PV linear concentrator market, which may eventually lead to mass production of cells specifically for PV linear concentrators.

References

1. M.A. Green, Z. Jianhua, A.W. Blakers, M. Taouk and S. Narayanan, IEEE Electron Device Letters, Vol. EDL-7, pp. 583–585, 1986
2. R.A. Sinton, P.J. Verlinden, D.E. Crane and R.M. Swanson, Proc 8th Photovoltaic Solar Energy Conf., Florence, p. 1472 (1988)
3. R. Hezel and R. Schroner, J. Appl. Phys., 52(4), 3076 (1981)
4. F.W. Chen, T.-T. A. Li and J.E. Cotter, Proc 4th World Conference on PV Energy Conversion, Hawaii (2006)
5. E. Maruyama, A. Terakawa, M. Taguchi, Y. Yoshimine, D. Ide, T. Baba, M. Shima, H. Sakata and M. Tanaka, Proc 4th World Conference on PV Energy Conversion, Hawaii (2006)
6. E. Yablonovich and G.D. Cody, Trans. Elec. Dev. ED-29, 300 (1982)
7. P. Campbell and M.A. Green, J. Appl. Phys. 62, 243 (1987)
8. P. Campbell and M.A. Green, Trans. Elec. Dev. ED-33, 234 (1986)
9. A.W. Blakers, J. Appl. Phys 71, 5237 (1992)
10. M. Stuckings and A.W. Blakers, Solar Energy Mater Solar Cells 59, 233 (1999)
11. R.M Swanson, S.K. Beckwith, D.E. Crane, W.D. Eades, Y.H. Kwark, R.A. Sinton and S.E. Swirhun, IEEE Trans. Elec. Dev. ED-31, 661 (1984)
12. P. Verlinden, F. Van de Wiele, G. Stehlin, F. Floret and J.P. David, Proc 19th IEEE PV Spec. Conf., New Orleans, p. 405 (1987)
13. P.J. Verlinden, R.M. Swanson, D.E. Crane, K. Wickham and J. Perkins, A 26.8% efficient concentrator point-contact solar cell.Conference Record, 13th European Photovoltaic Solar Energy Conference, Nice, October, 1995; 1582–1585
14. R.A. Sinton, P.J. Verlinden, D.E. Crane and R.M. Swanson, Contractor Report SAND96-2403, Sandia (1996)
15. http://www.sunpowercorp.com
16. http://www.entechsolar.com
17. S. Wenham and M. Green, Laser Grooved Solar Cell, Patent AU565214B (1987)
18. M.C. Morilla, J.M. Fernández, I. Antón, D. Pachón, G. Sala. Buried contact cell design optimisation for concentration system, 20th European Photovoltaic Solar Energy Conference and Exhibition, Barcelona (2005)
19. A. Blakers and K. Weber, Semiconductor wafer processing to increase the usable planar surface area, 2002220348 (2001)
20. E. Franklin, A. Blakers, K. Weber, V. Everett and P. Deenapanray, Towards a simplified 20% efficient Sliver cell, 4th World Conference on Photovoltaic Energy Conversion, Hawaii, May 2006

4 Multijunction Concentrator Solar Cells

A.W. Bett, F. Dimroth, and G. Siefer

4.1 Introduction

Tandem solar cells based on III-V materials have achieved the highest efficiencies of any present photovoltaic device. Conversion efficiencies up to 39% at ~ 240 sun concentration [1] have been reported, and efficiencies $> 40\%$ are foreseen in the near future. Additionally, these devices are presently the only available solar cells reaching efficiencies above 30%. The high efficiency is due to the reduction of thermalization and transmission losses in solar cells when the number of p-n junctions is increased (see Fig. 4.1); however, the higher costs of these solar cell materials compared with silicon or thin-film devices prohibit their application in flat-plate modules on earth. The solution to this

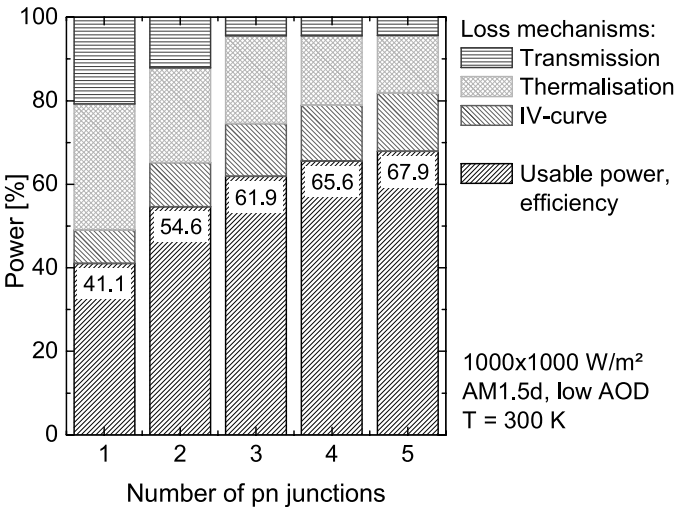

Fig. 4.1. Calculated maximum usable power of a solar cell vs the number of implemented p-n junctions. For the calculation, the radiative limit was assumed [2,3]. The given efficiencies for the multijunction cells always assume the optimum band-gap combination of the sub-cells. In addition, the percentages for the loss mechanisms of transmission and thermalization and due to the shape of the IV curve, are shown

cost-efficiency dilemma is their use in high-concentration systems, thereby replacing the expensive solar cell materials by cheaper optics.

In this chapter, we describe the background to the research development on multijunction solar cells. In the first part we discuss the early developments and approaches for realizing high-efficiency multijunction solar cells. Then we present state-of-the-art technologies for manufacturing multijunction solar cells. In the next sect. we concentrate on the characterization of monolithic multijunction solar cells, still a challenging issue which is often not properly addressed. (This is especially true for concentrator solar cells.) Finally, an overview of new approaches for reaching even higher conversion efficiencies $> 40\%$ in the future is given.

4.2 Overview of Tandem Solar Cell Development

Even in the early days of solar cell development it was obvious that the efficiency of the solar cell would have a strong impact on the cost of photovoltaic (PV) electricity. In a PV installation, several cost components are area related (e.g. structural costs, encapsulation, ground, etc.); therefore, systems with a higher efficiency require less area and lower overall costs can be expected. However, as shown in Fig. 4.1, when using single-semiconductor material, the efficiency is limited by transmission and thermalization losses in the solar cell. In order to convert the broad solar spectrum more efficiently, the multijunction concept was considered even more than 50 years ago. (The reader interested in a more detailed review of the history of multijunction solar cells is referred to work by Sharps et al. [4].)

Two technological approaches have been investigated over the years (see Fig. 4.2): In the mechanically stacked approach (Fig. 4.2a), solar cells with different band-gap energies are fabricated on their individual substrates and then brought together. Each solar cell has its own positive and negative contact and can be connected separately. In the monolithic approach (Fig. 4.2b), the different materials are all grown on a single substrate and connected in series by interband tunnel diodes. This approach allows several materials to be stacked, resulting in a final device with only one positive contact and one negative contact as in a conventional single-junction solar cell. The current in such a device is always limited by the lowest current generated by one of the p-n junctions. The band-gap energies of the materials and the overall device structure therefore have to be chosen carefully.

Table 4.1 shows a summary of efficiencies for a selected number of III-V concentrator cells. These cells were fabricated between 1988 and 2005 with different mechanically stacked and monolithic technologies. It is noteworthy that even the first cells in the 1980s and early 1990s show high efficiencies, but the cells were normally research samples of small size, not ready for production in larger quantities for commercial use.

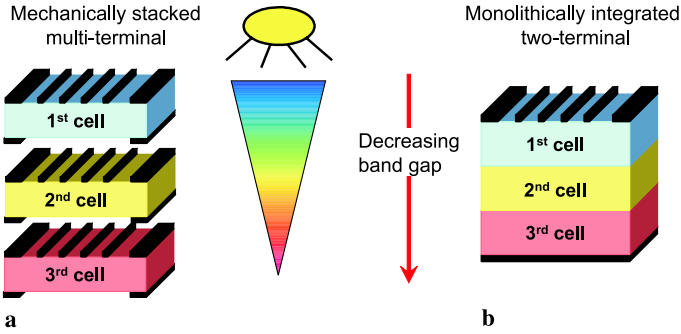

Fig. 4.2. Two approaches for multijunction solar cells. **a** Mechanically stacked approach: single-junction cells of different semiconductor materials are manufactured and stacked on top of each other. This leads to multiple terminals which have to be connected properly in the module. **b** Monolithic approach: semiconductor materials with different band-gap energies are grown epitaxially on top of each other. The internal series connection of the sub-cells is achieved by tunnel diodes. Note that neither approach is limited to three materials, as shown here

The more recent development of high-efficiency multijunction solar cells is based on a monolithic triple-junction device made of $Ga_{0.5}In_{0.5}P/Ga_{0.99}In_{0.01}As/Ge$. The history of this cell structure started back in 1984, when Jerry Olson invented the GaInP/GaAs tandem cell [12]. Current matching in this structure was achieved by reducing the thickness of the top cell layers to be partially transparent. Over the years it turned out that GaInP is easier to grow with high crystal quality than the better-known AlGaAs compound. This is the main reason for the success of this approach. The commercial use of the structure started in the 1990s as a $Ga_{0.5}In_{0.5}P/Ga_{0.99}In_{0.01}As/Ge$ triple-junction solar cell for space. The low-bandgap Ge (0.67 eV) substrate was activated as a third p-n junction. The Ge adds another 230 mV to the device voltage in this case and has several other advantages compared with the use of GaAs as the substrate, such as weight, robustness and price. This solar cell structure has been further developed and is produced presently by Azur, Spectrolab and EMCORE.

For space applications, the high power per mass ratio of the $Ga_{0.5}In_{0.5}P/Ga_{0.99}In_{0.01}As/Ge$ solar cell compared with Si outweighs the higher material cost. On earth, concentrators are becoming the key for making the multijunction technology cost-competitive. For this application, the solar cell structure has to be adapted to the terrestrial solar spectrum and the high current densities generated under concentrated illumination. Even with these important differences in the solar cell design, there is much in common between the technologies for space and terrestrial applications. At present, different research groups around the world have demonstrated solar cell efficiencies exceeding 35% under the concentrated terrestrial spectrum AM1.5d [1, 10, 13].

Table 4.1. Efficiencies of selected concentrator cells as published between 1987 and 2005. *AOD* aerosol optical depth

Year	Laboratory	Efficiency (%)	X (suns)	Comments	Reference
1988	Varian/Stanford Sandia	29.6	330	GaAs /Si: four terminals, mechanically stacked	[5]
1989	Boeing	32.6	100	GaAs /GaSb: four terminals, mechanically Stacked	[5]
1991	Spire	27.6	255	GaAs single junction	[5]
1994	NREL	30.2	160	GaInP /GaAs: two terminals, monolithic	[6]
2001	Fraunhofer ISE	31.3	300	GaInP /GaInAs: two terminals, monolithic	[7]
2001	IES-UPM/IOFFE	26.2	1000	GaAs single junction	[8]
2001	Fraunhofer ISE	33.5	300	GaInP /GaInAs//GaSb: four terminals, mechanically Stacked	[9]
2003	Sharp Corp.	36.0	500	GaInP /GaInAs/Ge: two terminals, AM1.5G spectrum	[10]
2005	Fraunhofer ISE Azur	35.2	600	GaInP /GaInAs/ Ge: two terminals, monolithic	[11]
2005	Spectrolab	39.0	236	GaInP /GaInAs/Ge: two terminals, low-AOD spectrum	[1]

In a monolithic triple-junction solar cell, only one substrate is needed, which is a cost advantage compared with the mechanically stacked approach; however, the growth of the solar cell structure and characterization is more complex. The following sect. gives more detailed information on how monolithic concentrator multijunction solar cells are fabricated at present.

4.3 Manufacturing of Tandem Concentrator Solar Cells

A monolithic tandem solar cell is a multilayer structure that consists of a variety of III-V compound semiconductor materials. The band-gap ener-

gies of the crystals can be varied by changing the composition in ternary and quaternary alloys such as $Ga_xIn_{1-x}P$ or $(Al_xGa_{1-x})_yIn_{1-y}As$. Besides the band-gap energy, also the binding energy of the atoms in the crystal, and therefore the lattice constant, is a function of the composition. The growth of high-quality crystals usually requires lattice-matched materials, which adds a restriction to the selection of suitable compounds. The most successful $Ga_{0.5}In_{0.5}P/Ga_{0.99}In_{0.01}As/Ge$ triple-junction solar cell is a completely lattice-matched layer structure. Besides the photoactive p-n junctions, the structure includes several additional layers with different compositions, as shown in Fig. 4.3. They serve as passivation layers, barrier layers for internal diffusion processes or as components of the integrated tunnel diodes. A typical triple-junction solar cell has more than 20 single layers with thicknesses between 10 nm and several microns, and doping levels between $10^{16}\,cm^{-3}$ and $10^{20}\,cm^{-3}$.

Multilayer structures of III-V compound semiconductors can be produced by epitaxial growth. Different methods, such as liquid phase epitaxy (LPE), molecular beam epitaxy (MBE), and metal-organic vapour phase epitaxy (MOVPE), have been investigated in the past. MOVPE has been proven to achieve the best economics of growth combined with a high crystal perfection, homogeneity and interface control. Presently, large-area commercial reactors with up to $12" \times 4''$ substrate configurations are available from the companies AIXTRON and VEECO. These systems are primarily designed for the mass

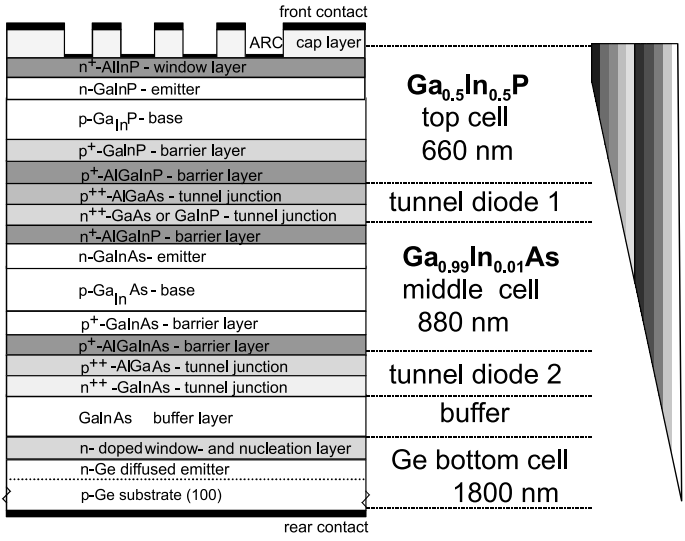

Fig. 4.3. A typical structure of a monolithic triple-junction solar cell. Each active sub-cell consists of at least a window-, emitter-, base-, and back-surface field layer. Between the sub-cells, highly doped thin layers act as tunnel diodes and interconnect the cells internally in series

production of light-emitting diodes with similar requirements on the epitaxial growth.

Due to the low-energy density of sunlight on earth, photovoltaic energy conversion always involves large areas. Even in the case of concentrators working at 500 suns, huge amounts of compound semiconductor material will be needed to make a significant contribution to the earth's energy supply. A 1-GW per year production line of GaInP/GaInAs/Ge triple-junction solar cells ($\eta = 35\%, C = 500$ suns), for example, will need 110 MOVPE reactors and consume 15 tons of Ge substrates, 18.2 tons of AsH_3, 10.5 tons of PH_3 and about 2 tons of metal-organic compounds such as trimethyl gallium and trimethyl indium per year [14]. Though these numbers are already quite large, they can be made available in a short time frame of 2-3 years. This technology may be limited by the availability of Ge raw material if the production volume exceeds 20 GW per year. In this case, either new approaches to gain Ge have to be pursued or multijunction solar cells have to be transferred to a different substrate material such as Si or GaAs.

One of the most important reasons for the success of III-V compound semiconductors for solar cells is the high crystal quality that can be achieved in material grown by MOVPE. In a solar cell, the lifetime of minority carriers is essential for achieving good device performance. This parameter is influenced by non-radiative recombination either in the crystal or at the interfaces. Until the end of the 1990s, a strong correlation between the material quality of crystals grown by MOVPE and the purity of the source materials could be found. Typical sources include hydrides, such as arsine or phosphine, and metal-organic precursors such as trimethyl gallium, trimethyl aluminium or trimethyl indium. The purity of these source materials has been significantly improved since then. The consequence is that the material quality now depends more on the growth conditions themselves. Further optimization now concentrates on finding optimum parameters for the growth temperature, reactor pressures, doping sources and profiles, material composition and interface switching sequences between different materials. All these are important parameters which influence the crystal perfection, the minority carrier lifetime and, therefore, the performance of the solar cell.

After growth of the layer structure by MOVPE, solar cell devices are fabricated by photolithography, wet-chemical processes and evaporation of metal films and dielectric anti-reflection coatings. The processing steps are performed in a clean-room environment and are similar to other optoelectronic devices. The mask design for the front contact metal grid has to be carefully optimized to avoid losses due to series resistance and shadowing. Important parameters for this optimization are the current density that is generated in the device and the resistance of the emitter layer, the contact and the metal itself. A high aspect ratio of the metal fingers additionally helps to reduce the solar cell area covered by metal. As concentrator solar cells typically operate at high current densities of several A/cm^2, series resis-

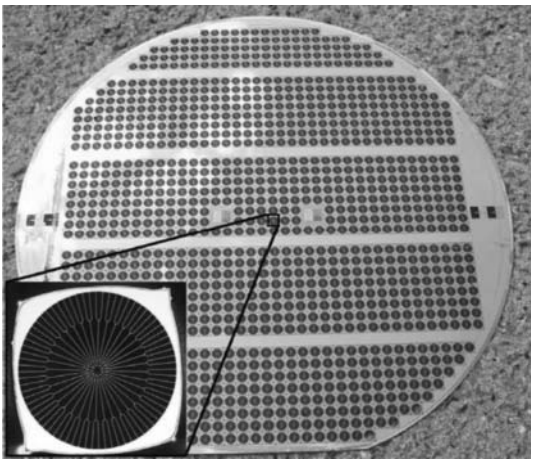

Fig. 4.4. Four-inch wafer with 1150 GaInP/GaInAs/Ge triple-junction solar cells (2 mm in diameter) grown on Germanium by MOVPE

tance losses are crucial and the configuration of the metal grid structure has to be carefully designed for each specific application.

Many papers have been published in this field and the general design rules can be found, for example, in work by Blieske et al. [15] and Algora and Díaz [16]. Photolithography and wet-chemical etching processes are used to define the solar cell area (mesa-etching process). The result is a wafer with many small concentrator solar cell devices, as shown in Fig. 4.4.

4.4 Characterization of Multijunction Concentrator Solar Cells

As is well known, an important issue for solar cells is their precise and reliable calibration. Compared with conventional single-junction solar cells, the calibration procedure for multijunction concentrator cells is more complex, time-consuming and often not correctly followed. In the following sect., we discuss the calibration procedure for monolithic III-V multijunction section concentrator cells which is used at Fraunhofer ISE.

The procedure consists of the following steps (see also Fig. 4.5):

1. The spectral response of the cell is measured (a check of the linear response of the cell's I_{SC} to the illumination level is included as a routine at Fraunhofer ISE) [17, 18].
2. The spectral response of the cell is used to perform the spectral mismatch correction and to adjust the simulator such that the generation of the cell current corresponds to the current which would be generated under standard test conditions.
3. Once the simulator is adjusted correctly, the 1-sun IV curve is recorded.

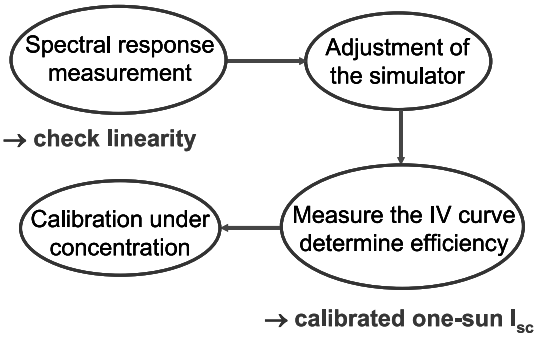

Fig. 4.5. Flow chart of the process sequence to calibrate a multijunction concentrator solar cell

4. Finally, IV curves under high light intensities are measured. The concentration C and efficiency η are determined as given in 4.1:

$$C = \frac{I_{\mathrm{SC}}}{I_{\mathrm{SC}}(1-\mathrm{sun})} \quad \eta = \frac{I_{\mathrm{SC}(1-\mathrm{sun})}}{I_{\mathrm{SC}}} \cdot \frac{P_{\mathrm{max}}}{P_{\mathrm{max}(1-\mathrm{sun})}} \cdot \eta_{(1-\mathrm{sun})} \tag{4.1}$$

where I_{SC}, $I_{\mathrm{SC}(1-\mathrm{sun})}$, P_{Max} and $P_{\mathrm{Max}(1-\mathrm{sun})}$ are the short-circuit currents and maximum power points under concentration and 1-sun conditions, respectively.

Standard test conditions for concentrator cells are: a cell temperature of 25 °C; a spectral distribution according to AM1.5 direct; and a total irradiance of 1000 W/m^2. The spectral distribution of the AM1.5 direct spectrum was recently the subject of controversial discussion. The standard was determined years ago [19], but it was found that the chosen spectral distribution does not fit the reality very well; therefore, a modified spectrum for AM1.5 direct was suggested, which uses a lower aerosol optical depth value [20]. The new spectrum is now accepted by the most important calibration laboratories around the world. It is used for the most recent measurement of concentrator devices; however, the different spectral conditions lead to confusion in the literature and one has to be careful when efficiencies are compared.

The Fraunhofer ISE procedure to calibrate a concentrator multijunction solar cell is summarized in Fig. 4.5.

4.4.1 Spectral Response Measurement

The principle of the spectral response measurement of a multijunction solar cell is similar to that for single-junction cells. The cell under test is illuminated with chopped monochromatic light and additional DC bias light. An I-V converter keeps the cell under test in short circuit conditions. The signal caused by the chopped monochromatic light is detected by a lock-in amplifier (see Fig.4.6).

The key issue in measuring the spectral response of multijunction cells is the correct choice of the DC bias light. This additional bias light has to

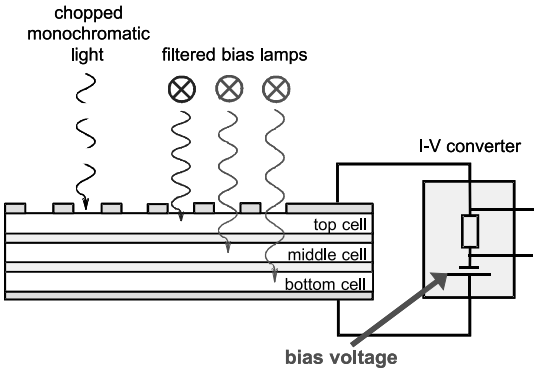

Fig. 4.6. The principle of a spectral response measurement. Filtered bias lamps are used to illuminate the individual sub-cells. The chopped monochromatic light causes an AC signal in the cell. It is detected with a lock-in amplifier (not shown)

ensure that the subcell under test is limiting the current of the whole device. Here, one makes use of the principle of current limitation in series-connected cells. Due to the series connection, the subcell generating the lowest current I_i will limit the total current I_{MJ} of the device and the voltages V_i of the subcells will add up to the total voltage V_{MJ} of the whole device (see 4.2).

$$I_{\mathrm{MJ}} = \mathrm{Min}\,\{I_i\} \quad V_{\mathrm{MJ}} = \sum_i V_i \tag{4.2}$$

The bias light used to measure the spectral response of multijunction cells is generated by applying appropriate filters to tungsten lamps. The filters are chosen such that the subcell under test will generate less current than the remaining subcells. An example of the bias light spectra used to measure a triple-junction cell as well as the measurement result is shown in Fig. 4.7.

Besides applying filtered bias light, the cell under test is voltage biased in the forward direction to ensure that the subcell under test is operating under short-circuit conditions [21]. Without a voltage bias, the subcell under test would operate at a negative voltage which is approximately equal to the sum of the V_{oc} of the remaining subcells. If the cell under test has a low shunt resistance, however, often measurement artefacts are observed. These artefact signals can be minimized by using a correct forward bias voltage. Details of the procedure for applying the forward bias correctly are given by Meusel et al. [22].

In order to check the linearity of the cell under varying intensity levels, the external quantum efficiency is determined at different intensity levels. As long as the EQE remains the same, the cell is assumed to be linear [17,18,23]. At Fraunhofer ISE, linearity is observed between 0.1 and 100 suns for the GaInP top cell and between 0.1 and 20 suns for the Ga(In)As middle cell.

4.4.2 Calibrated IV Curve Under 1-Sun Conditions

The correct setting of the solar simulator can be calculated easily from the relative spectral response of the (single-junction) cell under test together

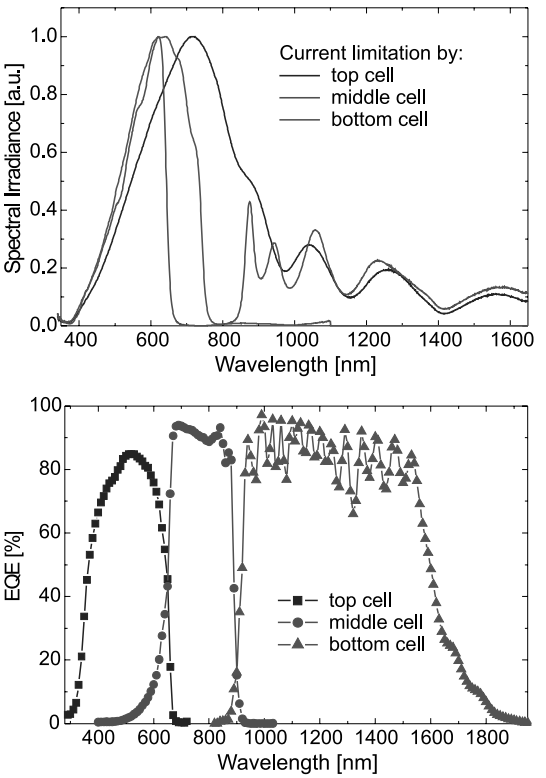

Fig. 4.7. *top*: Spectra of the bias light used to measure the spectral response of a triple-junction solar cell and *bottom*: the measured external quantum efficiency of the triple-junction cell *right*: The main part of the bias light spectrum for each subcell to be measured falls within the spectral response range of the other two sub-cells

with the relative spectral distribution of the simulator spectrum and the (absolute) spectral response of the reference cell. This means that the current generation of the test cell under simulator illumination equals the current generation under the standard spectrum. In the case of single-junction cells, this is commonly done using the spectral mismatch correction procedure [24].

A generalization of this mismatch correction procedure for multijunction cells (see e.g. [25,26]) leads to an iterative process involving re-measuring the simulator spectrum repeatedly. An alternative approach developed at ISE CalLab using a multisource simulator obviates this iterative process. The simulator spectral setting in this case is calculated as the additive mixture of the spectra of the individual light sources [27].

Generalized Mismatch Factor Procedure for Multijunction Solar Cells

The photocurrent generation of any solar cell with an absolute spectral response $S(\lambda)$ under a given reference spectrum $E_{\mathrm{ref}}(\lambda)$ can be calculated us-

ing 4.3:

$$J_{\text{photo}} = \int S(\lambda) \cdot E_{\text{ref}}(\lambda)\,\mathrm{d}\lambda \tag{4.3}$$

For the calibration of the multijunction solar cell, the simulator has to be adjusted such that

$$J_{\text{sim}}^{\text{test},i} = J_{\text{ref}}^{\text{test},i} \tag{4.4}$$

holds for each junction i of the multijunction cell to be calibrated.

To fulfil this condition in the case of a multijunction cell, it must be possible not only to adjust the total intensity of the solar simulator, but also to change the intensity on each subcell individually. This is only possible when the spectral distribution of the simulator spectrum can also be changed. This can be achieved by introducing a set of different filters. Concerning the intensity of the simulator, this leads to the following condition for a reference cell:

$$J_{\text{sim},i}^{\text{refcell}} = \frac{J_{\text{ref},i}^{\text{refcell}}}{M_i} \tag{4.5}$$

where M_i is the spectral mismatch factor for each junction i (note that for this procedure, adapted reference cells for each subcell are advantageous):

$$M_i = \frac{\int e_{\text{sim}}(\lambda) s^{\text{test},i}(\lambda)\,\mathrm{d}\lambda \int e_{\text{ref}}(\lambda) s^{\text{ref},i}(\lambda)\,\mathrm{d}\lambda}{\int e_{\text{ref}}(\lambda) s^{\text{test},i}(\lambda)\,\mathrm{d}\lambda \int e_{\text{sim}}(\lambda) s^{\text{ref},i}(\lambda)\,\mathrm{d}\lambda} \tag{4.6}$$

Here $e_{\text{sim}}(\lambda)$ and $e_{\text{ref}}(\lambda)$ represent the simulator and reference spectra, respectively. The spectral response of junction i of the multijunction cell under test is $s^{\text{test},i}(\lambda)$, whereas $s^{\text{ref},i}(\lambda)$ is the spectral response of the reference cell corresponding to subcell i. The lower-case characters in 4.6 indicate that only relative quantities are needed, thus eliminating the additional uncertainty in determining absolute values of spectral response and spectrum; however, an iterative process is necessary to adjust the simulator spectrum correctly, and involves measuring the (new) simulator spectrum, recalculating the mismatch factors for each subcell and finally measuring the short-circuit currents of the corresponding reference cells. This process is repeated until $|M_i - 1| < 1\%$. Then the 1-sun IV curve is recorded for these simulator settings.

ISE CalLab Procedure for the 1-Sun Calibration of Multijunction Cells

The ISE CalLab procedure for calibrating multijunction cells under 1-sun conditions makes use of a multisource solar simulator (MuSim). Figure 4.8 shows the multisource simulator used at ISE CalLab as well as the spectra of the three light sources.

The derivation of the equations used to adjust the simulator also starts from 4.3, which can be transformed to:

$$J_i^{\mathrm{ref}} = \int S_i(\lambda) \cdot E_{\mathrm{ref}}(\lambda)\,\mathrm{d}\lambda = C_i \int s_i(\lambda) E_{\mathrm{ref}}\,\mathrm{d}\lambda \tag{4.7}$$

Here, the absolute spectral response $S_i(\lambda)$ from 4.3 is replaced by the relative spectral response $s_i(\lambda)$. C_i in this case is the ratio of the absolute to the relative spectral response.

If now the multijunction cell under test is placed under a multisource solar simulator composed of n individual and independent light sources with relative spectral distributions $e_j(\lambda)$ (n being equal to the number of junctions of the test cell), the photocurrent generation of junction i can be calculated according to:

$$J_i^{\mathrm{sim}} = \sum_{j=1}^{n} C_i A_j \int s_i(\lambda) e_j(\lambda)\,\mathrm{d}\lambda \tag{4.8}$$

where A_j is the ratio of absolute to relative spectral irradiance of light source j. For the calibration, the current generation of each junction must be equal to the current generation under standard test conditions (i.e. under the reference spectrum).

Equation 4.7 and 4.8 are set equal for every junction i:

$$J_i^{\mathrm{sim}} = \sum_{j=1}^{n} C_i A j \int s_i(\lambda) e_j(\lambda)\,\mathrm{d}\lambda = C_i \int s_i(\lambda) E_{\mathrm{ref}}\,\mathrm{d}\lambda = J_i^{\mathrm{ref}} \tag{4.9}$$

C_i cancels out, leading to:

$$\sum_{j=1}^{n} A_j \int s_i(\lambda) e_j(\lambda)\,\mathrm{d}\lambda = \int s_i(\lambda) E_{\mathrm{ref}}\,\mathrm{d}\lambda \tag{4.10}$$

Equation 4.10 now represents an n-dimensional, inhomogeneous linear equation system with n unknowns A_j. To ensure positive solutions for A_j (negative solutions are unphysical), the light sources of the multisource simulator are chosen such that one light source mainly generates current in one junction of the cell under test (see Fig. 4.8, upper right).

The absolute spectral distribution $E_j(\lambda)$ of the light source j can be obtained from the coefficients A_j and the relative spectral distribution $e_j(\lambda)$:

$$A_j e_j = E_j(\lambda) \tag{4.11}$$

This absolute spectral distribution can now be used to calculate the current generation in a (single-junction) reference cell where the absolute spectral response $S^{\mathrm{ref}}(\lambda)$ is known:

$$J_{E_j}^{ref} = A_j \int S^{\mathrm{ref}} e_j(\lambda)\,\mathrm{d}\lambda \tag{4.12}$$

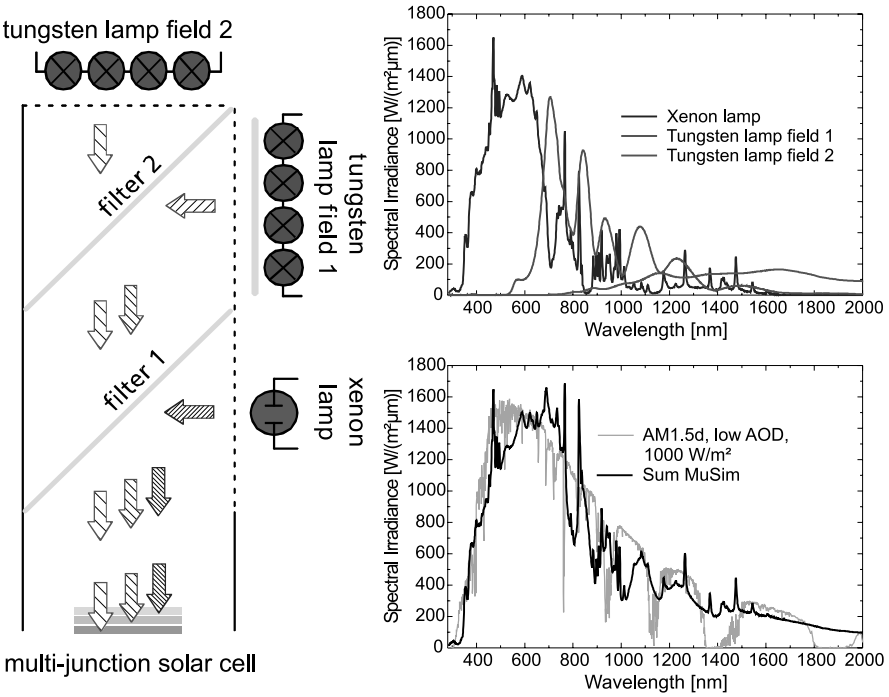

Fig. 4.8. *Left*: Schematic diagram of the multi-source simulator used at ISE CalLab *upper right*: as well as the individual spectra of the three light sources *lower right*: and the combination of the three spectra as used for the calibration of a triple-junction cell at AM1.5d, low AOD, 1000 $\mathrm{W/m^2}$

The multisource simulator is now adjusted such that 4.12 holds for each light source j. For all of the calculations above, only relative data are needed. (The only absolute quantities used are the spectral distribution $E_{\mathrm{ref}}(\lambda)$ of the reference spectrum and the absolute spectral response of the reference cell $S^{\mathrm{ref}}(\lambda)$ which are, of course, available.)

Compared with the generalized mismatch factor procedure given in the previous paragraph, the main advantage of the ISE procedure is that the iterative process of re-measuring the simulator spectrum is avoided. If the simulator is adjusted correctly, the 1-sun IV curve of the concentrator solar cell can be measured. As an example, the IV curve of a triple-junction concentrator solar cell is shown in Fig. 4.9.

The important information from this measurement is the short circuit current, because it is later used to determine the concentration ratio. This is possible if the cell shows linear dependence of the generated current on the incident intensity. In our experience, this is the case for cells characterized by high-efficiency values; however, some cells show non-linearity, e.g. introduced by interface recombination effects. These cells show also lower performance

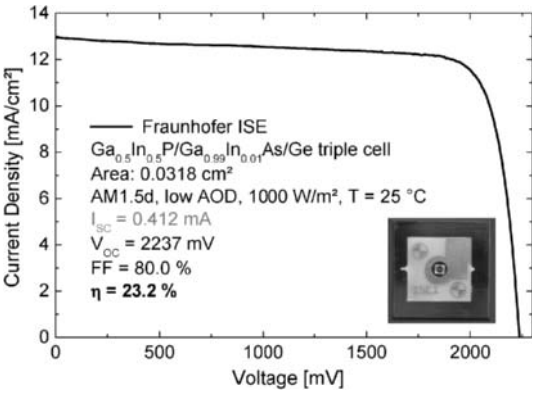

Fig. 4.9. Example of a calibrated IV-curve measurement of a triple-junction concentrator solar cell under standard test conditions. The important information is the short-circuit current, which is needed to determine the concentration ratio

if correctly measured (the non-linearity introduces additional challenges to determining the correct concentration value).

4.4.3 Calibration Under Concentration

The calibration of multijunction cells under concentration is preferably performed with a flash simulator. The main advantages compared with a DC simulator are the negligible heating of the test samples and the fact that the high light intensity level in the case of a flash simulator is usually realized simply by shortening the distance between the test sample and light source. No lenses are used to focus the light and thus no chromatic aberration will occur to change the simulator spectrum; however, in real applications, this effect, and inhomogeneous illumination, have to be considered and will influence the performance of the cell. On the other hand, the question arises of how to change the flash spectrum in order to adjust the spectrum for the cell under test. In principle, a multiflash simulator would be needed but is not available at present for the desired high concentration range.

The currently available flash simulator at Fraunhofer ISE is known to show a change in its spectral distribution with the age of the flash bulb (the spectrum shifts to the "red" with the number of triggered flashes); thus, using flash bulbs of different age in combination with appropriate filters does not allow free adjustment of the simulator spectrum as in the case of a multisource simulator, but at least this gives the opportunity to choose a flash bulb/filter combination which fits best to the cell under test together with the desired spectral condition. Figure 4.10 (left) shows the measured spectrum of the bulb/filter combination used to perform a calibrated measurement. In addition, the AM1.5 direct spectrum and the external quantum efficiency (EQE) of the top and middle cell are displayed. Obviously, the spectra are quite different; however, integration with the EQE data shows that the same currents are generated in each subcell. Here we are not concerned about the Ge bottom subcell, because in a lattice-matched triple-junction cell it

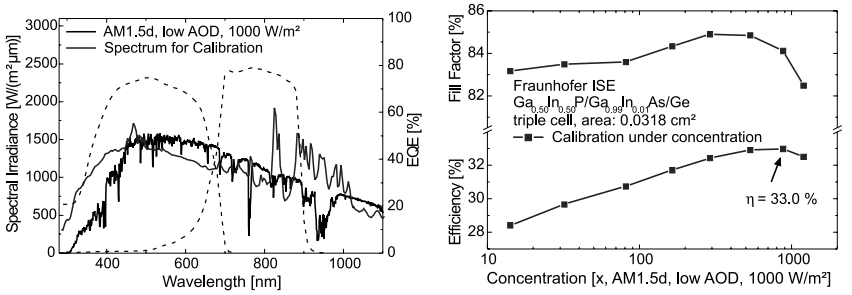

Fig. 4.10. *Left*: the measured spectrum of the flash bulb and for comparison the AM1.5 direct spectrum. In addition, the external quantum efficiencies of the top and middle cell are displayed. *Right*: the measured fill factor and efficiency vs concentration ratio of a triple-junction lattice-matched concentrator solar cell taken from the Fraunhofer ISE production

generates a large excess current in comparison with the top and middle subcells.

The calibrated efficiencies were determined depending on the concentration ratio and light intensity, respectively (see Fig. 4.10, right). The concentration ratio was derived by dividing the measured high-intensity I_{sc} by the 1-sun I_{sc}.

4.4.4 Measurements Using an Unmatched Spectrum

In order to demonstrate the impact of an incorrectly chosen spectral distribution for the high-intensity measurement, we applied a "redder" flash spectrum. The spectrum used is shown in Fig. 4.11(left). This leads to a higher photocurrent generation in the middle cell compared with the calibration condition. As a consequence, the operation point of the middle cell shifts and

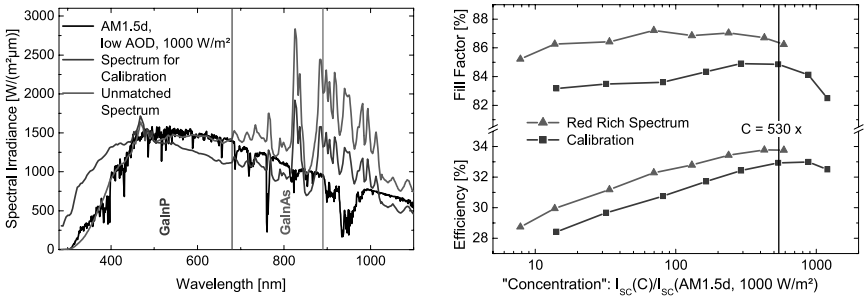

Fig. 4.11. *Left*: comparison of the AM1.5 direct spectrum, a flash bulb spectrum used for the calibration and a "redder" flash bulb spectrum is shown. *Right*: the measured fill factor and efficiency vs concentration for the calibrated and redder spectra of the flash bulb

higher fill factors are measured for the triple-junction solar cells. This leads to higher efficiency values if the concentration ratio is still determined as usual: by dividing the measured high-intensity and (calibrated) 1-sun short-circuit currents. A comparison of the results obtained for the calibrated and the "redder" conditions are given in Fig. 4.11(right).

This example shows that the calibration of a multijunction concentrator solar cells has to be performed with great care but is well understood in principle. Further details of the calibration of multijunction cells under concentration as well as effects caused by the use of an unmatched simulator spectrum can be found in [23, 28, 29].

As shown above, the calibration of one triple-junction concentrator solar cell is challenging; however, since concentrator solar cells are becoming an industrial product, their characterization and qualification testing in an industrial environment poses another kind of challenge. For example, more than 1000 tiny concentrator solar cells on one wafer have to be measured and classified; thus, new characterization tools have to be developed to characterize the cells in a tolerable amount of time and at low costs; therefore, Fraunhofer ISE collaborated with the company Aescusoft GmbH to develop a system called "MAPCON", in which up to 8 cells can be contacted and measured at the same time [11]. The system, based on a fully automated wafer-probing station, can handle different wafer and cell sizes. Equipped with high-concentration light sources suitable for a concentration ratio of more than 300 suns, with multipin probe cards and high-accuracy multichannel measurement devices, the IV-MAPCON system is able to perform full maps of all relevant electrical parameters of small concentrator solar cells on wafers, with high speed and high resolution.

4.5 New Solar Cell Concepts[1]

The most successful multijunction solar cell today is a triple-junction device with p-n junctions in $Ga_{0.5}In_{0.5}P$, $Ga_{0.99}In_{0.01}As$ and Ge (Fig. 4.12a). This cell is the product of choice for most of the present satellite projects. The reason for the success of this solar cell structure is the high material quality that can be achieved in these lattice-matched materials.

There are numerous other material combinations with higher theoretical efficiency, but the $Ga_{0.5}In_{0.5}P/Ga_{0.99}In_{0.01}As/Ge$ cell has come closer to its theoretical efficiency limits than any other triple-junction cell. The Ge in the $Ga_{0.5}In_{0.5}P/Ga_{0.99}In_{0.01}As/Ge$ structure usually absorbs about the same number of photons as the GaInP and GaInAs layers combined; thus, theoretically, a higher efficiency would be achieved if a 1 eV material could be added between the GaInAs and Ge junctions, as shown in Fig. 4.12b. GaInNAs has been shown to have the desired band gap (1 eV) and lattice

[1] part of this chapter was prepared for MRS-Builletin Vol 32, March 2007, p. 230 ff.

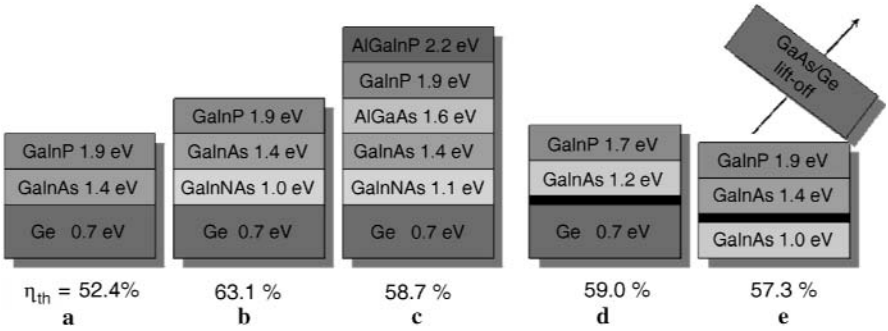

Fig. 4.12. Five advanced high-efficiency multijunction solar cell concepts are shown. The compounds of the active solar cell layers are given together with their respective band-gap energies. The fig. also includes the thermodynamic efficiency limit $\eta_{\rm th}$ of each structure under 500×AM1.5d conditions. A *black bar* indicates a grading in the lattice constant in the metamorphic approaches **d** and **e**. Each sub-cell consists of a p-n junction, front- and back-surface passivation layers, and the interband tunnel junction. This can add up to 50 individual layers for a six-junction device, as shown in **c**. **e** All layers are grown upside down and transferred to a different substrate afterward

constant (matched to Ge). Unfortunately, the addition of N to GaInAs has detrimental effects on the material quality.

There is evidence that the N causes non-radiative recombination that decreases both the photocurrent and photovoltage of a GaInNAs solar cell [30]. It is possible to improve the photocurrent collection by using a built-in electric field, but it appears that it will not be possible to achieve an ideal photovoltage for this material. The GaInNAs p-n junction can also be incorporated as the fifth subcell in a six-junction solar cell, as indicated in Fig. 4.12c. This structure generates only half the current density of a $Ga_{0.5}In_{0.5}P/Ga_{0.99}In_{0.01}As/Ge$ solar cell, and the requirement on the GaInNAs photocurrent is therefore reduced.

A complementary approach for reaching higher efficiencies is the use of lattice-mismatched materials. The theoretical efficiency of the lattice-matched triple-junction solar cell can be improved by lowering the band gaps of the first two subcells [14]. A combination of $Ga_{0.35}In_{0.65}P/Ga_{0.83}In_{0.17}As/Ge$ (Fig. 4.12d) nearly reaches the theoretical efficiency limit of a triple-junction solar cell on Ge. This structure can be realized by growing metamorphic buffer structures between the Ge substrate and the upper cell layers. If the growth conditions for the graded layer are carefully optimized, the relaxation and associated crystallographic defects can be contained within the graded layer, preserving the single-crystal quality of the active layers [31]. An example of such a metamorphic buffer structure is shown in Fig. 4.13. No threading dislocations are observed in the active solar cell layers by transmission electron microscopy. In high-resolution X–ray diffraction, a full-width

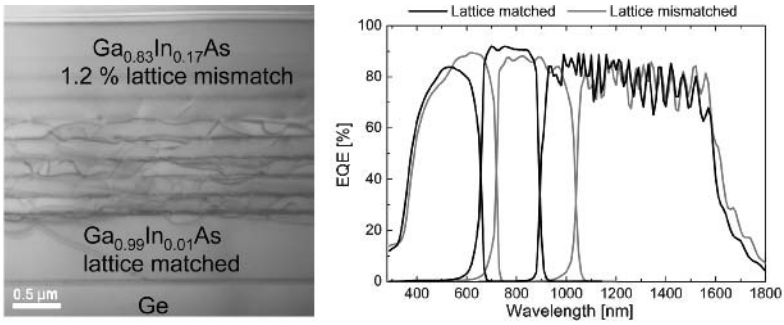

Fig. 4.13. *Left*: cross-sectional transmission electron micrograph of a step-graded $Ga_{1-x}In_xAs$ buffer layer grown on Ge [31]. The steps in the In content are visible because of the formation of a misfit dislocation network (*dark lines*). Threading dislocations are not observed. *Right*: Comparison of the external quantum efficiency of a lattice-matched $Ga_{0.5}In_{0.5}P/Ga_{0.99}In_{0.01}As/Ge$ solar cell and a lattice-mismatched $Ga_{0.35}In_{0.65}P/Ga_{0.83}In_{0.17}As/Ge$ solar cell. The differences in band-gap energy are clearly visible

half-maximum value of 45 arcsec was measured for $Ga_{0.83}In_{0.17}As$ grown on Ge, implying a dislocation density of less than $8 \times 10^5\ cm^{-2}$. The threading dislocation density can be further quantified by cathodoluminescence measured for an epitaxially grown single layer, or by electron-beam-induced current measured for a completed solar cell. One of the best measures of the overall material and interface quality, however, is the solar cell performance itself. The offset between the band gap of a material, E_g/e, and the open-circuit voltage, V_{oc}, is a good indication of non-radiative recombination losses in the materials [1]. For the lattice-matched growth of a GaAs ($E_g = 1.44\,eV$) solar cell, an offset of 387 mV is typically observed. Lattice-mismatched $Ga_{0.83}In_{0.17}As$ ($E_g = 1.18\,eV$) solar cells show very similar values of 390 mV, in contrast to nearly 600 mV for a GaInNAs ($E_g = 1.07\,eV$) solar cell. This shows the high overall crystal quality that can be achieved for the lattice-mismatched growth.

The external quantum efficiency (EQE) of a solar cell is a measure of the carrier collection efficiency of the p-n junctions. Figure 4.13 shows a comparison of the EQE for lattice-matched and mismatched triple-junction solar cells. Similar values for the EQE have been achieved in both cases. The metamorphic material growth is more difficult to control than that of lattice-matched materials; however, recently metamorphic solar cells have reached similar efficiencies compared with the best lattice-matched structures, approaching 40% [1]. In yet another promising configuration (Fig. 4.6e), first a $Ga_{0.51}In_{0.49}P$ and GaAs subcell are grown lattice-matched to GaAs or Ge, followed by a gradient in the lattice constant and a final $Ga_{0.7}In_{0.3}As$ cell. The substrate only serves as a template for the growth and is later removed to allow illumination of the triple-junction cell from the side that was grown

first. This cell has already achieved 37.9% at 10 suns [32] and has the potential to reach efficiencies > 40% in the future.

4.6 Conclusion

In this chapter we show how the efficiency of a solar cell can be increased through the use of multiple materials with different energy gaps spanning the solar spectrum. Multijunction solar cells made of III-V compound semiconductors reach the highest photovoltaic conversion efficiencies at present with up to 39% (300× AM1.5d) [1]. This is mainly due to the excellent material quality which has been achieved in materials grown by MOVPE. Further improvements will be obtained in the future as new compounds, such as GaInNAs, are investigated in more detail and material properties are improved. New cell designs with higher theoretical efficiency make use of lattice-mismatched growth as well as wafer bonding and transfer techniques, which have become available more recently.

The question of how to perform an accurate indoor calibration of the IV characteristics of a monolithic multijunction solar cell under concentrated sunlight is still unsolved. Some of the characterization techniques which are used presently are described in the text. Whatever measurement procedure is applied, it is most important to understand the influence of spectral variations and uncertainties on the measurement results.

Acknowledgement. The authors thank all members of the group "III-V Solar Cells and Epitaxy" as well as the ISE CalLab for their support. We specifically acknowledge the contributions of S. Kurtz from NREL, A. Marti from UPM, J. Luther, W. Wettling and G. Willeke from Fraunhofer ISE. Financial support was given by various German Ministries via several contracts as well as the European Commission via the contract FULLSPECTRUM (Ref. no.: SES6-CT-2003-502620).

References

1. R.R. King, D.C. Law, C.M. Fetzer, R.A. Sherif, K.M. Edmondson, S. Kurtz, G.S. Kinsey, H.L. Cotal, D.D. Krut, J.H. Ermer, N.H. Karam, Pathways to 40%-efficient concentrator photovoltaics, Proc 20th European Photovoltaic Solar Energy Conference, Barcelona, Spain, 2005, pp. 118–123
2. W. Shockley, H.J. Queisser, Detailed balance limit of efficiency of p-n junction solar cells, J Appl Phys 32(3), 1961, pp. 510–519
3. G. Létay, A.W. Bett, EtaOpt: a program for calculating limiting efficiency and optimum bandgap structure for multi-bandgap solar cells and TPV cells, Proc 17th European Photovoltaic Solar Energy Conference, Munich, Germany, 2001, pp. 178–181
4. P.R. Sharps, M.A. Stan, D.J. Aiken, F.D. Newman, J.S. Hills, N.S. Fatemi, High efficiency multi-junction solar cells: past, present and future, Proc 19th European Photovoltaic Solar Energy Conference, Paris, France, 2004, pp. 3569–3574

5. M.A. Green, K. Emery, D.L. King, Y. Hishikawa, W. Warta, Solar cell efficiency tables (Version 27), Progr Photovoltaics Res Appl 14(1), 2006, pp. 45–51
6. D.J. Friedman, S.R. Kurtz, K.A. Bertness, A.E. Kibbler, C. Kramer, J.M. Olson, D.L. King, B.R. Hansen, J.K. Snyder, GaInP/GaAs monolithic tandem concentrator cells, Proc 1st World Conference on Photovoltaic Energy Conversion, Waikoloa, Hawaii, 1994, pp. 1829–1832
7. F. Dimroth, R. Beckert, M. Meusel, U. Schubert, A.W. Bett, Metamorphic $Ga_yIn_{1-y}P/Ga_{1-x}In_xAs$ tandem solar cells for space and for terrestrial concentrator applications at $C > 1000$ suns, Progr Photovoltaics Res Appl 9(3), 2001, pp. 165–178
8. C. Algora, E. Ortiz, I. Rey-Stolle, V. Diaz, R. Peña, V.M. Andreev, V.P. Khvostikov, V.D. Rumyantsev, A GaAs solar cell with an efficiency of 26.2% at 1000 suns and 25.0% at 2000 suns, IEEE Trans Electron Devices 48(5), 2001, pp. 840–844
9. A.W. Bett, C. Baur, R. Beckert, F. Dimroth, G. Letay, M. Hein, M. Meusel, S. van Riesen, U. Schubert, G. Siefer, O.V. Sulima, T.N.D. Tibbits, Development of high-efficiency mechanically stacked GaInP/ GaInAs−GaSb triple-junction concentrator solar cells, Proc 17th European Photovoltaic Solar Energy Conference, Munich, Germany, 2001, pp. 84–87
10. T. Takamoto, T. Agui, K. Kamimura, M. Kaneiwa, M. Imaizumi, S. Matsuda, M. Yamaguchi, Multijunction solar cell technologies: high efficiency, radiation resistance, and concentrator applications, Proc 3rd World Conference on Photovoltaic Energy Conversion, Osaka, Japan, 2003, pp. 581–586
11. C. Baur, A.W. Bett, F. Dimroth, G. Siefer, M. Meusel, W. Bentsch, K. Köstler, G. Strobl, Triple-junction III-V based concentrator solar cells: perspectives and challenges, J Solar Energy Eng, 2006
12. J.M. Olson, T. Gessert, M.M. Al-Jassim, GaInP/GaAs: a current- and lattice-matched tandem cell with a high theoretical efficiency, Proc 18th IEEE Photovoltaic Specialists Conference, Las Vegas, Nevada, 1985, pp. 552–555
13. F. Dimroth, M. Meusel, C. Baur, A.W. Bett, G. Strobl, 3-6 junction photovoltaic cells for space and terrestrial concentrator applications, Proc 31st IEEE Photovoltaic Specialists Conference, Orlando, Florida, 2005, pp. 525–529
14. F. Dimroth, High-efficiency solar cells from III-V compound semiconductors, Phys Status Solidi C 3, 2006, pp. 373–379
15. U. Blieske, A.W. Bett, T. Duong, C. Schetter, O.V. Sulima, Optimization of GaAs solar cells for application in concentrator modules, Proc 12th European Photovoltaic Solar Energy Conference, Amsterdam, Netherlands, 1994, pp. 1409–1412
16. C. Algora, V. Díaz, Influence of series resistance on guidelines for manufacture of concentrator p-on-n GaAs solar cells, Progr Photovoltaics Res Appl 8(2), 2000, pp. 211–225
17. G. Stryi-Hipp, A. Schoenecker, K. Schitterer, K. Bucher, K. Heidler, Precision spectral response and I-V characterisation of concentrator cells, Proc 23rd IEEE Photovoltaic Specialists Conference, Louisville, Kentucky, 1993, pp. 303–308
18. A. Schönecker, A. Zastrow, K. Bücher, Accurate spectral response measurements of non-linear high-efficiency solar cells, Proc 12th European Photovoltaic Solar Energy Conference, Amsterdam, Netherlands, 1994, pp. 500–503
19. ISO, Solar energy: reference solar spectral irradiance at the ground at different receiving conditions, Part 1: Direct normal and hemispherical solar irradiance for air mass 1.5, 9845-1, 1992

20. D.R. Myers, K. Emery, C. Gueymard, Proposed reference spectral irradiance standards to improve concentrating photovoltaic system design and performance evaluation, Proc 29th IEEE Photovoltaic Specialists Conference, New Orleans, Louisiana, 2002, pp. 923–926
21. J. Burdick, T. Glatfelter, "Spectral response and I-V measurements of tandem amorphous-Silicon alloy solar cells", Solar Cells 18, 1986, pp. 301–314
22. M. Meusel, C. Baur, G. Létay, A.W. Bett, W. Warta, E. Fernandez, Spectral response measurements of GaInP/Ga(In)As/Ge triple-junction solar cells: measurement artifacts and their explanation, Progr Photovoltaics Res Appl 11(8), 2003, pp. 499–514
23. K. Emery, M. Meusel, R. Beckert, F. Dimroth, A.W. Bett, W. Warta, Procedures for evaluating multijunction concentrators, Proc 28th IEEE Photovoltaic Specialists Conference, Anchorage, Alaska, 2000, pp. 1126–1130
24. IEC, Photovoltaic devices, Part 7: Computation of spectral mismatch error introduced in the testing of a photovoltaic device, IEC 904-7, 1995
25. T. Glatfelter, J. Burdick, A method for determining the conversion efficiency of multiple-cell photovoltaic devices, Proc 19th IEEE Photovoltaic Specialists Conference, New Orleans, Louisiana, 1987, pp. 1187–1193
26. G.F. Virshup, Measurement techniques for multijunction solar cells, Proc 21st IEEE Photovoltaic Specialists Conference, Kissimmee, Florida, 1990, pp. 1249–1255
27. M. Meusel, R. Adelhelm, F. Dimroth, A.W. Bett, W. Warta, Spectral mismatch correction and spectrometric characterization of monolithic III-V multijunction solar cells, Progr Photovoltaics Res Appl 10(4), 2002, pp. 243–255
28. G. Siefer, C. Baur, M. Meusel, F. Dimroth, A.W. Bett, W. Warta, Influence of the simulator spectrum on the calibration of multi-junction solar cells under concentration, Proc 29th IEEE Photovoltaic Specialists Conference, New Orleans, 2002, pp. 836–839
29. G. Siefer, A.W. Bett, Calibration of III-V concentrator solar cells and modules, Proc 4th World Conference on Photovoltaic Energy Conversion, Waikoloa, Hawaii, 2006, pp. 745–748
30. S.R. Kurtz, S.W. Johnston, J.F. Geisz, D.J. Friedman, A.J. Ptak, Effect of nitrogen concentration on the performance of $Ga_{1-x}In_xN_yAs_{1-y}$ solar cells, Proc 31st IEEE Photovoltaic Specialists Conference, Orlando, Florida, 2005, pp. 595–598
31. A.W. Bett, C. Baur, F. Dimroth, J. Schöne, Metamorphic GaInP-GaInAs layers for photovoltaic applications, Mater Res Soc Symp Proc 836, 2005, pp. 223–233
32. M. Wanlass, P. Ahrenkiel, D. Albin, J. Carapella, A. Duda, K. Emery, D. Friedman, J. Geisz, K. Jones, A. Kibbler, J. Kiehl, S. Kurtz, W. McMahon, T. Moriarty, J. Olson, A. Ptak, Monolithic, ultra-thin GaInP/GaAs/GaInAs tandem solar cells, Proc 4th World Conference on Photovoltaic Energy Conversion, Waikoloa, Hawaii, 2006, 729–732

5 Very-High-Concentration Challenges of III-V Multijunction Solar Cells

C. Algora

5.1 Introduction

This chapter focuses on the challenges that III-V multijunction cells (MJCs) must face when operating at very high concentrations inside optical concentrators. Only monolithically grown MJCs are considered because, in the opinion of the author, although mechanically stacked MJCs are able to achieve higher efficiencies (with the subsequent interest in their technological development) they are not cost competitive. The reason for this is the use of two or more semiconductor substrates as well as the strict optical alignment requirements between the stacked cells that lead to a very complicated manufacturing process. Although both issues could be overcome in the future, the present situation is that all the attempts to commercialize concentrator PV modules are based on monolithically grown MJCs [1–4].

Consequently, the first sect. of this chapter is devoted to the analysis of the operation of MJCs under real conditions. A description of the real operation factors limiting the MJC's performance, such as non-uniform illumination impinging on the cell, paying special attention to the tunnel junction performance and its influence on the effects caused by series resistance, are presented. The second sect. is devoted to a specific approach able to circumvent the aforementioned effects: "the LED-like approach". Finally, the third section presents a cost analysis of complete PV installations based on modules including MJCs manufactured following the "LED-like approach".

5.2 MJCs Operating Under Real Conditions

The majority of the concentrator solar cell characterizations are provided at conditions very far from their usual real operational conditions. For example, efficiency is given under AM1.5D (low AOD), uniform illumination and at a temperature of 25 °C. None of these conditions are given in the real operation of concentrator cells inside a module. That efficiency must be provided at given standard conditions, of course, but what we suggest is that standard conditions for concentrator cells would be closer to real operation and that together with the efficiency at standard conditions, a description would

indicate the given solar cell performance under certain real operational conditions. Several attempts in this direction are being considered in the International Standard for Concentrator Photovoltaic Modules and Assemblies, which is expected to be approved in 2006 by the IEC [5].

We must start to consider that a solar cell with a given performance inside a given optical concentrator could produce a different performance inside a different concentrator. Ideally, a concentrator solar cell should be designed together with the consideration of the performance of the optical concentrator [6]. In addition, we should consider that the easy and commonly widespread calculation that the efficiency of a solar cell inside an optical concentrator is the solar cell efficiency under standard conditions multiplied by the optical efficiency is only a upper limit. For the calculation of the real efficiency, the aspects described herein must be considered.

5.2.1 Non-Uniform Illumination

A real optical concentrator does not produce a uniformly illuminated spot on the solar cell. So, the concentration level is an average of the concentration profile impinging upon the solar cell. To know the illumination profile produced by the optical concentrator is a key point in matching the solar cell properly, as we can see below, by means of several real examples.

A very interesting optical concentrator is the RXI which has very good properties [7] such as (a) a geometrical concentration higher than 1200, (b) an acceptance angle of $\pm 1.6^\circ$ for 90% of the maximum value and (c) an aspect ratio of 0.27; however, behind the 1200× nominal concentration level produced on a $1\,\mathrm{mm}^2$ solar cell, there were regions in the centre of the solar cell receiving about 20,000 suns [8]. In fact, one of the reasons for the RXI's evolution towards a new concentrator was to decrease the difference between both the highest and the nominal concentration regions on the solar cell. This evolution produced the TIR-R concentrator [9] having as the main characteristics: (a) a geometrical concentration higher than 1000×; (b) an acceptance angle (for 90% relative transmission) $\alpha = \pm 1.3^\circ$; (c) aspect ratio < 0.3; and (d) a total planarity of the top surface. Many of its optical properties required in this analysis are given by Hernández et al. [10].

One of these key properties of the TIR-R concentrator is the achievement of average concentrations of 1000 suns with peak efficiencies on the cell lower than 3000 suns. In spite of this clear improvement, we will see the influence of this non-uniform illumination on the performance of the solar cell. Let us consider a representative case in which the sun is placed at 0.8° from normal incidence of the TIR-R concentrator. In this situation, the irradiance distribution on a $1\,\mathrm{mm}^2$ GaAs solar cell is shown in Fig. 5.1 where a region with a concentration higher than 2400 suns can be seen, whereas close to the bus bar the irradiance is lower than 200 suns.

In order to evaluate this effect theoretically, a 3D model is necessary. A first approach by means of a 2D model was carried out in [11]. The 2D

model can be applied, for example, to the sect. between arrows in Fig. 5.1c in which the irradiance distribution has a maximum of about 1600 suns. So, the irradiance profile in 2D is represented in Fig. 5.1b and is applied to a complete sect. of the solar cell. As the bottom Fig. 5.1c shows, all the elements of the solar cell are included at their proper scale: bus bars at horizontal extremes separated by 15 metal fingers with a thickness of 0.5 μm and a width of 3 μm. The semiconductor structure includes all the layers: cap (n−GaAs); window (n−GaInP); emitter (n−GaAs); base (p−GaAs); BSF (n−GaInP); and GaAs substrate (although in Fig. 5.1c, the substrate is not shown because of the magnification).

The photogeneration is shown in a false colour scale from 10^{22} (pink) to 10^{25} e-h pairs $\cdot$ cm^{-3} s^{-1} (red). As can be seen, the depth of the photogeneration reproduces the shape of the irradiance profile. The local photogeneration is connected directly to the local photocurrent. Although the solar cell presented in Fig. 5.1 is a single-junction type, a similar photogeneration (photocurrent) profile would be obtained for an MJC. In this situation, the series-connected cells would be locally current mismatched.

An especially sensitive case of non-uniform illumination is that of the tunnel junctions. These junctions are specifically designed and manufactured to operate below a given concentration. The less resistant tunnel junctions for solar cells are in the range of 15 A/cm^2 with only 13 mV voltage loss [12] and 20 A/cm^2 with 20 mV voltage loss [13]. Both cases correspond to concentrations ranging from about 1000 to 1300 suns. Of course, the tunnel junctions described in both references have a much higher peak tunnelling current (200 – 400 A/cm^2) but with higher resistances.

Perhaps the highest peak tunnelling current is 560 A/cm^2 at about 0.32 V presented in [14]; therefore, although some of these excellent tunnel junctions were implemented in MJCs located inside an optical concentrator with the illumination profile shown in Fig. 5.1b, the tunnel junction would exhibit locally higher resistances.

An interesting method for evaluating this fact experimentally consists of focusing the solar beam irradiation concentrated outdoors into a high-transmissivity optical fibre that can deliver flux levels of up to 10,000 suns indoors onto a part of the solar cell being tested [15]. The main conclusion is that the MJCs must implement tunnel junctions with peak tunnelling current densities higher than the short-circuit current density produced in a portion of the solar cell at the maximum concentration produced by the optics [16]. Moreover, operation of the tunnel junction close to its peak current means a higher resistance with the subsequent solar cell efficiency loss.

Relative intensity profiles for triple junction solar cells expected from 400× Fresnel lenses have also been calculated, resulting in a significant non-uniformity [17]. In addition, attempts to characterize the performance of solar cells experimentally under different non-uniform light patterns are already underway [18].

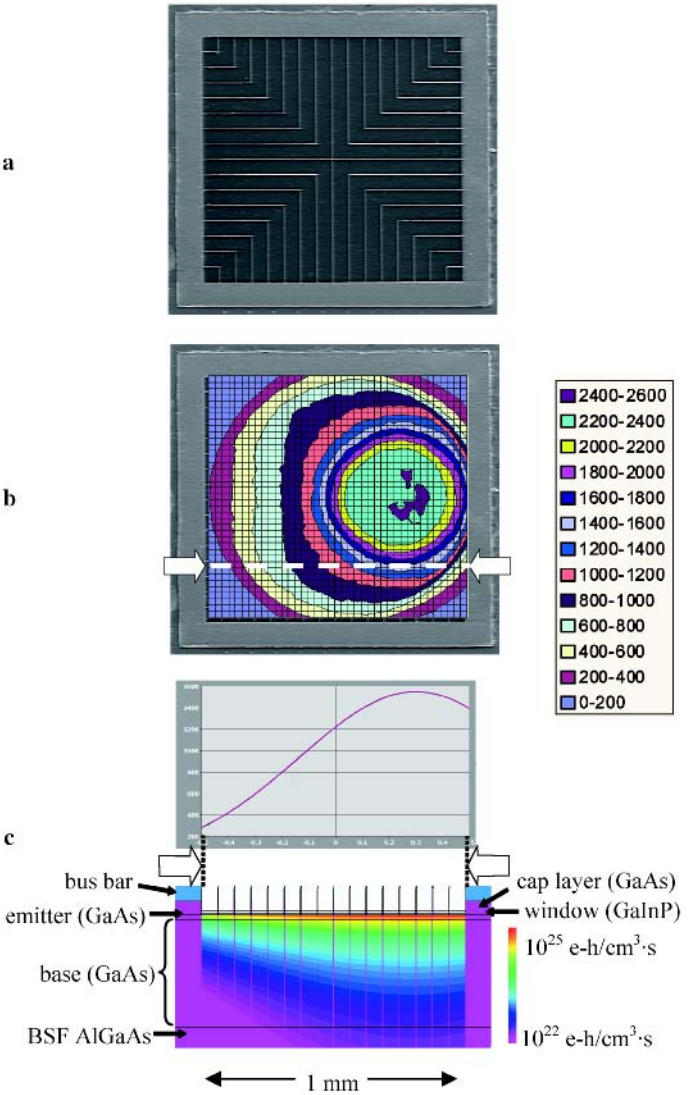

Fig. 5.1. Photograph of the GaAs cell with a 1 mm^2 inside bus bar **a**. A 2D irradiance profile (in suns) on the solar cell surface. The integration of this profile produces an average of 1000 suns **b**. The irradiance profile between the arrows is presented in 2D with the horizontal scale in millimetres **c**, *top*. Photogeneration produced by the top profile over the GaAs solar cell. The vertical dimension of the cell is magnified and is about 5 µm **c**, *bottom*

5.2.2 Localized Heating Effects

The illumination of the cell produced by any optical concentrator generates a temperature gradient. This gradient is three-dimensional because the non-uniformity of light produces a horizontal temperature distribution while the different light absorption of the semiconductor layers produces a vertical gradient; therefore, each point of the MJC will be at a different temperature. In a first approach, as the temperature increases, the band gap decreases; thus, the hottest regions can absorb a larger portion of the incident spectrum.

A 3D model of this situation requires the accurate illumination profile as the input together with an exhaustive knowledge of the temperature dependence on material parameters such as absorption coefficient, mobility, band gap energy, intrinsic carrier concentration, etc., for a wide variety of semiconductors such as Ge, InGaAs, GaAs, GaInP, AlInP, AlGaInP, AlGaAs, etc. When available, this 3D modelling will be of great help in detecting conflictive points in the solar cell as a consequence of the high temperature. This kind of modelling is underway in our institute [11].

5.2.3 Solar Spectrum Modification by the Concentrator

In recent years, the classic AM1.5D spectrum as defined by ASTM 891-87 has been questioned as being a good reference for concentrator solar cell characterization, and consequently, for its simulation and optimization. As a consequence, the new adopted standard for concentration is a redefinition of the AM1.5D with a lower aerosol optical depth (low AOD) [19].

However, the influence of one or other standard spectrum in the final performance of the solar cell can be negligible in comparison with the variation in the spectrum produced by the spectral transmission of the optical concentrator. As Fig. 5.2 shows, for wavelengths lower than 900 nm (close to the cut-off wavelength of GaAs), the transmission variation of the TIR-R concentrator is almost negligible. Nevertheless, for wavelengths higher than 1300 nm, the spectral transmission variation becomes important and it is much more restrictive than the consideration of one or another standard solar spectrum.

Figure 5.2 emphasizes the three characteristic valleys of PMMA (at about 900, 1300 and 1600 nm) of which the majority of present micro-concentrators are built. Quartz exhibits a much flatter curve, but we do not know of plans to commercialize it because of its high cost. The change in the optical transmission at wavelengths higher than 900 nm (longer than the cut-off wavelength of GaAs) is of great importance. This is because, on one hand, GaInP/GaAs dual-junction cells would not be significantly affected by the optical concentrator, but, on the other hand, triple-junction solar cells operating at wavelengths higher than 900 nm would.

In fact, experimental verification of this fact is currently appearing. So, the current mismatch of GaInP/GaAs dual-junction cells operating inside

Fig. 5.2. Spectral transmission of the TIR-R concentrator. (Data supplied by P. Benítez)

compact concentrator optics changes only 0.2% with regard to their operation at AM1.5D (low AOD) [20]. On the other hand, GaInP/GaAs/Ge triple junction solar cells experienced a current mismatch higher than 10% for Fresnel lenses with maximum concentration ratio at about 180× [21]; therefore, our recommendation is to consider the spectral transmission of the optical concentrator when GaInP/GaAs/Ge triple junction cell are modelled and manufactured while this is not so crucial for GaInP/GaAs dual-junction solar cells.

5.2.4 Current Matching and Solar Spectrum

Optimization of the solar cell performance at solar noon is different than the optimization for annual electricity production; some attempts at evaluating the latter are usually addressed by defining hourly data for different types of days. For example, as stated by McMahon et al. [22], the most accurate and least confusing way to simulate cell performance (and design cells) would be to use the AM1.5 (low AOD) spectrum together with an elevated temperature (not 300 K). When it comes to uncertainties in the operating temperature and spectra, it is more recommendable to make the top cell of the triple junction cell a little thicker rather than a little thinner [22].

Measurements in terms of efficiency distribution of test modules containing dual- and triple-junction cells for more than 1 year have been recently presented [23]; however, the sensitivity of the MJC current matching to the real operation spectrum has not yet been studied experimentally. In fact, this is a difficult task that must comply with the following steps: (a) the determination of the illumination produced by a given optic on the cell; (b) the specific optimization and manufacturing of MJC matched to the given optic; (c) the manufacturing of several concentrator modules containing solar cells each of them slightly different. In addition, the modules should allow

Fig. 5.3. View of the two-axis tracking where several III-V concentrator modules are installed on the flat roof of IES-UPM (Madrid) in order to measure annual electricity production and real time reliability

individual access to each cell for measuring purposes; (d) the measurement of the annual energy produced by each cell; and (e) the determination of the best MJC structure matching the given optics.

This protocol is now being developed in our institute by using the two-axis tracking shown in Fig. 5.3 together with an automatic measurement acquisition. This system is also used for assessing both the MJC and concentrator module reliability within the framework of an overall strategy including accelerated ageing tests [24].

The variable transmission of the optics shown in subsect. 5.2.3 together with the changing spectrum makes (in the opinion of the author) the use of 5-, 6- or even 4-J solar cells unsuitable for operation inside optical concentrators. The reason is the very tight current matching required between all of the junctions that make up the MJC which is very complicated to achieve for a standard solar spectrum. This current matching becomes almost impossible for a given optic and with the changing spectrum during the day as well as during the year.

5.2.5 Series Resistance

Series resistance is perhaps the most influential parameter in achieving a high efficiency at very high concentrations. Traditionally, series resistance of concentrator solar cells has been considered as a lumped parameter in 1D models [25]; however, the series resistance of a solar cell operating at

high concentrations cannot be properly modelled by a lumped parameter but only by distributed ones. The first distributed models [26, 27] appeared in the 1980s. Additional models appeared later in an attempt to explain several series resistance origins, but none of them linked all of the effects together.

Because many effects appearing in concentrator cells have a 3D distribution, the only accurate modelling for the series resistance is the 3D theoretical analysis of the solar cell [11]. This model must be able to include the aforementioned issues, such as non-uniform illumination, localized heating effects, impinging spectrum, etc., and is currently being developed in our institute.

A very useful approach consists of a quasi-3D model based on distributed circuit units. The complete solar cell can be modelled by the electrical circuit obtained by the suitable interconnection of every unit circuit. Three main types of elementary units are implemented (Fig. 5.4): (a) the illuminated area; (b) the dark area (bus bar and front grid); and (c) the perimeter region [28].

By using this model, a very accurate fit with experimental measurements of fill factor, open circuit voltage and efficiency of GaAs solar cells operating within the range from 1 to more than 3000 suns has been achieved [28]. The model is very useful in order to supply a quick azimuthally view of the series resistance losses. For example, Fig. 5.5 shows the voltage drops regarding the voltage at the four corners where current is extracted (by means of wire bonding) in open-circuit conditions for both concentrations of 1000 and 2000 suns. It must be noticed that in open circuit voltage the majority of the models assume no voltage drops because in these models there is no current flow; however, this quasi-3D model is able to determine such low drops accurately ($< 25\,\text{mV}$ for $2000\times$) in the emitter, fingers and bus bar.

This quasi-3D model is also a very useful tool in designing an optimum front metal grid adapted to a given contact technology. The mistakes when designing grids using the classic 1D model in comparison with this quasi-3D model are stated by Galiana et al. [29]. Although the aforementioned results correspond to homogeneously illuminated single junction cells, the model also allows the analysis of non-homogenously illuminated MJCs [29]. Both tasks are currently being developed in our institute.

As a first result of this development, Fig. 5.6 shows the theoretical I-V curve of a GaAs single junction solar cell. The cell has two kinds of illumination: (a) a $1000\times$ homogenous beam; or (b) an inhomogeneous beam going from 0 at the bus bar and linearly increasing until reaching $4000\times$ at the centre, so that the average illumination on the cell is $1000\times$. In both illumination cases, two different-quality front contacts are also considered, which we call "good" and "medium quality". In all cases the semiconductor structure and the shape and shadowing factor of the front metal grid is the same.

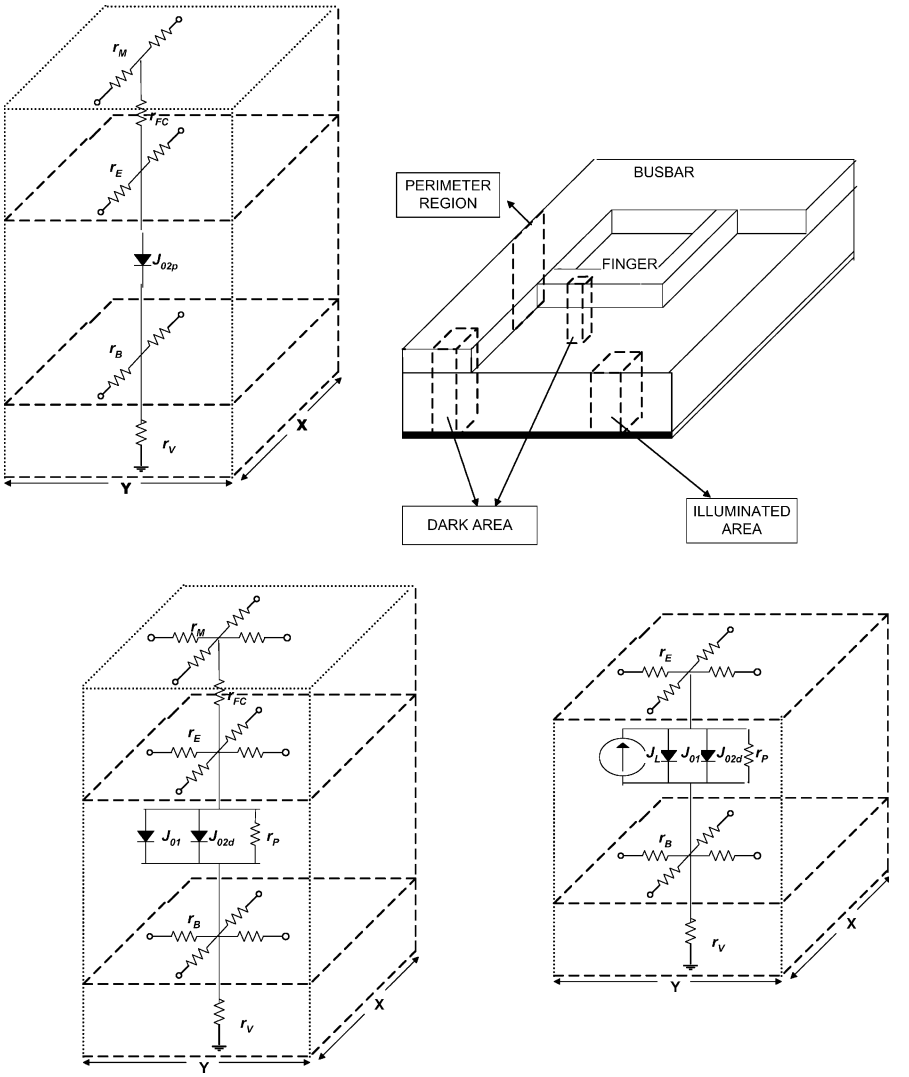

Fig. 5.4. Quasi-3D distributed model for a single-junction solar cell containing the main types of elementary units. (From [28])

As Fig. 5.6 shows, the inhomogeneous illumination produces the decrease in the fill factor and, to a lesser extent, the slight decrease in the open circuit voltage. We could say that the effect of an inhomogeneous illumination would be similar to the increase in the "effective series resistance" of the cell. The worse the quality of the front contact, the greater the decrease in both fill factor and open circuit voltage.

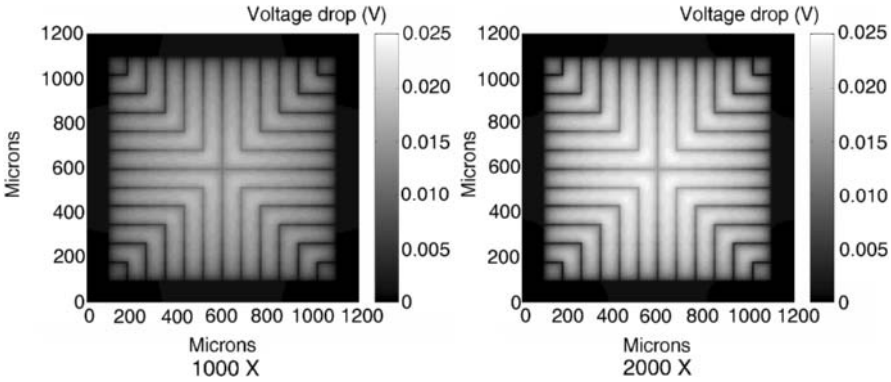

Fig. 5.5. Voltage drop (in false colour) with regard to the voltage of the four corners where current extraction is assumed. The GaAs solar cells are 1 mm^2 (same as in Fig. 5.1a), although with fewer fingers. (Both figs. courtesy of Dr. Beatriz Galiana)

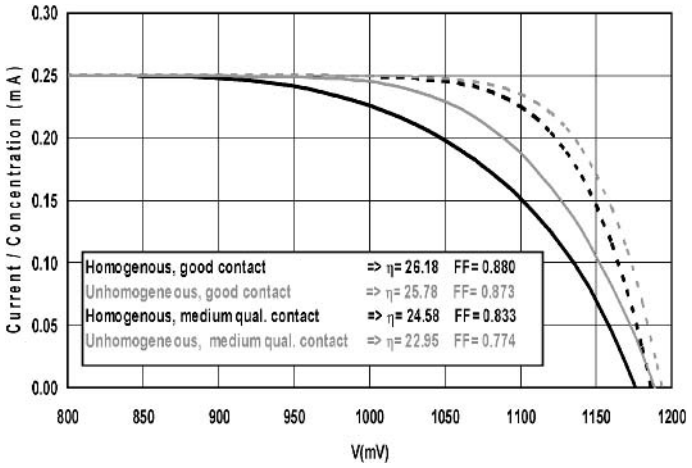

Fig. 5.6. Theoretical illumination I-V curve of a GaAs single junction solar cell. Two illumination cases are considered: 1000× homogeneous illumination and 1000× (average) inhomogeneous illumination. In addition, each case considers two situations connected with "medium" and "good quality" front contacts

5.3 Solar Cells As Light-Emitting Diodes (LEDs): "The LED-Like Approach"

Perhaps the most mature concentrator companies at present are Amonix/Guascor Fotón (USA/Spain) and Solar Systems Pty (Australia) whose current concentrator systems are based on very efficient silicon solar cells with efficiencies of about 25% operating at 250 – 400 suns. The cost analysis carried out by these companies is $\$\,5.25/W_{\mathrm{p}}$ at present and $\$\,3/W_{\mathrm{p}}$ is envisaged

once the system operates at 400 suns together with some increases in production [30].

The III-V MJCs have a tremendous potential for increasing efficiency; thus, the aforementioned silicon systems are designed to include III-V cells. In fact, Solar Systems Pty has already built the first prototype operating at 400 suns and its demonstration of the concept has been recently presented by Verlinden et al. [1]. In spite of its envisaged cost analysis of $\$\,2/W_{\mathrm{p}}$, our opinion is that an increase in cell efficiency from 25% (silicon) to 35% (III-V) both operating at the same concentration does not offset the higher cost (about ten times) of III-V MJCs substrates (GaAs or Ge) with respect to silicon ones. This is because at medium concentrations, such as 400 suns, the highest part of the whole PV installation cost remains due to the solar cell manufacture including substrate cost [31].

Therefore, a different strategy is required for the III-V MJCs to really beat the low cost of concentrator silicon-based systems. One of the most suitable approaches is to develop III-V MJCs able to operate at 1000 suns (or more) as LEDs; thus, we call it the "LED-like approach" [31]. In fact, the approach to manufacturing III-V MJCs in a manner similar to that of LEDs is being identified as one of the most solid ones for having success in reducing PV costs [32, 33].

5.3.1 Synergies Connecting III-V MJCs and LEDs

The increasing interest in a new illumination concept with solid-state lighting technology, namely LEDs, is currently valuing the LED industry at about $\$\,2.5$ billion, that is, similar to PV. Because both technologies are based on III-V semiconductors, the parallel growth of III-V PV and LED industries could help in reducing costs for both.

Although the boom in LED illumination is very recent, the "LED-like approach" for III-V MJCs has not been proposed recently. In fact, to the best knowledge of the author, in 1997 we first proposed the use of optoelectronic technologies together with a decrease in the size of concentrator GaAs solar cells to about $1\,\mathrm{mm}^2$, as a way of reducing the cost of PV technology. As is stated by Algora and Díaz [34]:

"... the device size is the factor which reinforces the strategy of connecting PV technology with micro/optoelectronic industries."

The projected concentration level for the operation of these solar cells at competitive prices was stated by Algora et al. [35]: at least 1000 suns. Just 1 year later, in 1998, we showed some of the advantages of a solar cell of about $1\,\mathrm{mm}^2$ [35]:

1. Higher solar cell efficiency as a consequence of the trade-off between series resistance and recombination at the perimeter
2. Better heat extraction
3. Lower cost of the optics and encapsulation

As a headline of the approach, Algora et al. [35] stated:

"... the long-standing joke within the semiconductor community: GaAs *is the material of the future, and it always will be, has only been turned a deaf ear by optoelectronics (and also by microwave) companies. So, why cannot* GaAs*-based Photovoltaics take advantage of Optoelectronics? ..."*

After refining several aspects, we proposed the patent application entitled: *"High efficiency photovoltaic converter for high light intensities manufactured with optoelectronic technology"* [36]. From then on, several laboratories and pilot production lines have followed our approach.

The biggest overlapping issues between LEDs and III-V MJCs are [37]:

1. Need for good crystalline quality of III-V semiconductor layers
2. Encapsulation
3. Antireflecting coating and passivation
4. Automated visual inspection
5. Thermal-mechanical modelling
6. Wafer bonding and substrate release
7. Reliability physics

With regard to operation, LEDs and MJCs have similarities and differences. The LEDs and solar cells share the p-n junction structure as the basis of their performance. Their layer designs must also consider the passing of light. Although LEDs work in the opposite way to solar cells, and LEDs pursue intensive radiative recombination, while solar cells try to avoid any kind of recombination, lessons can be learned from LED operation to MJCs. For example, a very useful characterization method for solar cells consists of their forward biasing as in the LED operation [38]. From the light emission pattern of the solar cell, information on series resistance, semiconductor defects, perimeter recombination, etc., can be derived [39]; therefore, the connections between III-V PV and LEDs seem clear so, in the following sub-sects., the main advantages of the "LED-like approach" are described.

5.3.2 Determination of the Optimum Solar Cell Size

The size of the solar cell is usually determined by reasonable factors such as the size of the available optics and sometimes for no particular reason; however, the size of the solar cell has a key influence on the efficiency. In fact, there is a trade-off between the influence of series resistance and perimeter recombination [40]. This is because, on the one hand, the bigger the size, the higher the series resistance, while, on the other hand, the smaller the size, the higher the perimeter recombination.

A multidimensional optimization of the whole concentrator GaAs solar cell (antireflection coatings, series resistance and semiconductor structure) was carried out for the first time by Algora and Díaz [25]. As Fig. 5.7 shows, the optimum size was determined for the GaAs solar cell operating

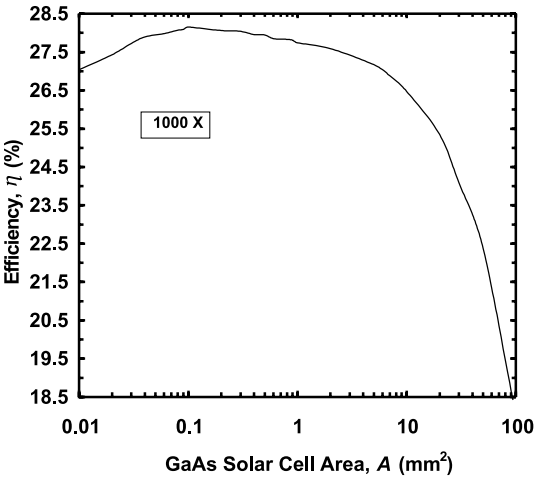

Fig. 5.7. Calculated efficiency as a function of the GaAs cell area at 1000 suns for a square grid such as that shown in Fig. 5.1. At each concentration, a different GaAs solar cell structure has been optimized. (From [25])

at 1000 suns. The trade-off between series resistance and perimeter recombination shows a great tendency towards very small areas owing to the slight influence that the recombination perimeter current exerts at very high concentrations in comparison with the decisive role played by series resistance. An optimum area of $0.1\,\mathrm{mm}^2$ is found for 1000-sun operation. However, because this value is unusually low in PV, the question that arises is: Could a larger area be used without significant performance losses?

In order to help make the correct choice for the 1000-sun operation, Fig. 5.7 shows a very slight decrease in efficiency as the device area increases from its optimum; therefore, any device area from its optimum ($0.1\,\mathrm{mm}^2$) to around $6\,\mathrm{mm}^2$ could be chosen with negligible efficiency losses (1% absolute). In addition to the fact that such a small size maximizes the efficiency, a size within this range (about $1\,\mathrm{mm}^2$) is close to that of LEDs; therefore, such small III-V MJCs could be manufactured by using optoelectronic techniques. Optoelectronic manufacture yields 95 – 98%, whereas PV is within a lower range of 90 – 95%. Once the optimum-sized solar cell is established from electrical efficiency considerations, the final size must be determined by additional factors, such as the final price of the modules, heat extraction, etc., which will be considered in the following sub-sects.

Figure 5.7 also shows a sharp decrease in efficiency for areas of $10\,\mathrm{mm}^2$ and larger, which, in fact, are the most widespread sizes; therefore, the influence of solar cell size on its performance that traditionally has not been taken into account should be carefully considered in the manufacture of concentrator solar cells. Although III-V multijunction solar cells operate at lower photocurrents than single-junction GaAs solar cells, and consequently, the deleterious effect of series resistance is lower, the resulting optimum size for these cells is very similar.

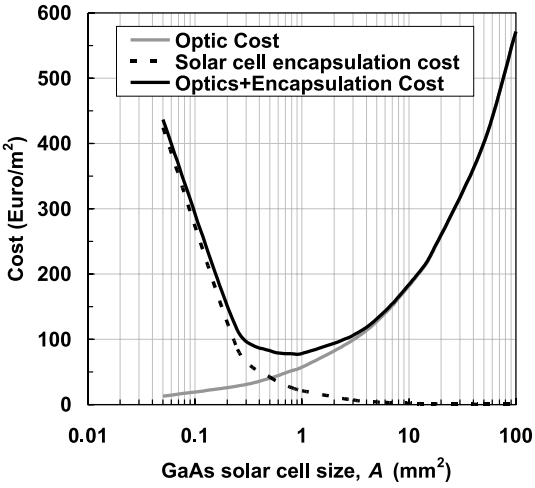

Fig. 5.8. Calculated cost of several manufacturing processes as a function of the GaAs cell area operating at 1000 suns. The cost of the optic for the RXI concentrator and the encapsulation cost is derived from LEDs. Data contained in [35] have been taken into account

5.3.3 Encapsulation and Assembly

The cost of the optical concentrator as well as that related to the assembly and encapsulation of cells involves a solar cell size dependence. Consequently, by considering both processes, an optimum solar cell size can be determined.

In a plastic injection process for an array of concentrators, the main cost contribution is the time expended during the injection which is proportional to the cell size. Assuming a given concentration and a module with a fixed nominal power, as the size of the cell decreases, the concentrator aperture diameter as well as the cost of optics decrease, too, but the number of cells making up the module and thus the number of operations related to a single cell (assembly, interconnections, etc.) also increase.

Fortunately, the cost of assembly can be dramatically reduced for small-sized cells thanks to the use of well-experimented optoelectronic technologies in managing small-sized devices, such as, wire bonding, dicing, pick and place, etc. In fact, as Fig. 5.8 shows, the optimum solar cell size when considering both the cost of the optics and assembly would be around $1\,\mathrm{mm}^2$.

5.3.4 Heat Removal

Operation at 1000 suns means an impinging light power density upon the cell of $1\,\mathrm{MW/m}^2$. A first impression suggests the need for an intensive active cooling for the heat extraction from concentrator solar cells; however, this is not required if the "LED-like approach" is followed.

If we consider a triple-junction solar cell with a size of $1\,\mathrm{mm}^2$ operating at 1000 suns, the light power received by the solar cell is 1 W. Assuming an efficiency of 35%, 350 mW are converted into electricity while

650 mW are transformed into heat. The heat extraction of 650 mW is an easy task that does not require active cooling and is well known for high-power LEDs.

In order to assess the overall temperature increase in a solar cell manufactured following the "LED-like approach", a MJC bonded with solder or conducting paste to a copper support in the shape of a truncated cone is now assumed. This cone is stuck to a layer of material which is an electric insulator and a relatively good thermal conductor which is deposited on a finned heat sink. There are, of course, other options for heat evacuation. Our intention is simply to demonstrate that active cooling is unnecessary as well as to assess the influence of the solar cell size on the increase in temperature.

Realistic values of thermal conductivities, κ, thicknesses and the specific thermal resistances r_{th} (for an area unity, in $\mathrm{K\,cm^2\,W^{-1}}$) of each layer (III-V semiconductors/paste/copper/choterm/aluminium fins) have been used. The specific thermal resistance multiplied by the irradiance fraction $(1-\eta)$ not converted into electricity gives the thermal drop in each layer. For an irradiance of $100\,\mathrm{W/cm^2}$ (a standard 1000-sun concentration), the multiplication factor assuming an MJC's efficiency of 35% is 65.

For the sake of simplicity, all the III-V semiconductor layers are considered with the thermal conductivity of GaAs; therefore, GaAs is considered as an additional layer because most of the heat is generated on its surface where the light is absorbed. In all the layers, excluding the copper part, the specific thermal resistance r_{th} is calculated by $r_{\mathrm{th}} = thickness/\kappa$. A simple model of heat conduction considering the guidelines of Algora et al. [35] is now being followed.

The specific series resistance of this heat sink is estimated based on approximate calculations for the case of calm air valid for the noon summer hours (at 40° latitude), when the inclination of the module, makes the flow of the heated air difficult. These considerations constitute the so-called pessimistic scenario giving different temperature increments of the MJC as a function of its size (see Fig. 5.9).

However, the appearance of light winds, of $1\,\mathrm{ms^{-1}}$, may reduce the thermal resistance of the heat sink by four times. In addition, choterm ($\kappa = 0.015\,\mathrm{W\,cm^{-2}\,K^{-1}}$) could be substituted by alumina ($\kappa = 0.375$ $\mathrm{W\,cm^{-2}K^{-1}}$), although it needs two additional soldered layers. These situations constitute the so-called optimistic scenario that produces a dramatic reduction in the temperature increase (see Fig. 5.9).

As can be seen in Fig. 5.9 for MJC sizes $> 10\,\mathrm{mm^2}$, a significant increase in temperature takes place. For $1\,\mathrm{mm^2}$, the temperature increase ranges from 17 to 43 K, above the ambient temperature; therefore, the thermal resistance effect has a great influence on the MJC's performance and when heating is considered, the size of the solar cell must be as small as possible.

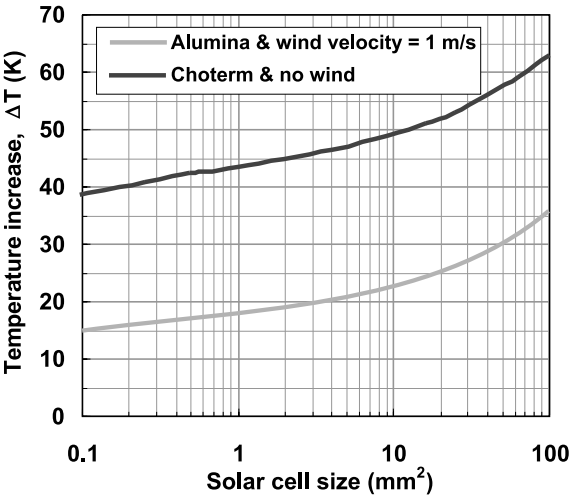

Fig. 5.9. Solar cell temperature increase above the ambient temperature as a function of its size. Concentration: 1000 suns; MJC's efficiency: 35%

5.3.5 Solar Cell Manufacture Using Optoelectronic Techniques

Consequently, the aforementioned approaches and processes in the manufacture of LEDs can be considered when manufacturing III-V MJCs. The adaptation of LED manufacture to that of III-V cells can be summarized in the following steps:

1. MOVPE growth of the semiconductor structure
2. Front grid definition through photolithography
3. Front and back metallic contacts: thermal or e-gun evaporation plus contact alloy
4. ARC deposition
5. Assembling and encapsulation: wire bonding for the front; conductive epoxy; or solder paste for back plus the use of other techniques, such as dicing, pick and place, etc.

Different aspects in the manufacture of MJCs following the LED-like approach can be seen in Fig. 5.10. A direct consequence derived from using both, similar semiconductor materials and manufacturing steps of LEDs, is the achievement of similar prices for the MJCs. In fact, the cost of manufacturing $1\,\mathrm{mm}^2$ III-V MJCs would be $\sim 15\,\mathrm{c}€$ ($18\,\mathrm{c}\$$) per device [6], similar to the cost of LEDs of the same size. This low price can be achieved only for small-sized cells that can take advantage of the well-developed automation processes for LEDs.

5.3.6 Additional Advantages: Reliability and Modelling

In addition to the aforementioned advantages, let us describe some additional ones.

The long-term reliability of the MJCs operating at high concentrations is an open aspect. Before obtaining a cost-competitive commercial product based on concentrator III-V MJCs, a complete assessment of their reliability must be done. An important effort has already been made in this sense for the last years, but the accumulated knowledge on reliability and degradation is still scarce.

Two different kinds of ageing tests should be carried out: (a) real time degradation tests; and (b) accelerated tests, for shortening the evaluation time, taking into account that MJCs are due to last at least 20 years.

The evaluation of accelerated tests can be more easily assessed if the MJCs are manufactured following the "LED-like approach". This is because many degradation aspects of concentrator cells are the same than those of LEDs. Consequently, several reliability standards of LEDs and semiconductor lasers can be taken into account when evaluating the reliability of concentrator III-V cells [24, 37].

At the end of the set of experiments proposed by González et al. [24], the following goals should be achieved: (a) the discovery of the weak points in the design and fabrication of the product and their solutions; (b) statistical treatment of the data in order to get the reliability function, the failure rate and the medium time to failure (MTTF) of the device; (c) the estimation of the device's useful life in real operating conditions; (d) the study of the statistical distribution of failures caused by degradation in real operation conditions; and (e) the analysis of the characteristic failure modes and find solutions to avoid their appearance.

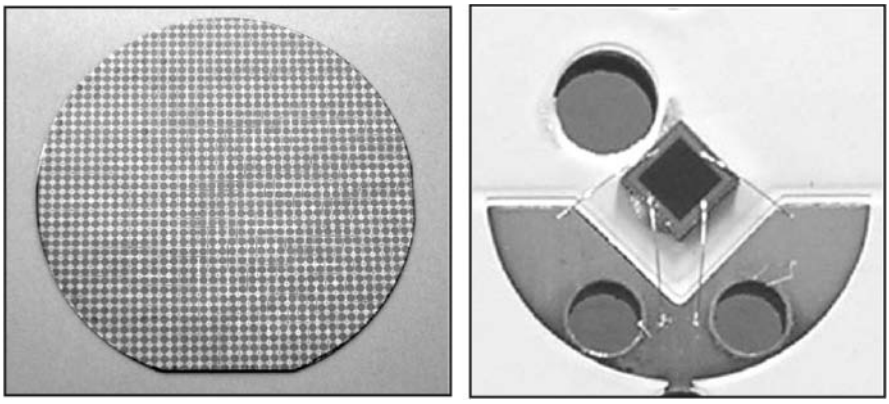

Fig. 5.10. *left*: a two-inch GaAs wafer containing about 1000 dual-junction solar cells manufactured at IES-UPM. Assuming an efficiency of 30% at 1000 suns, this wafer would produce about 250 W_p (Courtesy of J.R. González). *right*: a photograph of one of our 1 mm^2 concentrator III-V solar cells following the LED-like placed and connected on the base of the module. (Courtesy of Isofotón)

Finally, as it has been previously stated, the performance's improvement of III-V MJCs requires a careful theoretical optimization of the cells for real conditions of operation inside optical concentrators. In order to carry out such careful analysis, a 3D modelling is required. Because of the small solar cell size (about $1\,\mathrm{mm}^2$) derived from our "LED-like approach", the 3D modelling can be more properly performed by using the existing commercial software packages [41] than in the case of bigger size solar cells.

5.4 Cost Analysis

In the end, the approach for developing solar cells as LEDs entails a huge reduction in cost. We have always proposed the need for using concentrations of 1000 suns or higher for III-V cells; however, many people are claiming the use of III-V cells at a lower concentration range, such as 200 – 500 suns [30]. From our point of view, a reason for considering this concentration range as insufficient is the fact that the commercial concentrator products based on silicon cells are already operating at similar concentrations (250 – 400 suns), although with efficiencies of about 25%; thus, we have already argued that the higher efficiency of III-V MJCs to offset the lower cost of silicon cells is not enough because silicon wafers are several times cheaper than the gallium arsenide or germanium ones used in III-V MJCs.

Another reason for the operation at 1000 suns also derives from our experience in close proximity to manufacture of complete prototype concentrator PV modules which started in 1996. Firstly, we demonstrated the concept of operation at 1000 suns by using an RXI optical concentrator plus a GaAs solar cell [8]. After this remarkable experience financed by the European Commission, in 1999 we received other grant for the industrialization of the concept. The project was called INFLATCOM: "INdustrialization of ultra-FLAT COncentrator Module of high efficiency". At the beginning of the INFLATCOM project, a fully commercial photovoltaic system at $€2.8/W_\mathrm{p}$ was expected as a result of the proposed industrialization and always above $10\,MW_\mathrm{p}$ of cumulated production. As a result of the project, a cost of $€4.38/W_\mathrm{p}$ was envisaged for the same production volume. Several unpredicted additional costs arose and the operation at 1000 suns appeared to be a key factor in order to offset the unexpected extra costs.

In a second phase of industrialization, significant advances were achieved. A cost of $€2.5/W_\mathrm{p}$ was stated as being very feasible. This second phase was also financed by the EC under the HAMLET project: "High-efficiency III-V based solar cells under concentrated sunlight: Advanced concepts for Mass production and Low-cost photovoltaic ElecTricity". Again the operation at 1000 suns was identified as a key factor to offset the unexpected extra costs.

In order to highlight the importance of operating at 1000 suns or more, we have carried out a numerical cost analysis based on the "LED-like approach" [6], which has recently been defined as "*useful and exciting*" by

McConnell et al. [42]. It is shown in our cost model [6], for example, that the nominal price for a complete PV installation based on MJCs with efficiencies of 30% and operating at 1000 suns would be about €2.5/W_{p} after a cumulated production of 10 MW_{p}, whereas for installations based on MJC with efficiencies of 38% but operating at 400 suns, it would be about €3.0/W_p.

Going ahead with differences in efficiency and concentration, Algora et al. [31] shows the different contribution of each installation element to the final cost. The case of using 40% efficient cells operating at 250 suns produced (after a 10 MW_{p} cumulated production) a final price of €3.8 /W_{p}, mainly because of the huge impact (66%) that the expensive solar cells have on total cost. On the other hand, the case of using less-efficient cells of 26% but operating at 1000 suns produced (after a 10 MW_{p} cumulated production) a price of 2.8€ per watt peak mainly because of the reduced impact (35%) that the expensive solar cells have on the final cost thanks to the very high concentration level.

For this book we have prepared a cost estimate by considering updated costs of several processes from some starting productions (see Fig. 5.11). As expected, these new costs are higher than those predicted in the past. Figure 5.11 shows the tremendous impact that concentration level has on the price of a complete grid connected installation. For example, the final price of an installation operating at 400 suns is about €1/W_{p} higher than if the installation operates at 1000 suns almost independently of the cell efficiency

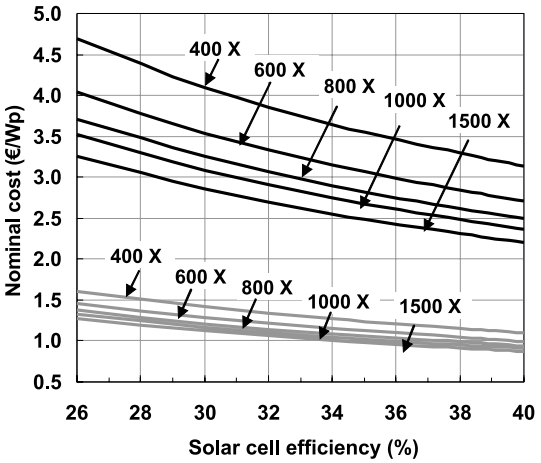

Fig. 5.11. Nominal cost of a complete MJC-based PV plant as a function of the MJC's efficiency manufactured following the LED-like approach. Concentrations ranging from 400 to 1500 suns are considered. Two different production scenarios are taken into account: **a** cumulated production of 10 $\mathrm{MW_p}$ *black curves*; and **b** cumulated production of 1000 $\mathrm{MW_p}$ when learning is considered *grey curves*

(after 10 MW_p of cumulated production). Another remarkable aspect is the huge influence that learning (after 1000 MW_p of cumulated production) has on the final price. Thanks to this learning, the price could be well below €1/W_p for concentrations of 1000 suns or higher and by using MJCs with efficiencies close to 40%.

Therefore, the main conclusion is that the hierarchy in the factors governing costs is: (a) learning; (b) concentration; and (c) efficiency. Presently, of course, with several companies trying to enter the III-V concentration market, the learning factor cannot be taken into account as the greatest factor. However, companies should consider that the concentration level has a greater impact on cost than efficiency has, contrary to what many people think; therefore, a proper combination of concentration level together with efficiency should be matched.

Acknowledgement. The author expresses his gratitude to the current and former members of the Group of III-V Semiconductors of the Solar Energy Institute of Madrid (IES-UPM) for their close collaboration and involvement in the subjects covered in this chapter. The author also thanks I. Antón and E. Katz for their interesting comments. This work was supported by the European Commission under contract SES6-CT-2003-502620 (FULLSPECTRUM project) and also by means of FEDER funds for scientific infrastructure managed in collaboration by the Spanish Ministry. The Spanish Ministry of Education and Science contributed with the CONSOLIDER-INGENIO 2010 program by means of the GENESIS FV project (CSD2006-004) and also of the research projects with references TEC2004-22300-E and TEC2005-02745. The programme NUMANCIA, financed by the Comunidad de Madrid under contract S-05050/ENE/0310, also supported this work.

References

1. P.J. Verlinden, A. Lewandowski, C. Bingham, G.S. Kinsey, R.A. Sherif, H.B. Lasich. Performance and reliability of multijunction III-V modules for concentrator dish and central receiver applications. Proc 2006 IEEE 4th World Conf Photovoltaic Energy Conv pp. 592–597 (2006).
2. V. Díaz, J. Alonso, J.L. Alvarez, C. Mateos. The path for industrial scale production of very high concentration PV systems. International Conference on Solar Concentrators for the Generation of Electricity or Hydrogen 1–5 May, 2005 Scottsdale, Arizona
3. A.W. Bett et al. FLATCON concentrator PV-technology ready for the market. Proc 20th European PVSEC 114–117 (2005)
4. K. Araki, M. Hiramatsu, Y. Kemmoku, A. Akisawa, M. Yamaguchi. A small sun in an etui – possibilities in HCPV-. Proc 2006 IEEE 4th World Conf Photov Energy Conv, pp. 603–608 (2006).
5. International Standard IEC 62108, Draft 8A. Concentrator photovoltaic (CPV) modules and assemblies. Design qualification and type approval (2006)
6. C. Algora. The importance of the very high concentration in 3rd generation solar cells. Chapter 6 of the book "Third generation photovoltaics for high effi-

ciency through full spectrum utilization". Ed. A. Martí and A. Luque, Institute of Physics Publishing (Bristol, UK), 2004
7. J.C. Miñano, J.C. González, P. Benítez. RXI: a high gain, compact, nonimaging concentrator. Appl Optics 34, pp. 7850–7856 (1995)
8. C. Algora, J.C. Miñano, P. Benítez, I. Rey-Stolle, J.L. Álvarez, V. Díaz, M. Hernández, E. Ortiz, F. Muñoz, R. Peña, R. Mohedano, A. Luque, G. Smekens, T. de Villers, V. Andreev, V. Khvostikov, V. Rumiantsev, M. Schvartz, H. Nather, K. Viehmann and S. Saveliev. Ultra compact high flux GaAs cell photovoltaic concentrator. Proc 16th European Photov Solar Energy Conference, pp. 2241–2244, Glasgow (UK), 2000
9. J.L. Álvarez, M. Hernández, P. Benítez, J.C. Miñano. TIR-R concentrator: a new compact high-gain SMS design. Nonimaging optics: maximum efficiency light transfer VI. Proc. pp. 32–42 (2001)
10. M. Hernández, P. Benítez, J.C. Miñano, J.L. Alvarez, V. Diaz, J. Alonso. Sunlight spectrum on cell through very high concentration optics. Proc 3rd World Conf Photovoltaic on Solar Energy Conversion 3P-C3-77, Osaka, Japan, 2003
11. C. Algora, M. Baudrit, I. Rey-Stolle, D. Martín, R. Peña, Beatriz Galiana, J.R. González. Pending issues in the modelling of concentrator GaAs solar cells. Proc 19th European Photovoltaic Solar Energy Conference, pp. 34–37, 2004
12. K.A. Bertness, D.J. Friedman, J.M. Olson. Tunnel junction interconnects in GaAs-based multijunction solar cells. Proc 1994 IEEE 1st World Conf Photov Energy Conv, pp. 1859–1862
13. S.M. Bedair et al. Analysis of p−AlGaAs/n−InGaP tunnel junction for high solar concentration cascade solar cells. Proc 26th IEEE PVSC, pp. 1154–1156 (2000)
14. K. Nishioka et al. Evaluation of InGaP/InGaAs/Ge triple-junction solar cell under concentrated light by simulation program with integrated circuit emphasis. Jpn J Appl Phys 43 (3), pp. 882–889 (2004)
15. J.M. Gordon, E.A. Katz, W. Tassew, D. Feuermann. Photovoltaic hysteresis and its ramifications for concentrator solar cell design and diagnostics. Appl Phys Lett 86: 073508 (2005)
16. E.A. Katz, J.M. Gordon, D. Feuermann. Effects of ultra-high flux and intensity distribution in multi-junction solar cells. Progr Photovoltaics 14, pp. 297–303 (2006)
17. M. Stan et al. Progress report on the integration of the Emcore triple-junction solar cell into a high concentration ratio Fresnel lens-based receiver. NCPV and Solar Program Review Meeting 2003, pp. 215–217 (2003)
18. I. Antón, R. Solar, G. Sala, D. Pachón. IV testing of concentration modules and cells with non-uniform light patterns. Proc. 17th EPSEC, pp. 611–614 (2001)
19. K. Emery, D. Myers, S. Kurtz. What is the appropriate reference spectrum for characterizing concentrator cells? Proc 29th IEEE PVSC, pp. 840–843 (2002)
20. C. Domínguez, I. Antón, G. Sala, J.L. Álvarez, V. Díaz. Spectral characterization of mini concentrator optics for its use with MJ cells. Proc 2006 IEEE 4th World Conf Photov Energy Conv, pp.675–678 (2006).
21. A. Yoshida et al. Characteristics of concentrator triple junction cell optimized for current matching. Proc 2006 IEEE 4th World Conf Photov Energy Conv
22. W.E. McMahon, S. Kurtz, K. Emery, M.S. Young. Criteria for the design of GaInP/GaAs/Ge triple-junction cells to optimize their performance outdoors., NCPV and Solar Program review Meeting 2003, pp. 727–730 (2003)

23. A.W. Bett, B. Burger, F, Dimroth, G. Siefer, H. Lerchenmüller. High concentration PV using III-V solar cells. Proc 2006 IEEE 4th World Conf Photov Energy Conv. pp. 615–620 (2006).
24. J.R. González et al. Strategy for certified reliability analysis of III-V high concentration solar cells. Proc 2006 IEEE 4th World Conf Photov Energy Conv. pp. 702–705 (2006).
25. C. Algora, V. Díaz. The influence of series resistance on the guidelines for the manufacture of concentrator p-on-n GaAs solar cells., Prog. Photovoltaics 8, 211–225 (2000).
26. L.D. Nielsen. Distributed series resistance effects in solar cells. IEEE Trans Electron Devices 29 (5), pp. 821–826 (1982)
27. H.C. Hamaker. Computer modeling study on the effects of inhomogeneous doping and of composition in GaAs solar cell devices. J Appl Phys 58 (6), pp. 2344–2351 (1985)
28. B. Galiana, C. Algora, I. Rey-Stolle, I. García. A 3D model for concentrator solar cells based on distributed circuit units. IEEE Trans Electron Devices 52 (12), pp. 2552–2558 (2005)
29. B. Galiana, C. Algora, I. Rey-Stolle. Comparison of 1D and 3D analysis of the front contact influence on GaAs concentrator solar cell performance. Solar Energy Mater Solar Cells 90 (16), pp. 2589–2604 (2006)
30. G. Hering. Focused on concentration. Photon International 7/2005 pp. 50–60
31. C. Algora et al. Strategic options for a LED-like approach in III-V concentrator photovoltaics. Proc 2006 IEEE 4th World Conf Photov Energy Conv. pp. 741–744 (2006).
32. S. Kurtz. Synergies connecting the photovoltaic and solid-state lighting industries. NCPV and Solar Program Review Meeting pp. 315–318 (2003)
33. G. Purvis. LED and nano could boost compound photovoltaics. III-Vs review. The advanced semiconductor magazine 17 (6), pp 36–39 (2004)
34. C. Algora, V. Díaz. Guidance for reducing PV costs using very high concentrator GaAs solar cells. Proc 14th European Photovoltaic Solar Energy Conference, pp 1724–1727 (Barcelona, Spain) 1997
35. C. Algora, V. Díaz, J.C. Miñano, A. Luque. Cost reduction in concentrator GaAs solar cells based PV plants: going from photovoltaics to optoelectronic processing. Proc 2nd World Conference on PV Solar Energy Conversion, pp. 2225–2228 (Vienna, Austria) 1998
36. Universidad Politécnica de Madrid (C. Algora). High efficiency photovoltaic converter for high light intensities manufactured with optoelectronic technology. EP1278248A1 and US2002/0170592A1
37. J.R González, I. Rey-Stolle, C. Algora. Degradation mechanisms and reliability testing of high concentrator III-V solar cells. Lessons learned from optoelectronics. Proc 19th European Photovoltaic Solar Energy Conference, pp. 3618–3621 (2004)
38. R. Peña, P. Cubilla, C. Algora. Characterisation of GaAs photovoltaic converters by infrared emission imaging. IV Conferencia de Dispositivos Electrónicos, Libro de Comunicaciones en CD, V-10, ISBN: 84-607-6770-1, Calella (Barcelona) 2003
39. J.R. González, I. Rey-Stolle, C. Algora, B. Galiana. Microplasma breakdown in high-concentration III-V solar cells. IEEE Electron Device Lett 26 (12), pp 867–869 (2005)

40. C. Algora, V. Díaz. Design and optimization of very high power density monochromatic GaAs photovoltaic cells. IEEE Trans Electron Devices 45 (9), pp. 2047–2054 (1998)
41. M. Baudrit, C. Algora. 3D modelling of III-V double-junction concentrator solar cells. Proc 2006 IEEE 4th World Conf Photov Energy Conv, pp. 826–829 (2006).
42. R. McConnell, S. Kurtz, M. Symko-Davies. Concentrator photovoltaic technologies. Refocus July/August 2005, pp. 35–39

6 Concentrator Optics

J.M. Gordon

6.1 Introduction

The past few years have witnessed a paradigm shift in photovoltaic (PV) power generation. It stems from the confluence of (a) dramatic advances in commercial high-efficiency multijunction solar cells, now capable of 40% conversion efficiency [1–4], and (b) optical designs capable of delivering flux levels of hundreds to thousands of suns at high collection efficiency - ($1\,\text{sun} = 1\,\text{mW/mm}^2$) [5–8]. In these high-concentration systems, even with cells that are two orders of magnitude more expensive on an area basis than conventional PVs, the cost contributed by the cell becomes attractively small. The burden then shifts to the optical design to provide a cost-effective and practical system. This chapter focuses on new classes of high-flux, ultra-compact, practical optics, traced from the initial concepts through commercial realization (Fig 6.1).

The target concentration levels of previous generations of high-efficiency PVs were constrained by the optical and thermal limitations of lens-based and large-dish collectors. Miniaturized mirrored concentrators overcome these hindrances. The issue of establishing optimal flux levels is then transferred from that of concentrator design to material engineering and cell architecture.

In tailoring optical devices to PV cells, production, material and implementation cost realities impose severe constraints that demand pragmatic solutions without compromising high concentration or collection efficiency. The classes of optical designs presented here can achieve the fundamental compactness limit of 1/4 aspect ratio, as well as being amenable to affordable mass production. They approach the constrained thermodynamic limit to concentration with pure imaging aplanatic optics, and can accommodate sizable gaps between the solar cell and the concentrating mirrors. Their optical performance is competitive with, and even superior to, that of high-flux non-imaging systems. They are also essentially achromatic.

The first prototypes (Fig 6.1, right) produced a net flux of 500 suns (625×), as designed, and can readily be reconfigured for up to 2000 suns. The second generation of all-dielectric (all-glass) planar concentrators (Fig 6.1, left) are currently being prototyped and tested. With built-in terminal optical elements, the all-dielectric concentrators should be able to achieve an average net flux of 4000 suns at liberal optical tolerance. In fact, because

Fig. 6.1. Prototype modules of two generations of commercial high-flux PV concentrators. *Right:* module compromising 16 identical dual-mirror concentrators each 310 mm across and transmitting 50 W onto a 100 mm^2 triple-junction solar cell [9]. *Left:* all-glass counterpart, constituting 160 identical concentrators, each 31 mm across, with 0.5 W irradiating a 1.0 mm^2 ultra-efficient triple-junction PV. Both modules are essentially achromatic, with an aspect ratio of about 1 to 4. (Courtesy of the SolFocus Corporation, Palo Alto, Calif.)

their attainable concentration strictly for the actual sun (4.7 mrad angular radius) is so much higher than needed, their high-flux capability is also exploited as allowing substantially relaxed optical tolerances for the range of 500 – 4000 suns. We show that, with current technology, it is feasible to anticipate net DC power delivery of 1 W from a 1 mm^2 cell.

In depicting these two generations of high-flux tailored imaging PV concentrators, we review the optical strategy involved, portray the fundamental and practical constraints imposed by PV technology, and report how these modular, nominally optimized designs are being stewarded to large-scale production.

6.2 Aplanatic Optics for Maximum-Performance PV Concentration

Concentrators capable of approaching the thermodynamic limit to radiative transfer have commonly been regarded within the realm of non-imaging optics [5]. It turns out, however, that the alternative of a purely imaging strategy is capable of realizing flux levels above those of even the best pragmatic non-imaging designs [6]. Each of two mirrored contours is tailored to eliminate one order of geometric aberration. With the liberty to tailor two surfaces, both spherical and comatic aberration can be overcome (aplanatism). The value of aplanats for radiation concentration remained unexplored until recently [6,7].

The motivation derives from the practical value of simultaneously satisfying: (a) ultra-compactness; (b) maximum concentration at high collection efficiency; (c) a sizable gap between the absorber and the mirrors; (d) an upward facing absorber; and (e) negligible chromatic aberration. Furthermore, the analytic solutions that fortuitously emerge for the aplanatic mirror contours facilitate the analysis of a broad range of high-performance optical designs [6].

Many non-imaging designs are not compact and do not accommodate a large gap at the receiver, unless a significant loss in either efficiency or concentration is incurred [5]. Common parabolic and Cassegrain designs provide some, but not all, of these goals. For example, high-f-number systems exhibit small aberrations but require large aspect ratios and generate low flux. While compactness and high flux can be achieved with Cassegrains, they incur excessive shading.

Figure 6.2 portrays the aplanatic design strategy for concentrating uniform radiation with numerical aperture NA_1 onto a flat single-sided absorber at an exit NA_2. NA_1 represents the convolution of the actual solar size with system optical errors. The constrained thermodynamic limit to flux concentration is [5]:

$$C_{\max} = (NA_2/NA_1)^2 \tag{6.1}$$

therefore, the absorber diameter should not be less than

$$d_{\min} = D\ NA_1/NA_2 \tag{6.2}$$

where D denotes the entrance diameter. Larger absorber diameters can raise collection efficiency, but at the expense of diminished average flux concentration. The fundamental trade-off between concentration and collection efficiency is discussed below.

The fundamental bound of 6.1 can be interpreted in two equivalent ways. At fixed optical tolerance (i.e. for a given NA_1), there is a maximum attainable flux. Alternatively, 6.1 provides the most liberal optical tolerance NA_1 for a prescribed flux concentration. The latter construal is especially relevant in PV concentration, where cost reduction by relaxing demands on optical and mechanical precision is crucial.

Satisfying (a) Fermat's constant-string-length prescription and (b) Abbe's sine condition constitutes the correction for spherical and comatic aberration, respectively [6]:

$$L_0 + L_1 + L_2 = \text{ constant} \tag{6.3}$$

$$R = (\text{constant}')\sin(\phi) \tag{6.4}$$

where L denotes string length, R is the radial coordinate at the entry, and ϕ is the angle at which a ray reaches the focus ($NA_2 = sin(\phi_{\max})$, established by the extreme ray from the rim of the primary mirror). The focus is selected

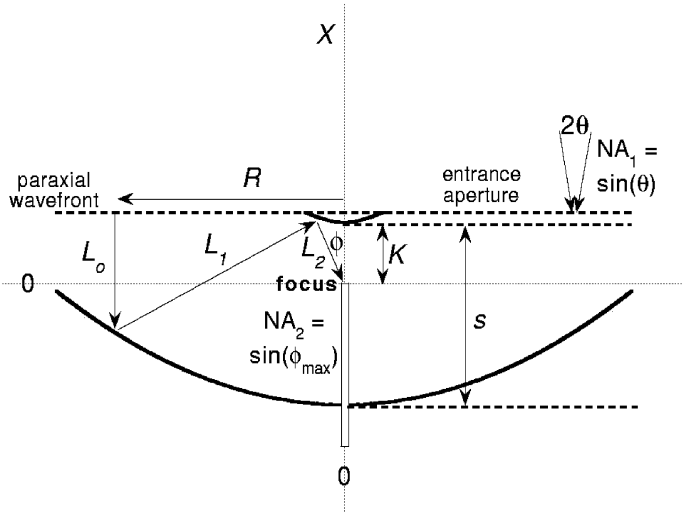

Fig. 6.2. Aplanatic concentrator design [6]. Mirror contours are tailored such that **a** all paraxial rays are focused, and **b** the Abbe sine condition is satisfied. Radiation from the extended far-field source has $NA_1 = \sin(\theta)$, to be concentrated onto an upward-facing disc, depicted here as the entrance to an equi-diameter light guide

as the origin of the coordinate system, and can lie near or even behind the apex of the primary for sufficiently low NA_2. One then incorporates the law of specular reflection (a differential equation), and specifies two geometric parameters which we choose as the distances between (a) the apex of the primary and secondary (s), and (b) the focus and the apex of the secondary (K).

The parametric solutions for the axial (X) and radial (R) coordinates for the primary (subscript p) and secondary (subscript s) shapes are [6]:

$$
\begin{aligned}
R_P &= \frac{2T}{1+T^2} \qquad X_P = s - \frac{(s-(1-s)T^2)(1-Kg(T))}{s(1+T^2)^2} \\
R_s &= \frac{2sKTg(T)}{s-(1-s)T^2+KT^2g(T)} \\
X_s &= \frac{sK(1-T^2)g(T)}{s-(1-s)T^2+KT^2g(T)} \\
\text{where } T &= \tan(\phi/2) \quad g(T) = \left|1 - \frac{(1-s)T^2}{s}\right|^{\frac{-s}{1-s}}
\end{aligned}
\tag{6.5}
$$

The radius of the primary here is NA_2. Equation 6.5 is the solution on one side of the optic axis; the other half is its mirror image.

It turns out that there is a compactness limit for any concentrator that satisfies Fermat's principle of constant optical path length (6.3) [7]. Consider the type of concentrator depicted in Fig 6.2, but where the secondary mirror

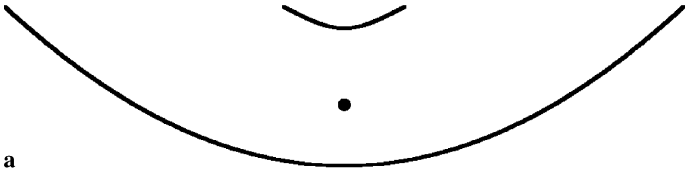

a

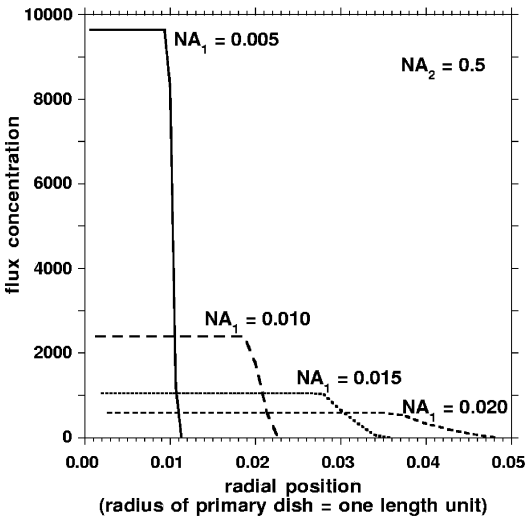

b

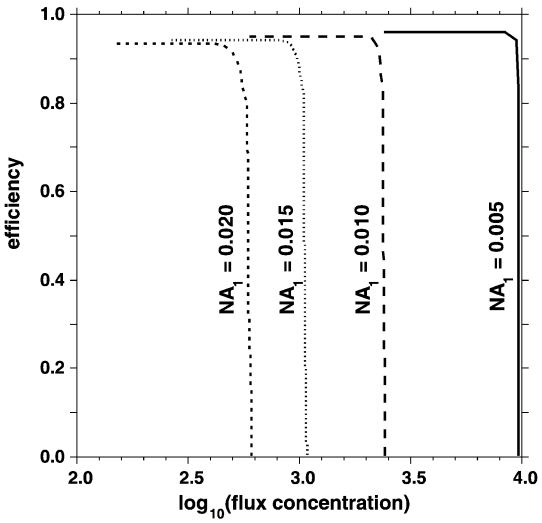

c

Fig. 6.3. Aplanatic concentrator design and performance [6]. **a** Design with $NA_2 = 0.50$. The absorber is situated in the focal plane (the *dot* indicates the focus). **b** Flux maps are plotted for a range of NA_1 values. **c** Geometric efficiency-concentration curves

is free to reside above or below the primary's entry. The device aspect ratio AR is the quotient of (a) the distance between the plane of the primary's vertex and the plane of the rim of whichever of the primary or secondary is higher, to (b) the diameter of the primary. Now trace a ray to the focus from each of the two points on the incident paraxial wavefront: (a) the rim of the primary, and (b) along the optic axis. Stipulating a constant optical path length to the focus and requiring that AR be minimized yields the results that (a) the primary and secondary are coplanar (as in Fig. 6.3a), and (b) $AR_{\min} = 1/4$. (Coplanar means that the uppermost points of the primary and secondary mirrors lie in the same plane.)

Extensive ray-trace simulation results for optical performance are summarized by Gordon and Feuermann [6]. Here, we offer the example of Fig 6.3 which includes flux maps at assorted feasible NA_1 values, and was adopted for the commercial PV concentrator in Fig 6.1 (right side, larger units) [9]. In Fig. 6.3 geometric efficiency accounts for ray rejection and shading. Absorption in the specular reflectors is not included but is readily estimated as $1 - \rho^2 (\rho = \text{reflectivity})$ since each ray experiences exactly two reflections. Fresnel reflections from the protective glazing and the absorber are also not accounted for since they are material-specific and easily quantified.

Two key aims are achieved by the $NA_2 = 0.50$ design of Fig. 6.3: (a) ultra-compactness ($AR = 1/4$); and (b) the coplanarity of the rims of the primary and secondary that is essential to certain low-cost/high-volume production techniques [9; SolFocus, Corp., pers. commun.]; however, the focus must be sited above the apex of the primary in order to avoid excessive shading.

The optical performance of imaging concentrators worsens as NA_1 grows and higher-order aberrations are magnified. The sensitivity to NA_2 and to compactness is subtler. As NA_2 is raised, it becomes increasingly difficult to realize compact configurations without introducing excessive shading or ray rejection. Deeper concentrators tend to be more tolerant to larger NA_1. Similarly, a larger secondary reduces the sensitivity to NA_1, but at the expense of greater shading.

Efficiency-concentration relations for aplanats are superior to those of corresponding conventional imaging devices. This appears to derive from the dependence of aberrations on f-number (f). Comatic aberration is proportional to $1/f^2$ (conventional compact imaging systems incur severe coma), whereas the next highest order of aberration (astigmatism and field curvature) is proportional to $1/f$.

6.3 Realization of High-Flux, Compact, Passively Cooled Commercial PV Prototypes

This sect. reports on the translation of the aplanatic strategy of the preceding sect. into viable commercial PV concentrator prototypes with a net flux of 500 suns (625×), and the potential of an increase to 2000 suns (2500×).

The air-filled aplanatic design of Fig. 6.3 is supplemented by a tapered glass rod (Fig. 6.4) that (a) permits the solar cell to be sited outside the primary mirror, and (b) accommodates greater optical errors. The final designs were severely constrained by the need for (a) ultra-compact modules, (b) simple passive heat sinks, (c) liberal optical tolerances, (d) employing commercial off-the-shelf solar cells, and (e) being conducive to inexpensive fabrication technologies. Each concentrator is intended to irradiate a single $100\,\mathrm{mm}^2$ square triple-junction high-efficiency solar cell with 50 W at peak solar radiation.

The scale of the optical design was constrained by the dimensions of the commercially available PV cells at the time, purchased from the existing inventory of a multijunction concentrator-cell manufacturer. The square $100\,\mathrm{mm}^2$ cells were optimized for 350 suns with a nominal peak efficiency of 30% [4].

The combination of (a) the dependence of cell efficiency on flux, (b) the effectiveness of passive heat sinks, and (c) the dimensional limits of high-volume mirror production techniques, limited the target flux concentration to around 500 suns. With a realistic system optical efficiency of about 80%, a geometric concentration of 625 is mandated. Also, the need to (a) concentrate the solar disc onto a square cell, as well as (b) pack concentrator units with minimal unutilized area (subject to module mechanical integrity), requires a dilution of power density. These considerations dictated a concentrator linear dimension of roughly 30 cm.

Production, material and implementation cost realities militated against concentrator aspect ratios greater than about 0.3. The aplanat of Fig. 6.4 realizes the fundamental compactness limit of a 1/4 aspect ratio with a coplanar design, incurs negligible chromatic aberration, and is well-suited to the aims and constraints noted above. The two mirrors require accurate alignment with

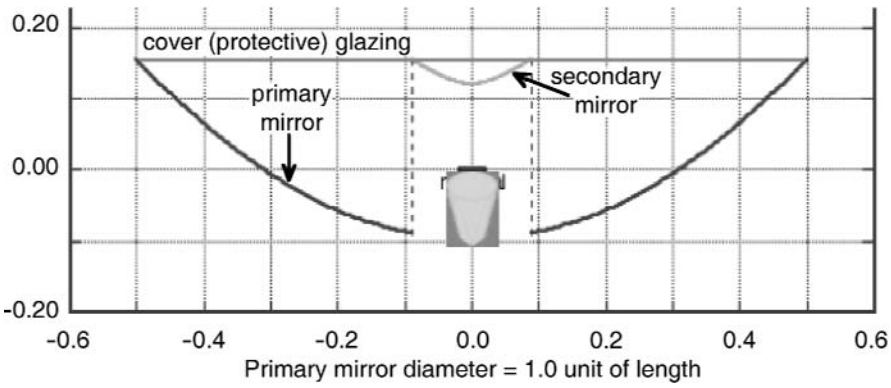

Fig. 6.4. Example of a coplanar, ultra-compact, aplanatic concentrator. The focus is at the origin. The actual entry width is 310 mm. The solar cell is optically coupled to the exit of the tapered glass rod

respect to (a) the optic axis and (b) the protective flat glazing. The coplanar design allows attaching both mirrors to the glazing and significantly simplifies matters.

Siting the focus at the apex of the primary (or even behind it) is especially attractive because it facilitates mounting and positioning the cell directly on its heat sink. It turns out, however, that when the constraints of (a) coplanarity and (b) a focus at the primary's apex are imposed, there is a trade-off between attainable concentration and shading of the primary by the secondary. No solutions exist for shading below 8.5%, and the maximum acceptable shading was established as 4%.

Additional constraints on the road to maximum concentration included: (a) the optical rod in the dish not being longer than about 30 mm (for cost, assembly and tolerance reasons); (b) power density must be diluted because of the shape mismatch among the solar disc, square cell and concentrator entry; and (c) an overall optical tolerance of 15 mrad ($NA_1 = 0.015$) based on affordable large-volume manufacturing, alignment and dual-axis solar tracking. Combining all these considerations, we arrived at the design shown in Fig. 6.4.

The compromise between construction limitations and minimizing inactive collection area prompted a module structure comprising rounded-hexagonal units (Figs. 6.1, 6.5). Flux is diluted by a factor of 1.12 (the ratio between the circle circumscribing the rounded hexagon and the rounded hexagon itself).

The square cell target further diminishes averaged flux by a factor of $\pi/4$. Given the fundamental concentration bound (6.1) of $(NA_2/NA_1)^2$, our highly constrained optical design would correspond to a nominal NA_2 value of 0.45; however, in order to accommodate the image spread that results from the additional requirement of a *second*-surface primary mirror (detailed below), we opted for $NA_2 = 0.50$. The hexagon's long linear dimension is then

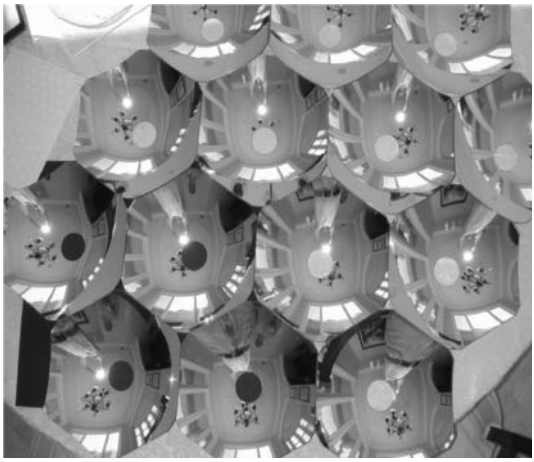

Fig. 6.5. Top view of the rounded hexagonal primary mirrors prior to concentrator assembly. The rounded edges ease secure and robust assembly with minimally unutilized area

310 mm. Concentrator depth for the coplanar design is 78 mm. The secondary mirror diameter is 55 mm, and shading is 4%.

A simple copper heat sink, thermally bonded to the solar cell, is fitted onto the back of the primary mirror. The PV temperatures at peak solar radiation, even at open circuit, are only around 20 K above ambient temperature [10,11]. Such heat sinks and simple inexpensive variations thereof are also suitable to future higher-concentration units [10–12].

While large-volume coating techniques allowed first-surface (but protected) silver for the 55 mm secondary, the 310 mm primary necessitated second-surface silvering. The glass thickness profile could not be ascertained in advance and was projected to average 2 – 3 mm. For these dimensions, the thickness of the primary results in non-negligible optical distortion.

To accommodate the optical spillover in the nominal focal plane, we (a) enlarged the entrance of the optical rod that transports light from the focal plane to the cell behind the dish to 19 mm, and (b) tapered the rod with a linear profile (the simplest and least expensive contour to produce) over its 30 mm depth, from a circular entry onto a square cell, while ensuring total internal reflection is respected (Fig. 6.6). The rod was molded from BK7 glass. Experiments with concentrated sunlight established an attenuation of around 1%. Ray-trace simulation of the final assembled concentrator confirmed that, with all absorptive, reflective and distortion losses, a net flux of 500 suns should be realized.

The square exit of the rod was reduced from 100 to 81 mm^2 out of concern for the precision of its positioning on the 100 mm^2 square cell (the affiliated increase in slope does not result in any light leakage). The flux inhomogeneity

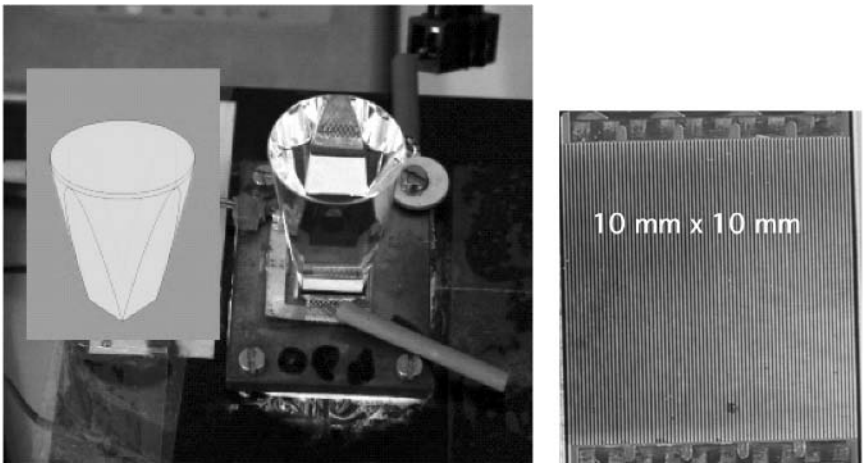

Fig. 6.6. Tapered optical rod (including a design *inset*) and testing of the rod on the solar cell used in each concentrator unit

on the cell does not impact its efficiency due to the cell's low series resistance [13]. In fact, the experiments that support this assertion also revealed that far harsher flux non-uniformities, as well as flux levels up to several thousand suns, can be tolerated with a sacrifice in cell efficiency of no more than a few percent (relative) [13].

Figure 6.7 shows assembly drawings, including attachment and alignment elements, as well as the heat sink. The first assembled prototype was photographed during testing (Fig. 6.8). Figure 6.9 offers a depiction of four modules comprising an array atop a dual-axis tracker. Injecting current to the solar cell gives rise to visible luminescence (Fig. 6.10) that can be used to characterize concentrator optical errors when the optic is used in the reverse (illumination) mode as a collimator.

We have confirmed experimentally that the prototypes generate a net flux of 500 suns, i.e. that the net solar radiation on the 100 mm^2 square triple-junction solar cell in each concentrator unit is 50 W at peak solar radiation. Concentrator design permits use of the same mirrors for higher concentration if [9; SolFocus Corp., pers. commun.] (a) manufacturing tolerances can be tightened (i.e. NA_1 in 6.1 is reduced) and/or (b) a suitable non-imaging

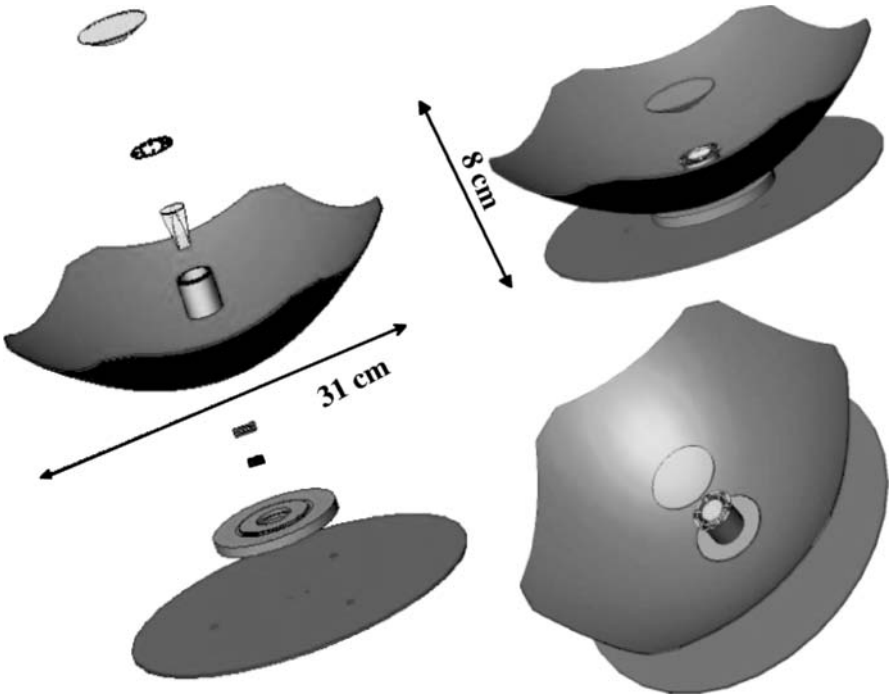

Fig. 6.7. Explosion and assembly of elements that constitute the PV aplanatic concentrator prototype

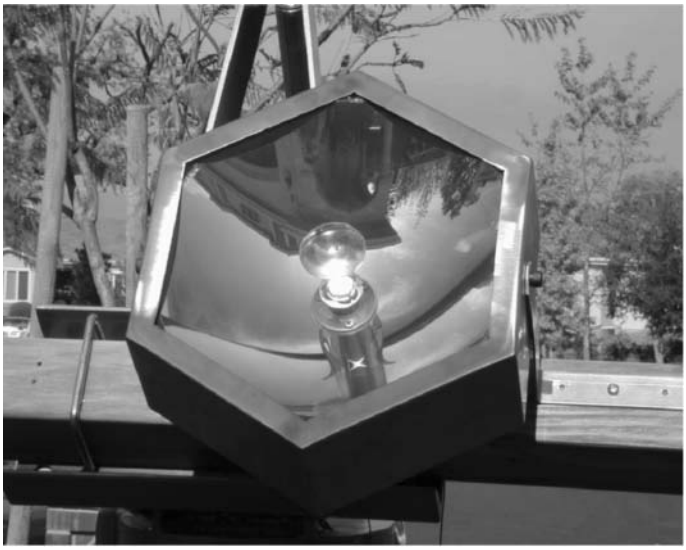

Fig. 6.8. Photograph of a single assembled concentrator unit during testing

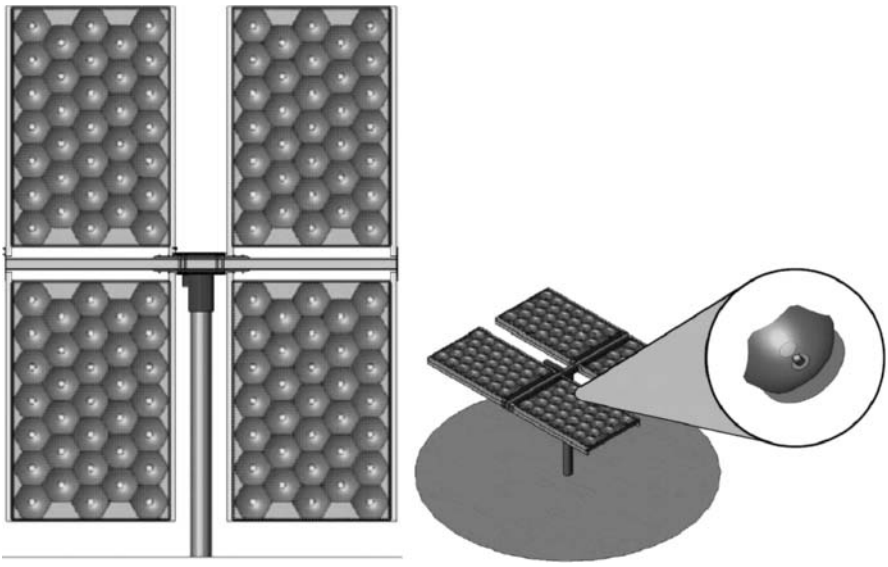

Fig. 6.9. Four modules atop a two-axis solar tracker

contoured glass rod terminal concentrator is introduced instead of the simple linear taper used here. These steps could easily yield net flux concentration values of 1000 – 2000 suns.

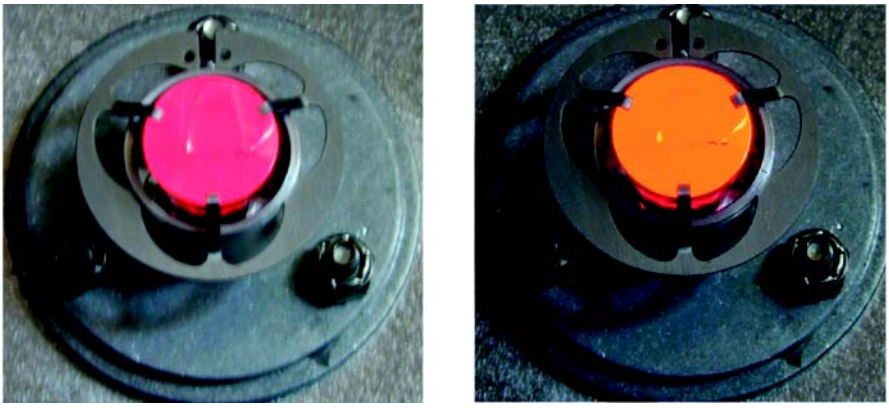

Fig. 6.10. Solar cell as a visible luminescent source used in characterizing concentrator optical quality when deployed in illumination (collimation) mode. Two different levels of current injection result in different luminescent spectra (*red* on the left, *orange* on the right). The cell is situated at the distal (narrow) end of the tapered glass rod

6.4 All-Dielectric Planar PV Concentrators

The aplanatic concentrator designs detailed in sect. 6.2 can be integrally combined with non-imaging flux boosters to produce ultracompact planar glass-filled concentrators that perform near the constrained thermodynamic limit [7]. As demonstrated below, in the highest-concentration designs that still accommodate liberal optical tolerances, it is feasible to generate 1 W from a 1 mm^2 solar cell. All-glass planar concentrators are presently being prototyped and tested as low-cost, easily fabricated monolithic all-glass modules (SolFocus Corp., pers. commun.; see sect. 6.5).

If we fill the aplanatic concentrators portrayed in sect. 6.2 with dielectric (e.g. glass) of refractive index n, then with target $NA_2 = n\sin(\theta_2)$, concentration can be increased by n^2 for the same effective solar NA_1 (provided the absorber is optically coupled to the concentrator). For materials transparent in the solar spectrum, $n^2 \approx 2.25$. Alternatively, one could exploit the dielectric to relax optical tolerance by a factor of n at fixed concentration.

Suppose that we now place a non-imaging concentrator in the focal plane. Both entrance and exit apertures are flat. Which of the numerous examples of dielectric-filled non-imaging concentrators that have been developed [5] is most suitable? The design falls under the category of $\theta_{\rm in}/\theta_{\rm out}$ non-imaging concentrators (Fig. 6.11) [5]. $\theta_{\rm in}$ is selected to match the exit angle of the dielectric-filled imaging stage, whereas $\theta_{\rm out} = \theta_2$ is constrained to satisfy a subsidiary condition such as maintaining total internal reflection (TIR) and/or accounting for high cell reflectivity at large $\theta_{\rm out}$.The concentration

boost of the terminal stage approaches its fundamental limit of

$$C_{\text{terminal,max}} = (NA_{\text{out}}/NA_{\text{in}})^2 = \{n\sin(\theta_2)/\left[n\sin\left(\theta_{\text{in}}\right)\right]\}^2 = \left[\sin\left(\theta_2\right)/\sin\left(\theta_{\text{in}}\right)\right]^2 \ . \tag{6.6}$$

The combined total concentration can approach the constrained thermodynamic limit of 6.1, $(NA_2/NA_1)^2$. (The unconstrained thermodynamic limit here refers to the case of $\theta_2 = 90^\circ$ with concentration $\left[n/NA_1\right]^2$.)

The condition for TIR is

$$\theta_{\text{in}} + \theta_{\text{out}} \leq \pi - 2\theta_c \ , \tag{6.7}$$

where θ_c is the critical angle, $\sin^{-1}(1/n)$. Alternatively, the exterior of the $\theta_{in}/\theta_{\text{out}}$ concentrator could be mirrored, thereby not restricting θ_{out} but in-

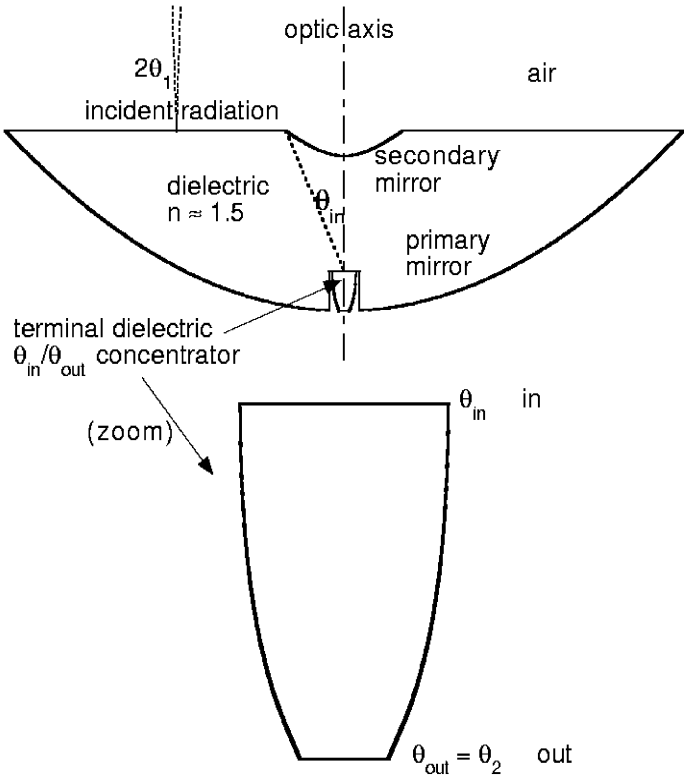

Fig. 6.11. Aplanatic planar imaging concentrator with two mirrored surfaces [7]. Filling the unit with a transparent dielectric (e.g. glass) increases attainable flux by a factor of n^2 or, equivalently, relaxes optical tolerance by a factor of n. A $\theta_{\text{in}}/\theta_{\text{out}}$ non-imaging final stage is introduced here to considerably boost flux concentration at no increase in device depth. In this illustration, $\theta_{\text{in}} = 24^\circ$, $\theta_{\text{out}} = \theta_2 = 72^\circ$, shading is 3%, and the PV absorber is located at the vertex of the primary

curring an optical loss of approximately one additional reflection ($\sim 4\%$). Ray-trace simulations of representative systems reveal that no more than a few percent of all incident rays either fail to reach the exit plane of the terminal concentrator or are rejected by it.

Because such high-flux devices will ultimately be constrained by dielectric thickness (volume), we focus on the most compact designs possible. As derived in sect. 6.2, this corresponds to coplanar units (planar concentrators) with the minimum achievable aspect ratio of 1/4 (as in the illustration in Fig. 6.11).

The design choice for θ_{in} has considerable freedom despite the constraint of coplanarity. The most practical design when accounting for fragility, cell attachment and heat sinking would appear to site the PV absorber at the vertex of the primary. This spawns a trade-off between increasing θ_{in} and shading by the secondary. For a given design, shading is proportional to $\sec(\theta_1)$ and hence independent of NA_1 for the small but pragmatic NA_1 values considered here. For example, $\theta_{\text{in}} \leq 24^\circ$ if shading is not to exceed 3%. $\theta_c = 42^\circ$ when $n = 1.5$. Then from 6.7, $\theta_{\text{in}} + \theta_{\text{out}} \leq 96^\circ$. The example in Fig. 6.11 has $\theta_{\text{in}} = 24^\circ$, $\theta_{\text{out}} = 72^\circ$ and 3% shading.

Concentrators would be simpler to manufacture and less costly if optical coupling to the cell were omitted. In this case, light would be extracted into air and then projected onto the cell. Achievable concentration is then reduced by a factor of n^2. The integral ultracompact design of Fig. 6.11 is still applicable, including siting the cell at the vertex of the primary, but the terminal concentrator must then have $\theta_{\text{out}} \leq \theta_c$ to avoid ray rejection by TIR. Retaining the same cell position then requires redesigning the aplanatic dielectric concentrator with a focus closer to the secondary.

All dielectrics that are transparent in some wavelength range will have dispersion, a consequence of absorption outside the window of transparency. Even when dispersion is only a few percent over the solar spectrum (as for glass), this significantly limits the solar concentration achievable by any dielectric with a contoured aperture. The only refracting interface here is the entry, normal to the incident beam, where angular dispersion is

$$\delta\theta_1 = -\tan(\theta_1)\delta n/n \tag{6.8}$$

which is negligible since $\theta_1 \ll 1$. (In designs where light is extracted into air, and hence projected onto the cell at sizable angles, the distance between the exit aperture and the cell is typically so small as to render additional dispersion losses negligible, too.) For practical purposes, the dielectric slab concentrator is achromatic.

Two limiting cases are worth noting: (a) the $\theta_{\text{in}}/\theta_{\text{out}}$ concentrator is a cylinder (no concentration boost from the terminal stage), which allows higher θ_{in}, for the coplanar design with the focal plane closer to the secondary; and (b) the aplanatic unit is without a terminal non-imaging concentrator, but retains coplanarity and maintains the focal plane at the vertex of the pri-

mary (concentration is still enhanced by a factor of n^2, or optical tolerance is still relaxed by a factor of n, relative to the corresponding air-filled device).

It is helpful to consider examples to illustrate the usefulness of this concept. What are reasonable power densities? Consistent with current technology [1–4], we assume (a) a 30% system conversion efficiency (cell-peak efficiency of 40%), and (b) flux on the cell of $3.33\,\mathrm{W/mm^2}$ (3300 suns). The cell then generates $\sim 1\,\mathrm{W}$ of electricity per square millimetre of cell area. This would imply a geometric concentration $C_g \approx 4600$, which accounts for losses from mirror absorption, Fresnel reflections, attenuation in the glass, shading, a few percent ray rejection and a modest dilution of power density to accommodate the full flux map in the focal plane.

With a 1-mm-diameter cell, the concentrator of Fig. 6.11 would be 68 mm in diameter with a maximum depth of 17 mm and a mass per unit area equivalent to a flat slab 8.5 mm thick. Considerably thinner concentrators can be designed (for the same size cell) with a lower concentration and hence lower electricity generation per cell area, as is shown in the commercial prototypes described in the sect. that follows. The corresponding angular field of view is given by

$$NA_1 = n\sin(\theta_2)/\sqrt{C_g}\,; \tag{6.9}$$

thus, $NA_1 \approx 0.021$ for the above example. A tighter optical tolerance would generate a smaller spot on the cell. Fortunately, experiments have shown that cell performance can be relatively insensitive to such flux inhomogeneities even at flux levels of thousands of suns [10, 13].

Ray-trace simulations indicate that NA_1 can be as large as 0.02 in air-filled concentrators before (a) the fraction of rays that fail to reach the focal plane exceeds a few percent, and (b) the absorber area must be enlarged by more than around 10% to accommodate essentially all rays that reach the focal plane. The largest corresponding optical tolerance for dielectric-filled concentrators would be $nNA_1 \approx 0.03$. The cell itself might be 1 or several square millimetres. Since the volume per unit module area is proportional to cell size, this is an engineering optimization. In any case, the heat rejection load of the order of 1 W per cell can be dissipated passively [10–12] such that temperature increases do not exceed $\sim 30\,\mathrm{K}$.

So far, our dielectric concentrators have been viewed as axisymmetric, with circular apertures and circular cells. Given the relative ease of reaching high flux, maximizing collection efficiency is paramount, including concentrator packing within modules. Also, given that economic PV fabrication and cutting techniques yield square cells, one could consider concentrating from a square or hexagonal entry onto a square target. Producing the same power density at no loss in collection efficiency then mandates increasing geometric concentration by a factor of $(4/\pi)^2 \approx 1.62$ for a square entry (or one could dilute power density at fixed geometric concentration). The coplanar designs portrayed here can accommodate high NA_{in}, but only with the focal

plane in close proximity to the apex of the secondary. Inequality – and hence TIR – cannot be satisfied, so the terminal concentrator would need to be externally silvered. In fact, for sufficiently large NA_{in}, a terminal concentrator may be unwarranted, but cell attachment and heat sinking would be more problematic than in the design of Fig. 6.11.

6.5 Realization of Practical All-Glass Planar High-Flux PV Concentrators

The second generation of SolFocus commercial PV concentrators (Figs. 6.1, 6.12, 6.13, 6.14) constitutes a special case of the modular all-glass devices described in sect. 6.4. These designs could not be considered for the original $100\,\text{mm}^2$ solar cells because they call for inadmissibly thick concentrators; however, the subsequent development of ultra-high-efficiency triple-junction cells of area $1.0\,\text{mm}^2$ [1, 3, 4] creates new possibilities. The lower series resistance in these smaller-area cells enables the attainment of higher efficiencies that also peak at flux levels of the order of 10^3 suns [1–4].

The all-glass generation-2 design constitutes a single-piece module that is housed in a flat, molded and externally mirrored glass tile. The module has minimal components, and assembly technology is automated–features favourable for improvements in cost, size, durability and scalability.

While the ultimate performance potential and optics for the $1\,\text{mm}^2$ cells are depicted in sect. 6.4, the first (current) commercial realization has been

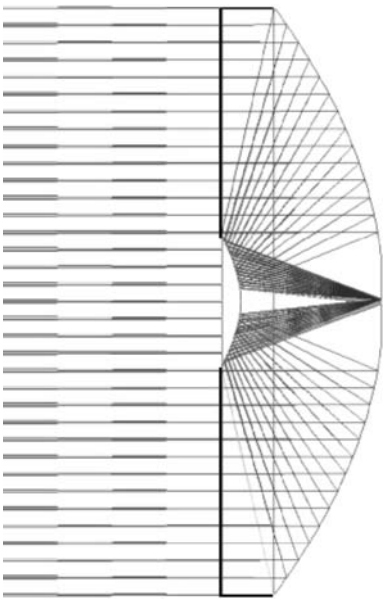

Fig. 6.12. Cross-section and ray trace of the glass-filled achromatic aplanatic concentrator design. *Blackened lines* indicate the *un*mirrored glass surfaces

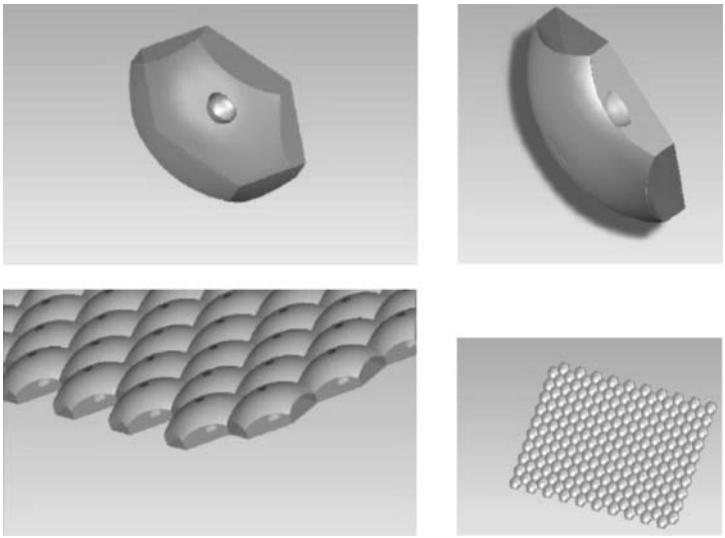

Fig. 6.13. The all-glass aplanatic concentrator. *Above*: top and side view of an individual concentrator unit, 31 mm wide. *Below*: Close-up and distant views of an assembled module

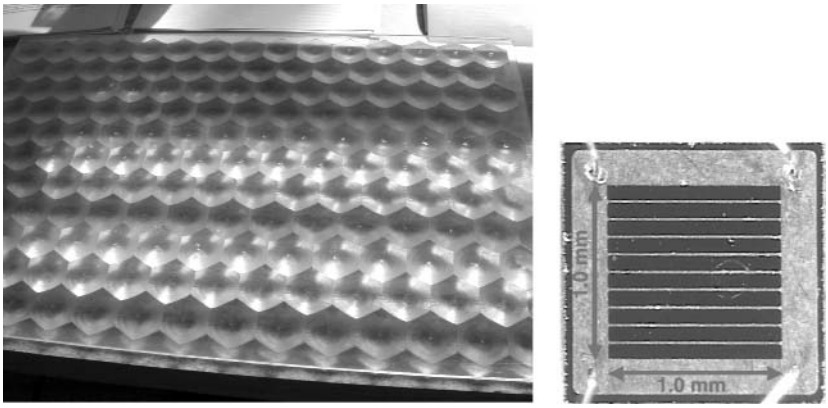

Fig. 6.14. The top view of a sample module, and the 1.0 mm^2 cell at the focus of each concentrator unit

limited by the precision of existing large-volume inexpensive glass molding techniques that, at least for now, militated against (a) a contoured terminal concentrator with an entry as small as ~ 2 mm, (b) solar cell placement inside the concentrator (with the associated need for partial heat-sink insertion), (c) the sharp edges affiliated with a coplanar design, as well as (d) tight optical tolerances. Hence, the first all-glass prototypes were designed (a) without a terminal concentrator, (b) with the cell residing at the vertex of the primary

mirror, (c) with a 2 mm "lip" (distance between the rims of the primary and secondary; Fig. 6.12), and (d) for a net flux concentration of 500 suns. The optical efficiency of about 80% derives from (a) Fresnel reflection at the entry and at the glass-cell interface, (b) absorption in the two mirrored surfaces, (c) absorption in the glass, and (d) a small extent of ray rejection; hence a geometric concentration of 625× is required.

Figure. 6.13 presents several views of the design for square 1 mm^2 cells. Each unit has a hexagonal entry (to maximize packing efficiency) with a diagonal of about 31 mm. The 41 × 27-cm module in Fig. 6.14 has a mass per unit area equivalent to a 5-mm-thick pane of glass. Towards accounting for assembly tolerances, the optic is tailored to produce a circle of light about 0.9 mm in diameter on the cell. Both modelling and experimental results confirm that this degree of flux non-uniformity (i.e. 34% of the active cell area being unilluminated) will not perceptibly diminish cell efficiency [10, 13].

The same type of integral flat metallic heat sink used in generation 1 (Fig. 6.7) is fitted on the back of the all-glass module and maintains the cells within about 10 – 20 K of ambient temperature. This modest temperature rise mitigates the prime thermal concern of material integrity (rather than cell efficiency). The temperature coefficient of cell efficiency for these cells is around $-0.002\,K^{-1}$ at 1 sun (substantially smaller in magnitude than that of silicon PVs); however, this coefficient increases (i.e. grows less negative) linearly with the logarithm of the irradiation. At delivered flux values of 500 – 2000 suns, the temperature coefficient reaches the range of $-0.001\,K^{-1}$ to 0 (and can actually become positive at sufficiently high flux) [14]; therefore, there is little, if any, concern over thermal management for the sake of cell efficiency.

6.6 Conclusion

A quiet revolution in solar electricity generation is underway thanks to progress in the parallel tracks of PV materials and optical design. Commercial multijunction PV technologies have already demonstrated solar cell efficiencies of about 40%-efficiencies that can only be realized at flux levels of hundreds to thousands of suns. At these elevated concentration values, the cost of these new ultra-efficient cells becomes attractively small, even though they are far more expensive on an area basis than conventional silicon and thin-film PVs. The challenge shifts to the development of pragmatic, inexpensive yet efficient high-flux optics that can realize this potential.

High-flux PV systems (all of which require dual-axis solar tracking) have rapidly evolved to modular one-concentrator/one-cell configurations. Both the concentrator and cell are miniaturized, e.g. cell areas not exceeding 1 cm^2 with unit concentrator areas up to 400 cm^2. Large systems are assembled from numerous identical modular units. With inexpensive lens-based optics, net (delivered) flux concentration in commercial PV installations has been

limited to about 100–400 suns. Both the geometric and chromatic aberrations of lenses have combined with incompact designs (depth-to-diameter ratios of around unity) to limit the achievable flux and the practicality of many such systems.

Thermal engineering is also germane because material integrity typically suffers with excessive heating. By their very nature, large concentrators (e.g. large mirrored dishes) must incorporate sizable PV targets, and therefore require problematic forced-circulation water cooling as well as noticeable parasitics. In addition, since voltage requirements dictate connecting many cells in series within a single module, the inhomogeneous flux map typical of large concentrators can result in substantial power dissipation as the module operates at the current of the most weakly irradiated cell.

This chapter reviews classes of tailored imaging (aplanatic) optics currently being stewarded through commercialization. The devices are planar, essentially achromatic, and can attain high flux efficiently. Two mirror contours are tailored to achieve the complete elimination of spherical and comatic aberration. The aim, however, is unrelated to image formation and instead focuses on efficient maximum flux transfer. The dual-mirror aplanat can also achieve the fundamental limit for concentrator compactness: an aspect ratio of 1/4.

If the concentrator is filled with transparent dielectric of refractive index n (e.g. glass with $n \approx 1.5$) then either (a) concentration can be increased by n^2 (provided the cell is optically coupled to the concentrator), or (b) overall optical tolerance can be relaxed by a factor of n thereby reducing system cost. Because the entrance aperture is the only refracting interface and is normal to the solar beam, chromatic aberration is negligible. The dielectric slab concentrator is basically achromatic.

Figures 6.1–6.14 illustrate the evolution of our optical designs for two generations of these aplanats to experimental and commercial realization by the SolFocus Corporation (Palo Alto, Calif.) with commercially available triple-junction solar cells that are being tailored to progressively smaller cell areas. Generation 1 was tailored to a square 100 mm^2 triple-junction cell. The air-filled concentrator includes a tapered glass rod that contributes toward a liberal optical tolerance and flux homogenization, as well as allowing the cell to be conveniently sited near the vertex of the primary mirror. A protective glazing tops the unit and a thin metal sheet encloses the back of the module, serving as a passive heat sink that limits cell temperature to no more than around 20 K above ambient. Net delivered flux values of 500 suns were measured in the field (the geometric concentration is 625).

The success of generation 1 prompted a thin, all-glass generation-2 unit predicated on a 1.0 mm^2 cell of higher efficiency thanks to lowered internal resistance. Amenable to existing precision mass-production techniques from the semiconductor industry, prototype fabrication and testing are underway as this chap. is being written – at first manufactured for a net flux of 500 suns, subsequently to be scaled to 1000 – 2000 suns subject to economic optimization.

References

1. T. Takamoto, M. Kaneiwa, M. Imaizumi, M. Yamaguchi, InGaP/GaAs-based multijunction solar cells, Progr Photovoltaics 13, 495–511 (2005)
2. M.W. Wanlass, S.P. Ahrenklel, D.S. Albin, J.J. Carapella, A. Duda, K. Emery, J.F. Geisz, K. Jones, S. Kurtz, T. Moriarty, M.J. Romero, GaInP/GaAs/GaInAs monolithic tandem cells for high-performance solar concentrators, International Conference on Solar Concentrators for the Generation of Electricity or Hydrogen, Scottsdale, Ariz., Proc NREL/CD-520-38172, Publ. NREL, Golden, Colorado (2005)
3. K. Nishioka, T. Takamoto, T. Agui, M. Kaneiwa, Y. Uraoka, T. Fuyuki, Evaluation of InGaP/InGaAs/Ge triple-junction solar cell and optimization of solar cell's structure focusing on series resistance for high-efficiency, Solar Energy Mater Solar Cells 90, 1308–1321 (2006)
4. Spectrolab Corp., 12500 Gladstone Ave., Sylmar, CA. Technical prospectuses and private communications (2005)
5. R. Winston, J.C. Miñano, P. Benítez, Nonimaging optics, Elsevier, Oxford (2005)
6. J.M. Gordon, D. Feuermann, Optical performance at the thermodynamic limit with tailored imaging designs, Appl Optics 44, 2327–2331 (2005)
7. R. Winston, J.M. Gordon, Planar concentrators near the étendue limit, Optics Lett 30, 2617–2619 (2005)
8. K. Araki, H. Uozumi, T. Egami, M. Hiramatsu, Y. Miyazaki, Y. Kemmoku, A. Akisawa, N.J. Ekins-Daukes, H.S. Lee, M. Yamaguchi, Development of concentrator modules with dome-shaped Fresnel lenses and triple-junction concentrator cells, Progr Photovoltaics 13, 513–527 (2005)
9. D. Feuermann, J.M. Gordon, S. Horne, G. Conley, R. Winston, Realization of compact, passively-cooled, high-flux photovoltaic prototypes, SPIE Proc 5942, 250–255 (2005)
10. J.M. Gordon, E.A. Katz, D. Feuermann, M. Huleihil, Toward ultrahigh-flux photovoltaic concentration, Appl Phys Lett 84, 3642–3644 (2004)
11. K. Araki, H. Uozumi, M. Yamaguchi, A simple passive cooling structure and its heat analysis for 500× concentrator PV module, 29th IEEE Photovoltaic Specialists Conference, New Orleans, Publ. IEEE, pp. 1568–1571 (2002)
12. J. Sun, T. Israeli, T.A. Reddy, K. Scoles, J.M. Gordon, D. Feuermann, Modelling and experimental evaluation of passive heat sinks for miniature high-flux photovoltaic concentrators, J Solar Energy Eng 127, 138–145 (2005)
13. E.A. Katz, J.M. Gordon, D. Feuermann, Effects of ultra-high flux and intensity distribution in multi-junction solar cells, Progr Photovoltaics 14, 297–303 (2006)
14. K. Nishioka, T. Takamoto, T. Agui, M. Kaneiwa, Y. Uraoka, T. Fuyuki, Annual output estimation of concentrator photovoltaic systems using high-efficiency InGaP/InGaAs/Ge triple-junction solar cells based on experimental solar cell's characteristics and field-test meteorological data, Solar Energy Mater Solar Cells 90, 57–67 (2006)

7 Solar Cell Cooling

G. Martinelli and M.Stefancich

7.1 Introduction

This chapter deals with the thermal issue in concentrator photovoltaic with particular emphasis on point focus systems, where the issue is more complex. The point can be stated in a very simple way: concentrating radiation on a photovoltaic converter means that the excess energy that is not converted in electricity accumulates in the component in form of phononic vibration, also known as heat.

The issue is to remove this heat from the cell in the cheapest and most reliable way. After an introductory analysis of the consequence of temperature and thermal cycles on the photovoltaic radiation receiver, an in-depth analysis of the generic structure of a thermal stack for cell interconnection and cooling follows.

Performance, cost and reliability are considered based on real systems.

7.2 Effects of Temperature on Solar Cells

The open circuit voltage (V_{oc}) of an illuminated solar cell decreases with temperature. This fact can be viewed as a consequence of the second principle of thermodynamics imposing a limit on the conversion efficiency of energy coming from a source at a given temperature by a converter/sink having a finite temperature. It can otherwise be seen as the effect of an increase in the diode-dark current with the temperature, which is another aspect of the same limitation. It is, in any case, an issue to be dealt with when a concentrator system is designed.

Following the decrease in Voc, the overall cell efficiency decreases almost linearly with the temperature of the material, for a given light flux [1].

As shown in Fig. 7.1 [2], the behaviour is sketched of the V_{oc} for commercial, 1-sun Si solar cells with temperature, for slightly different illumination levels. This value strongly depends on the different processing of silicon solar cells and the bulk lifetime properties. The global effect exists, in any case, regardless of the semiconductor.

A reduction of the cell fill factor (FF) exists in relation with the temperature. This variation, measured for GaAs solar cell [3], is shown in Fig. 7.2.

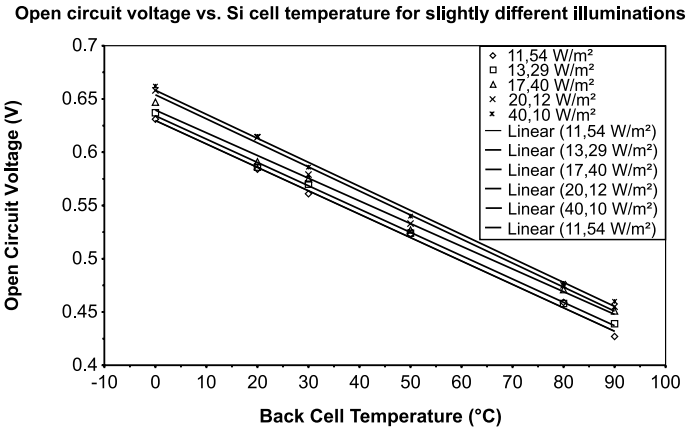

Fig. 7.1. Open-circuit voltage vs Si cell temperature for slightly different illuminations. (From [2])

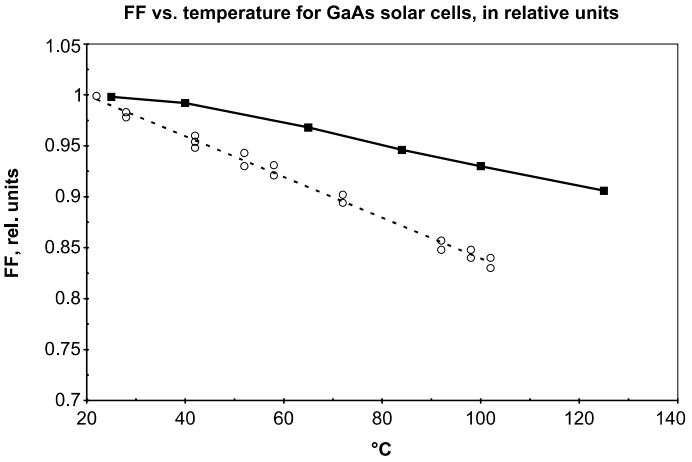

Fig. 7.2. Fill factor *FF* vs temperature for GaAs solar cells, in relative units [3]; The *dashed curve* represents the effect with non-uniform illumination

It is noteworthy that, in general, temperature is not uniform across the cell. The front junction is in the more critical situation both because it is, typically, the farthest away from the heat exchanger, and also because the photons with higher energy are absorbed in the first few microns of the cell. But the high-energy photons carry a high load of excess energy, with respect to the band gap, being dissipated as heat in the crystal lattice; thus, the temperature is higher in the junction region, reducing the voltage of the device over what can be expected from a simple uniform temperature model.

A mitigating effect, however, is the fact that the temperature coefficient improves with the concentration level, so the detrimental effect of temperature is partially limited; For example, the HCPV Amonix silicon solar cells have a voltage temperature sensitivity of about $-1.78\,\mathrm{mV/°C}$ at 1 sun and about $-1.37\,\mathrm{mV/°C}$ at 250 suns [5], whereas for GaAs it is from $-2.4\,\mathrm{mV/°C}$ to $-1.12\,\mathrm{mV/°C}$ at 250 suns [4].

7.3 Mechanical Effects of Temperature

Another important issue related to concentrator photovoltaic receiver is the mechanical impact of the receiver temperature varying during the on-off state following, for example, the day/night cycle. The main cause of the problem is the fact that the receiver includes several different materials in intimate contact having, however, strongly different thermal expansion coefficient (CTE). During operation of the system the temperature of the receiver, while being controlled by the cooling system, changes following, at least, the day/night cycle. The components undergo consequent dimensional changes with the buildup and release of mechanical tension.

Failure can follow the buildup of critical stress levels inducing immediate failure in fragile components or cyclical buildup and release of sub-critical levels inducing fatigue. The first class of problems appears in components where no plastic deformation is possible, such as the front glass. Since glass is known to have poor resistance to thermo-mechanical stress and relatively high CTE, it is mandatory to avoid large temperature difference in the glass (avoiding point contacts with cold components and large shaded areas) and to allow for a certain amount of space (possibly filled with soft resin) around the glass itself to accommodate its dimensional changes. Use of tempered glasses is also strongly advised.

The unavoidably cyclical nature of temperature variation therefore raises the problem of fatigue-related failure for some components. Fatigue is often related to the formation and growth of micro-cracks and voids in correspondence to stress buildup and relaxation. This is a key issue also in the electronics design field (which shares several complexities with our component) where the most critical part appears to be the necessary solder interconnect level [6–8] between the component and the printed circuit board substrate (PCB).

7.4 Cost and Value of Thermal Load

There is a main difference between point concentrators (dish-like systems) and Fresnel-like concentrator (one lens to one cell approach) in the disposal of the waste heat. Both systems have, indeed, the problem of removing the heat from the cell driving it in some 'cold' heat sink, but then things become

pretty different. In lens concentrator there is typically large space among the cells and plenty of dissipative surface on the back of the system. It is therefore pretty easy to cool the system by some sort of convection mechanism, possibly increasing the surface by a proper choice of fins. In point concentrator, on the other side, there is little surface for passive convection and other mechanism must be applied to remove and dispose of the heat.

While this may appear as an extra burden for point focus systems it can also be, if a proper utilization of the heat is found, an added value. For example, home applications where a point focus concentration system dumps its thermal energy in a hot water tank for sanitary uses transforms the heat from a cost to a value.

7.5 Typical Structure of a Cell-to-Sink Interconnect

To properly understand the cell-cooling problem we have to consider in detail the path of heat from the cell to its ultimate disposal in the environment. We refer to this as the heat chain. This part of the problem is common to both point focus or Fresnel-like systems. Heat is carried by concentrated radiation. In rough terms the part of radiation impinging on the cells that is not transformed in useful electric power determines entirely the thermal load (A straightforward, but not obvious, consequence of this is that cells connected to a well-matched electrical load will be subject to a lower thermal load than cells in open circuit of short circuit configuration.)

The concentrated radiation is absorbed and generates "hot" carriers in the cell. ("Hot" carriers refers to the carrier energy exceeding the band gap. The excess energy is almost immediately freed in form of heat.) In silicon cells radiation below 0.5 μm of wavelength is not efficiently converted and embodies, therefore, an high thermal load that is released in less than 5 μm (optical absorption exceeds $10^4\,\mathrm{cm}^{-1}$ for radiation below 0.5 μm). In thin film cells all the radiation, and consequently the thermal load, is absorbed in the very thin cell layer at the top of the structural substrate. In both cases the cell top surface must be, from the thermal point of view, considered the source of the heat. The purpose of a proper thermal design is to minimize the global thermal resistance of the cell assembly and, consequently, the cell operating temperature.

Typical cells have one contact on the front side and the opposite contact on the back side. (A notable exception is the interdigitated back contact cell where both contacts are on the cell back.) In any case, the back surface of the cell must be electrically connected either to other cells' front (for series connection) or, in a more general way, to external circuitry. Since, however, many cells are typically mounted on the same substrate, it is also necessary to insulate each cell back from the nearby ones. The problem has a lot in common with power-electronics printed circuit boards where SMD

components must be properly interconnected and supported by a thermally conductive substrate that causes, however, no unwanted short circuits.

The solution is therefore to have a patterned copper layer providing the desired cells' interconnection on the top of a structural substrate being a thermal conductor and an electrical insulator. In Fig. 7.3 an example of thermoconductive PCB is presented where the solder compound has been already deposited on the copper pattern where the cells are going to be placed.

Following the state of the art in power electronics two are the main solution to this issue, directly bonded copper substrate (DBC) and insulated metal substrate (IMS); the first, and most common, is where a layer of copper (from 25 to 200 µm thick) is bonded at high temperature on both sides of a ceramic tile (typically alumina). The top copper layer can be patterned by selective chemical etch (with the same technique used for standard FR-4 printed circuit boards) to obtain the desired cell interconnection layout. The bottom layer is often used to solder it on a heat spreader or heat exchanger.

The ceramic layer is the main contributor to thermal resistance of the stack and to the thermal mismatch with the cell material, and alumina is a good choice for silicon. Materials used in DBC include:

1. Alumina (Al_2O_3), the most commonly used material due to cost; brittle and not the optimal thermal conductor
2. Aluminium nitride (AlN); more expensive but a better thermal conductor
3. Beryllium oxide (BeO); good from the thermal point but has some toxicity issues

The cheap alternative is the insulated metal substrate (IMS) constituted by a metal baseplate (aluminium is commonly used) covered by a thin layer of dielectric (usually epoxy based) and a layer of copper. In spite of its simplicity,

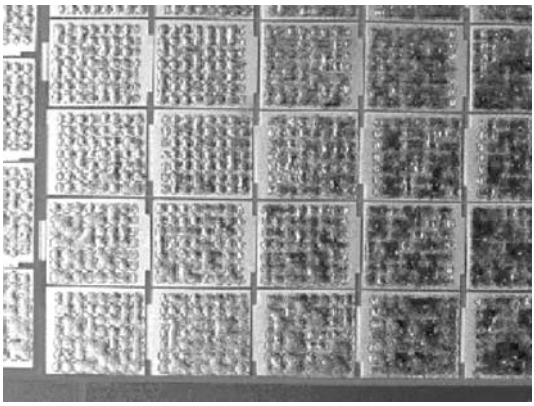

Fig. 7.3. Detail of a thermoconductive printed circuit board substrate where the patterned copper surface had been prepared for the cell soldering stage. (Courtesy Hybritec, Muggiò, Italy)

the insulating epoxy layer introduces, while being around 100 μm thick, an higher thermal resistance with respect to DBC.

The interconnection between the (metal covered) cell back and the copper pattern is typically obtained by soldering the cells in their positions in a way very similar to what occurs with SMD components. Computer-aided pick and place, components self-alignment and reflow soldering techniques allow to industrialize this phase of cell assembly. Soft soldering operates, according to lead-free regulations, around 217 °C requiring an evaluation of thermal stability of cells.

Using DBC on alumina a final assembly may look as shown in Fig. 7.4. The interconnection between the DBC and the heat exchanger or heat sink may raise some extra problems due mainly to the fact that heat exchangers are typically made of aluminum that cannot be directly soldered on copper and must therefore be coated with some solderable material, such as nichel, prior to the soldering stage. Copper or plated steel heat exchanger may be used, as an alternative, for some applications.

Assuming that the heat exchanger can be soldered on the back of the DBC still, problems may arise due to the mass and dimension of the heat exchanger itself. In a typical configuration, cells will be soldered on standard DBC substrates in an industrial production line employing standard machinery. The DBC to heat exchanger soldering occurs therefore at a second stage (often many DBC will be placed on the same exchanger board), raising potential problems with furnace size and thermal masses. The lead-free regulation worsens the problem because, with lead-based solder materials, it is possible to perform this second stage with low melting point compounds ($(Sn_{62}Ag_2Pb_{36})$ at 179 °C), whereas the cells could have been soldered by lead-free compounds at 217 °C. This would leave the cell interconnection unaffected by the second soldering stage. The inability to use lead strongly limits the available window of temperature variability rendering critical the temperature regulation. The high mass and large dimension of the heat exchanger may require special fur-

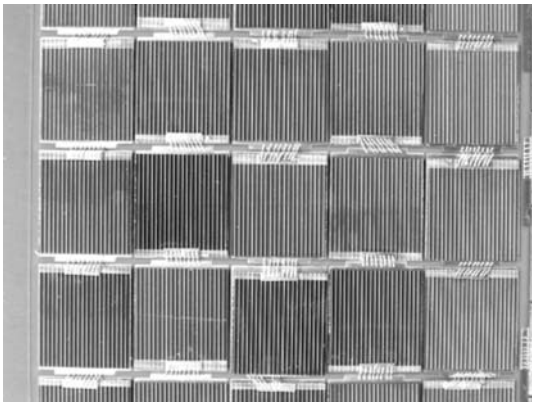

Fig. 7.4. A view of an assembled directly bonded copper substrate with cells already interconnected in series

naces and controls to comply with the requested parameters. An alternative is to employ hard soldering compounds (at much higher temperature) for the cell interconnection if the thermal stability of the cells is proven. If the direct soldering of the heat exchanger is not feasible, an alternative solution must be found relying on a mechanical contact between DBC and heat exchanger.

Although theoretically a mechanical pressure allows to obtain a good thermal contact between different (flat) surfaces, the reality is very different. Due to the finite level of flatness and surface finish of real surfaces, the contact between two 'flat' surface does actually occur only in very limited number of points greatly affecting (obviously in a negative way!) the resulting thermal conductivity.

For this reason it is necessary to introduce a mechanically soft interface layer between high-power electronics components and their relative heat exchanger. This soft layer adapts itself, under pressure, to the roughness of the two surfaces acting as a thermal bridge. On the other side, this component introduces an extra thermal interface and a possible cause of long-term failure.

The application of a constant pressure to maintain the thermal contact can be a problem since the front of the DBC is completely occupied by cells and the DBC itself, being based on a fragile ceramic substrate, and has difficulties withstanding strong concentrated forces such as those caused by clamps of screws.

A possible solution may be to solder, simultaneously with the cells on the front, a thick layer of copper (or plated aluminum) on the back of the DBC such that 'co-soldering' is possible. The interconnection with the heat exchanger is then obtained by some mechanical media (e.g. screws) tapping in this metal layer.

7.6 Global Thermal Resistance of the Thermal Stack

In a typical system cell cooling occurs on the back of the cell and the heat must therefore cross each layer of the stack to the final heat disposal fluid. All the layers contribute to the global thermal resistance being the sum of each separate component. The design of the thermal stack ends with the connection of the DBC with the heat exchanger that will handle the heat flux.

We employ a simple steady-state thermal resistance model for a $10 \times 10\,\mathrm{mm}$ sample. The first layer is the cell itself. Since the heat is mostly released in the top layer, we consider the full thickness of the cell as a layer. The most common materials for cell substrates are silicon, germanium and GaAs, introducing, for a $300\,\mu\mathrm{m}$ thickness, the resistances shown in Table 7.1.

The solder level is assumed to have a thickness ranging $100-250\,\mu\mathrm{m}$ and a thermal conductivity in the region of $0.5\,\mathrm{W\,cm^{-1}\,K^{-1}}$. This layer has the characteristics given in Table 7.2.

Table 7.1. Materials and characteristics

Material (μm)	Thermal conductivity ($W\,cm^{-1}\,K^{-1}$)	Thermal expansion coefficient (K^{-1})	Thermal resistance for $1\,cm^2$(K/W)
Silicon 300	1.3	2.6×10^{-6}	0.023
Germanium 300	0.58	5.8×10^{-6}	0.052
GaAs 300	0.55	6.5×10^{-6}	0.055

Table 7.2. Characteristics of the solder level

Solder level thickness (μm)	Thermal conductivity ($W\,cm^{-1}\,K^{-1}$)	Thermal expansion coefficient (K^{-1})	Thermal res. for $1\,cm^2$(K/W)
100	0.5	$25 - 35 \times 10^{-6}$	0.02
250	0.5	$25 - 35 \times 10^{-6}$	0.05

The use of thicker layer introduces an increase in thermal resistance but, at the same time, allows for a better relief during the thermal cycling of the mechanical stress caused by differential thermal expansion of the upper (semiconductor) and lower (DBC) layers.

The following level is the copper layer with thickness from 35 to 300 μm. Due to the high electric currents that will be produced by the cells, a choice of at least 100 μm is advisable. In any case, the high thermal conductivity of copper ($4\,W\,cm^{-1}\,K^{-1}$) renders its contribution to the global thermal resistance negligible (Table 7.3).

Table 7.3. Characteristics of the copper layer

Copper thickness (μm)	Thermal conductivity ($W\,cm^{-1}\,K^{-1}$)	Thermal expansion coefficient (K^{-1})	Thermal res. $1\,cm^2$ (K/W)
35	4	17×10^{-6}	< 0.001
100	4	17×10^{-6}	0.0025
300	4	17×10^{-6}	0.0075

The inner substrate of the DBC is an issue with alumina (Al_2O_3) being the most used material followed by aluminum nitride (AlN) and beryllium oxide (BeO). Standard thickness is of 0.635 mm but, with alumina, it can be decreased to 250 μm (mechanical stability issues become fairly stringent at this level). AlN and BeO are typically used in the standard thickness. The thermal expansion coefficient must be also kept under control to minimize dif-

ferential expansion with respect to the semiconductor (e.g. silicon has a value of 2.6×10^{-6}).

The thermal resistance contribution is given in Table 7.4. Although alumina is the most typical choice, AlN is, due to its good CTE and thermal conductivity, the best choice for silicon assemblies.

The back of the ceramic is then covered with another level of copper that is used for adhesion on the heat exchanger. It is a good practice to have the same copper thickness (and possibly similar patterns) on both sides of the ceramic tile. This way, the stress introduced by the copper layer, and large CTE, will be balanced on both sides of the ceramic, preventing unwanted bending.

Table 7.4. Characteristics of substrates

Substrate and thickness (µm)	Thermal conductivity ($\mathrm{W\,cm^{-1}\,K^{-1}}$)	Thermal expansion coefficient ($\mathrm{K^{-1}}$)	Thermal res. for 1 $\mathrm{cm^2}$ (K/W)
Al_2O_3 (635)	0.24	7.1×10^{-6}	0.26
Al_2O_3 (250)	0.24	7.1×10^{-6}	0.11
AlN (635)	1.8	4.5×10^{-6}	0.035
BeO (635)	2.8	7×10^{-6}	0.023

This concludes the design of the thermal stack for the cell assembly. The resulting thermal resistance for the following assembly is easily calculated:

$$\text{SI } 300\,\mu\text{m} \geq \text{Solder } 100\,\mu\text{m} \geq \text{Cu } 200\,\mu\text{m} \geq \text{AlN } 635\,\mu\text{m} \geq \text{Cu } 200\,\mu\text{m} \rightarrow 0.088\,\mathrm{K/W\,cm^{-2}}$$

Although the proper stack design is concluded, here it may be necessary, as previously discussed, to introduce another thick metal layer to ease the interconnection with the heat exchanger. This introduces an extra solder layer (e.g. 250 µm) and a thick (5 – 10 mm) layer of metal, such as, for example, aluminum (with a proper nickel coating for example). The use of copper, due to its lower CTE, may partially reduce the overall mechanical stress. Table 7.5 details the added thermal resistances in both cases. As is apparent, this contribution completely dwarfs the DBC part resulting in an added 0.175 – 0.47 K/W.

Table 7.5. Additional thermal resistances of substrates

Substrate and thickness (µm)	Thermal conductivity ($\mathrm{W\,cm^{-1}\,K^{-1}}$)	Thermal expansion coefficient ($\mathrm{K^{-1}}$)	Thermal res. for 1 $\mathrm{cm^2}$ (K/W)
Sn/Ag 250 µm	0.5	$25 \times 10^{-6} - 35 \times 10^{-6}$	0.05
Al 5 mm	2.37	23×10^{-6}	0.21
Al 10 mm	2.37	23×10^{-6}	0.42
Cu 5 mm	4.01	17×10^{-6}	0.125
Cu 10 mm	4.01	17×10^{-6}	0.25

7.7 Mechanical Stability of the Stack

The evaluation of the stability of the stack at the operating and qualification temperature requires the evaluation of the differential expansion of the layers. A shortcut procedure, a 1D linear model, is proposed that offers an idea of the level of stress on the structure. A more precise approach requires an in-depth analysis of the specific assembly.

Considering that the adhesion between all the levels is stable, the 'average' CTE of the assembly can be obtained with a 'balance-of-forces' approach. The highest CTE layers will 'pull' the lower CTE layers until the elastic and thermal forces in play come to equilibrium. Assuming a unitary width and length of the sample (so the section coincides with the thickness), and disregarding these factors in the calculation, we can assume that the system will have a global CTE of x.

The copper layer, for example, will apply a 'pull' for each degree and for unit of length and width, as follows:

$$\wp_{cu} = (CTE_{Cu} - x) \cdot Th_{Cu} \cdot Y_{Cu} \ . \tag{7.1}$$

At the same time, the AlN layer will do the same:

$$\wp_{AlN} = (CTE_{AlN} - x) \cdot Th_{AlN} \cdot Y_{AlN} \ , \tag{7.2}$$

where Th indicated the thickness of the layer, CTE is the coefficient of thermal expansion and Y indicates the material Young's modulus (considered isotropic). Considering Table 7.6 and including the contribution of each layer, a simple first-degree algebraic equation is obtained. Taking into account all the characteristics of the different levels.

Table 7.6. Young's modulus and thermal expansion coefficient of layers

Material/thickness (μm)	Young's modulus (GPa)	Thermal expansion coefficient (K^{-1})
Si 300	150	2.6×10^{-6}
Sn/Ag 100	41	30×10^{-6}
Copper 200	110	17×10^{-6}
AlN 635	345	4.5×10^{-6}
Copper 200	110	17×10^{-6}

We can calculate the average CTE of the assembly as being $6.32 \times 10^{-6}\,K^{-1}$ in the hypothesis of no failure. At the same time, considering the 'native' CTE and Young's modulus of each layer, it is possible to calculate the mechanical compression/traction state and the shear stress level of each layer for a given temperature. If the extra layer of aluminum or copper is included, its contribution must enter the model.

A possible failure mechanism is, as a matter of fact, caused by the interlayer shear stresses building up due to different CTE of each layer. The most likely candidate for this failure is, as in conventional electronic devices, the solder layer due to its limited yield and large CTE. An in-depth study of thermo-mechanical fatigue of the solder interlayer is beyond the scope of this chapter, but in general, thermal cycling induces a modification of the microstructure of the solder layer with reduction in tensile and shear resistance. Since shear stress is then applied during the standard day/night cycle, a progressive reduction in shear resistance will ultimately lead to solder failure. The qualification standards requires several hundreds of cycles between -20 and +150 °C with enough time at the extremes for full stress build-up, whereas operative conditions may require up to 12,000 cycles, during the system lifetime, between 10 and 60 °C with fully functional cooling. More information on solder layer fatigue and reliability can be found in electronics reliability literature [6–8].

7.8 Interconnection with the Heat Exchanger

Assuming now that the stack has been correctly designed and is stable, there is a global thermal resistance lower than $0.09\,\mathrm{K/W\,cm^{-2}}$ from the cell to the back of the DBC or, if the thick best choice for back layer is used, of $0.265\,\mathrm{K/W\,cm^{-2}}$.

The following step is to drive the heat into the heat exchanger, which has the duty to drive it away from the receiver. Since heat exchanger appears, on the 'hot' side as a flat metallic plate it is necessary to introduce some intermediate layer to allow for a proper heat flux between two otherwise rigid metal surfaces.

If no soldering is possible between the DBC and the heat exchanger, the most common approaches rely on the introduction between the two surfaces of (a) thermal pad (e.g. Akasa: ShinEtsu Thermal Interface Pad), (b) a thermal layer (e.g. Kerafol: Keratherm 90 series), (c) a thermal compound (e.g. Artic Silver: Arctic Silver 3), and (d) a thermal glue (e.g. Arctic Silver: Artic Alumina Thermal Adhesive). The problem is, with the topmost three solutions, to establish a stable mechanical connection between the two parts and to maintain a constant pressure of approximately 70 kPa. The adhesive requires pressure only during the assembly phase.

The above-indicated solutions are commonly used for power devices in electronics and for high-performance processor in computing application. The thicknesses and the thermal resistance for $1\,\mathrm{cm^2}$ of surface are given in Table 7.7.

As is easily noted, this layer introduces a significant contribution to the global thermal resistance, becoming one of the most critical interfaces. Moreover the stability of such a thermal resistance upon multiple thermal cycles is not completely established, introducing, therefore, a global reliability issue.

Table 7.7. Thicknesses and the thermal resistance for $1\,\mathrm{cm}^2$ of surface

Material	Thickness (μm)	Thermal resistance ($\mathrm{K\,cm}^2/\mathrm{W}$)
ShinEtsu; thermal interface pad	50	0.20 – 0.45
Keratherm 90 series; thermal layer	100	0.1 – 0.4
Arctic Silver 3; thermal compound	80 – 120	0.33
Artic alumina; thermal adhesive	90 – 120	0.4

The mechanical compression between the heat exchanger and the DBC must be warranted through the use of mechanical media such as screws or clamps. If the thick-metal approach is used, screws will solve the problem; otherwise, the issue becomes complex. A frequently used alternative solution consists in a metallic frame connected to the heat exchanger by screws applying a uniform force on an extended peripheral region of the DBC. Still a bending condition tends to occur in the centre of the DBC jeopardizing the correct thermal contact.

Glues induce fewer problems, but their conduction is not optimal and temporal stability must be carefully evaluated.

If soldering is possible, the situation is significantly improved, since no extra-thick metal layer must be included in the calculation but only an extra contribution of a thick solder layer in the region of a $0.05\,\mathrm{K/W\,cm}^{-2}$.

Still soldering raises the problem of a rigid transversal connection between DBC and heat exchanger. The heat exchanger must therefore be introduced in the calculation of the global thermo-mechanical stability.

An interesting technology that claims to allow for the soldering to the heat exchanger in a second stage without disrupting cell placement is the use of reactive multilayer foils as local heat sources. The foils are a new class of nano-engineered materials, in which self-propagating exothermic reactions can be initiated at room temperature with a hot filament or laser. Inserting the foil between the DBC and heat exchanger should allow for soldering them without affecting the component side. This technology is, however, still experimental.

7.9 The Heat Exchanger

The final part of the heat path is the heat exchanger itself being a metal structure that interfaces the above-considered stack with a proper circulating fluid. A large amount of material can be found on this subject [9–11] since it is involved in the operation of almost every power system (both electrical and not). The fluid can be a gas (typically air) or a liquid (typically water based) that adsorbs the heat from the surface of the heat exchanger and carries it, by mass transport, to a heat stocking or dumping structure. The fluid movement can be induced by temperature difference between the source and the heat

exchanger (passive air cooling, thermo-siphons and heat pipes) or be induced by some external mechanical system (forced air and forced liquid cooling).

In all the cases the heat transfer between the metallic body of the heat exchanger and the fluid occurs by convection at the interfacial layer. From the thermal resistance point of view there are, therefore, three separate components: (a) conductive resistance of the heat exchanger; (b) convective resistance between metal and fluid; and (c) capacitive resistance of the fluid.

The first component is simply connected with the thickness and composition of the metallic part of the heat exchanger from the 'heat entrance' to the exchange surface with the fluid. This component is independent of the operative conditions of the heat exchanger (heat and cooling fluid flux) and is related mainly to mechanical stability and cost issues. Copper, for example, is a better thermal conductor than aluminium, but its higher weight and cost tend to favour aluminium heat exchangers.

The second component, the convective resistance, is often the dominant one. Global convective resistance is inversely proportional to the exchange area and weakly dependent on the fluid velocity (assumed that turbulent flow is maintained). For this reason both air and liquid heat exchangers are characterized by high exchange surfaces resulting in a large number of fins being developed in the metallic body to increase such exchange surface. There is then a fluid specific coefficient for the exchange with the metallic area that varies one order of magnitude between gas and liquids and less significantly among the same fluid class. Velocity weakly affects the heat exchange coefficient, but if the fluid flow becomes laminar (low Reynolds number), a stationary interface forms between the fluid and the exchanger wall strongly impairing its heat transfer capability [3]. The third component in the thermal resistance is the capacitive components related to the 'heat up' of the fluid during the heat uptake phase. The fluid enters in the heat exchanger at a given (low) temperature and, while traveling into it, collects heat due to its temperature difference with respect to the heat exchanger itself. At the same time, in a way determined by its specific heat capacity, the fluid itself changes (increases) its own temperature resulting in a smaller and smaller temperature difference with the heat exchanger and, consequently, in a lower heat absorption capacity. This third component becomes, therefore, increasingly more important, decreasing the mass flow of the fluid and increasing the amount of heat to be exchanged. Higher thermal capacity fluids are also favoured. The simplest solution is to increase fluid velocity, but this, in turn, increases pressure drops across the heat exchanger and, therefore, energy consumption of the cooling system. Another possibility to significantly increase both the convection coefficient and to reduce capacitive effects is to induce a first-order phase transition (between liquid and gaseous phase, for example) in the cooling fluid. The vaporization process contributes in an efficient mixing mechanism regardless of the Reynold's number and the latent heat of vaporization enters in the account of the adsorbed heat without a corre-

sponding temperature increase in the fluid. This is the working principle of heat pipes.

7.10 Forced Air Heat Exchanger

Where no heat recovery system can be placed in operation, the cooling fluid must be freely available and easily disposable. Air is, in most cases, the unique and best candidate (!). Passive air cooling, where air flow is driven only by density difference between cold and hot air, is limited to low heat draining capacities (with specific resistances in the region of $20\,\mathrm{C/W\,cm^{-2}}$), whereas forced air cooling may be, if correctly designed, a reasonable choice.

In forced air cooling there is a fan pushing the air across the finned surface of the heat exchanger. The heat exchanger performance is limited by conductive and convective components, whereas the capacitive component can be reduced by a proper choice of the air flow. Given the air flow, however, the geometry of the exchanger determines the pressure drop across the exchanger itself. Increasing the air flow increases the pressure drop. At the same time fans are characterized by a curve relating air flow and pressure drop (Fig 7.5). Increasing pressure drops results in decreased air flow; therefore, the choice of fan and heat exchanger must be combined and determined on the basis of the specific problem.

As a case study we can consider a surface for the heat flow of $400\,\mathrm{cm^2}$ with an heat flow of $1600\,\mathrm{W}$ ($4\,\mathrm{W/cm^2}$). With an air flow of $4\,\mathrm{m/s}$ exchangers can be found inducing a pressure drop of $40\,\mathrm{Pa}$ and a thermal resistance of $7.5\,\mathrm{C/W\,cm^{-2}}$. Global air flow will be in the region of $200\,\mathrm{m^3/h}$ with an

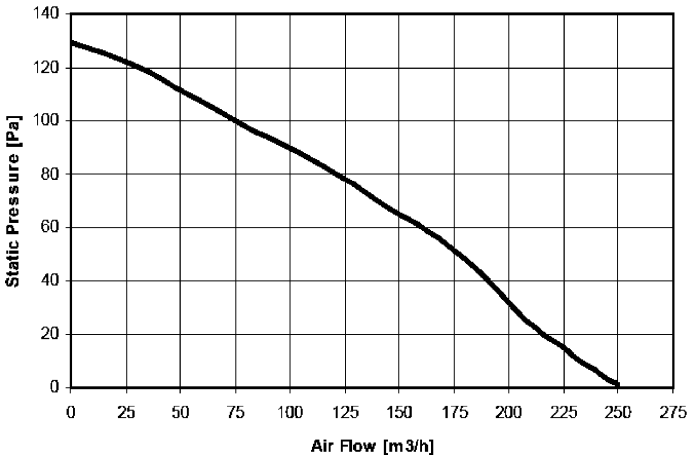

Fig. 7.5. A typical performance curve for a commercial fan. Increasing the pressure drop across the exchanger reduces, according to the curve, the available air flow

increase of air temperature across the exchanger of around 30 C. A good-quality fan capable of maintaining the requested flow and pressure drop will have an electrical consumption in the region of 20 W.

From the reliability point of view, the only critical component is the high-performance fan but, for ball-bearing fan, a typical figure for L10 [4] exceeds 60,000 h being, in ordinary operating conditions, more than 13 years. Extreme temperature conditions may, however, adversely affect these numbers but, at the same time, more reliable fans exist.

7.11 Forced Liquid Cooling

Due to the higher convection coefficient and thermal capacity, liquid cooling offers the best performance on the market. On the other hand, water cannot be considered a 'disposable' fluid (unless specific conditions occur). The added complexity steams, therefore, form the necessity of a closed-loop system, including a pump and some device for the final heat removal (often a cooling tower or a water-to-air heat exchanger). In a liquid heat cooling system the fluid acts, in fact, only as a heat displacement system moving the hot fluid (and therefore the heat) from the hot spot to another point where a suitable heat disposal procedure is applied (and the fluid is therefore cooled before being cycled again). A typical heat exchanger for liquid fluids appears as a flat plate inside which some pipes are placed in deep thermal contact with the metal of the plate. In some cases the pipes are directly obtained from the metal base. The diameter, number and length of the pipes determines both the global exchange surface and the pressure drop. As may be evident, a large number of thin pipes offers the best final surface but, at the same time, causes significant pressure drops.

A reasonable compromise can be attained with an heat flow of 1600 W over 400 cm^2, a global thermal resistance of 2.2 $K/W\,cm^{-2}$ with water flows of 8 l/min and pressure drop of 0.22 bar. Extreme performances require specialty copper plates attaining resistances as low as 0.4 $K/W\,cm^{-2}$ with similar flows and pressure drops, but prices of the exchanger increase three to five times. In any case, the performances are significantly better than air cooling and allow for heat recovery if a suitable system is in place (such as a hot-water tank). The liquid needs, however, to be moved in the circuit, which requires the presence of an electric pump. This is, probably, the weakest point of the system since pump energy efficiency is not extremely high. For our case study energy consumption in the range of 30–40 W must be considered. Larger systems may take advantage of larger pumps with higher overall efficiency. From the reliability point of view, the pump is the only critical component with MTBF [5] in the range of 50,000 h (11 years).

7.12 Heat Disposal-Recovery

If air cooling is the solution of choice, or if plenty of free-flowing water is available, the final disposal of the removed heat is not a problem. It becomes an issue if closed-loop water cooling is employed. Heat production is typically three times as big as electric energy production and lack of heat removal will result in forced shutdown of the photovoltaic generator.

From a purely thermal point of view there are three approaches to heat disposal: (a) transferring it to a freely available disposable media (typically air); (b) transferring it to an essentially infinite heat reservoir (ground); and (c) storing it for subsequent usage (hot-water tank or phase-change materials).

The first approach has the advantage of not requiring any external connection, allowing for the design of a self-contained photovoltaic system, but it adds an extra cost to the heat management without any added value. Electric consumption of the liquid pump and the fans must also be taken into account when evaluating the global efficiency of the photovoltaic system.

The system consists essentially of a group of finned pipes inside which a pump circulates the hot water and around which a fan circulates air. This system adds the cost and complexity of the already present pump for water circulation to the fans for air circulation. The only advantage of this solution with respect to a direct air cooling system is that the extent of the fin surface is independent of the dimension of the receiver, and that the water-to-air heat exchanger is physically displaced from the receiver itself.

An alternative path, requiring, however, a significant amount of installation work, is to exchange the heat with the underground soil. Long buried pipes where the hot water is circulated will exchange with a substantially infinite heat reservoir. Reliability and low operating cost are the main advantage of such an approach that still, however, dumps the heat without creating any value for it.

A simpler and more efficient version of this approach can be applied if a large water basin is available (e.g. sea, pond or pool). The design is technically simpler, but local regulations must be taken into account for the specific installation.

Whereas in the previous approaches heat was considered only as a problem, it may indeed have an added value for the integration of the concentrator system in residential or industrial buildings. Solar concentrator systems with closed-loop water cooling offer a combination of a photovoltaic and solar thermal unit and, due to the reduced surface of the receiver, their low thermal losses allow for heat production during the whole year.

The hot water produced at the receiver may, in this approach, be stored in stratification hot-water tanks such as those used for solar water-heating systems.

It must be taken into account that the temperature of water is limited by cell requirements. High temperature reduces electric output. Temperatures in

the range of 30 – 50 °C can, however, be maintained and are compatible with low-temperature heating systems and with preheating of sanitary water.

Another key point, in case of heat storage, is that electric and heat production are necessarily simultaneous. Exhaustion of the heat storage capacity implies, therefore, shutdown of the system in case no secondary heat disposal scheme is applied. Emergency operation may, in some cases, resort to evacuation of hot water through the sewer system if this is allowed by local regulations. In any case, this approach remains the most convenient from the economical point of view since it adds a significant value to the heat part.

References

1. A. Antonini: Flat facetted PV concentrator systems and dichroic evolution. Phd thesis, Ferrara, Italy, 2006
2. M.A.M. Shaltout, M. El-Nicklawy, A.F. Hassan, U.A. Rahoma, M. Sabry: The temperature dependence of the spectral and efficiency behaviour of Si solar cell under low concentrator solar cell. Renewable Energy, 445–448, 2000
3. V. Andreev, V. Grilikhes, V. Rumyantsev, N. Timoshina, M. Shvarts: Proceedings of WCPEC-3, Osaka, Japan, 2003
4. G. Siefer, P. Abbott, C. Baur1, T. Schleg, A.W. Bett: Determination of the temperature coefficient of various III-V solar cells. Proceedings of 20th European Photovoltaic Solar Energy Conference, 6–10 June 2005, Barcelona, Spain
5. S. Yoon, V. Garboushian: Reduced temperature dependence of high-concentration photovoltaic solar cell open circuit voltage (Voc) at high concentration levels, 1st World Conference on Photovoltaic Energy Conversion, 1500–1504, 1994
6. F.A. Stam, E. Davitt: Effects of thermomechanical cycling on lead and lead-free (SnPg and SnAgSu) surface mount solder joints. Microelectron Reliability 41, 1815–1822, 2001
7. M. Amagai, M. Watanabe, M. Omiya, K. Kishimoto, T. Shibuya: Mechanical characterization of Sn–Ag-based lead-free solders. Microelectron Reliability 42, 951–966, 2002
8. S. Nurmi, J. Sundelin, E. Ristolainen, T. Lepisto: The effect of solder paste composition on the reliability of SnAgCu joints. Microelectron Reliability 44, 485–494, 2004
9. E.U. Schlünder (Ed.): VDI heat atlas, Woodhead Publishing Limited, 1993
10. R.H. Perry, D.W. Green (Eds.): Perry's chemical engineers' handbook, 7th edition, McGraw-Hill, 1997, Section 11
11. D.Q. Kern: Process heat transfer. McGraw-Hill, New York, 1950

8 Terrestrial Concentrator PV Systems

V.D. Rumyantsev

8.1 Introduction: III-V Cells and Concentrator Approach in Terrestrial Application

The beginning of research on the concentrator photovoltaics with III-V solar cells has been, apparently, marked by James and Moon [1]. This work was pioneering in that it demonstrated such an important property of heteroface AlGaAs/GaAs cells, namely, their capability to operate effectively at sunlight concentration ratios of several hundred 'suns'. Since then, for more than 30 years, different research groups of the U.S., Europe and Japan have been engaged in development of such aspects of this approach as improvements in a photocell structure and fabrication technology, creating effective concentration optical systems, designing the modules and sun trackers and solution of the heat-removal problem. Interest in concentrator PV grew substantially after promoting in practice that higher-efficiency multi-cascade solar cells demonstrated a perspective to achieve photovoltaic conversion efficiencies around 40 – 50% [2, 3]; however, the variety of problems, which required recruiting experts in very different fields, resulted in considerable duration of further developments. As a result, commercialization of the solar concentrator systems with III-V cells is only just commencing.

Not least of the confounding factors affecting the developments was a lack of close evaluation of the specific problems in the initial stage. The mindset of the developers, who embarked on experiments in the late 1970s to early 1980s to create solar photovoltaic systems with concentrators, included an image of a system in which each 'concentrator–photocell' pair would ensure as high as possible absolute output power. Such an approach was fully in line with that having been actively devised at the time for designing powerful semiconductor devices of the electricity-converting techniques – rectifiers, thyristors, transistors and others; however, it is noteworthy that there exists a very important distinction between conversion systems such as 'sun-power-to-electricity' and 'electricity-to-electricity' systems (e.g. $AC \rightarrow DC$). One such difference lies in the character of delivered power. Sun power has a distributed character with low density, whereas electric power is 'concentrated' in delivering wires. In addition, in the case of sun-power conversion, dissipated heat appears to be at least by an order of magnitude higher that in the case of electricity-to-electricity conversion. In this context, an ideal

situation for the sun-power conversion would take place when a high optical concentration of the sunlight is achieved, but the distributed character of heat dissipation would persist, which is inherent in the flat-plate photovoltaic modules without concentrators. This situation, which seems to be paradoxical, can nevertheless be realized in a concentrator PV system with small absolute dimensions of concentrators and, correspondingly, of photocells.

The PV Lab of the Ioffe Institute, St. Petersburg, at its foundation at the end of the 1970s, inherited a wide experience of pioneering investigations in the field of optoelectronic devices, based on III-V semiconductors, firstly, semiconductor lasers and LEDs, and secondly, AlGaAs/GaAs solar cells for space applications [4]. At the very beginning solutions for all of the concentrator photovoltaics problems seemed at hand: solar cells; optical concentrators; cooling systems; sun trackers; and characterization equipment; however, in keeping with the conventional approach in designing the first concentrator modules and installations, large-area mirrors of 0.5 – 1 m in diameter focused the sunlight on cells of several square centimetres in size, cooled by water or by means of thermal pipes (see also Fig. 8.1, on the left) [5]. Appearance of the technology accessible for fabricating Fresnel lenses determined revision of the photovoltaic module design. The solar cells now could be placed behind the concentrators. The module housing could serve as a protector from atmospheric actions (Fig. 8.1, center). Since the Fresnel lenses had smaller

Fig. 8.1. Photographs of the concentrator PV systems early developed at the Ioffe Institute and employing different types of concentrators (see the text): parabolic mirrors [5]; acrylic Fresnel lenses of a conventional size [6]; and small aperture area smooth-surface lenses [7, 8]

dimensions – of the order of $25 \times 25\,\mathrm{cm}^2$ – the photocell dimensions were also decreased to less than $1\,\mathrm{cm}^2$. Characteristics of such photocells were improved due to reducing the internal ohmic losses and simplifying the assembly. For cooling the cells, it was sufficient to use heat conduction of the module metallic housing with a bottom and walls of a reasonable thickness [6].

Tracing the tendencies in that development allowed, as proposed in the late 1980s, a concept of radical decrease in the concentrator dimensions in retaining a high sunlight concentration ratio [7, 8]. The first experimental modules of such a type consisted of a panel of lenses, each $1 \times 1\,\mathrm{cm}^2$, focusing radiation on the AlGaAs/GaAs cells of sub-millimetre dimensions (see Fig. 8.1, right). At the same time, the main advantages of a module with small-aperture-area concentrators were formulated. The requirements were essentially lowered based on the capability of the cell heat-sinking material to conduct heat, on its thermal expansion coefficient and its thickness. The focal distance of small-aperture-area lenses appeared to be comparable with the structural thickness of conventional modules without concentrators. Consecutive optimization of all construction parts, with allowing for specific features of assembly and optical matching of the 'lens-cell' pairs, resulted in creation, by the late 1990s, of 'all-glass' photovoltaic modules with panels of small-aperture-area (each of $4 \times 4\,\mathrm{cm}^2$) Fresnel lenses [9, 10]. The lens panels had a 'glass-silicone' composite structure, similar to that described in much earlier work [11], but having not found a following advancement at that time.

In the late 1990s to just a few years ago, concentrator modules of the 'all-glass' design equipped with single-junction AlGaAs/GaAs cells and, later, with dual-junction cells, were fabricated and tested. This work was carried out owing to close co-operation of the research teams from the Ioffe Institute (St. Petersburg, Russia) and Fraunhofer Institute for Solar Energy Systems (Freiburg, Germany) [12–14]. At present, a commercial project on organizing the production of 'all-glass' concentrator modules with a registered name 'Flatcon' is underway.

In recent years, the team of the Ioffe Institute, PV Lab, has developed both modified concentrator module design [15, 16] and sun-tracking systems for practical PV installations [17]. A prominent place in the development was occupied by special equipment intended for indoor testing of the concentrator solar cells and for assembling concentrator modules.

8.2 Concentrator Module Design

Concentration ratios above 100× are considered to be high, and concentrations can reach several thousands. Sophisticated Si cells can be used in the range up to 250×, whereas III-V solar cells can be applied for higher (up to several thousands) concentrations. Recently, material shortage has caused the price increase for c-Si modules, which has had an impact on the PV-system cost-reduction schedule. High-concentration PV is an alternative solution to

the application of solar PV as a dependable energy resource; however, the solar cells are only one aspect of the peak watt performance of a concentrator system. The module design should be kept deliberately simple to ensure low-cost manufacturing, at high optical efficiency of the concentrators and effective heat sinking. Also, long-term operational capabilities are of vital importance.

The advantages of the concentrator PV modules with small-aperture-area sub-modules are as follows:

1. Low ohmic losses in the small-area ($1-2\,\mathrm{mm}^2$) solar cells
2. No need to compensate for the thermal expansion difference between materials of a cell and a heat sink
3. Reduced (down to several centimetres) thickness of modules
4. Reduced detrimental effect of chromatic aberrations (for the case of the refractive concentrators) on cell operation
5. Low consumption of module housing and heat sink materials
6. Possibility to apply for PV module manufacturing the highly productive mounting methods developed for production of electronic components

In the case of the small-aperture-area sub-modules, a very stable and cheap silicate glass can be used in a stack with a relatively thin heat-sinking material (copper or steel). In spite of poor thermo-conductive properties of glass, waste heat can be dissipated into ambient air, as it is in regular flat-plate modules without concentrators. Superior insulating properties of glass allow connection of the cells in an electric circuit of any configuration, ensuring electrical safety of a module as a whole. Even walls of a module housing may be made of glass, justifying this approach as 'all-glass' module design [10].

8.2.1 Concentrator Optics

The problem to be solved concerns long-term stability of the sunlight concentrators. For refractive concentrators (Fresnel lenses) a tendency exists to replace the 'traditional' acrylic material with more environmentally stable polymers (which is a know-how of any research team). Ioffe's research team is concentrating on a composite structure of the Fresnel lenses, in which a silicate glass sheet (front side of a module) will serve as a superstrate for transparent silicone (inside) with Fresnel microprisms. In turn, the microprisms themselves are formed by polymerization of the silicone compound directly on the glass sheet with the use of a negatively profiled mould. Advantages of this approach are based on a high UV stability of silicone, excellent resistance to thermal shocks and high/low temperatures and good adhesive properties in a stack with silicate glass. Prisms of small average thickness ensure lower absorption of sunlight in comparison with acrylic Fresnel lenses of a 'regular' thickness (see Fig. 8.2).

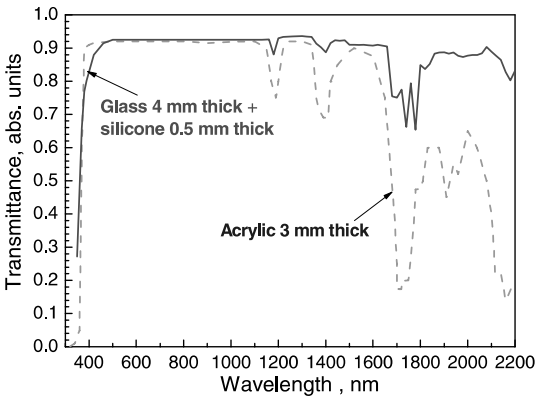

Fig. 8.2. Optical transmittance of a sample with a glass-silicone structure, simulating a composite Fresnel lens, in comparison with that of a conventional acrylic Fresnel lens

Optical diagrams of the concentrator sub-modules with Fresnel lenses of a composite structure are shown in Fig. 8.3. The version Fig. 8.3a ensures the highest optical efficiency of the system due to minimum reflection losses, but it implies hermetical sealing of the module housing as a whole, or special protection of the individual cell from environment. Heat dissipation is carried out through the bulk of a rear glass sheet. In Figs. 8.3b and 8.3c the cells are mounted on the trough-like heat spreaders placed behind rear glass sheet. In this case, heat dissipation occurs directly in environment, and a rear glass sheet serves as a protective cover glass for all the cells in a module. A module

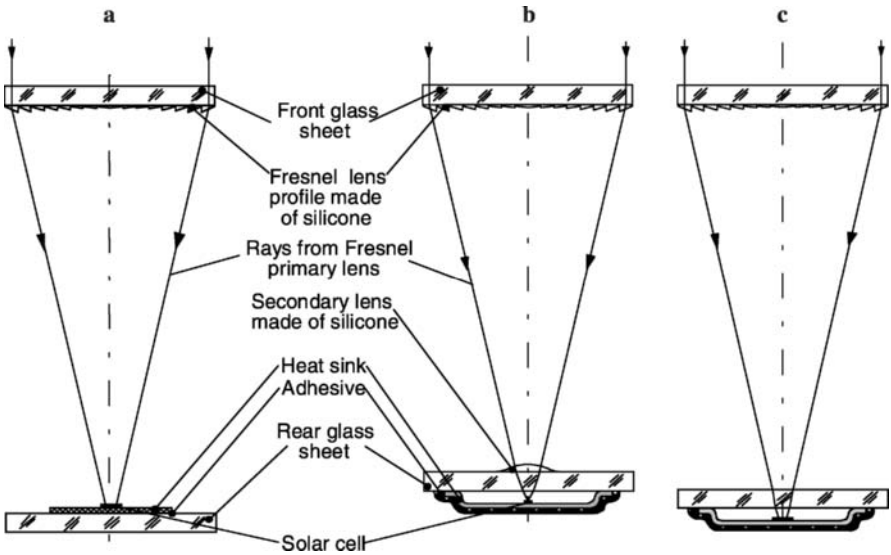

Fig. 8.3a–c. Optical diagrams of the concentrator sub-modules corresponding to the 'all-glass' module design

housing itself may have the channels for air for external/internal pressure equalization and escape of condensated water. In Fig. 8.3b the rear glass sheet is a substrate for a panel of the secondary lenses. The latter circumstance may be beneficial at further increase of the concentration ratio in a system.

Measured absolute optical efficiencies versus the input aperture (L) of square composite Fresnel lenses are shown in Fig. 8.4 for different lens focal distances (F) and receiver diameters (d). A small decrease in optical efficiency at low lens apertures and variation of d from 3 to 1.5 mm (when diameter of an 'ideal' sun image is small for given focal distances) indicates certain scattering of light on facet imperfections. At $d = 0.9$ mm this decrease is more significant due to probable cutting off the part of 'basic sun image'. When the area of the lenses begins to become comparatively large, chromatic aberration and scattering of light by shape imperfections in more deep peripheral grooves becomes more important. There exists only minor effect of focal distance F on lens efficiency, though a short-focus lens would be more efficient for small receiver diameters. The use of composite Fresnel lenses $40 \times 40\,\mathrm{mm}^2$ in aperture area with focal distances around 80 mm seems to be justified at cell diameters around 2 mm without secondary optics.

Optical efficiency measurements help to choose the designated area diameter of a solar cell operating in a primary plus secondary lens (PL + SL) system. A thin smooth-surface quartz lens characterized by definite optical efficiency of 91% at definite (and low enough) aperture area was involved in the measurement procedure as a 'reference' lens. Figure 8.5 presents the results of such measurements with regard to dependence on the photoreceiver diameter. There are four variations of measurements:

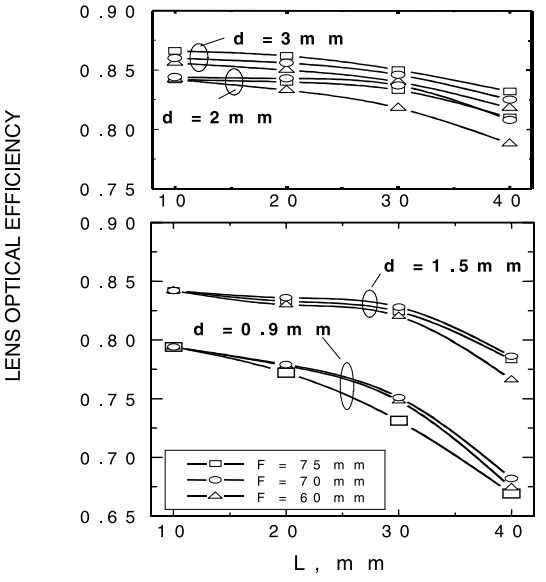

Fig. 8.4. Measured absolute optical efficiencies vs input aperture (L) of square composite Fresnel lenses without antireflection coatings for different lens focal distances (F) and receiver diameters (d)

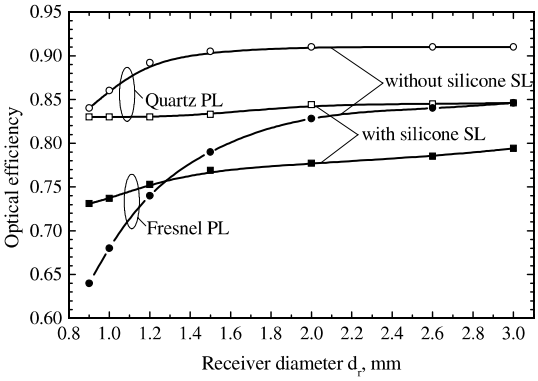

Fig. 8.5. Dependences of optical efficiency on receiver diameter. *Upper curves:* the quartz 'reference' lens is used as a primary concentrator without and with silicone SL. *Lower curves:* the 40×40-mm^2 composite Fresnel lens is used as the primary concentrator

1. The quartz 'reference' lens ($F = 85$ mm) is installed without SL and rear glass sheet for set-up calibration.
2. The quartz lens is installed with silicone SL to obtain an 'idealized' situation with respect to optical efficiency, when a 'PL + SL' system is practically free from lens aberrations and surface imperfections.
3. The 40×40-mm^2 Fresnel lens ($F = 80$ mm) is installed without silicone SL.
4. The case of optical layout of Fig. 8.3b is represented for measurements.

It can be seen from Fig. 8.5 that introduction of an SL improves considerably the optical efficiency in a practical case 'Fresnel PL + silicone SL' at smaller d_r. The initial drop in efficiency is caused by Fresnel's reflections on two additional interfaces. If, for a concentrator system without SL, the $d_r = 2$ mm is a reasonable choice, for the 'PL + SL' system such a choice could be $d_r = 1.2$ mm, leading to increase in the average concentration ratio by a factor of ~ 2.5. Optical efficiency of the 'PL + SL' system may be improved by applying an ARC, especially in the case of secondary lenses made of silicate glass. The panel of secondary lenses may have a monolithic structure together with the rear glass sheet, being protected from abrasive particles in module versions (Fig. 8.3b,c).

Of great importance is off-normal accuracy, which has to be realized in a concentrator system. Corresponding results of measurements are presented in Fig. 8.6. The upper diagram shows an off-normal behaviour of the submodules without SL at $d_r = 2$ mm, whereas the lower ones are for the case of the 'PL + SL' systems at $d_r = 1.2$ mm. The main result, which may be deduced from Fig. 8.6, is that the off-normal behaviour of the 'Fresnel PL + silicone SL' system at $d_r = 1.2$ mm is quite similar to that of the Fresnel lens concentrator alone at $d_r = 2$ mm. Due to a slightly larger focal

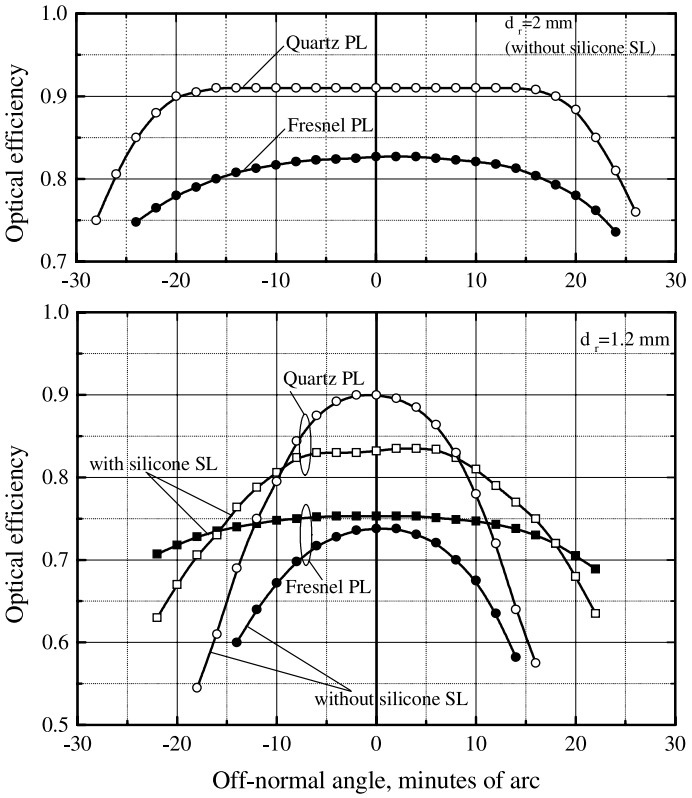

Fig. 8.6. Off-normal curves for the experimental sub-modules with and without secondary lenses at receiver diameters of 2 and 1.2 mm

spot, the optical efficiency is lower than in the case of the 'ideal' system with quartz PL at a normal position, and higher, starting from definite off-normal angles.

It is clear that in high-concentration systems the local concentration ratios may significantly exceed the average value. Indeed, optical efficiency of a 'lens-cell' concentrator system achieves its maximum value if whole focal spot, including the tails, is placed within designated aperture area of a cell. Besides, room for possible misalignments at module assembling and future sun tracking should be taken into account. At focal spot measurements for the small-aperture-area lenses, a probe cell with a hole of 0.12 mm in diameter calibrated with respect to photocurrent, scanned a 'sun image'. The results for the cases with and without silicone SL are shown in Fig. 8.7. Concentration ratio as high as 3200× has been measured for the 'PL + SL' system. This value has to be taken into account at the structure and contact grid optimization of the cells intended for use with such concentrator systems. The concentration ratios may be increased in the systems with Fresnel lenses

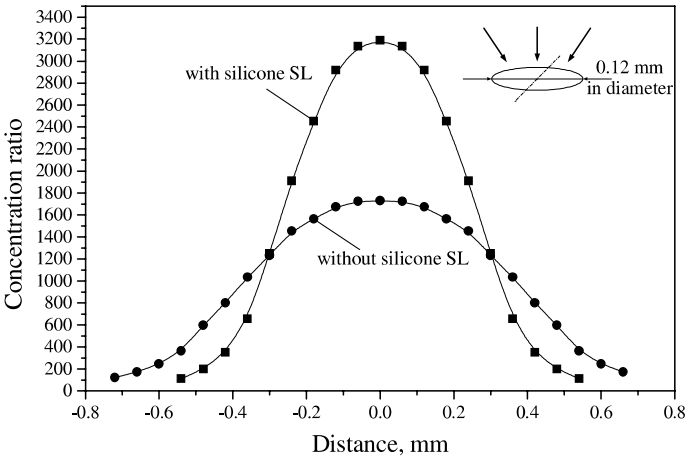

Fig. 8.7. Evaluation of the local concentration ratios across the focal spot in the 'Fresnel PL with/without silicone SL' system. The primary lens is $40 \times 40\,\mathrm{mm}^2$ in aperture area at the focal distance of 85 mm

of higher quality, as compared with results for 'ideal' quartz lens as shown in Figs. 8.5 and 8.6.

8.2.2 Heat Sinking

The input aperture area of each sub-module is $40 \times 40\,\mathrm{mm}^2$. An expected level of heat, which has to be dissipated by a similar area of heat sink, is about 1 W, corresponding to direct solar irradiation of $85\,\mathrm{mW/cm}^2$, concentrator system optical efficiency of 85% and cell conversion efficiency of 30%. Thermal models of the sub-modules were fabricated simulating its natural temperature behaviour at indoor measurements. The AlGaAs/GaAs cells 2 mm in diameter were soldered on the heat-sink plates (copper plates 0.5 mm thick) with configurations corresponding to certain fragments of heat sinks in a module. Heating under concentrated sunlight illumination was simulated by passing the forward current through the cells from a power supply. In accordance with Fig. 8.3, heat-sink fragments were glued on the upper (for the sub-module shown in Fig. 8.3a) and lower (for the sub-module shown in Fig. 8.3b,c) sides of $40 \times 40\,\mathrm{mm}^2$ glass plates. Appropriate conditions for heat dissipation were arranged by thermal isolation of the upper sides of plates and necessary spatial positioning of them. Overheating temperatures of the cells and glass plates (on the outer sides) were measured with respect to ambient temperature. Measurement results are shown in Fig. 8.8. It is seen from this figure that expected overheating of the cells and glass base plates is low enough, being lower in the case of trough-like heat sinks placed on the outer side of a module.

Certainly, reduced temperature, not only of the cells, but of the glass base plate as well, should be regarded as a positive, if modules of larger sizes are

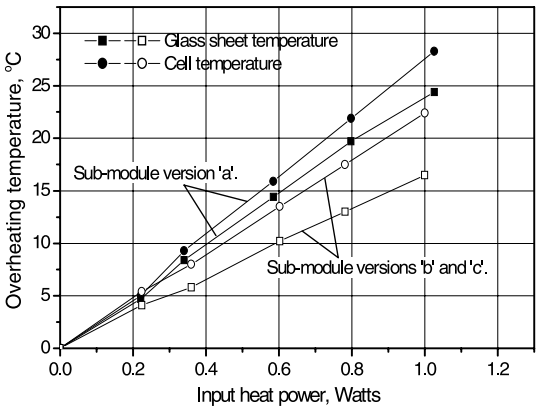

Fig. 8.8. Overheating temperatures (with respect to ambient temperature) of the cells and glass plates (see Fig. 8.3a-c) in dependence on input heat power

planned for fabrication. Indeed, any temperature difference between the front and rear (base) glass plates leads to certain misalignments of individual lenses and corresponding cells in the panels, bearing in mind small dimensions of the cells. Fortunately, a relatively low value of the thermal expansion coefficient for glass additionally mitigates this circumstance.

The above-mentioned indoor experiment did not regard heating the front glass plate with the panel of primary Fresnel lenses. It is evident that such a heating should take place due to absorption of the longer wavelength part of the solar spectrum; therefore, temperature difference between the front and rear glass plates is expected to be lower than overheating temperature as shown in Fig. 8.8.

8.2.3 Module Fabrication

In the module structure of Fig. 8.3c, light is focused onto multijunction cells through a rear glass sheet (see also Fig. 8.9). The panel of primary Fresnel lenses is arranged as a number of identical fragments. Each fragment is a string of six lenses. Similarly, the panel of cells is arranged as a corresponding number of identical units, where six cells and one by-pass diode are mounted in parallel on a common copper trough. Connections are performed by means of a contacting strip, or wires, if a wire bonder is used. The bottom of troughs is shaped with channels for placing silica gel for absorbing residual moisture in a sealed volume.

A full-scale $50 \times 50\,\mathrm{cm}^2$ module includes a 144-lens panel and 24 troughs with mounted cells. The accuracy in positioning the cells is of great importance because the cell should be in the centre of the focal point of a corresponding lens. This accuracy has to be around $100\,\mu\mathrm{m}$, which can be realized utilizing automatic processes and standard electronic industry machines. Structural silicone is used during module assembly to fasten the front and rear glass sheets together with the glass walls. Positioning of the troughs with

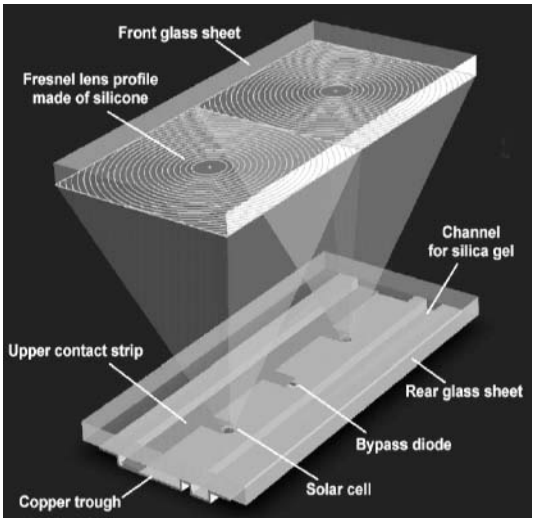

Fig. 8.9. Schematic of a module section

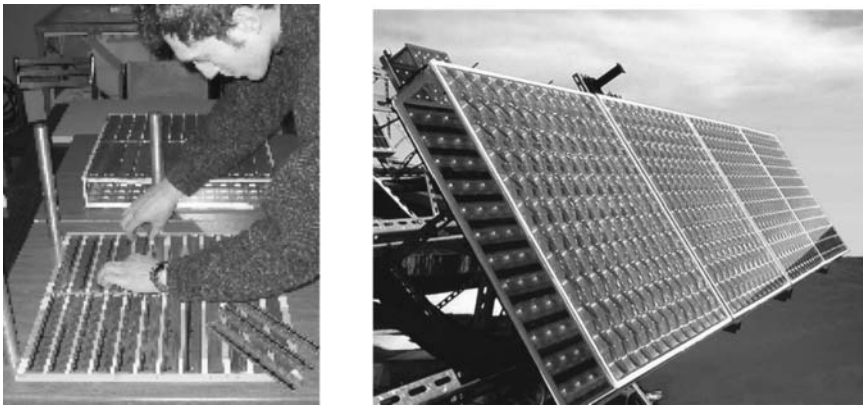

Fig. 8.10. Assembling the concentrator modules at PV Lab (*left*) and ready modules installed on a tracker of the Ioffe Institute (*right*)

mounted cells is not an elaborate procedure, even in using manual fabrication techniques if a special template is applied (see Fig. 8.10, left). Hermetical sealing is provided for the thin air body inside the troughs, whereas the entire volume between the front and rear glass sheets of the module housing is connected with atmosphere. Special tubes are utilized to exclude dust in the module. They are situated in diametrically opposite corners of a module housing, thus providing an exit for condensed water. After affixing the troughs, electrically connecting the cell strings and assembling the module, the rear module side is coated with a hermetic sealing compound.

Laboratory technology of a module assembly [16] as described above, has been developed employing one-junction AlGaAs/GaAs cells. Outdoor measurements for demonstration of the overall conversion efficiency potential were performed with test modules of reduced sizes equipped with GaInP/GaAs/Ge triple-junction cells (see below).

8.3 Indoor Characterization of the Concentrator Modules

A subject of much current interest is equipment for indoor and in-line characterization of the concentrator modules. Development of such equipment is becoming important due to the commercialization stage of a number of concentrator concepts.

Photoelectrical performance measurements of the multijunction solar cells and concentrator modules with such cells have imposed specific requirements on the solar simulating equipment and relevant testing methods. For the accurate indoor measurements, the following procedures and equipment have to be used:

1. Recording the spectral response curves in absolute units for a cell under steady-state colour and modulated monochromatic illuminations [18]
2. Obtaining the illuminated I-V curves by means of a solar simulator with adjustable spectrum: to check the tunnel diodes working abilities, studying of the I-V curves at non-uniform illumination, or a very strong one [18, 19]
3. Recording, after mounting the cells in a module, the I-V curve under illumination by means of a solar simulator, reproducing the sun angle size

Flash solar testers of two different types, developed at the PV Lab of the Ioffe Institute, may be used as the instruments for characterization of the individual concentrator cells. The tester of the first type (see Fig. 8.11, left) generates a flat light pulse with horizontal part duration of 1.5 ms. Corrected flash spectrum corresponds to AM 1.5D conditions. Concentration ratios up to C$\sim$ 7000$\times$ are achieved by changing the distance between the cell and lamp at uniform cell illumination. Also, a light collimating system may be installed, consisting of a hole in front of the lamp and a lens with output aperture diameter of 100 mm (see Fig. 8.12). In this case the flash solar tester reproduces 1-sun intensity, spectrum and beam divergence. A real PV system 'concentrator-cell' can be characterized by this instrument with respect to I-V curves at actually non-uniform illumination and possible off-normal module position, if concentrator dimensions are within output aperture area of the collimator.

The tester of the second type includes four flash lamps, regulated independently in intensity and activated simultaneously for flashing (see Fig. 8.11,

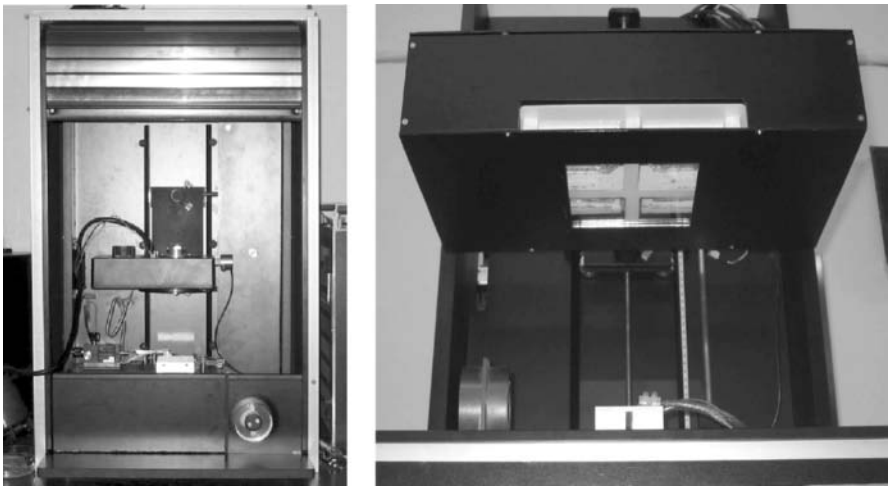

Fig. 8.11. Two types of the flash testers for characterization of the individual concentrator cells (see text)

right). In the four-lamp solar tester, the lamps are supplied with the band-pass glass filters, corresponding to specific parts of the spectrum, for instance, to sensitivity spectra of the sub-cells in a monolithic multijunction solar cell. Also, the lamps may operate without filtering. Gauss-like light intensity contour is 1 ms in duration at a 50% power level. Such a high-power flash solar tester can produce light fluxes up to $C \sim 25{,}000\times$ at a distance of several centimetres between the lamps and a cell.

A voltage-sweeping circuit characterized by internal resistance as low as 0.01 Ohm (due mainly to the resistor for measurement of current) has been developed as well (see Fig. 8.12). Its operation is based on alternative charging of a capacitor in a load of the tested cell from two other capacitors charged positively and negatively. Current and voltage magnitudes are measured by

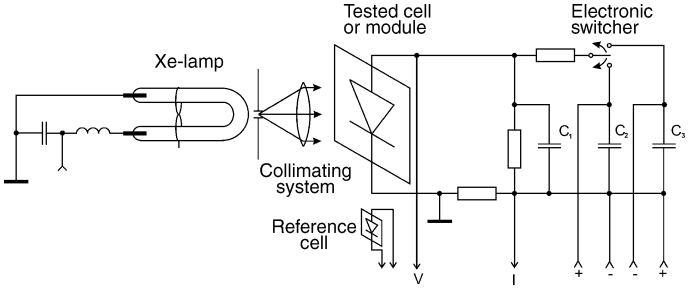

Fig. 8.12. The principles of the light collimation and I-V curve measurement in flash solar testers for characterization of the individual concentrator cells

a computerized system. In the case of the solar tester with a flat pulse, the entire I-V curve can be measured during one pulse. In the case of the four-lamp tester, pairs of voltage-current values are measured at maximum light intensity levels from flash to flash with approximately 10 s periodicity. Air cooling of the cells is employed to prevent heat accumulation.

Very high illumination levels and very low resistance of the measurement circuit may be required for characterization of the tunnel diodes commutating in series the sub-cells in a monolithic multijunction cell structure [19]. In Fig. 8.13, a family of the I-V curves is shown for a GaInP/GaAs/Ge triple-junction cell. The peak current for one of two tunnel diodes is revealed at the sun concentration ratio near to 2800×, whereas for revealing the peak current of the second tunnel diode concentration ratio as high as 6000× is necessary.

Indoor characterization of assembled concentrator modules is a new task for the PV community. A difficulty of this task consists in the necessity to represent all the parameters of the sunlight: spectral distribution within a wide wavelength range from UV up to about 1.7 μm; integral intensity in this range corresponding to that from the sun; and angular divergence of the rays around 0.5° of arc across the large aperture area of a light source corresponding to the module area. Solar tester for concentrator modules has been developed at PV Lab of the Ioffe Institute [16] utilizing a flash xenon lamp and a $50 \times 50\,\mathrm{cm}^2$ Fresnel lens collimator. The optical diagram and picture of this tester are shown in Fig. 8.14.

In the diagram of Fig. 8.14, light from a flash Xe-lamp is directed by a mirror to a large-area Fresnel lens. Collimated light is incident on a concentrator module. For initial alignment of the module, continuous illumination of it is carried out by means of a high-brightness LED through a specially shaped quartz rod and lamp bulb. If the front surface of the module was used as a basic one at assembling, initial alignment is achieved simply by placing the module on a tester glass plate. The lens focal distance and size of a hole are in the relation, ensuring the sun angle size of the collimated light. A glass filter, situated in front of the flash lamp and the hole, corrects the light spectrum with respect to relation between the 'blue' and 'red' parts. The second

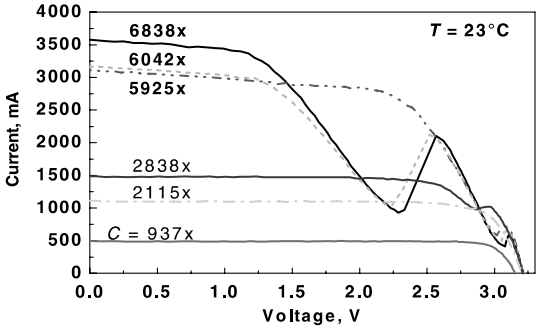

Fig. 8.13. A family of the illuminated I-V curves at different light intensities for one of the GaInP/GaAs/Ge triple-junction cells with designated illumination area of 2.3 mm in diameter. (From [19])

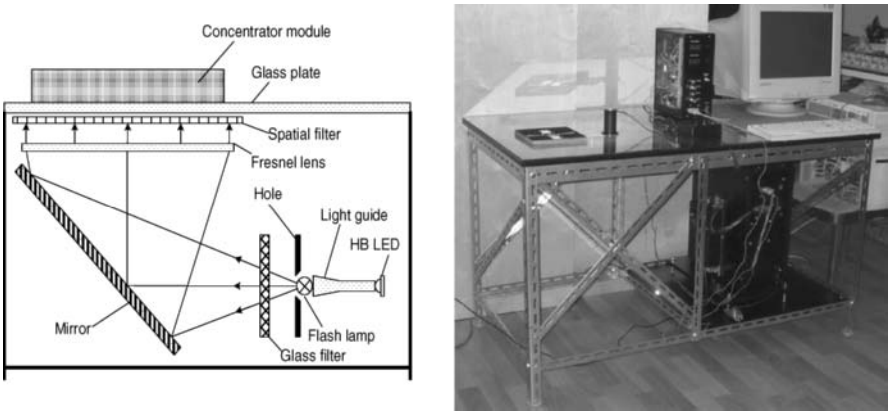

Fig. 8.14. Optical diagram and picture of the large-aperture area flash solar simulator for indoor I-V curve measurements of the assembled concentrator modules

filter of spatial type is situated between a Fresnel lens and a module under test. This filter makes uniform light distribution across the whole aperture area of the simulator within ±3%. An external view of the tester is shown in Fig. 8.14 (right).

8.4 Tracking to the Sun

High accuracy of tracking to the sun is a specific feature of the high-concentration PV method. Technical and economical aspects, concerned with necessity to ensure alignment in the 'sun-modules' system, are among the crucial ones, determining success in this field. The PV Lab of the Ioffe Institute has a certain experience in designing the trackers for installed capacities around 1 kWp. The last version of such a tracker is described in the following paragraph.

8.4.1 Mechanical Structure

The tracker consists of two main moving parts (see Fig. 8.15): a base platform moving around the vertical axis, and a suspended platform moving around the horizontal axis [17]. The base platform is equipped with three wheels, one of which is connected with an azimuth drive. Position of the suspended frame can vary in the range of ±45° symmetrically about a horizontal plane ensuring alignment of the modules in elevation.

The main principles of the tracker structure are as follows:

1. No elements are longer than 2 m
2. Only steel in a view of bended profiles and pressed parts (mainly protected with zinc cover) is used as a structural material at a minimum product range

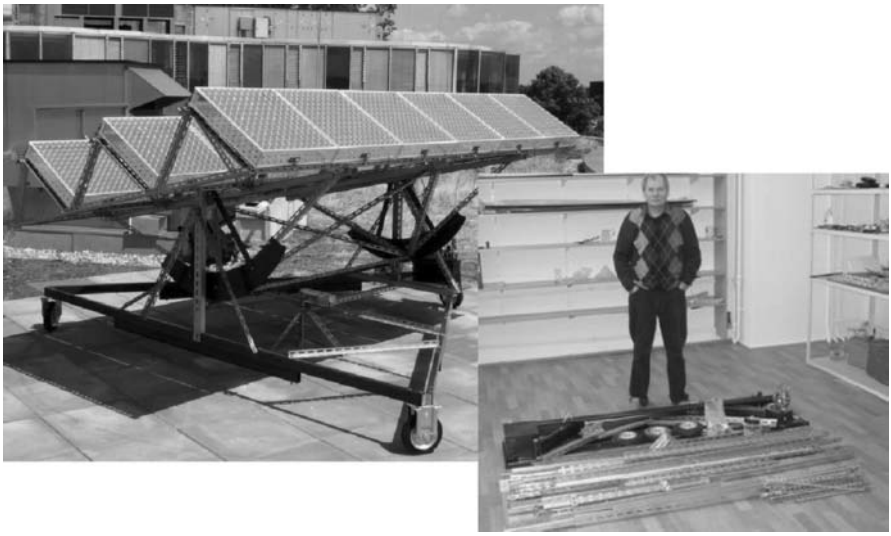

Fig. 8.15. Sun tracker with concentrator PV modules for 1 kWp of installed capacity. *Right:* tracker parts ready for transportation. (From [17])

3. Absence of welding processes at tracker parts' fabrication
4. Possibility to transport in a compact, disassembled form (see Fig. 8.15, right)
5. Possibility to assemble the tracker by one person

Two geared motor drives are situated in one protective box together with an electronic circuit and an accumulator. The parts of the horizontal driving mechanism in the final step of the gearing down are a wheel 200 mm in diameter and ground. A short vertical rod is fixed in ground as axis for rotation. For vertical driving, there are two cogwheels and two gear segments, situated symmetrically on two sides of the suspended frame. Continuous rotation of the motors is carried out for returning the tracker from 'sunset' to 'sunrise' position and for fast 'searching' the sun after cloudy periods. At normal tracking the motors are switched on periodically, every 5 – 8 s. Arrangement of the concentrator modules is in a form of stairs, reducing wind load on the tracker.

8.4.2 Sun Sensors and Electronic Board

The tracker is equipped with main (accurate) sensor and an additional one, both mounted on a suspended frame and operating as a part of an automatic closed-loop system. The main sensor (see Fig. 8.16) can align the tracker with the sun to within 0.05° of arc accuracy with acceptance angles of ±70° in both horizontal and vertical directions. An additional sensor makes wider the 'east/west' turning angle (up to 270°).

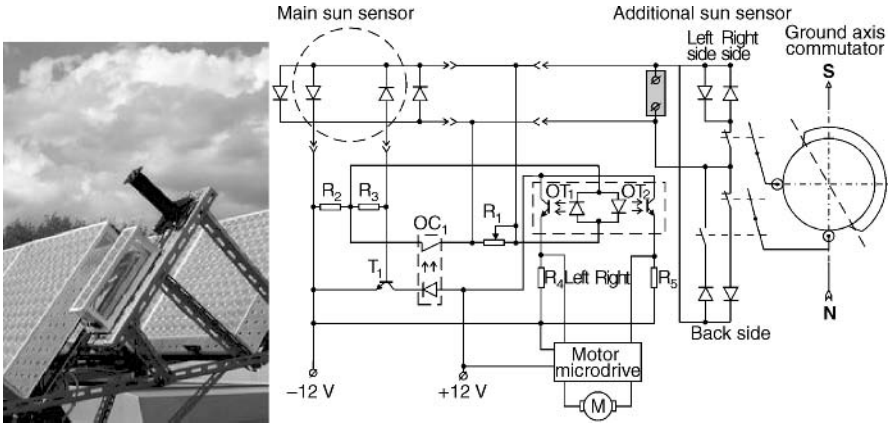

Fig. 8.16. A fragment of the electronic circuit of the tracking system. The main sensor in the circuit is assumed to consist of only azimuth channel

A high-concentration PV system can convert only direct sunlight. For this reason, in both sensors the multijunction III-V cells are used as the light-sensitive elements. In this case the sensors 'prefer' the direct sunlight, as they are less sensitive to diffused light. It is noteworthy that such cells generate a higher voltage, enough for forward biasing the LED in 'LED-phototransistor optoelectronic pairs. This allows creating a simple final-control electronic circuit with low power consumption in the 'sleeping' regime.

To increase the tracking accuracy, the main sensor includes two sub-channels, each one for horizontal and vertical movements. Each sub-channel includes two cells connected in a differential circuit. The additional sun sensor consists of four cells. These cells are located on the sidewalls and the back wall of a special element. Joint operation of both sensors may be considered regarding a fragment of the electronic circuit of the tracking system shown in Fig. 8.16. For simplicity, the main sensor is supposed to consist of only an azimuth channel. Switchers commutate the cells of additional sun sensor to ensure the right direction of rotation in azimuth with respect to various positions of the sun.

The cells, corresponding to the lower-accuracy sub-channels, are arranged outside of a shadowing tube of main sensor (dotted circle), but those for higher-accuracy sub-channels are arranged inside the tube. The shadowing tube limits acceptance angles of the inner-arranged cells to $\pm 1 - 2^\circ$. Illumination imbalance gives rise to activation of one of the optically biased transistors, OT1 or OT2, and commutating an azimuth motor in a proper direction. Near to alignment position, the sunlight penetrates the cells arranged inside the shadowing tube. A part of the photocurrent from these cells is used for activation of the transistor T1, which, in turn, causes disconnection of an optically switched solid-state relay OC1. From this moment, the signals for

motor rotations are generated only from the sub-channel characterized by a higher sensitivity and a reduced acceptance angle.

The developed combined sun sensor (the main and additional ones) ensures the motion and fast alignment of the tracking system with the sun in both clockwise and anti-clockwise directions only within an allowed sector (directed to the south, if operation occurs in the northern hemisphere), independently of the starting position. The above-mentioned requirement concerning allowed sector is sufficient for wiring the installation with external load. For operation in equatorial areas, where sun trace overpasses zenithal position, a built-in microprocessor with timer and calendar function has to be used in a tracker system instead of the above-described additional sun sensor. In this case the allowed sector for the tracker is directed to the east, being slightly wider than 360° of arc.

8.5 Outdoor Measurements of the Test 'All-Glass' Modules

Operational abilities of the modules of the 'all-glass' design have been checked with respect to overall conversion efficiency by fabricating and outdoor measurements of test modules of reduced sizes equipped with GaInP/GaAs/Ge triple-junction cells [16]. The cells have been produced by Spectrolab, Inc. In a module, described below, they were characterized by conversion efficiencies around 31.5% (AM 1.5D) at indoor flash measurements with uniform distribution of incident light.

The cells 2 mm in diameter were used in an eight-lens module (2×4 lenses) being connected in parallel. A hermetically sealed module was installed on the sun-tracking system (see Fig. 8.17). After the first outdoor characterization by a manual I-V measurement equipment, and by an automatic outdoor tester, the module was characterized indoors by a large-area flash solar simulator to compare corresponding results for outdoor and indoor measurements. In Fig. 8.18, I-V characteristics at illumination of the concentrator module are shown. The black curve was measured at noon on 18 October 2005 and the red one was obtained with the use of the above-mentioned solar simulator. Comparison of the curves demonstrates actual influence of heat on the cells in the module in continuous outdoor conditions. This difference in voltage due to temperature is low enough. Nevertheless, it is possible to introduce a temperature correction factor of 1.02 for the efficiency value. For the regarded measurement, the overall module efficiency value as high as 25.3% is estimated at room temperature of the cells.

It is noteworthy that there are obvious possibilities for efficiency improvements in modules of described design. One of the proposed improvements is to apply an anti-reflection coating (ARC) on both sides of the rear glass sheet (see Fig. 8.9). These sides are environmentally protected, so the ARC should work effectively. Another possibility lies in increasing the quality of

the Fresnel lens profile. A third improvement consists of using more efficient (up to 37 – 38%) cells. As a result, efficiencies of about 30% are expected in the developed modules.

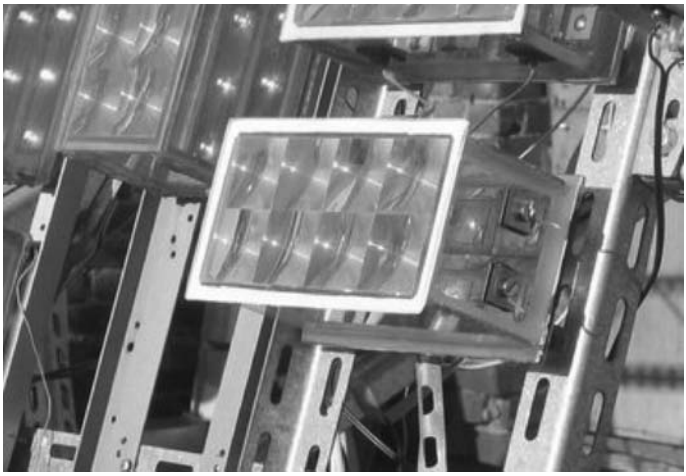

Fig. 8.17. Arrangement of the eight-lens module with Spectrolab's cells on a sun tracking system

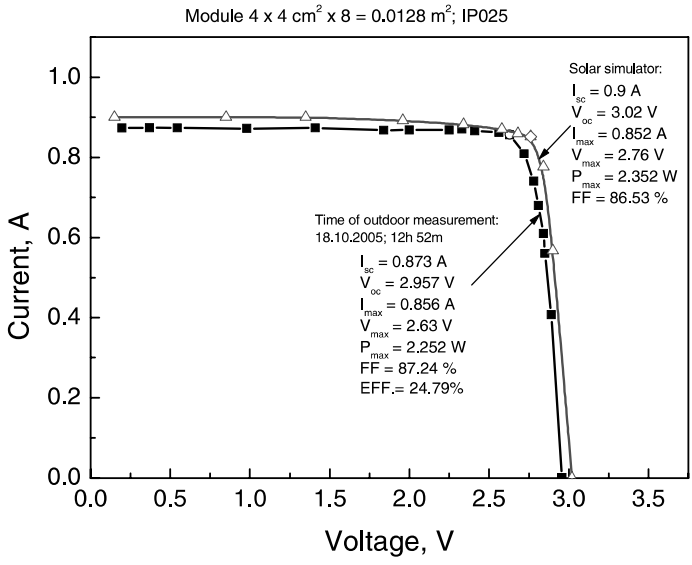

Fig. 8.18. Illuminated I-V curves of the experimental eight-lens module (see text)

8.6 Conclusion

Electronic instruments based on semiconductor devices have formed such areas of human activity as electric power conversion (rectifiers, invertors, etc.) and transmission and processing of information (radio-communication, computers, etc.). At present, a process of introduction of two new semiconductor devices and very wide fields of applications, i.e. large-scale electric power generation (for solar cells) and lighting technique (for LEDs), has been observed. This process was dictated by the recently achieved – and still expected for new achievements in the near future – drastic increase in efficiency of the corresponding devices. The fact that high-efficiency solar cells and high-brightness LEDs both have, as a base, III-V semiconductor compounds, is by no means accidental. Owing to the 'direct' energy band structure, these compounds are characterized by high absorption for the photons of the energy in the vicinity of the forbidden gap, and by high probability (approaching almost 100%) for radiative recombination of the minor charge carriers. Both these properties and, also, the feasibility to vary widely the forbidden gap value, type of layer conductivity, doping level of the material, and all of that for monolithic heterostructures, allows creation of the multijunction solar cells, which convert sunlight optimally within selected spectral bands.

The physical nature and crystalline perfection of the III-V materials potentially justify the principle of reversibility at photovoltaic conversion process in application to solar cells [20]. In particular, it is hypothetically possible to restore the radiation with the spectrum similar to that of the sunlight by passing a forward current through an actual multijunction solar cell based on a heterostructure of the direct band-gap semiconductors. The presence of the reversibility feature reflects the fact of the highest thermodynamically possible efficiency in a given power-conversion process. A 'physical alliance' of the III-V solar cells and LEDs in the PV Lab of the Ioffe Institute has permitted development of a variety of luminescence methods for investigation, control and possible improvement of parameters in both individual cells and solar modules on their basis. In fact, the first publication, where electroluminescence control of a p-n junction quality and sheet resistance in the AlGaAs-based solar cells was performed, was devoted to investigation of the cell heterostructures with intermediate conversion of solar radiation into luminescence with further use of it for generation of photocurrent [21].

In an early work [22], dealing with dual-junction monolithic AlGaAs/GaAs solar cells, electroluminescence, arising in a photoexcited wide-gap p-n junction, was identified as a reason for increased photocurrent in a bottom subcell. Subsequently, it was shown that it is possible to estimate, or even to evaluate, the main PV parameters of a direct band-gap cell with p-n junction (internal collection efficiency of the photogenerated carriers, open circuit voltage, sheet resistance and others) by contactless methods [20,23], analysing only photo- and electroluminescence signals from a cell wafer under photoexcitation. In the middle of the 1980s certain of these methods were applied at

industrial production of the space solar arrays with AlGaAs/GaAs solar cell, in particular, production of the array for the Soviet space station 'Mir'.

Turning back to the concentrator PV modules with III-V cells and small-aperture-area lenses (see Fig. 8.19), it is noteworthy that in this case there exists not only 'genetic cognation', but also a direct similarity in the constructional appearance of concentrator solar cells and LEDs (Fig. 8.20). Such a similarity is determined by the close values of geometrical dimensions, and, also, heat and current/voltage loads in both cases. The similarity in the epi-

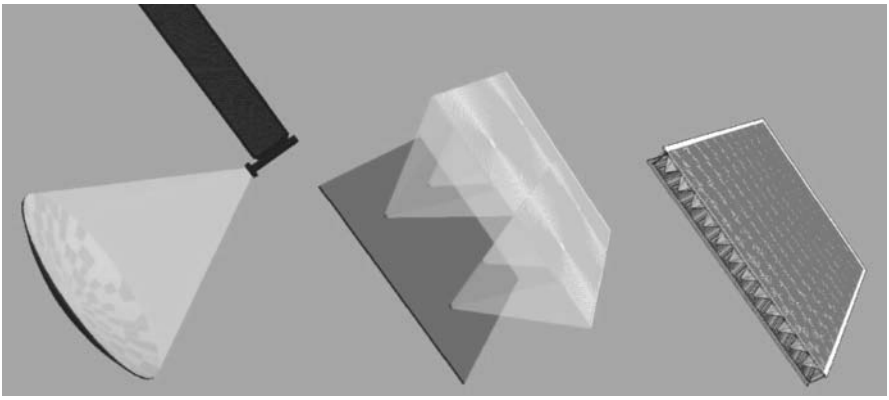

Fig. 8.19. Evolution of the concentrator modules with III-V solar cells

Fig. 8.20. The experimental modules with solar GaInP/GaAs/Ge triple-junction cells and AlGaInP LEDs, both equipped with small-aperture-area Fresnel lenses and being under forward bias conditions [17]; similarity of main features, favourable for promotion of both LED lighting arrays and solar concentrator modules

taxial growth processes (MOCVD) of the device structures, as well as similar methods for the post-growth treatment and assembly, allow, in a complementary fashion, development of effective equipment for production of semiconductor arrays for lighting purposes and solar modules for electric power generation. Taking into account the huge scales of these two markets, one may expect a significant economical effect from their interaction.

Solar PV modules with small-aperture-area concentrators, are compact, simple in structure and are characterized by lower material consumption in comparison with previous module designs They ensure an 'ideal' situation for sun-power conversion, when a high optical concentration of the sunlight is performed, but the distributed character of heat dissipation persists, inherent in the flat-plate photovoltaic modules without concentrators [24]; however, it is quite possible, that 'all-glass' approach in module design, as described herein, will be modified in accordance with requirements of industrial equipment, which has to be used in large-scale production of such modules.

Semiconductors, the technical development of which is only about 60 years old, have firmly dominated all fields of electric-power-conversion techniques and electronics, and are approaching a reputable position in the field of lighting techniques. Scientific and technological successes of recent decades encourage hope that a similar 'semiconductor revolution' may also take place in the field of electric-power generation.

References

1. L.W. James, R.L. Moon. GaAs concentrator solar cells. Appl Phys Lett 26, 1975, 467–470
2. J.M. Olson, D.J. Friedman, S. Kurtz. Handbook of photovoltaic science and engineering, ed. by A. Luque and S. Hegedus, Chap. 9, Wiley, New York, 2003
3. R.R. King, R.A. Sherif, G.S. Kinsey, S. Kurtz, C.M. Fetzer, K.M. Edmondson, D.C. Law, H.L. Cotal, D.D. Krut, J.H. Ermer, N.H. Karam. Bandgap engineering in high-efficiency multijunction concentrator cells. Proc on CD of the Second Int Conf on Solar Concentrators for the Generation of Electricity or Hydrogen, Scottsdale, Arizona, May 2005
4. Zh.I. Alferov. The double heterostructure: concept and its applications in physics, electronics and technology. Les prix Nobel, Norstedts Tryckeri, Stockholm, 2001, 65–93
5. Zh.I. Alferov, V.M. Andreev, Kh.K. Aripov, V.R. Larionov, V.D. Rumyantsev. Solar photovoltaic installation with 200 Watt output based on AlGaAs-heterophotocells and reflective concentrators. Geliotechnika, No 6, 3–6, 1981. Translated into English in Applied Solar Energy, No 6, 1981
6. A.A. Vodnev, A.V. Maslov, V.D. Rumyantsev, Sh.Sh. Shamukhamedov. Experience on creation of the solar installations based on AlGaAs/GaAs-photocells with concentrators. Sunlight concentrators for photovoltaic power installations, ed. by V.A. Grilikhes, Leningrad, Energoatomizdat, 1986, 25–29 (in Russian)

7. V.M. Andreev, A.A. Alaev, A.B. Guchmazov, V.S. Kalinovsky, V.R. Larionov, K.Ya. Rasulov, V.D. Rumyantsev. High-efficiency AlGaAs-heterophotocells operating with lens panels as the solar energy concentrators. Proc of the all-Union Conference 'Photovoltaic phenomena in semiconductors'. Tashkent, 1989, 305–306 (in Russian)
8. V.M. Andreev, V.R. Larionov, V.D. Rumyantsev, M.Z. Shvarts. High-efficiency solar concentrating GaAs–AlGaAs modules with small-size lens units. Eleventh European Photovoltaic Solar Energy Conference and Exhibition – Book of Abstracts; abstract no. 1A.15, Montreux, Switzerland, 12–16 October 1992
9. Project: INTAS96–1887. Photovoltaic installation with sunlight concentrators. Progress Reports, 1998 and 1999
10. Project: INTAS96–1887. Photovoltaic installation with sunlight concentrators. Final Report, 2000
11. E. Lorenzo, G. Sala. Hibrid silicone–glass Fresnel lens as concentrator for photovoltaic applications. Proc Int Solar Energy Soc (vol 1): Silver Jubilee Congress, Atlanta 1979, Pergamon Press, 536–539
12. V.D. Rumyantsev, M. Hein, V.M. Andreev, A.W. Bett, F. Dimroth, G. Lange, G. Letay, M.Z. Shvarts, O.V. Sulima. Concentrator array based on GaAs cells and Fresnel lens concentrators. Proc 16th European Photovoltaic Solar Energy Conference and Exhibition Glasgow, UK, 1–5 May 2000
13. V.D. Rumyantsev, V.M. Andreev, A.W. Bett, F. Dimroth, M. Hein, G. Lange, M.Z. Shvarts, O.V. Sulima. Progress in development of all-glass terrestrial concentrator modules based on composite Fresnel lenses and III-V solar cells. Proc 28th PVSC, Anchorage, Alaska, 2000, 1169–1172
14. A.W. Bett, C. Baur, F. Dimroth, G. Lange, M. Meusel, S. van Riesen, G. Siefer, V.M. Andreev, V.D. Rumyantsev, N.A. Sadchikov. Flatcon modules: technology and characterization. Proc 3rd World Conference on Photovoltaic Energy Conversion (2003) 3O-D9-05
15. V.M. Andreev, E.A. Ionova, V.D. Rumyantsev, N.A. Sadchikov, M.Z. Shvarts. Concentrator PV modules of 'all-glass' design with modified structure. Proc 3rd World Conference on Photovoltaic Energy Conversion (2003) 3P-C3-72
16. V.D. Rumyantsev, N.A. Sadchikov, A.E. Chalov, E.A. Ionova D.J. Friedman, G. Glenn. Terrestrial concentrator PV modules based on GaInP/GaAs/Ge TJ cells and minilens panels. Proc IEEE 4th World Conference on Photovoltaic Energy Conversion, Hawaii, 7–12 May 2006
17. V.D. Rumyantsev, A.E. Chalov, E.A. Ionova, V.R. Larionov, N.A. Sadchikov, V.M. Andreev. Practical design of PV modules for very high solar concentration. Proc CD of the Second Int. Conf. on Solar Concentrators for the Generation of Electricity or Hydrogen, Scottsdale, Arizona, May 2005
18. M.Z. Shvarts, A.E. Chalov, E.A. Ionova, V.R. Larionov, D.A. Malevskiy, V.D. Rumyantsev, S.S. Titkov. Indoor characterization of the multijunction III-V solar cells and concentrator modules. Proc 20th European Photovoltaic Solar Energy Conference, June 2005, Barcelona
19. V.M. Andreev, E.A. Ionova, V.R. Larionov, V.D. Rumyantsev, M.Z. Shvarts, G. Glenn. Tunnel diode revealing peculiarities at I-V measurements in multijunction III-V solar cells. Proc IEEE 4th World Conference on Photovoltaic Energy Conversion, Hawaii, 7–12 May 2006
20. V.M. Andreev, V.A. Grilikhes, V.D. Rumyantsev. Photovoltaic conversion of concentrated sunlight, Chap 4: Luminescent phenomena in concentrator solar cells. Wiley, Chichester, 1997, 294 pp

21. Zh.I. Alferov, Kh.K. Aripov, B.V. Egorov, V.R. Larionov, V.D. Rumyantsev, O.M. Fedorova, L. Hernandez. Investigation of heterophotocells with intermediate radiation conversion at high level of illumination. Fiz. i Techn Polupr 14, 685–690, 1980. Translated into English in Sov Phys Semicond 14, 1980
22. A.M. Allakhverdiev, Yu.M. Zadiranov, V.D. Rumyantsev. Mutual influence of wide- and narrow-gap photocells in the operation of multistage n-GaAs-p-AlGaAs-n-AlGaAs heterojunction solar cells. Fiz i Techn Polupr 17, 446–448, 1983. Translated into English in Sov Phys Semicond 17, 1983
23. A.B. Guchmazov, J.-A. Rodriguez, V.D. Rumyantsev. Contactless determination of the electrical and photoelectric parameters of p–n junction heterostructures in a luminescent material. Sov Phys Semicond 25 (1), 1991, 84–89 (see also: V.D. Rumyantsev, Proc 10th Eur Photovolt Solar Energy Conf, Lisbon, 1991)
24. Zh.I. Alferov,V.D. Rumyantsev. Trends in the development of solar photovoltaics. In: Next generation photovoltaics, IoP, 2004, 19–49

9 Solar Thermophotovoltaics

V. Andreev, V. Khvostikov, and A. Vlasov

9.1 Introduction

In solar photovoltaics, design and optimization of a converting system are strongly determined by the sun spectrum and by the fact that there is no 'reverse connection' between a receiver and the sun. On the other hand, there is a possibility to vary the operating concentration ratio (in other words, operating current density of the p-n junction). In a TPV system, the optimization may imply a choice of the emitter spectrum and a possibility to return a non-absorbed part of radiation from the receiver back to the emitter surface supplying it by an 'additional' power. One of the main common features in these systems is the following: in both systems, the energy source is characterized by a wide spectrum. This means that the most effective approach for improving the solar PV system efficiency – that is, the cascade approach – may be applied for the improvement of the TPV system parameters.

The investigations in the field of thermophotovoltaics started in the early 1960s [1], but the real advantage of the TPV approach has been demonstrated only in the past two decades. Theoretical and semi-empirical modeling [2–9] have shown that optimal band-gap energy is in the range of $0.4-0.6\,\mathrm{eV}$ in TPV cells designated for operation with black-body (grey-body) emitters at the temperatures of $1200-1500\,^{\circ}\mathrm{C}$. Germanium and silicon were the materials at first suggested and applied to TPV conversion of radiation from fuel-fired emitters; however, the first TPV systems based on these materials have not gained their advantages such as low cost and commercial availability. Among the III-V compounds, gallium antimonide ($0.72\,\mathrm{eV}$) was the first semiconductor widely used in TPV devices. InGaAsSb alloys ($0.5-0.6\,\mathrm{eV}$) lattice matched to GaSb as well as InGaAs lattice matched ($E_g = 0.74\,\mathrm{eV}$) and mismatched ($0.5-0.6\,\mathrm{eV}$) to InP substrates have been developed for TPV applications as well. Semiconductors with band gaps more than $0.75\,\mathrm{eV}$, such as Si, can also be applied to TPV systems with selective emitters, in which radiation maximum is shifted to a short-wavelength part of spectrum.

In solar thermophotovoltaic (STPV) systems, the sunlight is absorbed by an emitter and reemitted as a thermal radiation before illumination of PV cells (Fig. 9.1). The STPV system, as a variety of a TPV generator, allows utilizing selective filters/mirrors and sub-bandgap photon reflection to the emitter, which ensures increased efficiency.

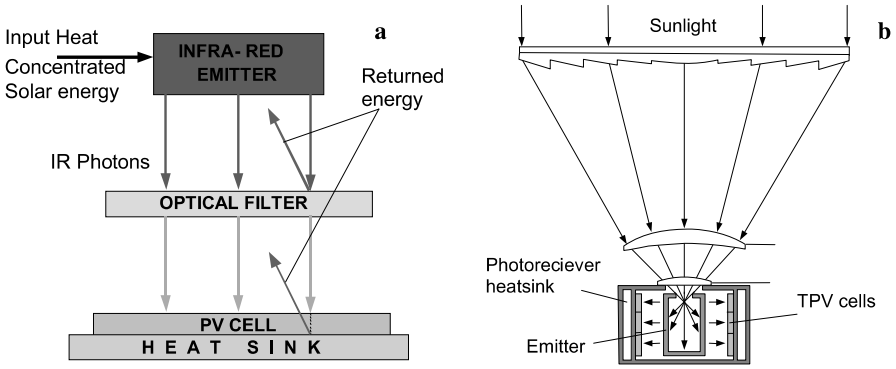

Fig. 9.1. a Key elements in a solar TPV system. **b** Concept of a solar TPV system with a Fresnel lens as a primary concentrator

Theoretical [10–18] and experimental [19–23] studies show an opportunity to achieve a high efficiency in STPV systems. For ideal system elements, the maximal theoretical efficiency was found to be 85.4%, which is close to the efficiency of an unlimited stack of tandem cells. In practice, the expected efficiencies of STPV converters are 20 – 30%.

Solar-powered or hybrid solar/fuel powered systems have some additional positive features: (a) the TPV fuel-fired part of the hybrid system would permit the operation during the night; (b) a hybrid system with PV conversion (or lighting) for a visible part and TPV for an infrared part of the solar spectrum can be created as well; (c) a high-temperature ($\sim$ 2000 K) emitter in a vacuum bulb can be used with a good-enough 'quality' of radiation in STPV systems; (d) like a concentrator photovoltaics, TPV conversion of concentrated sunlight has the ability to decrease solar electricity cost in comparison with non-concentrated photovoltaics, owing to the reduction of the PV cell area which is proportional to an increase of the output electrical power density from PV cells, achieving a value exceeding 1 W/cm^2 in high-concentrator STPV systems.

The following key problems exist with STPV system optimization:

1. Providing the high sunlight concentration
2. Changing the emission spectrum of the photon emitter
3. Filtering the radiation to utilize photon recycling process and to reduce the heat impact on photocells
4. PV cell design, including the tandem cell which allows increase of PV conversion efficiency of radiation from the emitter.

These problems may be interrelated. For instance, a selective filter may be deposited directly on the photocell surface reflecting long-wavelength radiation back to the emitter, or the photocell itself may play the role of such a filter, if there is a mirror on its back surface, which reflects the sub-bandgap photons non-absorbed in the PV cell material.

This chapter consists of the following main parts: firstly, the solar TPV system designs are described, including the design of sunlight concentrators and emitters. Then, photoconverters and evaluation of the achievable efficiency are considered. In the final part, the developed solar TPV converters based on GaSb PV cells are described.

9.2 Solar TPV System Design

9.2.1 Solar Concentrators

One of the most important parts of the concentrator photovoltaic module is the solar concentrator itself (Figs. 9.2, 9.3). Because of the use of a high-temperature emitter, the solar concentration ratio is not limited and needs to be as high as possible to obtain high emitter temperature values, however keeping the price of the concentrator reasonable. The maximum achievable solar concentration ratio for the terrestrial conditions is 46,164× and is determined by the angular dimensions of the sun. This value can

Fig. 9.2. Pseudo-parabolic facet concentrator made of four spherical dish mirrors installed on a sun tracker

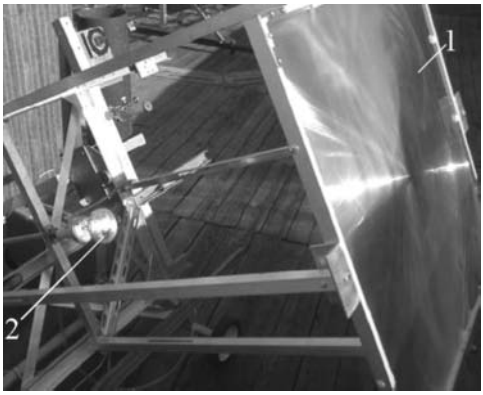

Fig. 9.3. Two-stage concentrator based on a primary Fresnel lens (1) and a secondary quartz concave-convex lens (2)

be achieved with an ideal parabolic mirror with an opening angle of 180°. Production of such mirrors is difficult, and the price will be corresponding high. Yugami et al. [19] used a ∅1.56 m parabolic mirror with ∼ 150° opening angle with concentration ratio (CR) of ∼ 25,000×. In practice, mirrors with lower ($60 - 70°$ or less) opening angles are more often used due to their lower price. Such mirrors can be produced, for example, by hot pressurized molding of a metal sheet (preferably aluminium [20]) or by a glass molding process. Also, multipiece compound mirrors can be used; thus, a 90-kW concentrator based on 82 dishes has been developed by Stone et al. [21] to be used with a STPV module. Similar large multi-dish reflectors are used by Solar Systems Pty Ltd [24] for concentrator PV modules. The concentration ratio obtained with these mirrors is about 500×. Figure 9.2 presents a four-segment pseudo-parabolic mirror, made at the Ioffe Institute ensuring CR of ∼ 1000×. The concentration ratio may be increased by the use of a secondary optics element: a CPC or a lens; thus, the four-segment mirror with the use of a secondary lens ensures CR = 5000 suns with 90% efficiency. This two-stage concentrator was used for the developed solar TPV module.

A Fresnel lens technology can be applied for concentrator fabrication. Small Fresnel lenses are often used for conventional PV concentrator systems [25,26]. Larger concentrators are necessary for STPV modules. A Fresnel-lens-based two-stage sunlight concentrator system developed for solar TPV system is shown in Fig. 9.3. It consists of a Fresnel lens 0.36 m^2 in area and 0.75 m focal length and a secondary quartz concave-convex lens. The light distribution in the spot was measured by scanning with a GaSb PV cell with a ∅1-mm aperture mounted on a water-cooled stage. It can be seen from Fig. 9.4 that more than 90% of the energy is collected by the ∅10-mm aperture, which corresponds to 4600× concentration ratio, and is high for this simple construction of a concentrator system.

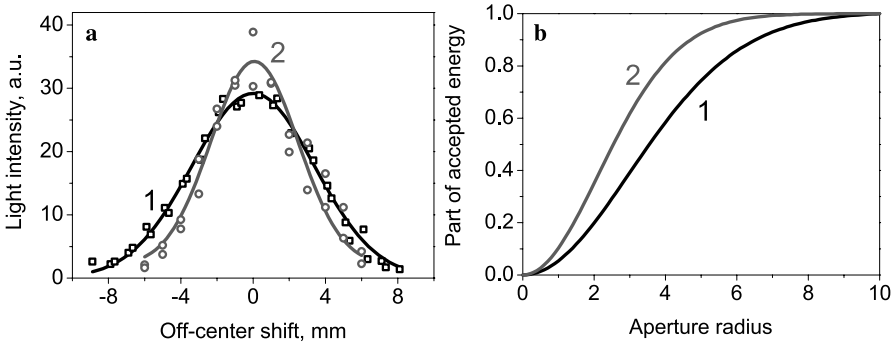

Fig. 9.4. a Measured light distribution in the developed concentrator system. Fresnel lens without (1) and with (2) a secondary lens. **b** Part of energy hitting the aperture of given radius without (1) and with (2) a secondary lens

The material of commercially available Fresnel lenses (PMMA) is, however, characterized by a poor outdoor stability. Recently, a technology for Fresnel lenses of a composite structure was developed: the microprisms are formed of the transparent silicone rubber contacting with the front silicate glass sheet as a protective superstrate [26,27]. The developed formation process allows fabricating a lens of $0.5\,m^2$ total area. Such a type of Fresnel lenses ensures much better environmental stability owing to the use of highly stable silicate glass, protecting the Fresnel lens made of silicone rubber, which is also characterized by high stability under the action of outdoor conditions. These Fresnel lenses are very promising for fabrication of concentrator PV modules and have potential for low-cost STPV systems.

9.2.2 Emitters for Solar TPV Systems

In solar TPV systems, the sunlight is concentrated on an emitter; hence, the first objective the emitter should conform to is the following: it should absorb the energy with the maximum possible efficiency. Then, it should transfer it to the PV cells. Choosing emitter parameters requires optimization of its temperature. For convenience a parameter called 'emitter efficiency' may be introduced. The emitter efficiency is determined as a ratio of the part of useful energy (which illuminates the PV cells) to the total energy, irradiated by an emitter (including the one through the aperture). With a certain aperture size, determined by the focusing system area and concentration ratio, the higher the emitter efficiency, the bigger is its size and the lower is its temperature. Increase in the concentration ratio leads to the decrease of the part of radiation, escaping through the aperture, and thus leads to an increase in efficiency for the emitter of the same size, or, in other words, to the temperature increase of an emitter of the same size. This parameter is important while optimizing the system; however, in the case of the hybrid STPV system with the mixed gas and solar power supply, this parameter may be neglected for it can be chosen relatively large. In this case the emitter temperature is controlled by the gas combustion, while the solar energy allows saving the fuel.

One of the best materials for solar energy absorption is polycrystalline SiC, which absorbs in the visible and IR spectral regions with the efficiency of 85 – 95% [28]. In addition, this material can be heated up to $\sim 1700\,^{\circ}C$ in the air; however, the spectrum of the polycrystalline SiC thermal radiation is not appropriate for the photovoltaic conversion, since a large part of the emitted photons have energy lower than the PV cell band gap (Fig. 9.5) and cannot be converted into electricity. For high efficiency of the TPV generator this radiation should be recycled. This can be done basically by two methods: reflecting the unused radiation back to the emitter or using an emitter material with selective emission spectrum. The first approach can be realized using non-absorbing selective filters inserted between the emitter and PV cells [20, 29–31], or by the use of a backside mirror inserted below the

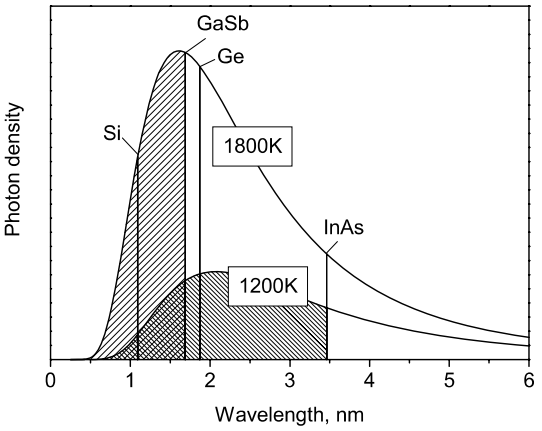

Fig. 9.5. Blackbody thermal radiation spectra for 1200 K and 1800 K band gaps of some materials are indicated. GaSb and InAs cells photoresponse regions are shown by *hatched areas* of 1800 and 1200 K spectra, respectively

PV cells. Selective filters are obtained by applying the textured structure on a regular IR mirror (so-called 2D photonic crystals) [20, 32, 33] or by the use of multi-layer coatings [29–31]. In the case of a backside mirror it can be deposited on the back surface of the cell, which must be transparent for the IR radiation [34–38].

In thermophotovoltaics, rare earth oxide ceramics (Y, Yb, Er, etc., aluminium garnet) is often used as a material with a selective spectrum [39–42]. It is noteworthy that these materials are almost transparent for nearly blackbody radiation of the absorber; however, with a thick and porous layer of rare earth AG (namely ErAG), the substrate radiation of SiC (whose emissivity is above 0.9) can be efficiently reflected back, and thus high selectivity of the emitter can be achieved [40]. Also, a buffer layer between the absorber and the emitter can be inserted. Such a buffer layer (presumably a metal film) should absorb or reflect the black absorber radiation and reemit it with much lower emissivity. This, however, means that the whole structure will become more complicated, considering mechanical stability of an emitter in a high temperature range. The simplest way to obtain a selective emitter is the use of refractory metals – tungsten, for example, the emissivity of which increases in the visible and near-IR regions up to 0.45 – 0.47, with a drop to 0.1 – 0.2 in the IR region [43]. The emitter can be made in a form of a cylinder with a sealed bottom. In this case it can be considered as a cavity, the emissivity of which can be calculated by solving the following set of iterative equations [44–47]:

$$\varepsilon_{\mathrm{ef}}(M_i) = \varepsilon_{\mathrm{ef}}(M_i) + R(M_i)\left[\int\limits_{F_1} K(M_i, N_1)\varepsilon_{\mathrm{ef}}(N_1)\,\mathrm{d}F_{N_1} + \right.$$
$$\left. + \int\limits_{F_2} K(M_i, N_2)\varepsilon_{\mathrm{ef}}(N_2)\,\mathrm{d}F_{N_2}\right], \qquad (9.1)$$

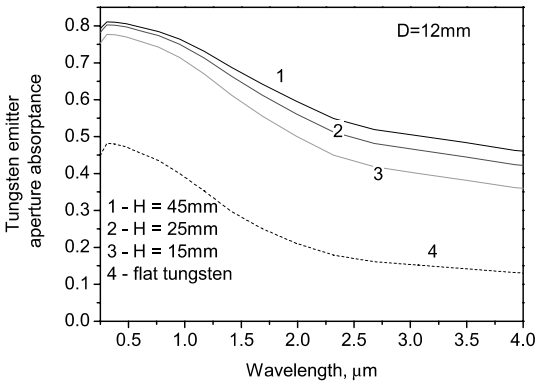

Fig. 9.6. Theoretical spectral dependence of the tungsten emitter ∅12-mm aperture absorptance for different emitter lengths. The emitter temperature is 1600 K.

where $\varepsilon_{\text{ef}}(N)$ is the effective emissivity of the cavity aperture, $K(M_i, N)$, the geometrical coefficient describing the viewing angle of heat exchanging surfaces (the viewing angle of a unit area on one surface to a unit area on another surface), F_1, F_2, cylindrical and flat surfaces of the emitter, $\varepsilon(M_i)$, emissivity, and $R(M_i)$, reflectance of the cavity material. Temperature is assumed to be constant over the surface. Precise calculation implies multiple order of reflection to ensure equality of the heat emitted by the cavity surface and the heat absorbed by the cavity itself and emitted through the aperture. The absorptance of a ∅12 mm tungsten cylinder 15 – 45 mm in length increases by a factor of two to three compared with the pure tungsten, reaching the maximum value of AA = 0.8 at 500 nm (Fig. 9.6). The total absorption efficiency of cylindrical tungsten emitters appears to be about 0.6 – 0.7 for the AM1.5 solar spectrum.

To prevent the tungsten emitter from oxidation (which starts at ∼ 400 °C for tungsten), it should be placed in a quartz bulb filled with a rare gas (Ar or Xe), which can be sealed. The selectivity of a tungsten emitter can be increased by surface microstructuring: formation of a 2D or 3D photonic crystal [39, 48].

9.3 Photovoltaic Cells and Efficiency Potentialities of Solar TPV Converters

For direct conversion of the solar spectrum with single-junction cells materials with band gaps PV $\Delta E_g = 1.1 - 1.5$ eV are used. The temperature of an emitter in a TPV system is -approximately two to three times lower than that of the sun. For TPV receiver fabrication the materials with the band-gap range TPV $\Delta E_g = 0.5 - 0.75$ eV should be used (Fig. 9.7). This corresponds to Ge, GaSb, InGaAsSb/GaSb and InGaAs/InP semiconductors. The cell technology is constantly being improved; thus, in analyzing the possible system performance ideal PV cells can be considered.

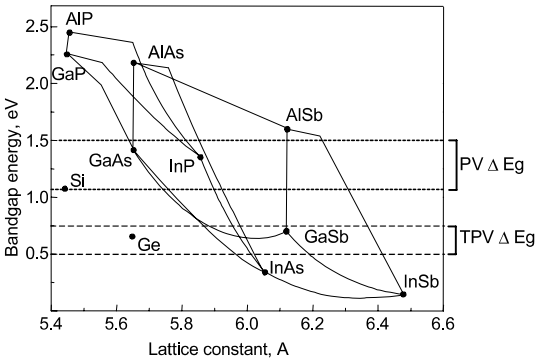

Fig. 9.7. Dependence of the band gap of Ge, Si and III-V compounds and their solid solutions on the lattice constant of these materials. PV ΔE_g, TPV ΔE_g: ranges of the single-junction cell band gaps optimal for solar PV and TPV applications, respectively

Theoretical estimations of STPV module performance have been carried out in the following papers: [10–17]. Efficiency values of 70% and more were obtained using the thermodynamic approach [16, 17]. Most authors used a more realistic approach [10–15], which implies consideration of modules with PV cells, calculated in the Shockley-Queisser model. Achievable efficiency values obtained are generally in the range of $\sim 20 - 40\%$, depending on a chosen model and its parameters.

Presented below are the results of total STPV module efficiency calculations for the system with a tungsten emitter, which are aimed to optimize the module parameters: the choice of emitter dimensions; PV cell band gap, etc.; and to analyse the ways and possible benefits of the system improvement: use of emitters with increased absorption efficiency; return of unused subbandgap radiation to the emitter; and use of monolithic tandem PV cells. All calculations were performed for an ideal PV cell (a Shockley-Queisser model). In order to avoid extremely high values of current densities, it was limited to $5\,\mathrm{A/cm^2}$, increasing the number of PV cells where needed. The concentration ratio was chosen as $2000\times$ and $8000\times$, the direct sun irradiation density of $850\,\mathrm{W/m^2}$. Convectional losses were not considered, as they can be significantly decreased by inserting the emitter in a thermos-like chamber. The unused radiation is partially returned to the emitter by a backside gold mirror with the return-efficiency RE.

First of all, one should consider the emitter size (and thus its temperature) and PV cell band gap. The emitter efficiency (Fig. 9.8, left scale) decreases with increasing emitter temperature; however, at higher concentration ratios this happens at higher temperatures. On the other hand, PV conversion efficiency has a maximum at emitter temperature $> 2200\,\mathrm{K}$ in PV cells with $\mathrm{Eg} = 0.7\,\mathrm{eV}$ (Fig. 9.8, right scale). At these temperatures the emitter efficiency is low for considered concentration ratios. Also, the process of photon

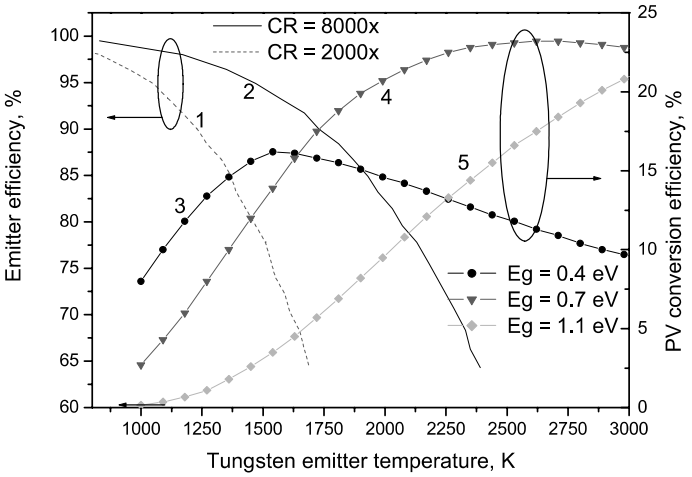

Fig. 9.8. Dependence of calculated emitter efficiency (*curves* 1 and 2) for two concentration ratios CR = 2000× (curve 1) and 8000× (curve 2) and PV conversion efficiencies for three cell band gaps Eg = 0.4 eV (*curve 3*), 0.7 eV (*curve 4*) and 1.1 eV (*curve 5*) from tungsten emitter temperature

recirculation affects these dependencies; thus, we present a complex analysis of the solar TPV module total efficiency.

Two principal system performances are considered: 'current technology' – with parameters of emitter aperture absorptance AA = 0.7 and return efficiency RE = 0.5 close to those available (Fig. 9.9a); and 'advanced technology' (Fig. 9.9b) with $AA = 0.9$ and RE = 0.9. As can be seen from Fig. 9.9, optimization of the sunlight absorption and unused light recycling processes

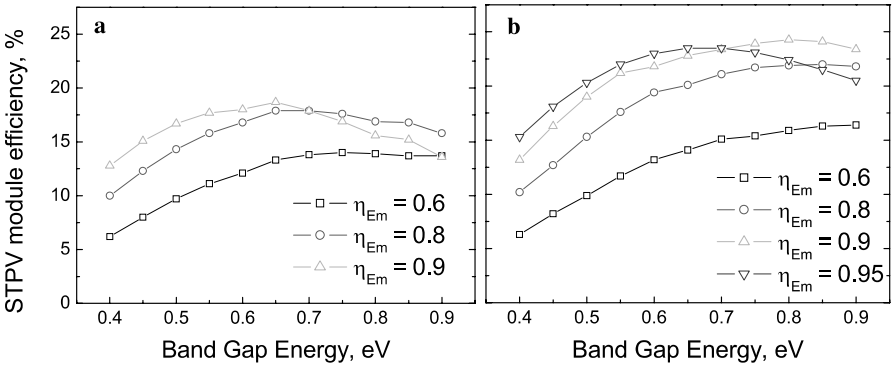

Fig. 9.9. Calculated efficiency of STPV module vs single-junction PV cell band gap for different values of tungsten emitter efficiency η_{Em} and two system configurations: **a** 'current technology' (AA = 0.7, RE = 0.5); and **b** 'advanced technology' (AA = 0.9, RE = 0.9)

lead to a sufficient increase in the STPV module efficiency accompanied with an increase in the optimal band gap and the emitter efficiency. This effect originates partly due to an increase in the emitter temperature (of the fixed efficiency) by $300 - 400°$. It is important to note that the maximum STPV efficiency takes place at the emitter temperature in the range of $1800 - 2300\,\mathrm{K}$; thus, according to the calculations presented, the maximum STPV efficiency of single-junction GaSb cells based STPV modules with a tungsten emitter may reach 18% ('current technology') with possible improvement up to 25% ('advanced technology').

In modern photovoltaics, monolithic tandem PV cells are widely used for the PV conversion efficiency increase. Below, the results of an analysis of the STPV system performance with monolithic tandem PV cells are presented. These calculations are aimed to estimate the possible benefits of the multijunction cell application in a STPV system. Figure 9.10 shows a set of graphs with calculated isoefficiency curves, plotted against top- and bottom-cell band gaps. The graphs are calculated for optimal emitter efficiencies in the 'current' and 'advanced' technology cases. Comparing this data with those of a single-junction case (Fig. 9.9) one can see that efficiency increases by $4 - 5\%$ with the use of dual-junction cells.

However, it is noteworthy that, since the monolithic tandem PV cells should always be adjusted with the incoming spectrum to implement an equal current requirement, the change of the sunlight intensity during daily operation may lead to a significant emitter temperature change, accompanied by the corresponding emission spectrum blue/red shift. The calculations show that reducing the incoming light power density leads to the optimal band-

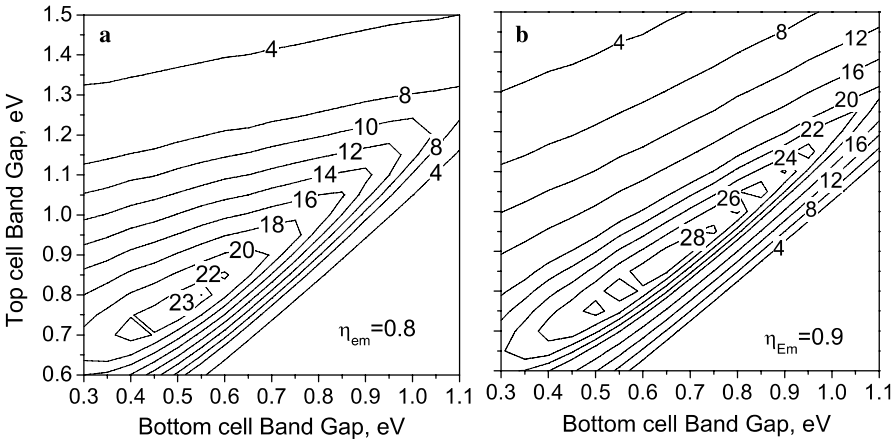

Fig. 9.10. Calculated efficiency of STPV module at current technology (**a**), and advanced technology (**b**) with the use of monolithic tandem PV cells for optimal tungsten emitter efficiencies η_{Em}. The graphs are plotted for various top and bottom band gaps as a set of isoefficiency lines

gap red shift. In Fig. 9.11, the calculated STPV efficiency is plotted against the bottom-cell band gap (assuming the top cell is always optimal) for three different sunlight intensities: 600, 800 and 1000 W/m^2 in the 'current technology' case. Maximum possible efficiency for 'advanced technology' is also shown. The effect of the optimal band-gap shift is not critical, and an average point may be chosen with only 1 – 2% efficiency loss retaining 22 – 23% of the total efficiency for the 'current technology' case and 28 – 30% for the 'advanced technology'.

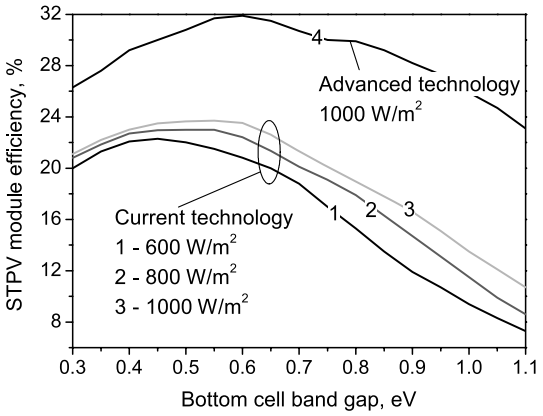

Fig. 9.11. Calculated efficiency of STPV module with tandem PV cells for different direct sun radiation levels and emitter efficiency of 0.8 (*curves 1-3*; 'current technology'). *Curve 4:* "advanced technology' case at 1000 W/m^2 solar radiation density. The graph is plotted vs bottom cell band gap with the top cell band gap optimal for the chosen band gap and sun intensity in each point

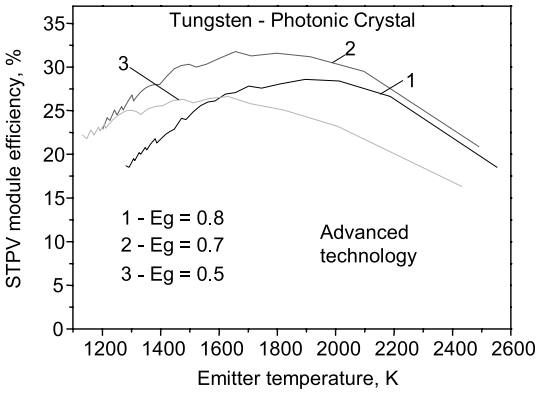

Fig. 9.12. Calculated STPV module efficiency as a function of emitter temperature. Emitter material: tungsten 3D photonic crystal. Advanced technology case

Another way to improve the STPV module performance lies in the emitter improvement: changing its emission spectrum to higher selectivity. The tungsten emitter radiation spectrum can be improved, for example, by microstructuring its surface. The improved emission area can be adjusted with the PV cell photoresponse by changing the period of the grids; thus, a significant (up to 32%) increase of the STPV module efficiency is observed in this case with the modules based on GaSb single-junction PV cells (Fig. 9.12). At the same time the use of PV cells with the band gaps not matched with the emission spectrum results in the efficiency decrease.

9.4 Developed GaSb Cells and STPV Modules

9.4.1 GaSb Cell Technology

At first, GaSb cells were developed as bottom cells for concentrator mechanically stacked GaAs/GaSb tandems. Recently, the study of GaSb TPV devices has been considerably intensified [49–53] for the application in fuel and solar-powered TPV systems.

The surface recombination rate for GaSb is lower than that for p-type GaAs. For this reason GaSb TPV cells with a high quantum yield were fabricated using the simple Zn-diffusion method without a lattice-matched AlGaAsSb window layer. A pseudo-closed-box diffusion technique was used. Mixtures of zinc and antimony, zinc and gallium, or zinc-gallium-antimony were used as the diffusion sources.

It was found from the SIMS data that, near the surface, the Zn concentration of $10^{20}\,\mathrm{cm}^{-3}$ is independent of the diffusion temperature at the selected

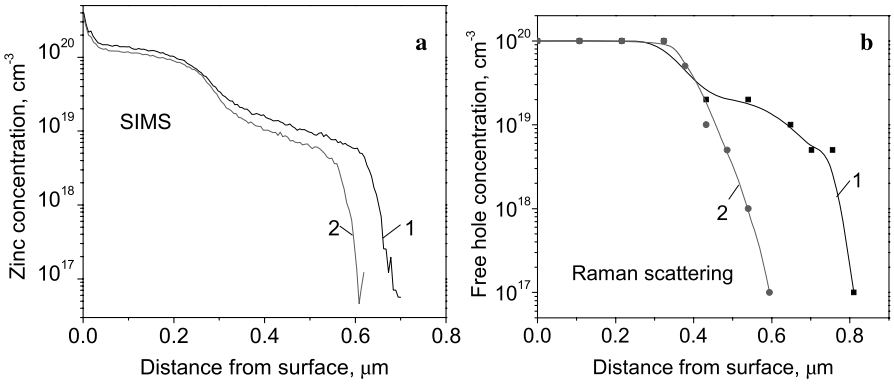

Fig. 9.13. Zinc (**a**) and free hole concentration (**b**) profiles of Zn-diffused GaSb structures, obtained by the SIMS (**a**) and Raman spectroscopy combined with precise anodic oxidation (**b**). Diffusion time is 50 min at 520 °C

zinc-antimony source, and that a sharp Zn concentration gradient takes place in these structures (Fig. 9.13a). The free-carrier (holes) distributions were recorded by the Raman scattering spectroscopy accompanied by a precise anodic oxidation of the structure (Fig. 9.13b) [54]. The comparison of SIMS and Raman profiles shows an admissible concentration correspondence of free carriers and Zn atoms. This fact indicates that almost all diffused Zn atoms are electrically active. The presence of Sb decreases the speed of the diffusion process and assists in obtaining a more planar profile of the dopant. This feature is observed also for Zn diffusion into GaAs and GaP [55, 56].

The concept developed at Fraunhofer ISE [50] for GaSb TPV cells is in the use of strong built-in electric fields (up to 8 kV/cm) in the p-type emitter formed due to a specific steep Zn diffusion profile regulated through the process of Zn diffusion parameters and precise etching. This leads to an improvement in the device performance. Formation of strong built-in electrical fields ensures a decrease in the surface carrier recombination influence, which results in an increase of the generated current and voltage in the TPV cells. The PV cells with an internal quantum yield exceeding 90% and an open-circuit voltage larger than 0.5 V at current densities higher than 3 A/cm^2 were fabricated [50] using this approach.

The MOCVD-grown AlGaAsSb/GaSb heterostructures with an AlGaAsSb (0.72 – 0.9 eV) window layer were fabricated at FhG-ISE as well [51]. It was found that the p-GaSb/n-AlGaAsSb heterostructure ensures quantum efficiency of photoresponse as in corresponding homojunction devices, whereas the open-circuit voltage increases by approximately 20 mV due to a reduced dark current in the device.

A two-stage diffusion process, as well as the epitaxial (LPE) GaSb cells, has been developed at the Ioffe Institute [52, 53]. At the first stage, GaSb wafers were exposed to Zn to form a shallow p-n junction in the photoactive area of a cell. During the second stage, a deep p-n junction (1 – 1.5 μm) was formed by an additional spatially selective diffusion process (Fig. 9.14) to reduce the current leakages under contact grid fingers. Then, anodic oxidation and selective etching were employed for precise thinning (to 0.2 – 0.3 μm) of the photoactive diffused *p*-GaSb layer. The maximum photocurrent was obtained in the cells with p-region thickness within the range of 0.15 – 0.3 μm [57]. The optimal p-n junction depth of about 0.25 μm ensuring the increase in the photocurrent density up to 30 mA/cm^2 under the sunlight with the AMO spectrum cut-off at $\lambda < 900$ nm was determined.

In attempts to prepare the material of high crystal quality, the epitaxial (LPE) GaSb cells were fabricated using epitaxial structures on GaSb substrates. The LPE growth of Te-doped GaSb layers was carried out at temperature of 450 – 350 °C [57].

Photoluminescence spectra were measured at 77 K on the epilayers grown from Ga-, Sb- and Pb-rich melts, as well as a 'bulk' substrate (Fig. 9.15). It can be seen that the highest photoluminescence peak with a band-to-band

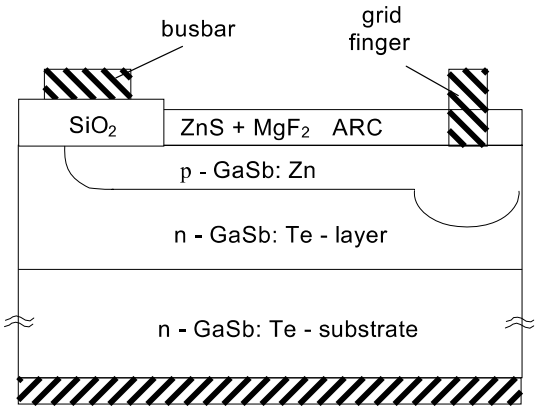

Fig. 9.14. Cross section of an epitaxial GaSb TPV cell fabricated by the two-stage Zn diffusion method

transition at $\sim 1.55\,\mu$m takes place in the case of the epilayers grown from Ga-rich melts.

The maximum spectral response is observed on cells prepared with the epilayer grown from Ga-rich melt (curve 1 in Fig. 9.16). It appeared to be better than that of the cells prepared from the bulk substrate (curve 2), whereas the two other epilayers (curves 3 and 4) show even worse performance than the bulk.

In solar photovoltaics, the methods for solar cell testing are quite well developed, which allows a precise comparison of different cells and modules to be made. Using solar simulators (or tabulated AMO or AM1.5 spectra) for the comparison of TPV cell efficiencies may give incorrect results because much higher short wavelength (visible) radiation takes place compared with the radiation from the emitters used in TPV generators. This approach may be partly applied if solar spectra are cut-off, for example, at $\lambda < 900\,$nm. Another approach is the use of black-body radiators (or tabulated BB spectra). A precise spectral response and I-V curves measured at different illumination

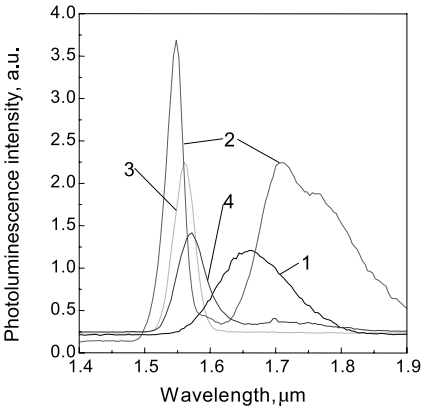

Fig. 9.15. Photoluminescence spectra (77 K) of 'bulk' GaSb wafer (1) and LPE layers grown from Ga-(2), Pb-(3) and Sb-(4) rich melts

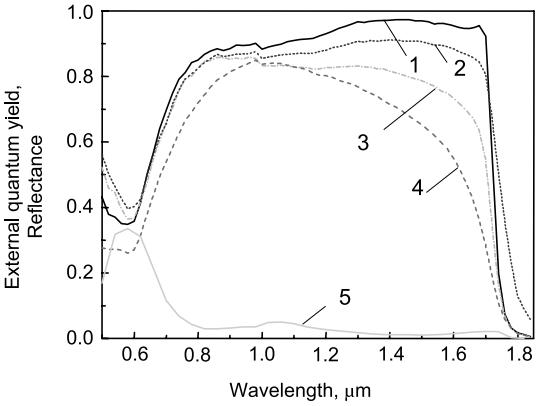

Fig. 9.16. Spectral responses of TPV cells based on *1* epilayer grown from Ga-rich melts, *2* 'bulk' substrates, *3* epilayer grown from Pb-rich melts, *4* epilayer grown from Sb-rich melts and *5* the reflectance of GaSb cell with ZnS+MgF2 antireflection coating

intensities corresponding to conditions in TPV systems allow to calculate the efficiency for any emitter with measured spectrum including the tabulated black-body spectra. Here, both these approaches are applied to compare the performance of TPV cells.

Cells of 1 and 2 cm^2 in area were developed for TPV generators. These cells were capable of generating the photocurrent up to 2 – 10 A in CW-operation with an I-V curve fill factor value of about 0.7. V_{oc}, and FF in the 1-cm^2 cells at $I_{sc} = 1$ A had the following ranges: $V_{oc} = 0.42 - 0.45$ V and $FF = 0.70 - 0.72$. The cells of 2 cm^2 in area generate photocurrents up to 9 A at $V_{oc} = 0.52$ V. Efficiencies of about 11% under the AM0 spectrum and 19% under a part ($\lambda > 900$ nm) of the AM0 spectrum at a photocurrent density of 2 – 7 A/cm^2 were achieved in these TPV cells.

The calculated efficiency exceeded 25% in the developed GaSb TPV cells assuming a black-body emitter temperature of 1400 – 1600 K and the radiation spectrum cut-off at $\lambda > 1820$ nm (Fig. 9.17).

Efficiency measurements under selective radiation have been carried out in the GaSb TPV converters in the wavelength region of 1300 – 1680 nm. These results could help to estimate the achievable efficiencies in practical

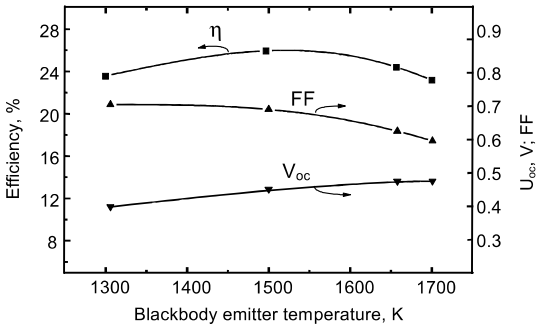

Fig. 9.17. GaSb TPV cell efficiency (η), fill factor (FF) and open circuit voltage (Voc) as a function of black-body emitter temperature. Efficiencies were calculated for radiation spectra cut-off at $\lambda > 1820$ nm

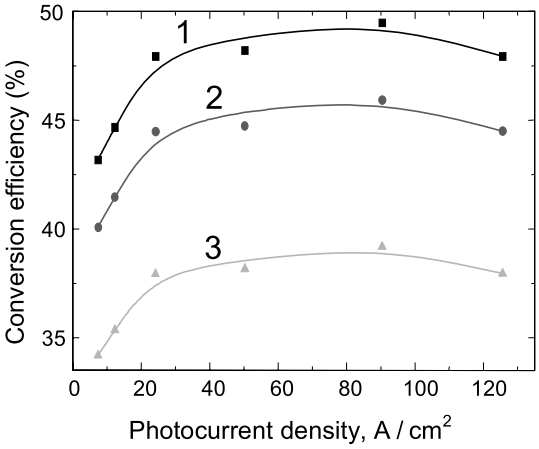

Fig. 9.18. Conversion efficiencies of the 'epitaxial' GaSb PV converter as a function of the photocurrent density at selective irradiation with wavelengths of 1 – 1680, 2 – 1550 and 3 – 1315 nm

GaSb converters with back-surface mirrors, ensuring the effective reflection and recirculation of sub-bandgap photons or conversion of radiation from selective emitters.

Efficiencies of 43 – 49% were achieved in the 'epitaxial' GaSb cells under selective irradiation with the wavelength of 1680 nm at photocurrent densities higher than 7 A/cm^2 (Fig. 9.18, curve 1).

Efficiency decrease to 40 – 45% at $\lambda = 1550$ nm (Fig. 9.18, curve 2) and to 35 – 39% at $\lambda = 1315$ nm (Fig. 9.18, curve 3) took place in the GaSb cells. The reason for efficiency decrease is a reduction of photoresponse from 1.18 A/W at $\lambda = 1680$ nm to 1.1 A/W at $\lambda = 1550$ nm and to 0.95 A/W at $\lambda = 1315$.

9.4.2 Solar TPV Modules Based on GaSb Cells

Two types of TPV systems shown in Fig. 9.19 have been developed and tested at the Ioffe Institute with both, outdoors with the Fresnel lens setup, shown in Fig. 9.2, and with a solar simulator [23], consisting of a high-power (5 – 10 kW) Xe lamp and an ellipsoidal reflector. The tungsten or tantalum emitter is placed in a quartz chamber filled with a rare gas (Ar or Xe) to prevent it from oxidation. The chamber may be sealed (Fig. 9.20a).

In the cylindrical system the PV cells surround the emitter, being mounted on the inner side of a cooled cylindrical base (Fig. 9.19a), while in the conical one (Fig. 9.19b,c) the thermal radiation is reflected to PV cells by an Au-coated cone-shaped mirror, and PV cells are mounted on a flat basement. The construction of the conical system allows the use of a flat emitter (Fig. 9.20b), which is preferable for the pilot studies of the new material application. At the same time, the cylindrical system is preferable for several advantages: it may consist of several stacked modules, the cooling of PV cells is easier, and it is more suitable for use in hybrid solar/fuel-fired systems.

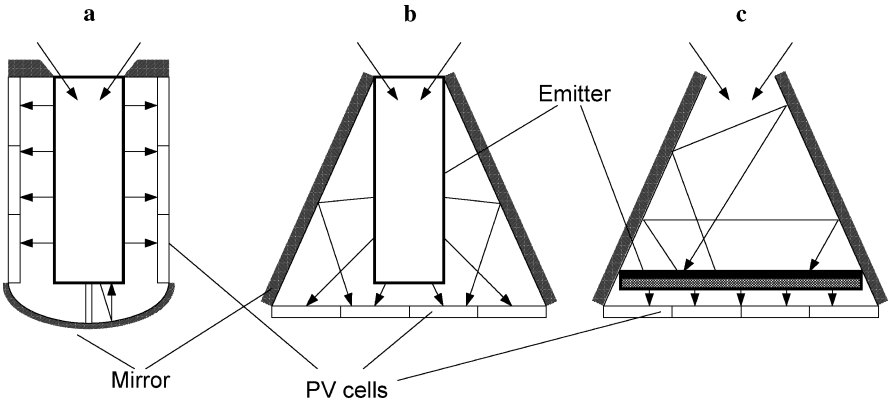

Fig. 9.19. The developed cylindrical (**a**) and conical (**b,c**) STPV modules

Fig. 9.20. a Part of a cylindrical TPV module with a tantalum emitter situated in an Ar-filled bulb under illumination from solar simulator. **b** Conical module with a SiC flat emitter installed and heated with the solar simulator

Figure 9.21 (curve 1, left scale) presents a dependence of a tantalum emitter temperature on different emitter sizes. All emitters presented were made with the same aperture of ⌀12 mm (95% of concentrated energy is collected) and varied in the cylinder length. The emitter temperature was recalibrated to ensure the equal direct sun intensity of 800 W/m^2 for better comparison. It is seen that the emitter temperature rises with decreasing the emitter size.

Theoretical calculations of the emitter temperature are shown in Fig. 9.21. It is noteworthy that this temperature estimation implied high ($> 30\%$) convectional losses to be included. It can be seen that longer emitters show the temperature to be even lower than expected. This is explained by growing convectional losses that accompany the emitter surface increase, which was

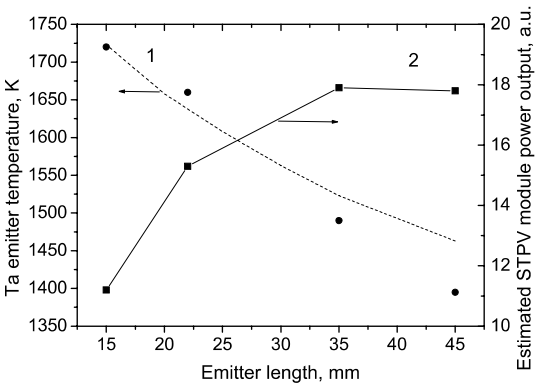

Fig. 9.21. Measured tantalum emitter temperature (the sunlight is concentrated by a 0.36-m^2 Fresnel lens set up with 800 W/m^2 solar radiation intensity) as a function of emitter length (*circles*). *Dotted line:* calculated emitter temperature (*curve 1*, left scale), and the estimated STPV module power output (*curve 2*, right scale) plotted for different emitter lengths

not taken into account. These losses can be significantly decreased by inserting the emitter in a thermos-like double-wall bulb. On the right scale of Fig. 9.21 (curve 2) the dependence of estimated power output of the GaSb cells is shown. The estimation is based on the I-V measurements of GaSb test cells. It is seen that the total estimated power output of the system has a maximum for emitters of 35 – 45 mm in length. This corresponds to the emitter efficiencies of 0.8 – 0.85, expected in calculations presented above.

The TPV cells are characterized by a low voltage (normally < 0.5 V); therefore, a series connection of the cells is very important. The operating conditions of the PV cells in an STPV system (high current densities up to 10 A/cm^2 and more, convectional heat from the emitter) require an efficient water cooling of the cells, which means that they must be electrically insulated from the heat sink [58, 59]. For the fabrication of photoreceivers, BeO ceramics is used to ensure the series connection of the cells. It has electrical resistivity of more than $10^{14}\,\Omega$/cm with the best thermal conductivity of 250 W/K·m. The thermal expansion coefficient of BeO ceramics is $6 \times 10^{-6}\,K^{-1}$, close to that of GaSb in the temperature range of 20 – 150 °C. Mo/Ni/Au contact composition to the BeO substrate allows a solution to the problem of adhesion of GaSb cells to ceramics.

The cell efficiency of 19% under illumination by a tungsten emitter heated up to 1900 – 2000 K has been derived from experimentally measured PV parameters (Fig. 9.22). This value is close to the theoretical maximum of $\sim 22\%$ for GaSb cells illuminated by a tungsten emitter. The PV conversion efficiency of 27% was estimated for the spectrum cut-off at 1820 nm. In the conical module the photocurrent density $J_{SC} = 5\,A/cm^2$, open-circuit voltage $V_{OC} = 0.49$ V and fill factor $\mathtt{FF} = 0.68$ were measured in a GaSb cell

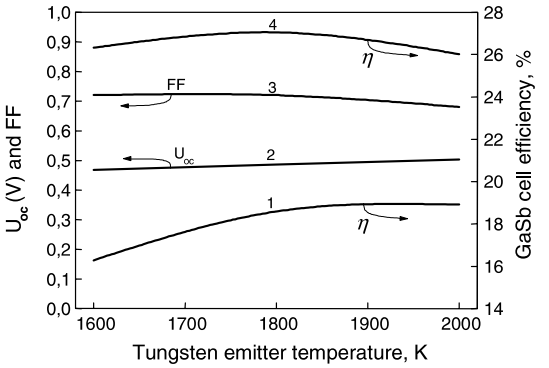

Fig. 9.22. Open-circuit voltage (V_{oc}, *curve 2*), fill factor (FF, *curve 3*) and efficiency (*curves 1, 4*) of GaSb TPV cell as a function of tungsten emitter temperature. Efficiency was estimated under the following radiation conditions: under the full radiation spectra: (*curve 1*); and under spectra cut-off at $\lambda > 1820$ nm (*curve 4*)

under the solar-powered emitter heated to a temperature of about 2000 K. In the cylindrical module, current densities of $\sim 2\,\mathrm{A/cm^2}$ have been registered with the same tungsten emitter. Lower values of current density in the cylindrical module are compensated by a larger number of cells.

9.5 Conclusion

The current status of a solar TPV system is presented in this chapter. The developed solar concentrators based on a Fresnel lens do not show the maximum performance possible (parabolic mirror would give higher concentration ratios and efficiency); however, it has a great advantage of low price, still enabling to reach high concentrations. The developed conical module allows the use of flat emitters, which is preferable for the pilot studies of the new material application. At the same time, a cylindrical system is preferable for the final system production due to the following advantages: it may consist of several stacked modules; the cooling of PV cells is easier; and it is more suitable for use in hybrid solar/fuel-fired systems.

Continuous progress is leading to the improvement of gallium-antimonide PV cells. Highly productive diffusion technologies of high-efficiency GaSb-based TPV cells have been developed by several teams. High conversion efficiency (up to 49%) of selective radiation by such cells has been demonstrated. Efficiencies exceeding 25% for in-band ($\lambda < 1800$ nm) black-body (1200 – 1700 K) radiation have been achieved as well. Efficiency of 19% has been measured in the developed GaSb cells in the STPV modules under the illumination by a tungsten emitter heated up to 1900 – 2000 K.

The developed GaSb PV cells are most relevant for use in STPV systems. As is shown, the achievable efficiency for a module based on a tungsten-selective emitter and GaSb TPV cells is 23 – 25%.

Acknowledgement. The authors thank the colleagues at Photovoltaics Laboratory of the Ioffe Institute: V.D. Rumyantsev; V.A. Grilikhes; V.R. Larionov; P.Y. Gazaryan; N.S. Potapovich; S.V. Sorokina; M.Z. Shvarts; N.Kh. Timoshina; and N.A. Sadchikov. The European Commission supported this work through the funding of the project Fullspectrum (SES6-CT-2003-502620).

References

1. Broman L (1995) Thermophotovoltaic bibliography. Prog Photovoltaics 3: 65–74
2. Woolf LD (1985) Optimum efficiency of single and multiple band gap cells in TPV energy conversion. In: 18th IEEE Photovoltaic specialist conference, pp 1731–1732
3. Wanlass MW, Ward JS, Emery KA, Coutts TJ (1994) $Ga_xIn_{1-x}As$ thermophotovoltaic converters. In: FirstWold conference on photovoltaic energy conversion, Hawaii, pp 1685–1691
4. Gray JL, El-Husseini A (1995) A simple parametric study of TPV system efficiency and output power density including a comparison of several TPV materials. In: Second NREL Conference on TPV generation of electricity, v 358, pp 3–15
5. Iles PA, Chu C, Linder E (1995) The influence of bandgap on TPV converter efficiency. In: Second NREL Conference on TPV generation of electricity v 358, pp 446–457
6. Coutts TJ, Wanlass MW, Ward JS, Johnson S (1996) A review of recent advances in thermophotovoltaics. In: 25th IEEE Photovoltaic specialist conference, Washington DC, pp 25–30
7. Coutts TJ (1999) A review of progress in thermophotovoltaic generation of electricity. Renewable Sustainable Energy Rev 3:77–184
8. Coutts TJ (1999) An overview of thermophotovoltaic generation of electricity. In: Technical Digest of the International Photovoltaic Solar Energy Conference, Sapporo, pp 137–140
9. Andreev VM, Khvostikov VP, Larionov VR, Rumyantsev VD, Sorokina SV, Shvarts MZ, Vasil'ev VI, Vlasov AS (1997) Tandem GaSb/InGaAsSb thermophotovoltaic cells. In: 26th IEEE Photovoltaic specialist conference, Anaheim, pp 935–938
10. Spirkl W, Ries H (1985) Solar thermophotovoltaics: an assessment. J Appl Phys 57:4409–4414
11. Davies PA, Luque A (1994) Solar thermophotovoltaics: brief review and a new look. Solar Energy Mater Solar Cells 33:11–22
12. Luque A, Marti A (1999) Limiting efficiency of coupled thermal and photovoltaic converters. Solar Energy Mater Solar Cells 58:147–165
13. Edenburn MW (1980) Analytical evaluation of a solar thermophotovoltaic (TPV) converter. Solar Energy 24:367–371

14. Harder N-P, Würfel P (2003) Theoretical limits of thermophotovoltaic solar energy conversion. Semicond Sci Technol 18:S151–S157
15. Cody GD (1998) Theoretical maximum efficiencies for thermophotovoltaic devices. In: Fourth NREL conference on TPV generation of electricity, v 460, pp 58–67
16. Badescu V (2001) Thermodynamic theory of thermophotovoltaic solar energy conversion. J Appl Phys 90:6476–6486
17. Badescu V (2005) Upper bounds for solar thermophotovoltaic efficiency. Renewable Energy 30:211–225
18. Andreev VM (2004) Solar cells for TPV converters. In: Next generation photovoltaics. High efficiency through full spectrum utilization. IoP, Ch. 11: 246
19. Yugami H, Sai H, Nakamuro K, Nakagama N, Ohtsuko H (2000) Solar thermophotovoltaic using $Al_2O_3/Er_3Al_5O_{12}$ eutectic composite selective emitter. In: 28th IEEE photovoltaic specialist conference, Anchorage, pp 1214–1217
20. Horne E (2002), Hybrid thermophotovoltaic power systems. Final report by EDTEK Inc. for the California energy comission
21. Stone KW, Fatemi NS, Garverick L (1996) Operation and component testing of a solar thermophotovoltaic power system. In: 25th IEEE photovoltaic specialist conference, pp 1421–1424
22. Khvostikov VP, Rumyantsev VD, Khvostikova OA, Shvarts MZ, Gazaryan PY, Sorokina SV (2004) Thermophotovoltaic cells based on low-bandgap compounds In: Sixth Conference on TPV Generation of Electricity, Freiburg, pp 436–444
23. Andreev VM, Khvostikov VP, Rumyantsev VD, Khvostikova OA, Gazaryan PY, Sadchikkov NA, Sorokina SV, Zadiranov YM, Shvarts MZ (2005) Thermophotovoltaic converters with solar powered high temperature emitters. In: 20th European Photovoltaic Solar Energy Conference, Barcelona, pp 8–13
24. Holland D (2003) Commercialisation of concentrator systems. In: International solar concentrator conference for the generation of electricity or hydrogen, Alice Springs
25. Garboushian V (2003) Roadmap for commercialization of multijunction solar cells for high concentrator solar systems. In: International solar concentrator conference for the generation of electricity or hydrogen, Alice Springs
26. Andreev VM, Rumyantsev VD, Bett AW (2000) Progress in development of all-glass terrestrial concentrator modules based on composite Fresnel lenses and III-V solar cells. In: 28th IEEE photovoltaic specialist conference, Alaska, pp 1169–1172
27. Rumyantsev VD, Chalov AE, Ionova EA, Larionov VR, Andreev VM (2004) Concentrator PV modules with multi-junction cells and primary/secondary refractive optical elements. In: 19th European photovoltaic solar energy conference, Paris, pp 2090–2094
28. Touloukian YS (1970) Thermophysical properties of matter. IFI/Plenum, New York
29. Abbott P, Bett AW (2004) Cell-mounted spectral filters for thermophotovoltaic applications. In: Sixth Conference on TPV Generation of Electricity, pp 96–104
30. Lindberg E, Broman L (2003) Fabergé optics and edge filter for a wood powder fuelled thermophotovoltaic system. Renewable Energy 28:373–384
31. Höfler H, Paul HJ, Ruppel W, Würfel P (1983) Interference filters for thermophotovoltaic solar energy conversion. Solar Cells 10:273–286

32. Joannopoulos JD, Meade RD, Winn JN (1995) Photonic crystals: molding the flow of light. Princeton University Press, Princeton
33. Koops HWP, Hoinkis OE, Honsberg MEW, Schmidt R, Blum R, Böttger G, Kuligk A, Liguda C, Eich M (2001) Two-dimensional photonic crystals produced by additive nanolithography with electron beam-induced deposition act as filters in the infrared. Microelectr Eng 57-58: 995–1001
34. Mauk MG, Shellenbarger ZA, Cox JA, Sulima OV, Bett AW, Mueller RL, Sims PE, McNeely JB, DiNetta LC (2000) Liquid-phase epitaxy of low-bandgap III-V antimonides for thermophotovoltaic devices. J Crystal Growth 211:189–193
35. Bitnar B (2003) Silicon, germanium and silicon/germanium photocells for thermophotovoltaics applications. Semicond Sci Technol 18:S221–S227
36. Abbott P, Rohr C, Connolly JP, Ballard I, Barnham KWJ, Ginige R, Clarke G, Nasi L, Mazzer M (2001) Characterisation of strain-compensated InGaAs/InGaAs quantum well cells for TPV applications. AIP Conf Proc 653:213–221
37. Wilt DM, Wehrer R, Palmisiano M, Wanlass M, Murray Ch (2003) Monolithic interconnected modules (MIMs) for thermophotovoltaic energy conversion. Semicond Sci Technol 18:S209–S215
38. Karlina LB, Vlasov AS, Kulagina MM, Timoshina NH (2006) $In_{0.53}Ga_{0.47}As$/InP thermophotovoltaic cells. Semiconductors 40:346–350
39. Gombert A (2003) An overview of TPV emitter technologies. AIP Conf Proc 653:123–131
40. Diso D, Licciulli A, Torsello G, Tundo S, Mazzer M, Lomascolo M (2004) Study and optimization of ceramic coatings for thermophotovoltaic applications. In: Sixth Conference on TPV Generation of Electricity, Freiburg, pp 237–243
41. Hampe C, Metz A, Hezel R (2001) Innovative silicon-concentrator solar cell for thermophotovoltaic application. In: 17th European Photovoltaic Solar Energy Conference, Munich, pp 18–23
42. Bitnar B, Durisch W, Palfinger G, von Roth F, Vogt U, Bronstrup A, Seiler D (2004) Practical thermophotovoltaic generators. Semiconductors 38:941–945
43. Malyshev VI (1979) Introduction to experimental spectroscopy (in Russian). Nauka, Moscow
44. Rusin SP, Peletsky VE (1987) Thermal irradiation of cavities (in Russian). Energoatomizdat, Moscow
45. Bedford RE, Ma CK, Chu Z, Sun Y, Chen S (1985) Emissivities of diffuse cavities. iv: isothermal and nonisothermal cylindro-inner-cones. Appl Optics 24:2971–2980
46. Bedford RE, Ma CK (1975) Emissitivies of diffuse cavities, ii: isothermal and nonisothermal cylindro-cones. J Opt Soc Am 65:565–572
47. Bedford RE, Ma CK (1975) Emissitivies of diffuse cavities, ii: isothermal and nonisothermal cones and cylinders. J Opt Soc Am 64:339–349
48. Lin SY, Moreno J, Fleming JG (2003) Three-dimensional photonic-crystal emitter for thermal photovoltaic power generation. Appl Phys Lett 83:380–382
49. Fraas L, Samaras J, Huang H-X, Seal M, West E (1999) Development status on a TPV cylinder for combined heat and electric power for the home. In: Fourth NREL Conference on TPV Generation of Electricity, pp 371–383
50. Stollwerck G, Sulima OV, Bett AW (2000) Large-area GaSb photovoltaic cells. IEEE Trans Electron Devices 47:448–457
51. Bett AW, Sulima OV (2003) GaSb cells for for applications in TPV generators. Semicond Sci Technol: Special issue on thermophotovoltaics 18:S184–S190

52. Rumyantsev VD, Khvostikov VP, Sorokina SV, Vasil'ev VI, Andreev VM (1999) Portable TPV generator based on metallic emitter and 1.5-Amp GaSb cells. In: Fourth NREL Conference on TPV Generation of Electricity 460:384–391
53. Andreev VM, Khvostikov VP, Rumyantsev VD, Sorokina SV, Shvarts MZ (2000) Single-junction GaSb and tandem GaSb/InGaAsSb & AlGaAsSb/GaSb thermophotovoltaic cells. In: 28th IEEE Photovoltaic Specialist Conference, Anchorage, pp 1265–1268
54. Andreev VM, Cherotchenko MV, Karlina LB, Mintairov AM, Khvostikov VP, Sorokina SV (1995) Laser Raman scattering characterization of A^3B^5 compounds and photovoltaic structures. In: First Int Symp on Semiconductor Processing and Characterization with Lasers: applications in photovoltaics, Stuttgart, pp 343–348
55. Nigren SF, Pearson GL (1969) Zn diffusion into gallium phosphide under high and low phosphorus overpressure. J Electrochem Soc 116:648–654
56. Casey HC, Panish MB (1978) Heterostructure lasers. Academic Press, New York
57. Shvarts MZ, Andreev VM, Khvostikov VP, Larionov VR, Rumyantsev VD, Sorokina SV, Vasil'ev VI, Vlasov AS, Chosta OI (1998) GaSb/InGaAsSb tandem thermophotovoltaic cells for space applications. In: Fifth European Space Power Conference, Tarragona, pp 527–532
58. Doyle EF, Becker FE, Shukla KC, Fraas LM (1999) Design of a thermophotovoltaic battery substitute. In: AIP Conference Proceedings 460:351–361
59. Schlegl T, Dimroth F, Ohm A, Bett AW (2004) TPV modules based on GaSb substrates. In: Sixth Conference on TPV Generation of Electricity, Freiburg, pp 285–293

10 Multijunction Concentrator Solar Cells: An Enabler for Low-Cost Photovoltaic Systems

N.H. Karam, R.A. Sherif, and R.R. King

10.1 Introduction

Over the past decade, multijunction (MJ) solar cell technology for terrestrial concentrator applications has experienced a rapid surge in demonstrated efficiency [1–5], as illustrated in Fig. 10.1. Multijunction cells have reached the point at which the next set of technology improvements are likely to push efficiencies over 42%. Spectrolab's roadmap for terrestrial concentrator solar cell technologies with ever-increasing cell efficiency is shown in Fig. 10.2. Very high solar cell efficiencies are crucial to the cost-effective commercialization of concentrator and flat-plate photovoltaic systems alike [6–9], because of the highly leveraging effect that efficiency has on module packaging and balance-of-system costs. In this chapter, we discuss the semiconductor device research paths being investigated with the aim of reaching > 40% efficiency,

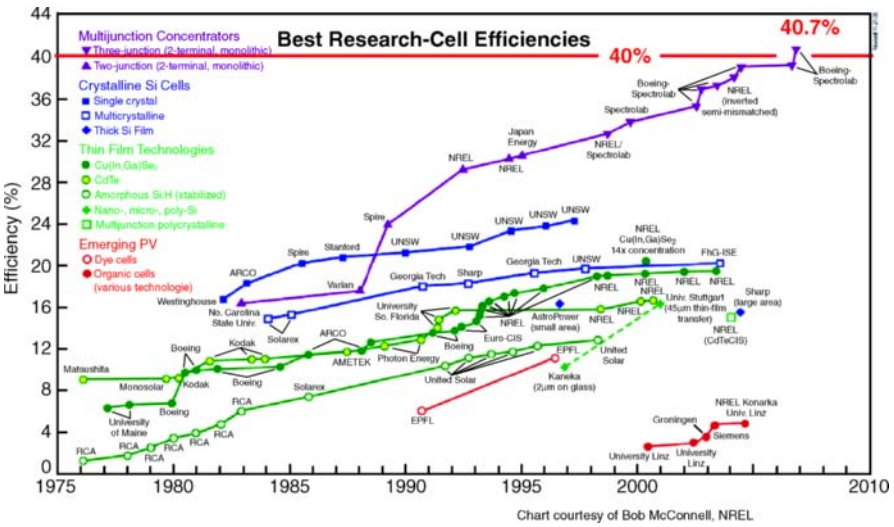

Fig. 10.1. Record solar cell efficiencies for multijunction concentrator cells and other photovoltaic technologies since 1975, as compiled by the National Renewable Energy Laboratory (NREL). (Courtesy of R. McConnell, NREL)

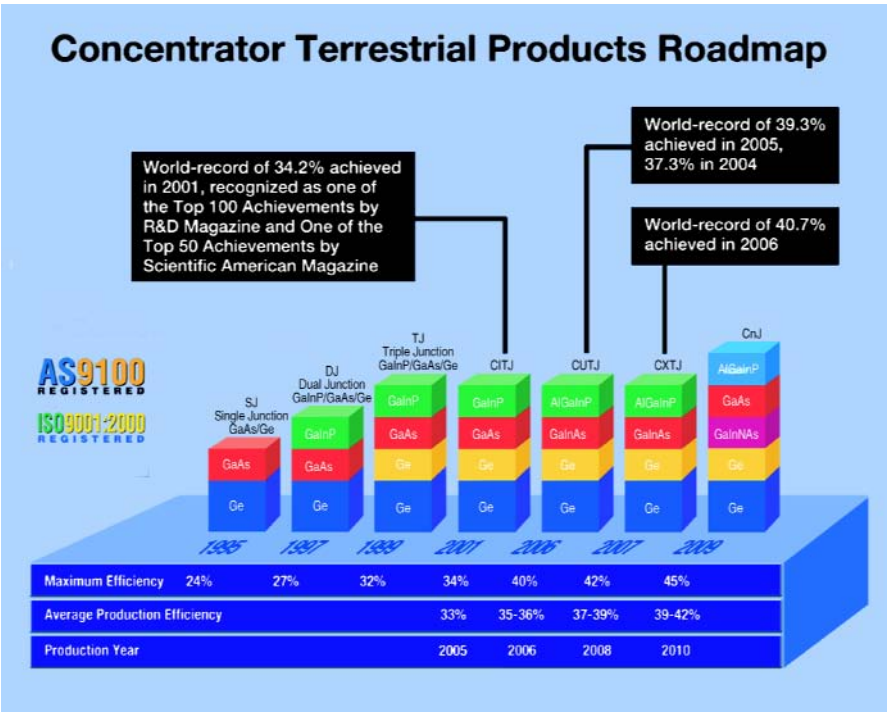

Fig. 10.2. Spectrolab terrestrial concentrator solar cell technology road map

and packaging, systems and economic considerations for cost-effective concentrator photovoltaics.

10.2 Multijunction Cell Design

A central theme for high-efficiency solar cell research is to modify the partition of the solar spectrum afforded by the subcell band gaps in MJ cells so that it is more advantageous for efficient energy conversion. To this end, lattice-mismatched, or metamorphic, subcell materials, unconventional alloys such as GaInNAs, and cell structures with more than three junctions are being investigated with the goal of exceeding 40% solar cell efficiencies.

10.2.1 Multijunction Cell Architectures

The division of the solar spectrum by the 1.8/1.4/0.67 eV combination of band gaps in a lattice-matched (LM) GaInP/GaInAs/Ge triple-junction cell leads to excess photogenerated current density in the Ge subcell. Part of this wasted current can be used effectively in the middle cell if its band gap is

lowered, as in lattice-mismatched, or metamorphic (MM) GaInP/GaInAs/Ge triple-junction cells with a 1.2- to 1.3-eV GaInAs middle cell [1, 10–16]. The challenge then becomes to maintain low Shockley-Read-Hall (SRH) recombination due to defects in these mismatched materials.

Higher lattice mismatches give still greater advantages if the crystal quality can be maintained. Studies of highly lattice-mismatched single-junction GaInAs cells were conducted with indium compositions ranging from 0 to 35% indium content in 0.95-eV $Ga_{0.65}In_{0.35}As$ cells with 2.4% lattice mismatch to the Ge substrate [1]. Minority-carrier properties of these mismatched GaInAs materials and GaInP at the same lattice constant were explored. At a band gap of 1.1eV, GaInAs cells with 1.6% lattice mismatch have nearly the same open-circuit voltage as record-efficiency silicon solar cells at the same band gap, indicating the degree to which defects have been suppressed by optimization of the step-graded buffers in these metamorphic devices. The dislocation density in these $Ga_{0.77}In_{0.23}As$ materials is $3-4\times10^6\,cm^{-2}$, as measured by plan-view TEM and cathodoluminescence [1]. The TEM imaging over a large sample area indicates a dislocation density of only $2\times10^6\,cm^{-2}$ for $Ga_{0.65}In_{0.35}As$ with $\sim$ 0.95-eV band gap, consistent with the observation that the minority-carrier lifetime measured by time-resolved photoluminescence (TRPL) is about 10ns for both the 1.1- and 0.95-eV materials [1]. These

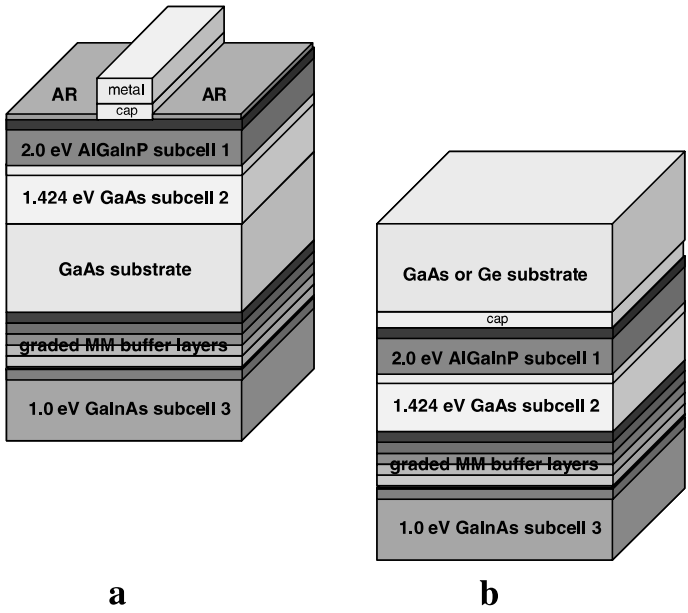

Fig. 10.3. Two configurations of triple-junction solar cells with a highly lattice-mismatched, inverted 1-eV GaInAs bottom subcell. **a** Growth on two sides of a transparent GaAs substrate. **b** Growth on the back of a GaAs or Ge substrate that is removed during cell fabrication

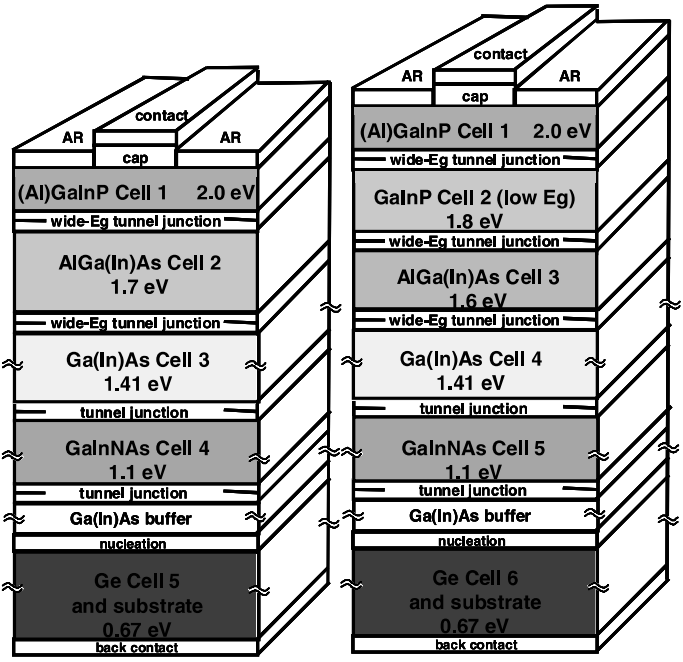

Fig. 10.4. Cross sections of five- and six-junction cells

metamorphic materials enable advanced MJ cell designs incorporating a 0.9- to 1.1-eV subcell.

Work in this area has yielded cell results on metamorphic $Ga_{0.44}In_{0.56}P/Ga_{0.92}In_{0.08}As/Ge$ triple-junction cells, with the upper two cells having a lattice constant 0.5% larger than the Ge substrate [1, 9]; $Ga_{0.35}In_{0.65}P/Ga_{0.83}In_{0.17}As$ cells [7]; double- and triple-junction $Ga_{0.29}In_{0.71}P/Ga_{0.77}In_{0.23}As/Ge$ cells [14, 15]; and on GaInP/GaAs/1-eV GaInAs triple-junction cells with the upper two subcells lattice matched to a GaAs substrate [17, 18]. Fig. 10.3 shows schematics of the latter cell design.

Another way to utilize the excess photogenerated current in the Ge subcell in triple-junction cells is to insert a $\sim$ 1-eV semiconductor, such as GaInNAs lattice-matched to Ge, above the Ge subcell. Five- and six-junction cell designs partition the solar spectrum into narrower wavelength ranges than triple-junction cells, allowing all the subcells to be current matched to the low-current-producing GaInNAs subcell. Additionally, the finer division of the incident spectrum reduces thermalization losses from electron-hole pairs photogenerated by photons with energy far above the band-gap energy, and the smaller current density in five- and six-junction cells lowers resistive I^2R losses. Cross-sectional diagrams of five- and six-junction cells are drawn in Fig.10.4

At a given lattice mismatch, higher efficiencies can be reached in many MJ cell designs if the GaInP top-cell band gap is increased since, thereby, less light needs to be leaked through the GaInP to the GaInAs cell beneath, and more can be converted at the higher voltage of the GaInP top cell. The effect of disordering Ga and In atoms on the group-III sublattice is known to increase the band gap by $\sim 100\,\text{meV}$ for the LM case. This effect has been confirmed to persist in lattice-mismatched, In-rich compositions of GaInP as well [12,15]. Use of AlGaInP to raise the top cell band gap also increases the MJ cell efficiency [2,12].

10.2.2 Theoretical Efficiency

The theoretical efficiency of MJ solar cells limited by the fundamental mechanism of radiative recombination was calculated as a function of subcell band gap in three- and six-junction cells, at 25 °C. The current density in each subcell was calculated from the photon flux in each photon energy range of the standard terrestrial AM1.5D, low-AOD spectrum [19] and the open-circuit voltage from the carrier concentration at which radiative recombination is in steady state with this photogenerated current density. The cell efficiency was found by combining the current-voltage characteristics of the subcells in the MJ stack.

The calculated efficiencies for triple-junction cells are plotted in Fig. 10.5. The familiar case of a GaInP/GaInAs/Ge triple-junction solar cell is shown

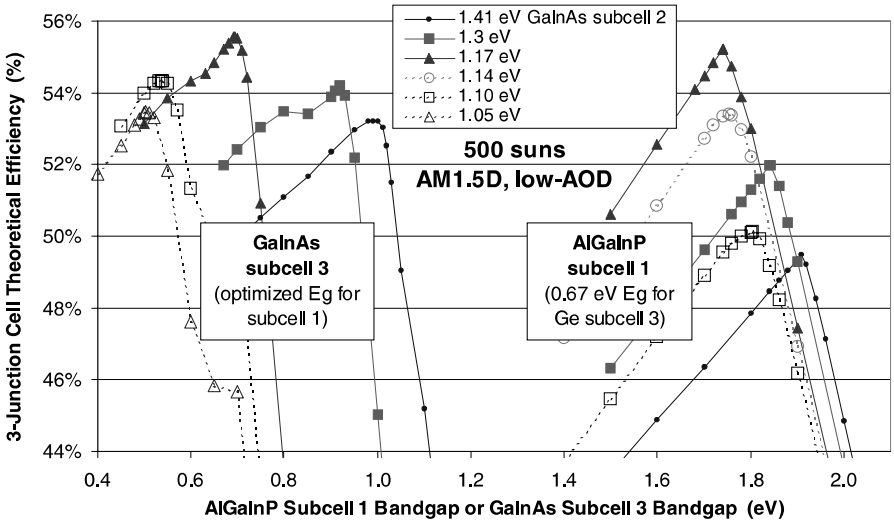

Fig. 10.5. Theoretical efficiency of triple-junction solar cells limited only by radiative recombination, as a function of the band gap of the subcell-1 material (*top*) such as AlGaInP, and the subcell-3 material (*bottom*), such as Ge, GaInNAs or lattice-mismatched GaInAsp

on the right. For the lattice-matched case with a 1.41-eV GaInAs subcell 2, the optimum top-cell band gap is about 1.9 eV. As one goes to lower band gaps for subcell 2, as for MM GaInAs, the optimum top subcell E_g shifts down as well, reaching $\sim$ 1.74 eV at the optimum subcell-2 band gap of 1.17 eV, for a calculated efficiency over 55%.

For a 1.4-eV subcell 2, a higher efficiency can be achieved with a 1.0-eV bottom subcell than for a Ge subcell, as is shown in Fig. 10.5 (left). The theoretical efficiency for this case with a 1.0-eV subcell 3, corresponding to the cell configurations sketched in Fig. 10.3, is $\sim$ 53%. Interestingly, as the middle subcell-2 band gap drops to 1.17 eV, the optimum subcell 3 becomes 0.69 eV, coinciding very closely with the band gap of Ge, with a calculated efficiency of over 55%.

Figure 10.6 plots the theoretical efficiency of six-junction cells under the concentrated terrestrial spectrum, again at 25 °C. The band gaps of subcells 2, 4 and 6 were assumed to be 1.8 eV corresponding to ordered GaInP, 1.41 eV for LM 1%-In GaInAs and 0.67 for the Ge substrate, respectively. Higher efficiencies are possible for full flexibility in band gap. For optimum top-subcell E_g of 2.3 eV and subcell 5 E_g of 1.18 eV, efficiencies over 56% are possible for a lattice-matched configuration using GaInNAs for subcell 5, or for metamorphic configurations using MM 1.18-eV GaInAs in subcell 5. Subcell-1 band gaps of 1.9 or 2.1 eV, which are easier to achieve, still yield theoretical efficiencies of 53.2% and 54.7%, respectively.

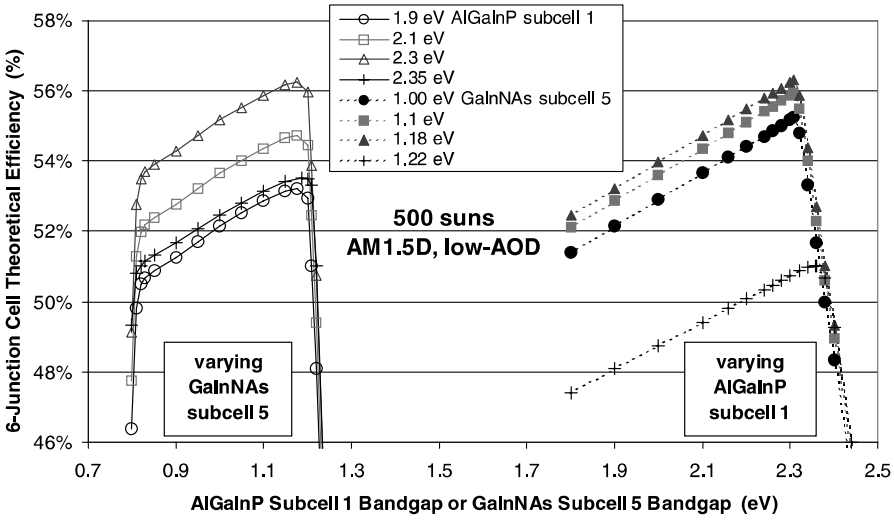

Fig. 10.6. Theoretical efficiency of six-junction solar cells limited only by radiative recombination, as a function of the band gap of the subcell-1 material (*top*) such as AlGaInP, and the subcell-5 material on top of the Ge subcell 6, such as GaInNAs, or lattice-mismatched GaInAs

10.3 Multijunction Concentrator Cells

10.3.1 Metamorphic Semiconductor Materials

A large part of the wide range of semiconductor band gaps needed to span the solar spectrum and realize the high-efficiency cell architectures and band-gap combinations described in the previous section can be reached using metamorphic GaInAs and GaInP materials. The ordering state on the group-III sublattice provides an additional lever for band-gap adjustment, and has a particularly strong effect with regard to GaInP. Figure 10.7 shows measured internal quantum efficiency as a function of photon energy for metamorphic GaInAs solar cells up to a high lattice mismatch of 1.6% to the Ge substrate for 1.1-eV 23%-In GaInAs, and external quantum efficiency for ordered and disordered metamorphic GaInP solar cells. The GaInAs long-wavelength response is nearly ideal up to the band edge of 1.12-eV GaInAs with 1.6% lattice mismatch, indicating long minority-carrier diffusion length in this metamorphic material. Disordered metamorphic GaInP with a lattice mismatch of 0.5%, corresponding to the lattice constant of 8%-In GaInAs, has an absorption edge in spectral response that is similar to that of ordered, lattice-matched GaInP, due to their similar band gaps. The ordered GaInP

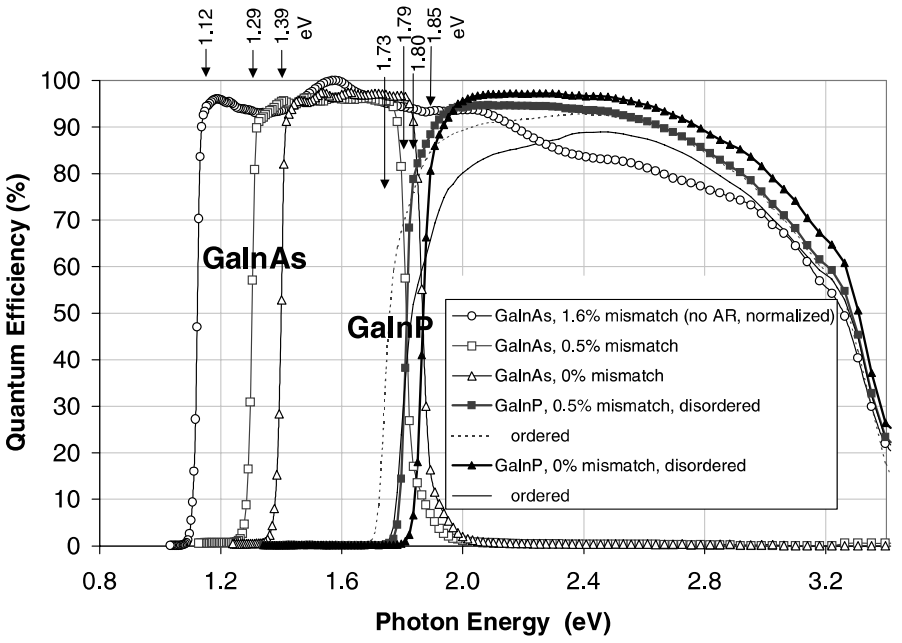

Fig. 10.7. Measured quantum efficiency for metamorphic and lattice-matched GaInAs and GaInP subcells. Both disordered and ordered cases for the group-III sublattice of GaInP are shown

bases were grown thinner in order to achieve the same current density as in the disordered bases, so their softer cut-on near the band edge is due primarily to lower photogeneration in the thin bases, rather than reduced carrier collection.

10.3.2 Triple-Junction Cell Results

Lattice-matched GaInP/GaInAs/Ge triple-junction cells have achieved a new independently confirmed record efficiency solar cell, with 40.1% efficiency [4] at 235 suns under the standard AM1.5D, low-AOD spectrum for terrestrial concentrator cells. Metamorphic GaInP/GaInAs/Ge triple-junction devices, with 8%-In in the middle cell base, at a 0.5% lattice mismatch with respect to the Ge substrate, have achieved 38.8% efficiency at 240 suns [4] under the AM1.5D, low-AOD spectrum, the highest independently confirmed efficiency of any solar cell at 40.7% surpassing the lattice-matched case in spite of the threading dislocations that can result from lattice mismatch. Figure 10.8 shows the measured current-voltage characteristics of the record efficiency lattice-matched and metamorphic concentrator cells under the AM1.5D low-AOD spectrum, as well as of record 32.0% efficiency LM and 31.3% MM 1-sun cells [13] under the AM1.5G spectrum [19] appropriate for flat-plate cells, all independently verified at the National Renewable Energy Laboratory (NREL). Figure 10.9 shows the NREL-measured parameters of the lattice-matched 40.7%-efficient cell.

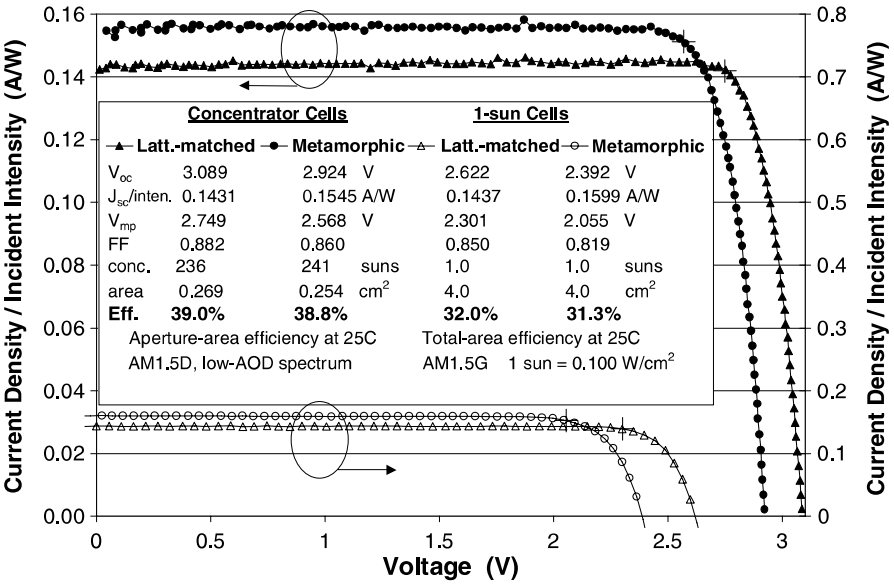

Fig. 10.8. Record efficiency metamorphic and lattice-matched cells, under concentration [4] and at 1 sun [13], independently confirmed at NREL

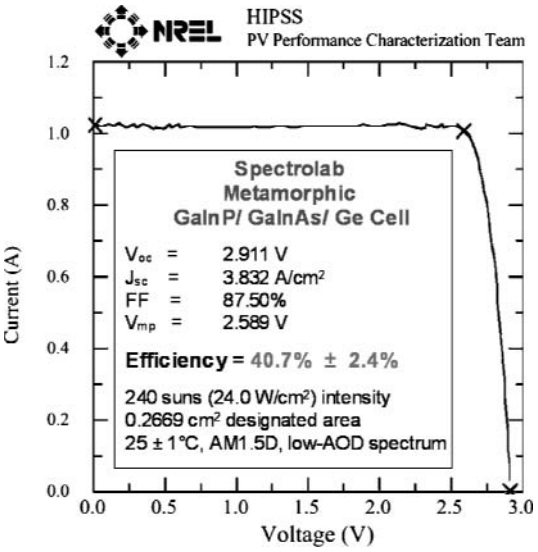

Fig. 10.9. Measurement of I-V characteristic of record 40.7%-efficient cell [4], independently verified at NREL

Even these high-performing cells are still far from the theoretically possible efficiencies discussed previously, allowing ample room to realize $> 40.7\%$ efficiency, or even 45% at concentration.

Since optical systems that concentrate light can only make use of sunlight with a limited angular width, the appropriate spectrum for testing concentrator cells is the direct normal component of sunlight, rather than the global, hemispherical component which includes diffuse sunlight from all parts of the sky. The AM1.5 Direct, low-Aerosol-Optical-Depth (AM1.5D, low-AOD) spectrum is the standard reporting spectrum for terrestrial concentrator solar cell measurements used by NREL [20], e.g. for documentation in the solar cell efficiency tables published periodically in *Progress in Photovoltaics* [21, 22], which tabulate advances in solar conversion efficiencies achieved to date. ASTM International has published a standard based on, and nearly identical to, the AM1.5D, low-AOD solar spectrum, designated the G173-03 standard [23], for the standard direct normal spectrum for concentrator cell testing. The G173-03 standard also includes an updated AM1.5 Global (AM1.5G) spectrum used for testing flat-plate solar cells.

10.4 Concentrator Cell and Receiver Reliability

The road to achieving cost-efficient concentrator modules involves the use of high concentration on MJ solar cells. As the concentration level on the solar cells increases, the relative cost of the MJ cells to the overall system cost drops. The question of how much concentration to put on a solar cell is closely tied to several factors including the cell size, the module optics,

thermal management and tracking accuracy. While the cell relative cost (in terms of cell dollars per watt) drops with higher concentration, the cost of everything else in the system increases with higher concentration. Ultimately, the optimum concentration level is decided by the overall system cost of energy produced over the system's lifetime.

The purpose of this section is to investigate issues related to the cell and receiver reliability, because as is shown, cell reliability cannot be discussed separately from receiver reliability.

10.4.1 Failure Mechanisms

Initial tests of MJ cells under high concentration frequently showed cell shunting after only a few minutes. In a typical concentrator module, several types of cell failures can occur. This section focuses on developing a better understanding of the failure mechanisms associated with concentrator cells under continuous illumination. After all, if a MJ solar cell is unable to sustain continuous operation under high concentration and temperature, the benefits of developing MJ cells with higher conversion efficiencies for the terrestrial markets will not be realized. To this end, we investigated the potential contributors to concentrator cell and assembly failures, as observed in one of the first demonstration projects with MJ cells. Figure 10.10 shows Spectrolab's dense array receiver inside the Concentrating Technologies, LLC, dish system. This particular system focuses 300× on the cells. In this array, there are three cells in parallel that are soldered to a kovar substrate, along with one bypass diode. In this receiver configuration, there are 26 cell assemblies in series, and each assembly is connected to the adjacent assembly by gold wire bonds. The substrates are connected to the heat sink by thermal adhesive.

Shortly after exposure to concentration, the following failure mechanisms were observed: (a) cell shunting; (b) electrical shorts; (c) cell cracking; and

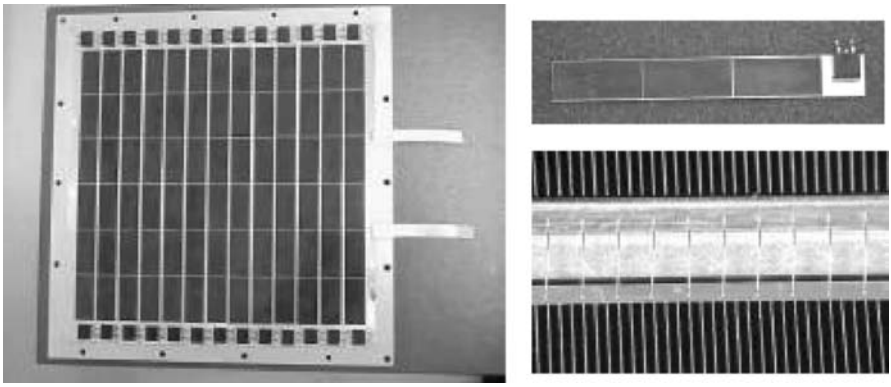

Fig. 10.10. First dense array receiver with multijunction cells in 2001

(d) loss of thermal management. Of these failure mechanisms, cell shunting is the one that can be attributed to internal cell defects; the other three are caused by external factors. For example, cell cracking is generally likely to be caused by thermal expansion mismatch between the cell and the substrate upon which it is connected via solder or conductive epoxy. Such cracking may have started during the cell-fabrication process or during the assembly and then was aggravated by continuous temperature cycling. Loss of thermal management may be associated with cracking in the solder or epoxy joint between the cells and the substrate, or due to cracking in the thermal adhesive between the substrates and the heat sink. Similarly, electrical shorts in this module were caused by water entering the module, causing shorting between the different assemblies.

Cell shunting has been the main failure mechanism observed in high-concentration tests. It happens very quickly (a few minutes after exposure to high concentration). Cell shunting is widely viewed to be associated with thermal runaway: as parts of the semiconductor draw more current, their temperature rises which, in turn, leads to more current crowding and eventual thermal runaway. In the case of the dense array receiver shown in Fig. 10.10, the local temperature in the shunted area has increased enough to cause the silver metal and the solder underneath the cell to melt.

Investigation of the causes for cell shunting involved the use of finite element modelling, to investigate the temperature profile of the cells under different concentration levels as well as doing experiments outdoor using a Fresnel lens based test unit. It also involved the use of a forward bias injection (FBI) test, where the cells are injected with current until failure. The benefit of the FBI tests is that it provided a more controlled way of testing different cell assemblies. As the current is injected, the cell is illuminated, with the locations of shunts tend to draw more current, leading to more intense local illumination than the rest of the cell.

Finite element modelling results are shown in Fig. 10.11 for the assembly of Fig. 10.10 assuming a perfect solder joint, for which the maximum cell temperature is about 77 °C. Assuming the presence of a large void of 35% by volume underneath the cell, while the flux distribution on the cells is assumed to be perfectly uniform, the maximum temperature rise in the cells due to the solder void is about 155 °C, or about 78 °C higher than the design point. Furthermore, the presence of solder voids caused a very large thermal gradient across the cell of about 80 °C, which is too large for the cell to remain physically intact.

Additional experimental work was done on assemblies with solder voids during forward bias injection tests. In Fig. 10.12, the presence of voids has shown to cause the formation of hot spots that eventually led to the creation of cell shunts. This combination of modelling and experimental work has led us to believe that the magnitude and location of voids in the solder joint between the cell and the substrate played a key role in creating cell shunts.

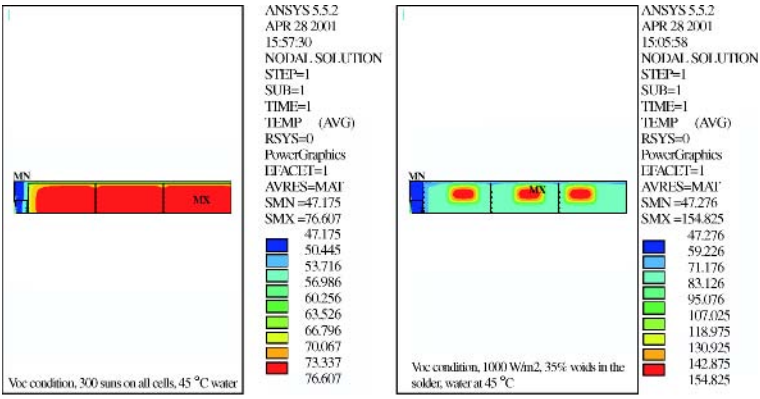

Fig. 10.11. Temperature distribution in the cell assemblies in a perfect solder joint (**a**) and assuming the presence of solder voids (**b**)

The presence of voids created hot spots which, in turn, led to current crowding and eventual thermal runaway. The hot spots led to the creation of shunts, causing the cells to fail high-concentration tests.

Another interesting factor in the creation of cell shunts is the receiver on which the cell is mounted. Specifically, if the substrate onto which the cell

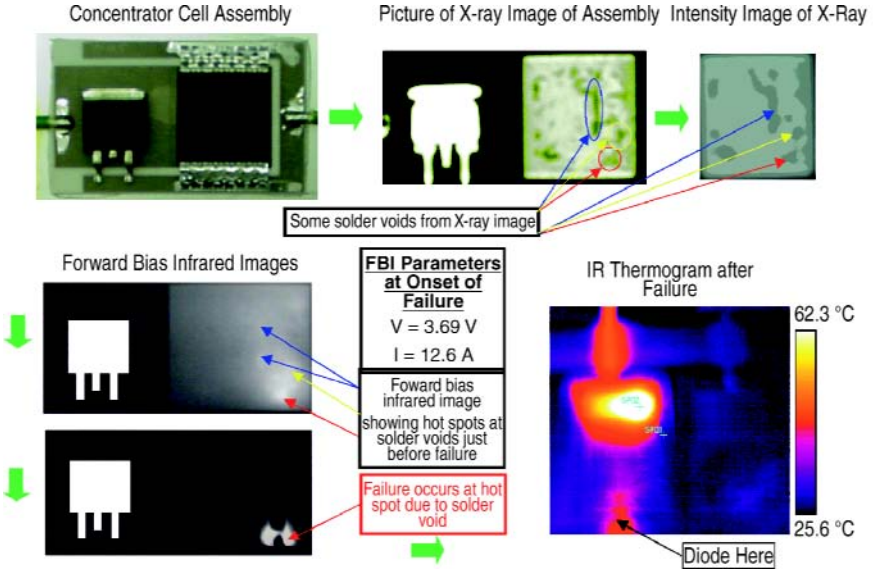

Fig. 10.12. Impact of solder voids on creation of hot spots and cell shunts during forward bias injection tests

is soldered is made of a material that has much higher coefficient of thermal expansion (CTE) than the cell, then cracks in the cell during assembly may cause the metal on the gridlines and the bus-bar to diffuse into the active cell layers, thus causing a shunt. The process of soldering the cells to the substrate and the solder material also play a role. Rapid cooling of the cell assembly after the solder reaches melting temperature does not allow for solder relaxation, making the solder stiffer and thus increases the stresses induced in the cell. Softer solders, on the other hand, are less likely to cause cell cracks during the solidification process or, subsequently, in the temperature cycling during operation.

An ideal cell receiver would thus include a substrate of a material that has a CTE close to that of the cell and a solder joint that is as close to void-free as possible. Spectrolab has developed a receiver package for point-focus CPV systems that involves the use of an alumina ceramic or aluminum nitride substrate with metal traces on the top to facilitate taking the current out of the cells, as shown in Fig. 10.13.

This particular cell assembly has a bypass diode to ensure that cells connected in series are adequately protected from reverse bias in case of shadow of one or more cells in the string. Furthermore, in order to provide protection from the environment, a conformal coating is applied on top of the cells. The above-mentioned assembly has been used extensively in outdoor tests. For example, the first grid-connected concentrator module of Concentrating Technologies, LLC, focuses 500× on 1.5 × 1.5-cm cells and has been running in the field for over 2 years. Figure 10.14 shows a picture of the system and a typical output over a period of 1 month. Another demonstration with the SunLine module at NREL is shown in Fig. 10.15, where 250× (average) and 1200× peak concentration is focused on two cells in parallel. Data is shown here for performance period of over 1 year.

Dense-array receivers pose substantially more difficult challenges to the designer. The MJ cells, unlike coplanar silicon cells, have the n-contact on top and the p-contact on the back. Furthermore, MJ cells do require bypass diodes, preferably one diode per cell. Diodes must therefore be located underneath the cells, not on the sides. Spectrolab has developed a cell assembly that integrates the diode in the substrate and connects it to the top of the cell (the n-contact) with the back of the assembly, as shown in Fig. 10.16.

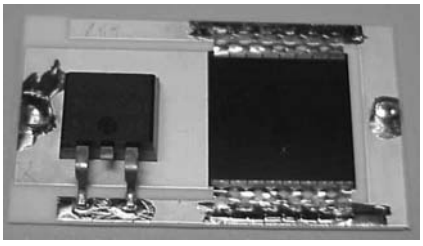

Fig. 10.13. A receiver for point-focus CPV systems

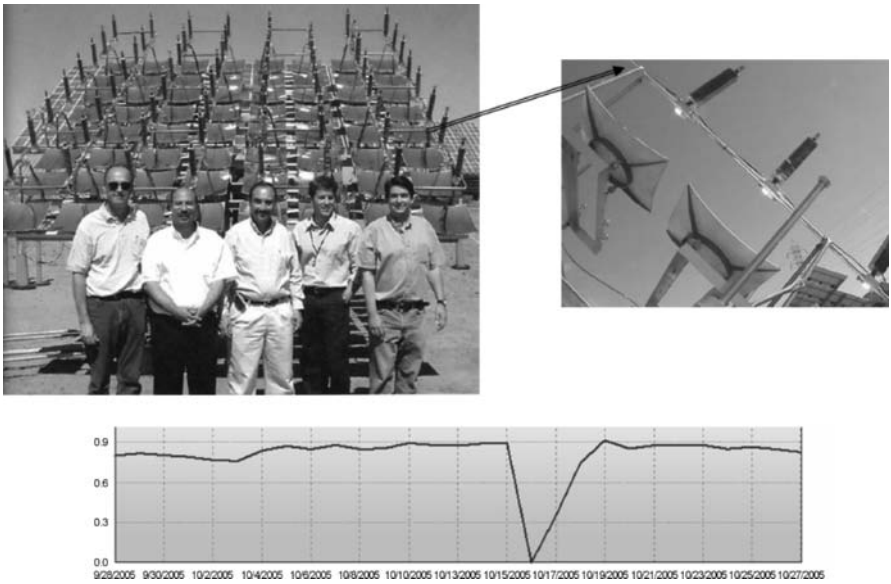

Fig. 10.14. The first grid connected 1kW CPV system using Spectrolab's triple junction solar cells in a point focus receiver. Concentrating Technology LLC installed the system in June 2004 which has been running for over two years; inset shows 30 days performance. (Photo: S. Kusek of CTech, and R. Sherif, N. Karam, G. Kinsey and R. King of Spectrolab)

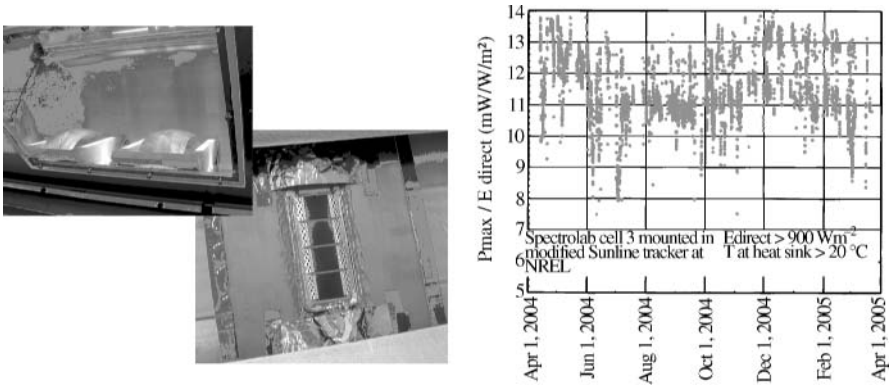

Fig. 10.15. Spectrolab receiver for point-focus inside the SunLine module at NREL

This has practically transformed a top-bottom MJ cell into a coplanar cell assembly with an integral diode, allowing integration of MJ cells in dense-array receivers.

Solar Systems (Melbourne, Australia) has developed an interesting solution to utilize MJ cells in a dense-array receiver. They reported, at the

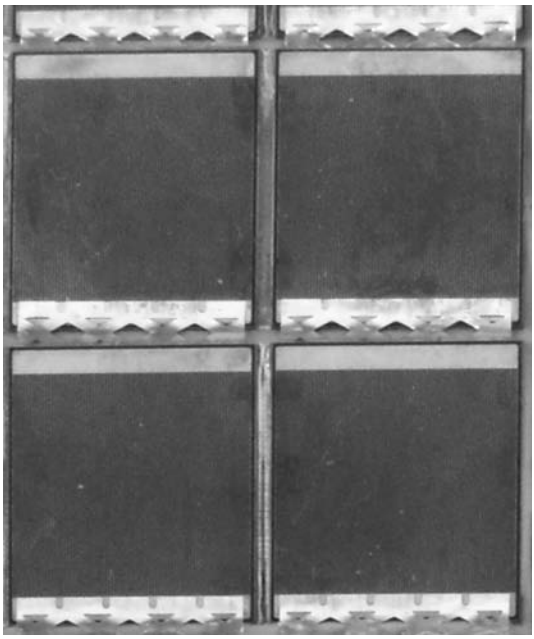

Fig. 10.16. Spectrolab cell assembly used in receivers for dense arrays

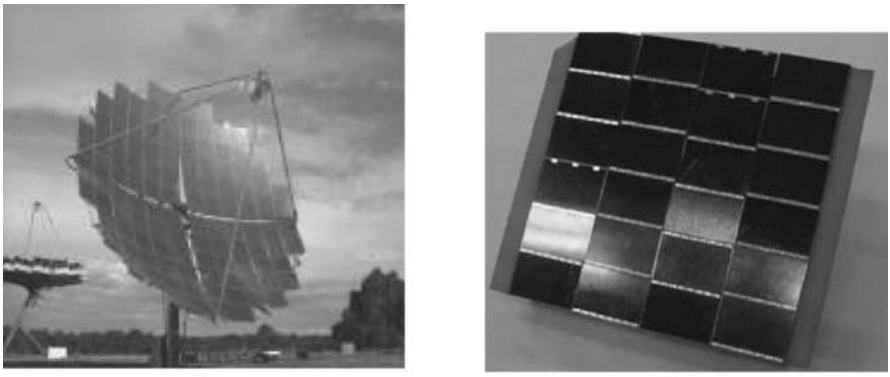

a b

Fig. 10.17. Solar Systems dish (**a**) and the MJ cell receiver module (**b**)

2006 IEEE World Conference on Photovoltaic Energy Conversion, a dish system that utilizes Spectrolab MJ cells and achieves 99% packing factor. The dish system produces 35 kW peak power under standard test conditions (STC), making it the world's largest demonstration of MJ cells under concentration. Figure 10.17 shows a picture of the system and the MJ cell receiver module. Performance data is shown in Fig. 10.18 for the 35% MJ receiver as compared with the 24% silicon dish.

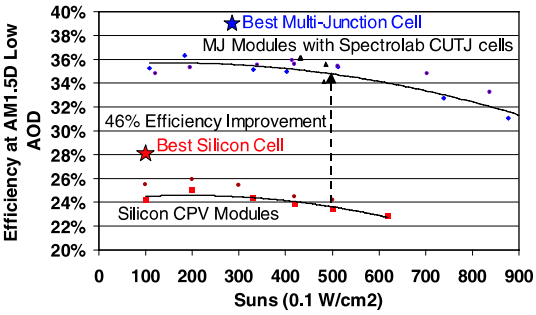

Fig. 10.18. Performance data from Solar Systems on MJ receivers vs silicon receivers. (Courtesy of Solar Systems, Melbourne, Australia)

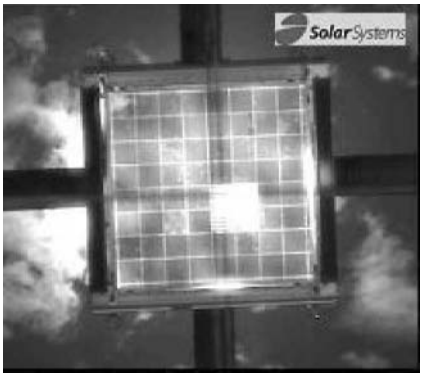

Fig. 10.19. A hybrid receiver from Solar Systems

In addition to the 35-kW system that Solar Systems has populated with the Spectrolab MJ cells, Solar Systems has also populated existing systems with hybrid receivers. A picture of one such receiver is shown in Fig. 10.19. This has allowed Solar Systems to collect field data on the MJ receivers for several months. Additionally, Solar Systems has published data that show the MJ receiver modules have passed the accelerated stress tests performed to assess the level of degradation in the modules after 20 years of field operation.

10.5 Concentrator Cell Economics

Use of the MJ cells is desirable because it leverages the cost of the entire CPV system. This can be clearly seen by examining a hypothetical CPV system using silicon cells of 24% vs the same system if it were to use 35% MJ cells.

Let us assume that an installed system capable of producing 100 kW using 500× on 24% silicon cells will cost $400,000 excluding the cost of the cells. This means that the receiver is using 8333 cm^2 of cell area (so that at 50 W/cm^2 incident on the cells and 24% cells, the system produces 100 kW). This corresponds to $4 per watt, for which the silicon-cells cost was zero. Now, let us assume that we are to populate that system with 35% MJ cells whose cost is $10 per square centimetre. This means that the MJ receiver

will cost $83,330, making the system's total cost $483,330. The output of that system, however, would increase from 100 – 145 kW. By increasing the installed system cost by about 20%, because of the MJ cell receiver, the overall system cost in terms of dollars per watt is actually cheaper than the CPV system using silicon cells (by about 17%, even though the silicon-cells cost is assumed to be zero). It is clear from this example how leveraging the high efficiency of the MJ cell is done. In fact, we can go further and calculate for the above system how much the cell cost might be before the MJ cell system becomes as popular as the system using silicon cells. Alternatively, we could assess the value of pursuing a 1% increase in absolute cell efficiency.

The foregoing logic leads us to believe that utilizing a single measurement for the cells (e.g. the cell $/watt) is simply not sufficient to determine whether paying more for a higher-efficiency cell is worth it. With regard to concentrator cell economics, a companion metric to the cell $/watt is the cell output power in watts. This latter measurement is a function of the cell efficiency, the optical concentration level, the cell temperature, the module and receiver design, etc.

Research has been ongoing to increase cell efficiency, as has been discussed. Additionally, work on reducing the cost of the cells is also very important in order to bring the cost of electricity generation to levels that are competitive with fossil fuels and natural gas (to bring the electricity cost under $0.1/kWh on the retail level). The combined impact of increasing cell efficiency and reducing cell cost on the overall system cost is shown in Fig. 10.20. This figure shows three types of technologies: flat-plate silicon modules; CPV with silicon cells; and CPV with MJ cells. It is clear from this figure that, although the objective of lower system cost of the flat-plate

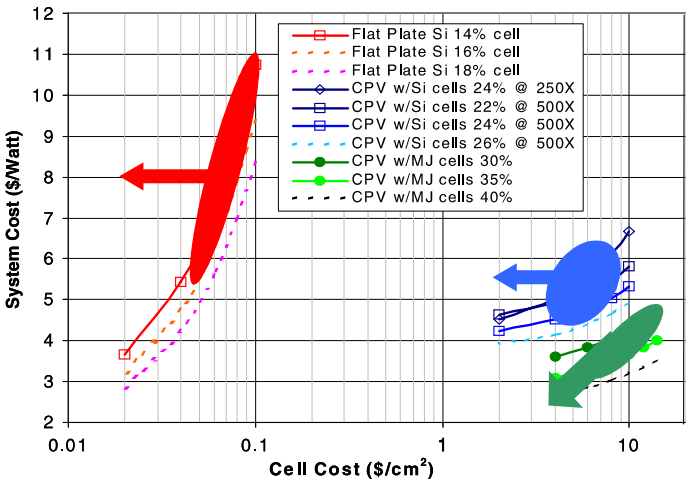

Fig. 10.20. Impact of cell efficiency and cell cost on the overall system cost

silicon modules is achieved primarily by reducing the cost of the silicon cells, CPV systems with MJ cells must achieve both, increasing cell efficiency and reducing cell cost.

We now take a close look at the cost of fabrication of MJ cells, to determine what the present status is, and how we can meet the cost targets as shown herein. The cost of fabrication of MJ cells involves four elements: (a) the germanium wafer cost; (b) the cost of growing the device structure in the metal organic vapor phase epitaxy (MOVPE) reactors; (c) the cost of cell fabrication, including deposition of the anti-reflection coating and the metal pattern on the wafer, and the saw-dicing process to separate the cells from the wafer; and (d) cell testing.

The breakdown of the costs of the above-mentioned elements is dependent on several factors, including the quality of the Ge wafers used, the size of the cells fabricated (which determines the number of cells to test and the number of cuts required to separate the cells from the wafer) and the cell efficiency specifications (which impact the electrical yield). The volume of production and the manufacturing efficiency (e.g. level of automated processes vs manual labor) are clearly some of the key factors that determine the final cell price.

Figure 10.21 provides the projected cell price for a 1×1-cm cell aperture area (physical cell size is 1.1×1.0 cm) at different volumes of production and under different scenarios. In this figure, case 1 refers to the baseline, where no specific material or process cost-reduction activities are included. For the baseline, price reduction with volume is driven primarily by the economies of scale. In case 2, price reduction is driven by a combination of the economies of scale and Ge wafer cost reduction. The Ge wafer cost reduction in this model is driven by the growth of the MJ cell structure on 'terrestrial-grade Ge wafers' allowing for higher defect counts in the wafer than what is typical for space-grade wafers. The motivation for the use of lower-grade Ge wafers is the fact that some minor shunts that are visible at 1-sun will be insignificant at the high current densities under concentrated sunlight. In case 3, no material cost reduction is implemented; instead, the cell price reduction is driven by economies of scale and cell-fabrication-process improvements including automated cell testing. The main driver here is the use of an alternative process

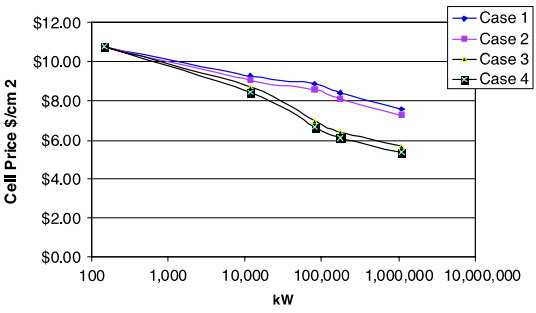

Fig. 10.21. Projected cell price at different volumes and different options

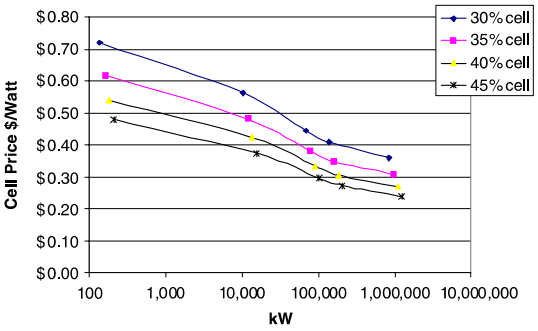

Fig. 10.22. Projected cell price at different volumes and efficiencies

to the saw-dicing process to separate the cells from the wafer and implement a more cost-effective approach, e.g. scribe-and-break or laser cutting plus automated cell testing. Case 4 combines everything, i.e. it includes cost reduction driven by economies of scale, the use of terrestrial-grade Ge wafers and the implementation of cell-fabrication-process improvements.

Another way of looking at the projected cell prices is to express the price as dollars per watt. In this case, the concentration level and the cell efficiency need to be specified. Figure 10.22 shows the projected cell price in terms of dollars per watt assuming 50-W/cm^2 incident energy on the cells. The data is presented for different cell efficiencies and takes full account of all cost-reduction activities discussed previously.

10.6 Conclusion

The device elements for a variety of solar cell architectures capable of reaching $> 41\%$ efficiency have been demonstrated. These elements include the use of metamorphic materials for greater freedom of band-gap selection, wider band-gap top-cell materials, such as AlGaInP and alloys with a disordered group-III sublattice, and cell architectures with three to six junctions that make use of the excess current density in the Ge subcell of conventional triple-junction cells. By combining these device-structure advances under investigation in research groups around the world, the goal of a practical greater than 40%-efficient photovoltaic cell and beyond is near. The reliability of the cell under high concentration, and the cost, are critical to the sustained growth of concentrating photovoltaic energy generation using MJ solar cell technology. The impact of cell efficiency and cost on the overall system cost can only be estimated. Concentrating MJ solar cell technology is an enabler for low-cost power generation using concentrating photovoltaic systems.

Acknowledgement. The authors thank M. Symko-Davies, B. McConnell, K. Emery, S. Kurtz, J. Kiehl, T. Moriarty, W. Metzger, R. Ahrenkiel, B. Keyes, M. Romero, D. Friedman and J. Olson at NREL; and G. Kinsey, H. Cotal, A. Paredes,

Y. Aguirre, P. Colter, T. Isshiki, M. Haddad, K. Barbour, M. Takahashi, M. Kalachian, and G. Glenn, and the entire multijunction solar cell team at Spectrolab. This work was supported in part by the Department of Energy through the NREL High-Performance PV program (NAT-1-30620-01), and by Spectrolab.

References

1. R.R. King, C.M. Fetzer, K.M. Edmondson, D.C. Law, P.C. Colter, H.L. Cotal, R.A. Sherif, H. Yoon, T. Isshiki, D.D. Krut, G.S. Kinsey, J.H. Ermer, S. Kurtz, T. Moriarty, J. Kiehl, K. Emery, W.K. Metzger, R.K. Ahrenkiel, N.H. Karam, Metamorphic III-V materials, sublattice disorder and multijunction solar cell approaches with over 37% efficiency, Proc 19th European Photovoltaic Solar Energy Conf., Paris, France, 7–11 June 2004, p. 3587
2. T. Takamoto, T. Agui, K. Kamimura, M. Kaneiwa, M. Imaizumi, S. Matsuda, M. Yamaguchi, Multijunction solar cell technologies: high efficiency, radiation resistance, and concentrator applications, Proc 3rd World Conf. on Photovoltaic Energy Conversion, Osaka, Japan, 11–18 May 2003, p. 581
3. A.W. Bett, F. Dimroth, M. Hein, G. Lange, M. Meusel, U. Schubert, G. Siefer, Development of III-V-based concentrator solar cells and their application in PV modules, Proc 29th IEEE Photovoltaic Specialists Conf., New Orleans, 19–24 May 2002, p. 844
4. R.R. King, D.C. Law, K.M. Edmondson, C.M. Fetzer, G.S. Kinsey, D.D. Krut, J.H. Ermer, R.A. Sherif, and N.H. Karam, "Metamorphic Concentrator Solar Cells with Over 40% Conversion Efficiency," Proc. 4th International Conference on Solar Concentrators (ICSC-4), El Escorial, Spain, 12–16 March, 2007. March 2007
5. R.R. King, D.C. Law, K.M. Edmondson, C.M. Fetzer, G.S. Kinsey, H. Yoon, R.A. Sherif, and N.H. Karam, "40% efficient metamorphic GaInP/GaInAs/Ge multijunction solar cells," Appl. Phys. Lett., Vol. 90, No. 18, 183516, 30 April 2007.
6. R.A. Sherif, R.R. King, N.H. Karam, D.R. Lillington, The path to 1 GW of concentrator photovoltaics using multijunction solar cells, Proc 31st IEEE Photovoltaic Specialists Conf., Lake Buena Vista, Florida, 3–7 January, 2005, p. 17
7. R.A. Sherif, H.L. Cotal, R.R. King, A. Paredes, N.H. Karam, G.S. Glenn, D. Krut, A. Lewandowski, C. Bingham, K. Emery, M. Symko-Davies, J. Kiehl, S. Kusek, H. Hayden, The performance and robustness of GaInP/InGaAs/Ge concentrator solar cells in high concentration terrestrial modules, Proc 19th European Photovoltaic Solar Energy Conf., Paris, 7–11 June 2004, p. 2074
8. K. Araki, M. Kondo, H. Uozumi, M. Yamaguchi, Development of a robust and high-efficiency concentrator receiver, Proc 3rd World Conf. on Photovoltaic Energy Conversion, Osaka, Japan, 11–18 May 2003, p. 630
9. A. Bett, C. Baur, F. Dimroth, G. Lange, M. Meusel, S. van Riesen, G. Siefer, V.M. Andreev, V.D. Rumyantsev, N.A. Sadchikov, FLATCON modules: technology and characterisation, Proc. 3rd World Conf. on Photovoltaic Energy Conversion, Osaka, 11–18 May 2003, p. 634
10. R.R. King, M. Haddad, T. Isshiki, P.C. Colter, J.H. Ermer, H. Yoon, D.E. Joslin, N.H. Karam, Metamorphic GaInP/GaInAs/Ge solar cells, Proc

28th IEEE Photovoltaic Specialists Conf., Anchorage, 15–22 September 2000, p. 982
11. F. Dimroth, U. Schubert, A.W. Bett, 25.5% Efficient $Ga_{0.35}In_{0.65}P/Ga_{0.83}In_{0.17}As$ tandem solar cells grown on GaAs substrates, IEEE Electron Device Lett, 21, p. 209 (2000)
12. R.R. King, C.M. Fetzer, P.C. Colter, K.M. Edmondson, J.H. Ermer, H.L. Cotal, H. Yoon, A.P. Stavrides, G. Kinsey, D.D. Krut, N.H. Karam, High-efficiency space and terrestrial multijunction solar cells through bandgap control in cell structures, Proc 29th IEEE Photovoltaic Specialists Conf., New Orleans, 19–24 May 2002, p. 776
13. R.R. King, C.M. Fetzer, P.C. Colter, K.M. Edmondson, D.C. Law, A.P. Stavrides, H. Yoon, G.S. Kinsey, H.L. Cotal, J.H. Ermer, R.A. Sherif, K. Emery, W. Metzger, R.K. Ahrenkiel, N.H. Karam, Lattice-matched and metamorphic GaInP/GaInAs/Ge concentrator solar cells, Proc 3rd World Conf. on Photovoltaic Energy Conversion, Osaka, 11–18 May, 2003, p. 622
14. C.M. Fetzer, R.R. King, P.C. Colter, K.M. Edmondson, D.C. Law, A.P. Stavrides, H. Yoon, J.H. Ermer, N.H. Karam, High-efficiency GaInP/GaInAs/Ge solar cells grown by MOVPE, J Crystal Growth, 261, pp. 341–348 (2004)
15. C.M. Fetzer, H. Yoon, R.R. King, D.C. Law, T.D. Isshiki, N.H. Karam, 1.6/1.1 eV metamorphic GaInP/GaInAs solar cells grown by MOVPE on Ge, J Crystal Growth, 276, pp. 48–56 (2005)
16. D.C. Law, C.M. Fetzer, R.R. King, P.C. Colter, H. Yoon, T.D. Isshiki, K.M. Edmondson, M. Haddad, N.H. Karam, Multijunction solar cells with subcell materials highly lattice-mismatched to Germanium, Proc 31st IEEE Photovoltaic Specialists Conf., Lake Buena Vista, Florida, 3–7 January, 2005, p. 575
17. J.C. Schultz, M.E. Klausmeier-Brown, M. Ladle Ristow, M.M. Al-Jassim, High efficiency 1.0-eV GaInAs bottom solar cell for 3-junction monolithic stack, Proc 21st IEEE Photovoltaic Specialists Conf., Kissimmee, Florida, 21–25 May, 1990, p. 148
18. M.W. Wanlass, S.P. Ahrenkiel, R.K. Ahrenkiel, D.S. Albin, J.J. Carapella, A. Duda, J.F. Geisz, S. Kurtz, T. Moriarty, R.J. Werner, B. Wernsman, Lattice-mismatched approaches for high-performance, III-V, photovoltaic energy converters, Proc 31st IEEE Photovoltaic Specialists Conf., Lake Buena Vista, Florida, 3–7 January 2005, p. 530
19. Standard ASTM 892-92, Standard for terrestrial solar spectral irradiance tables at air mass 1.5 for a 37° tilted surface, Am Soc Testing Mater, West Conshocken, Pennsylvania 1992
20. K. Emery, D. Meyers, S. Kurtz, What is the appropriate reference spectrum for characterizing concentrator cells? Proc 29th IEEE Photovoltaic Specialists Conf., New Orleans, 19–24 May 2002, pp. 840–843
21. M.A. Green, K. Emery, D.L. King, S. Igari, W. Warta, Solar cell efficiency tables (version 24), Prog Photovoltaics Res Appl, 12, pp. 365–372 (2004)
22. M.A. Green, K. Emery, D.L. King, Y. Hisikawa, W. Warta, Solar cell efficiency tables (version 27), Prog Photovoltaics Res Appl 14, pp. 45–51 (2006)
23. Standard ASTM G173-03, Standard tables for reference solar spectral irradiances: direct normal and hemispherical on 37-degree tilted surface, Am Soc Testing Mater, West Conshocken, Pennsylvania (2003)

11 Inspira's CPV Sun Tracking

I. Luque-Heredia, J.M. Moreno, P.H. Magalhães, R. Cervantes,
G. Quéméré, and O. Laurent

11.1 Introduction

Most PV concentrators use only direct solar radiation, and they must therefore permanently track the sun's apparent daytime motion, and hence integrate an automatic sun tracking structure able to mount and position the concentrator optics in such a way that direct sunlight is always focused on the cells. This sun tracker is basically composed of a structure presenting a sunlight collecting surface in which to attach concentrator modules or systems, which is somehow coupled to a one- or two-axis mechanical drive, and also of some sun tracking control system which operates over the drive axes and maintains an optimum aiming of the collecting surface or aperture towards the sun.

Static mounts are only feasible presently for low concentration factors (below 5×); however, in the long term, static concentrators with higher ratios may appear, making use of luminescence and photonic crystals; however, all these issues are beyond the scope of this chapter.

Line focus reflective concentrators, such as troughs, only require one-axis tracking to maintain the PV receiver along the focus line; however, due to the daily variations in the sun elevation, sunlight incidence on the tracker's aperture is usually somewhat oblique, thus reducing the intercepted energy and causing the sun's image to move up and down within the focus axis, and producing further losses whenever it surpasses the receiver's ends. Line focus refractive concentrators, such as those based on linear Fresnel lenses, experience severe optical aberrations whenever light incidence is not normal, thus requiring two-axis sun tracking, and the same happens to most point-focus concentration concepts developed, except for some low-concentration-factor devices with enough acceptance angle to admit the sun's altitude variations.

Nearly all PV concentrators already commercially available or currently under development use two-axis tracking, the so-called pedestal tracker, with its azimuth-elevation axes being the most common configuration, followed by the tilt-roll tracker operating on the declination-hour angle axes. With regard to sun tracking control, most of the early systems consisted of analogue sun-pointing sensors based on the unbalanced shadowing or illumination of a couple or quad of PV cells, integrated into an automatic closed loop with the tracker's driving motors. The advent of cheap microcontrollers motivated

the appearance of sun tracking control systems requiring no sun sensing and based only on the digital computation of precise analytic sun ephemeris equations. To date, the need for an efficient and reliable sun tracking control in CPV applications has driven the state of the art towards a blend of these two original approaches, producing hybrid strategies integrating both sun alignment error feedback and ephemeris-based positioning.

Since the late 1970s, when concentration systems first captured the interest of the PV community, because of, among other reasons, the clear evidence of significant cost reduction, a reasonable amount of field experience has been acquired which keeps emphasizing the underlying sun tracking systems as one of the most error-prone components [1,2]. These systems are probably among the most difficult obstacles which are delaying this technology's definitive industrial integration, to the point of having been dubbed 'the CPV Achilles' heel' [3,4].

The low performance of tracking systems up to now, however, is not at all unjustified; On the one hand, the tracker usually demanded by CPV technologies requires a structure able to maintain an overall stiffness within the sub-degree range, so as not to induce acceptance-angle losses on the supported concentrating systems, and considering, apart from its own weight, maximum service wind loads in the 10- to 20-m/s range. On the other hand, the tracking drive, by means of jointly conferring accurate speed control and low backlash, is to achieve a high positioning resolution and withstand usually heavy payloads – which, under some design options, introduce very high torques. This is, moreover, the case with the increasing trends in CPV concentration factors, which ultimately, on account of *étendue* conservation, further decrease acceptance angle [5]. In addition, the development of a fully reliable sun tracking control system, able to fulfil the accuracy requirements of the concentrator system, most frequently in the sub-degree range is of the utmost importance. This entails immunity to factors such as overcast and hazy skies, software failures, extreme weather conditions, as well as low-cost and qualified installation crews. Past PV concentration projects have shown that it is extremely difficult to successfully implement this development; moreover, all of the required solutions must be achieved under strong cost constraints, and with few alternatives.

11.2 Requirements and Specifications

Strictly speaking, the main commitment to be fulfilled by a CPV sun tracker is to permanently align the pointing axis of the supported concentration system with the local sun vector, in this way producing maximum power output. As we see later, there are several error sources to take into account, and therefore, some off-tracking tolerance is required. Usually this tolerance, or minimum tracking accuracy required, is characterized by means of the accep-

tance angle of the concentration system, usually defined as the off-tracking angle at which power output drops below 90%.

Reasons for the decrease of sun tracking performance can be classified into two main types: (a) those purely related to the precise pointing of the tracker to the sun; and (b) those which provoke shrinkage of the overall acceptance angle of the concentrator system, thus indirectly increasing the tracking accuracy required. Among the reasons related to the tracking accuracy, these are basically, on the one hand, the exactness of the sun-position coordinates generated by the control system expressed in terms of rotation angles of the tracking axes, either by sun ephemeris-based computations or derived from the feedback of sun-pointing sensor readings, or a combination of both, and which in any case is affected by numerous error sources. The other factor is the precision with which the tracker can be positioned at these dictated orientations, i.e. the positioning resolution of the tracking drive and its control system, which essentially depends on the performance of tracking speed control and on the mechanical backlash introduced by the drive's gearings. With regard to acceptance-angle losses caused by the tracking system, these are due to the accuracy which can be attained in the mounting and alignment of the concentrator system atop the tracker, which is basically a design problem having to do with the fixtures provided for this purpose. Their accurate assembly and the regulation means provide for in-field fine tuning, but also with the mounting protocols devised to carry out this tasks. The stiffness conferred to the tracker also results in acceptance-angle cuts, i.e. the bending allowed in the different elements of its structure under service conditions.

Characterization of service conditions for a CPV tracker deserves some discussion and basically consists of fixing a value for the maximum wind load, i.e. wind speed, to be withstood during sun tracking operation. The bigger this value, the heavier and more expensive tracking structure required to maintain bending under the threshold required for accurate tracking; thus, a cost-effective approach is to determine this value from the cross correlation between wind speed and direct radiation, in the location or set of locations in which the trackers are planned to be marketed and installed, above which stiffness specifications do not have to be met and the tracker can switch to some low-wind-profile stow position. These correlations have been estimated in a systematic way to aid the design of solar collectors employed in solar thermal plants by Sandia National Laboratories [6], by using records of insolation and surface meteorological conditions obtained at 26 weather stations of the U.S. National Climatic Center distributed over the contiguous United States and available through the SOLMET data tapes. These tapes provide hourly observations of wind speed and direction in addition to the normal direct irradiance spanning the 1952–1964 time frame. By computing cumulated direct irradiation below a certain wind speed for two- and single-axis trackers, it was seen that for 22 of the 26 SOLMET stations over 95% of the direct irradiation occurs at wind speeds up to 11 m/s. Great Falls, Montana,

which experiences the maximum of the 26 sites, achieves 95% of the direct insolation at wind speeds up to 13 m/s. The wind speed below which this 95% cumulated direct irradiation is comprised seems, at first glance, a reasonable choice to be taken as maximum service wind speed, over which the tracking control can order a stow position. A case example of this type of analysis is presented in Fig. 11.1, worked out with 1 year of continuous wind speed and direct irradiation (considering a two-axis tracker) hourly data, for the Spanish city of Granada.

Further fine tuning of this wind speed threshold can be achieved if we are able to obtain the function of tracker cost vs maximum service wind speed for the particular tracking design chosen for our project. Considering that we can also estimate the energy produced by the concentrator system for, say, its assumed operative lifetime, also as a function of the maximum service wind speed we will be able to obtain an electricity cost and determine its optimum value as the one in which a minimum occurs. This exercise was done for one of Inspira's early tracking designs [7], a 9-m^2 pedestal tracker produced for concentration applications, and in which service stiffness was specified in such a way that aperture bending was to remain always below 0.1°. This minimum, again using the 1-year data collected for Granada, was found to occur at a maximum service wind speed of 22 km/h, which, as seen in Fig. 11.1, allows for a direct irradiance collection in the 95% range.

In Fig. 11.2 we see how tracker cost increased with the maximum service wind speed for the referred 9-m^2 design and also for its scaling up to 16- and 25-m^2 apertures considering 1000 units/year production volumes. Even if design re-dimensioning at constant wind speed intervals, and seeking compliancy with the 0.1° maximum bending criterion, implies an almost linear smooth cost increase, some in metal structural elements, mainly driven by weight increase, some progress can be observed, as shown in Fig. 11.2. This leaps are due to the introduction of new models of drive components (bearings, gearing sets, etc.), the price of which is not only driven by their

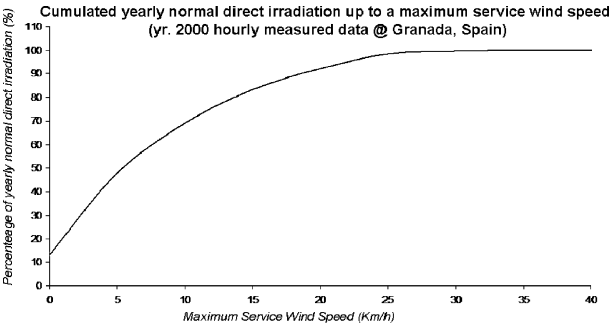

Fig. 11.1. Wind speed vs yearly NDI correlation for the determination of optimum service conditions regarding maximum operative wind load, here applied to Granada, Spain, and showing 95% NDI collection below 22 km/h

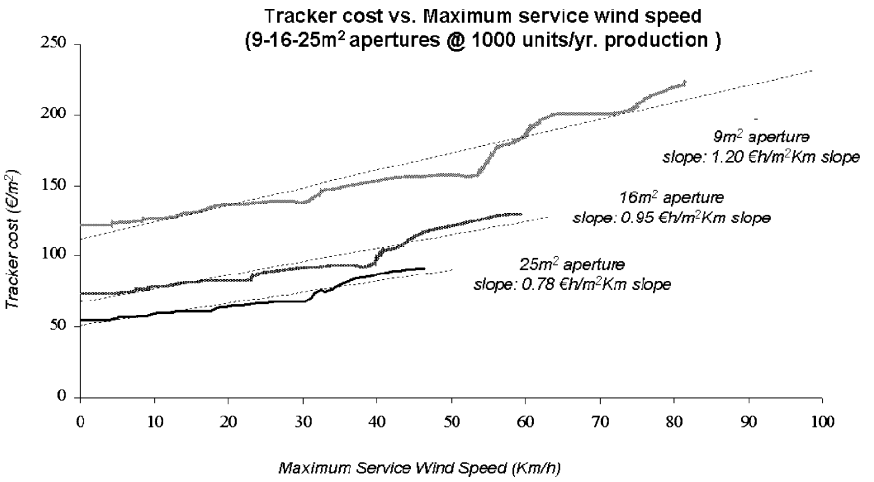

Fig. 11.2. Tracker cost vs maximum service wind speed for a specific tracker design dimensioned for three different aperture surfaces and 1000 units/year productions

nominal load, but also by their market (i.e. the demand and volumes in which manufacturers produce them).

We therefore see how structural dimensioning of a tracking design can be cost optimized for a given location, an option which may be worthwhile when building big CPV plants. The other variable involved in this characterization of service conditions – the maximum allowed structural bending measured in the aperture surface which, for this example, has been set to 0.1° – intends to place a bound on the losses caused by the tracker's flexure on the acceptance angle of its elementary CPV modules.

In the following section we present a procedure developed to provide an estimate of these losses for a design carried out in observance of this maximum bending criterion. Determining this maximum bending depends on the acceptance angle of the particular CPV technology object of the design, bearing in mind that the obtainable tracking accuracy is finally to be included in the overall CPV array acceptance angle.

Determination of this obtainable tracking accuracy is also presently an unsettled issue, because there is, to date, no standard instrumentation and measurement procedures that provide enough sensitivity to gauge the usual subdegree accuracy ranges. The CPV developers frequently overlook this critical issue and instead present the usually very high tracking accuracies they can achieve without any explanation as to how they are measured. Precise tracking accuracy measurement basically entails continuous monitoring of different angles with respect to the position producing maximum power output.

In the last section we present a system which based on solid-state image sensors. We also propose an efficient tool to determine the tracking accuracy statistics of a given CPV system.

Even if the main factors affecting sun tracking efficiency can be well characterized, i.e. tracking accuracy, and the maximum flexure under service conditions along with maximum service wind speed, the panoply of CPV designs released thus far, as usually occurs in the infancy stages of any technology, hinders the production of design standards which recommend target quantities for each of these variables. Instead, the designer must still obtain them by a costly and time-consuming trial-and-error process which usually involves the production and testing of prototypes.

Apart from this tracking performance in terms of efficiency, downtime is the other main enemy of a CPV tracker. Here the mechanical tracker is usually free of suspicion, provided that the pertinent structural codes are respected in its design. In addition, off-the-shelf drive gearings are subject to very mild operation conditions – one axis turn per day – when compared with their usual market applications in machine tools, cranes, etc. Instead, most of the reported problems arise in the electrical and electronic parts, which, first of all, are to be designed to operate reliably in outdoor conditions but also comply with a suitably chosen set of EMC and electrical safety standards, thus anticipating common field problems such as power spikes or surges. When considerable amounts of software are involved, as happens with the present tracking control systems which integrate microprocessors, it is not just a matter of a reliable and well-protected electronic design, but also of a redundant code immune to glitches and able to gracefully recover from power outages or sags.

11.3 The Tracker

We do not take the more usual taxonomic approach, which reviews the panoply of mechanical tracker designs presented to date and their respective pros and cons; instead, we focus on a more general design principle applicable to any tracker development project. As already stated, tracker performance is mainly a twofold problem: on the one hand, it is a matter of tracking control accuracy depending on the drive's positioning resolution and the effectiveness of the sun tracking controller. On the other hand, the tracking accuracy required is determined by the overall acceptance angle of the CPV system, and this is highly dependent on the stiffness of the tracker structure. In turn, stiffness specifications have a fundamental impact on the tracker's weight which, when entering volume productions, is its main cost-driving factor. Tracking control accuracy merit is commonly provided by components integrated into the tracker design, such as the tracking controller (below we see Inspira's general-purpose tracking control unit) or off-the-shelf industrial gearing blocks featuring high reduction ratios and low backlash. So, it is finally the determination and fulfillment of stiffness specifications that is the main concern of a tracker designer, regardless of the tracking configuration selected.

In this section an overview of how the stiffness issue is addressed in one of Inspira's CPV tracker designs is presented [8]. It corresponds to a two-axis pedestal tracker design, with a 30-m^2 aperture surface, and is customized for very high concentration ratio modules (Fig. 11.3). The modules had a nominal acceptance angle of $\pm 0.6^\circ$, determined through indoor lab measurements using collimated laser light. Subtracting the approximately 0.26° subtended half angle of the sun, we require a 0.34° minimum tracking accuracy. As we see below, a feasible value for the minimum tracking accuracy is 0.1° (i.e. 95% probability that the off-track angle remains below 0.1°); thus, acceptance-angle overall loss on the array must not surpass 0.24°. Introducing some overestimation to allow for extra acceptance-angle losses produced by aperture lack of planarity and module mounting unevenness atop of the aperture, a maximum 0.1° bending was the starting point set for the tracking structure design. This means that this is to be the maximum allowed turn induced by structural flexure for any vector normal to the aperture surface when subject to maximum service conditions (maximum operating wind speed 43 km/h, both blowing from the front or the back of the tracker) at any aperture elevation angle. The first step in the design of the metal structure forming the tracker's aperture is to choose its topology, where only the lengths of dimensionless metal beams and the connections among them and with the drive block are decided, seeking here the optimization of different aspects such as transportation, in-field installation, mounting of CPV modules, etc. Once the tracker frame is settled, it is to be dimensioned playing with the precise form of the structural beams, e.g. I-beams, angles and channels, tubes, etc., if directly opting for off-the-shelf construction standards or other methods requiring more processing such as trusses, and assessing their moments of inertia and manufacturing costs.

It is in this point that the stiffness criterion starts to rule over the design, and precise finite elements (FE) analyses are to be carried out over the complete tracker structure when subject to the specified maximum service loads (CPV modules payload and maximum operative wind loads). When this was done for the referred tracker, a solution based on standard structural beams was obtained, which resulted in the least tracker's self-weight, and according to FE simulations did not surpass the 0.1° bending at any aperture elevation. In the case of the pedestal tracker, the design was separately considered in three segments: (a) aperture frame; (b) pedestal and drive block; and (c) foundation. From the start, a certain percentage of that total maximum 0.1° maximum flexure was allocated to each segment, taking into account that while bending in the aperture will usually result in overall acceptance-angle shrinkage, bending in the pedestal or the foundation works as an overall pointing vector turn which, as is seen in the sun tracking control section, can eventually be characterized and handled by a tracking controller. In the case of the tracker's foundation, meeting its flexure quota requires a standard geotechnical analysis of the ground where it will be installed, in order

to choose the best suitable solution. Quite obviously, in a pedestal tracker with a rectangular aperture surface, maximum bending at whichever elevation will occur in its corners. Final results for this design are shown in Fig. 11.3, where maximum bending when maximum service wind load comes frontally is 0.076° and occurs at 57° aperture elevation, whereas when this same wind speed is received in the aperture's rear face, this maximum bending is slightly bigger (0.078°) and happens at 0° elevation. In any case, maximum structural bending remains under the 0.1° threshold.

Once this maximum bending threshold has been met, the next step is to estimate the acceptance-angle losses induced by structural flexure, using the bending rotation values of the set of vectors normal to the aperture, obtained in the FE simulation. For this purpose a first geometrical model was

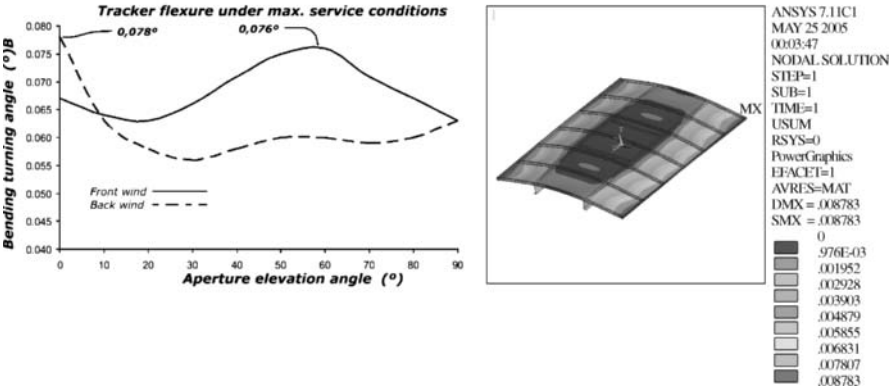

Fig. 11.3. The CPV pedestal tracker designed and produced by Inspira (*top*), subject of flexure analysis (*below left*) maximum bending turning angle in aperture surface when subject to maximum service conditions (43 km/h wind speed) as a function of aperture elevation function (*below right*). Finite Elements analysis of flexure bending

developed in which each CPV module mounted on the aperture could be considered to remain undeformed under service loads, and a single normal vector could be considered for each CPV module (Fig. 11.4). This normal vector is taken as the pointing vector of the module, i.e. the vector that, when aligned with the local sun vector, produces the module's maximum power output. Acceptance angle for each module is characterized by the cone drawn by the vectors at this angle from the pointing vector which is then the cone's axis. In other words, power is assumed to drop to zero outside the acceptance-angle cone, and a worst-case approach is taken regarding module electrical interconnection, in which all modules are supposed to be connected in series; thus, the set of tracker orientations producing nominal power output for a certain aperture elevation angle is taken as the set of vectors pertaining to the acceptance-angle cones of all the modules, i.e. their intersection. The acceptance angle at this aperture elevation can then be defined as the

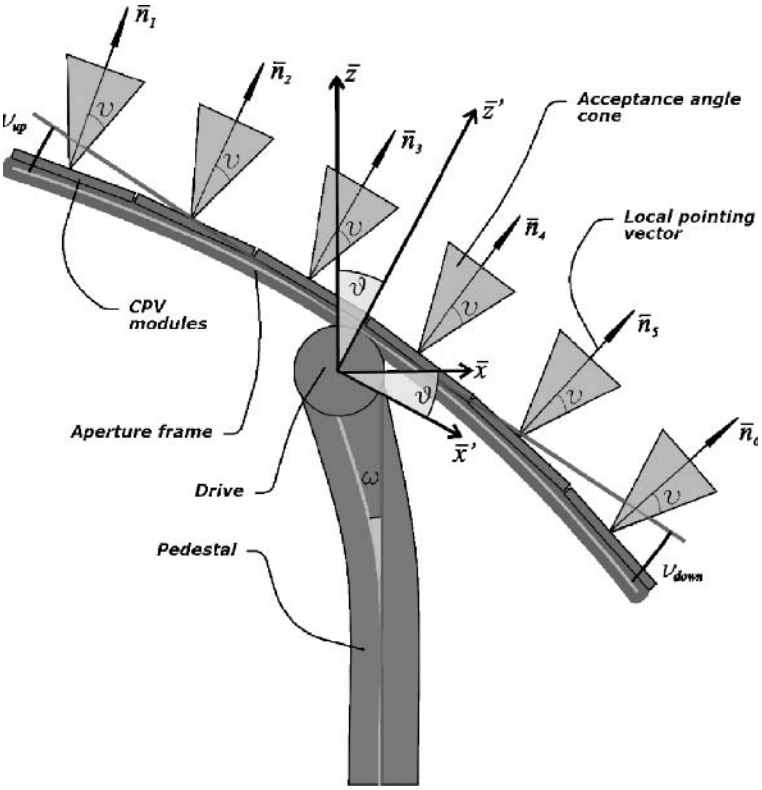

Fig. 11.4. Cross section of pedestal tracker subject to flexure, at a certain aperture elevation (zenith angle θ). The local pointing vector to each module n_i and its acceptance angle (υ) cone within the aperture's local reference system $(\bar{x}', \bar{y}', \bar{z}')$ are shown

maximum-angle cone contained in this intersection of cones, and the axis of this cone is taken as the overall concentrator pointing vector.

The problem of determining this overall acceptance-angle cone can be better viewed and solved if the pointing vectors and their respective acceptance-angle cones are projected in the plane, using the usual PQ plane projection of non-imaging optics. This means that it is the projection of the intersection of pointing vectors and cones with a unit radius sphere whose centre coincides with the origin of all the pointing vectors. In this way every module pointing vector is transformed into a point in the plane, having as Cartesian coordinates its direction cosines with respect to plane reference axes, and cones are transformed into ellipses (Fig. 11.5). The flexure turning angle of a certain pointing vector will be small, and therefore its projected coordinates will appear to be very close to the reference system origin, which represents the pointing vector of the concentrator if the tracker was ideally rigid and undeformable, and the distance of each pointing vector to the origin is its bending rotation angle. For the pointing-vector points located close to the origin, its corresponding acceptance-angle ellipse can be approximated by a circle, centred in the pointing-vector coordinates. On the other hand, high-concentration CPV modules usually have small acceptance angles, in the sub-degree range, and in this case the radius of the projected circle representing the acceptance-angle cone equals the acceptance angle itself; thus, after this projection, we can reformulate the problem of obtaining the maximum cone contained in the intersection of module acceptance-angle cones,

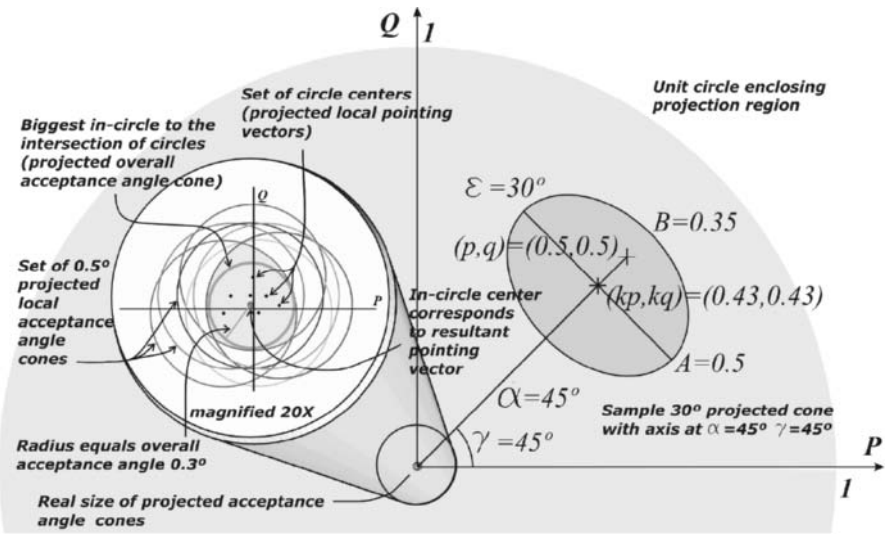

Fig. 11.5. Illustration of a PQ plane projection of the module local pointing vectors and associated acceptance-angle cones for the determination of worst-case complete-array pointing vector and acceptance angle

as the maximum incircle to the intersection of acceptance-angle circles in the plane, and the centre of this incircle – the incentre – represents the projection of the overall concentrator pointing vector. It can be proven that finding this maximum incircle is equivalent to determining the minimum enclosing circle (MEC) containing all the pointing-vector points, where the centre of this MEC coincides with the incentre of the maximum incircle and the radius of the maximum incircle, i.e. the overall acceptance angle, equals the single module acceptance angle minus the radius of the obtained MEC which, in this way, represents the acceptance-angle loss due to flexure. The MEC determination for a set of points in the plane is a classical computational geometry problem first stated by Sylvester in 1857 and for the solution for which we implemented the most efficient algorithm to date due to Welzl and achieving $O(n)$ linear running time [9].

Applying this model to the FE simulations obtained from the pedestal tracker of our case example produced the plot of acceptance-angle loss as a function of aperture elevation for both front and back maximum service wind speeds, as shown in Fig. 11.6. Also in this figure, the different MECs for aperture-elevation angles taken every 10° from 0 to 90° are shown along with the centres of each MEC, which shows how the overall pointing vector also moves due to flexure. In this case the local pointing vectors used at every elevation are only those of the modules placed in the aperture perimeter, which are the ones suffering the biggest bending. As can be seen from the acceptance-angle-loss graph, the maximum is 0.063° and it occurs with maximum service wind blowing from the front at 70° of aperture elevation; thus, our initial 0.1° maximum bending threshold, finally achieving 0.078°, has finally resulted in a maximum acceptance-angle loss of 0.063° which, again reviewing the starting figures regarding module nominal acceptance angle and feasible accuracy attainable, would give way to further relax the bending threshold in a second iteration, thus reducing the weight of the structure further and reducing its cost.

Aperture elevation angle producing maximum bending of local pointing vectors and maximum acceptance-angle loss do not necessarily coincide because, as stated in this analysis, the turning angle is also affected by the pedestal and global components which equally affect all aperture pointing vectors and do not contribute to acceptance-angle losses.

11.4 Sun Tracking Control

11.4.1 Background

Early sun tracking controllers were developed following the classical control system closed-loop approach by integrating a sun sensor able to provide pointing-error signals, one per tracking axis, which in turn generates motor-correction movements [10, 11]. This sun sensor is essentially composed of

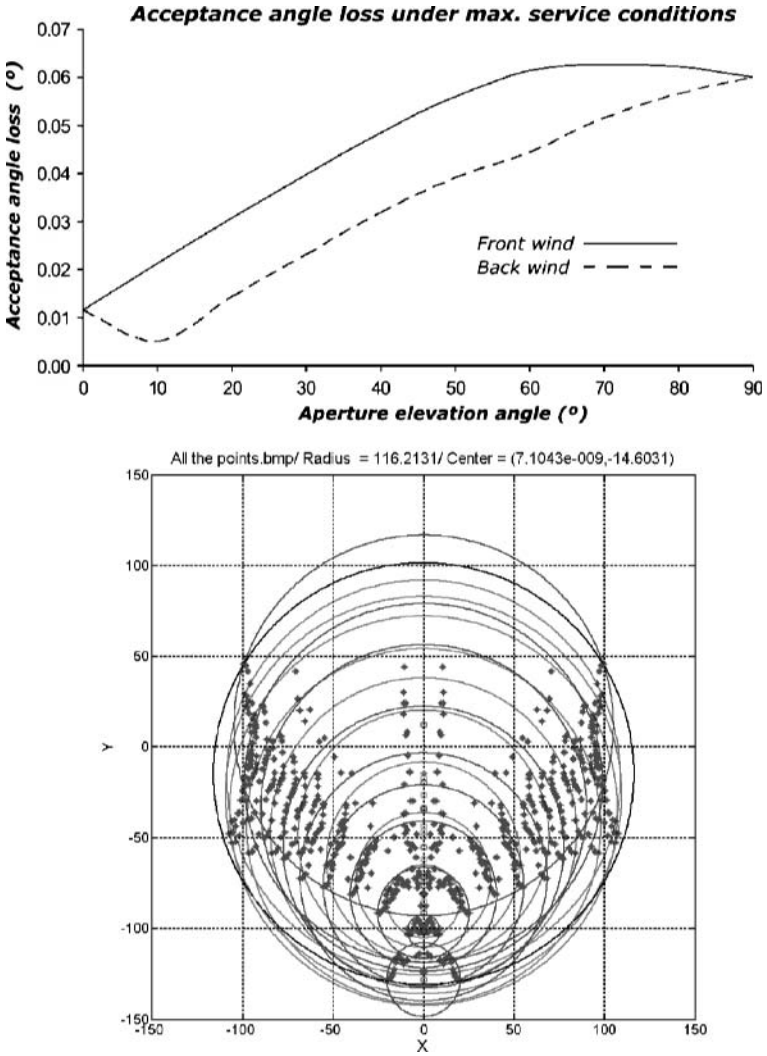

Fig. 11.6. Estimation of a worst-case acceptance-angle loss in the 30-m^2 pedestal tracker as a function of aperture elevation (*top*) and subject to maximum service conditions (*bottom*). Pointing vectors and minimum enclosing circles at different elevations with maximum service wind speed windward and leeward to module's active surface

a pair of photodiodes and a shading device which casts a different shade on these photodiodes, thereby generating different photocurrents whenever it is not aligned with the local sun vector (Fig. 11.7a). In addition, the photodiodes can be mounted on tilted planes in order to increase the photocurrent sensitivity (Fig. 11.7b) and, very commonly in CPV applications, the shading

device is presented as a collimating tube which prevents diffuse irradiation from entering the sensor and masking a precise measurement of the sun-alignment position (Fig. 11.7c).

Even if this closed-loop approach can be very inexpensive and simple to implement, it has already gathered significant field experience to point out some recurrent problems affecting its reliability [12], mostly caused by drifts in the analogue electronics involved and the requirement of cleanliness. This imposes the requirement of frequent maintenance, which may possibly be affordable in research centres where care if given by attentive technical personnel, but it is not feasible for the control of large-scale industrial tracker fields. Furthermore, closed-loop controllers have proved not to perform well under less than ideal illumination conditions, e.g. due to the fact that when the irradiance within a sensor's acceptance angle is averaged, there is an odd phenomenon in which the bright reflection of a nearby cloud can cause tracking errors in the 1° range even when the sun is visible. For example, when the sun is hidden, closed-loop controllers have been reported to track bright clouds drifting away from the sun. This simple closed-loop controller is also by itself unfit to manage non-tracking and stowing situations, and due to their limited acceptance angles, the reappearance of the sun after overcast periods is usually time-consuming and inefficient if not complemented with auxiliary control electronics.

Finally, in high-accuracy applications a fundamental handicap arises if they are to be aligned with the peak power output of the CPV array under control, which, being a difficult operator requirement in itself, may not even suffice in big aperture trackers where, as shown previously, structural flexure varying with the tracker orientation impede a stable alignment. Nevertheless, these sun-pointing sensors remain a fast pathway to CPV-compliant sun tracking control. Recently, highly integrated versions of these devices have been developed [13], and they remain an auxiliary constituent of the

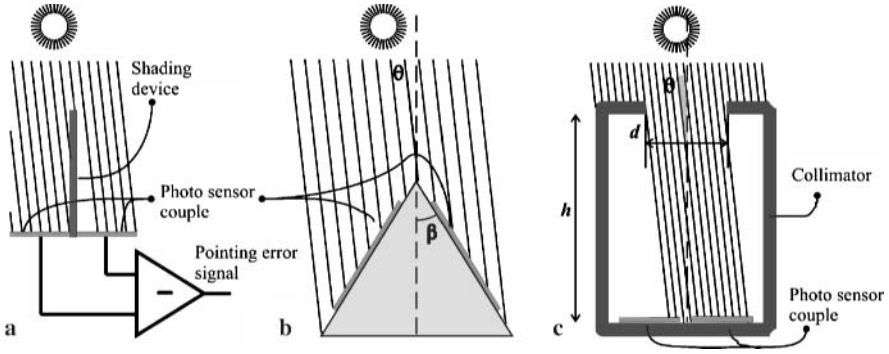

Fig. 11.7. Shade balancing principle (**a**) of sun-pointing sensors (**b**) Tilted mount of photo sensors to increase sensitivity (**c**); precise sun pointing by means of a collimator

tracking control system in several CPV technologies (see 'The Amonix High-Concentration Photovoltaic System' in this book).

In the early days of sun tracking, as another alternative to sun-pointing-sensor controllers, the possibility of digital computing of sun ephemeris, and converting this output into tracking-axes turning angles, gave way to (again using the control-theory term) open-loop controllers which required no feedback of sun-position measurements. These controllers were able, in principle, to continue tracking regardless of the degree of clarity of the sky, and easily programmed the management of non-tracking situations such as night or emergency stowing, e.g. when subject to high winds; however, a precise timing source must be provided to feed the computation of the ephemeris equations, and also, in implementations seeking sub-degree accuracy, some sensing device able to measure axes-turning angles must be provided. Heliostat fields in solar thermal energy, such as in DOE's precursory Solar One plant (10 MW, 1981), were the first to implement open-loop tracking, soon followed by a grand CPV forerunner such as ARCO's Carissa Plains plant (6 MW, 1985). Computers were still quite expensive at the time, so these first open-loop demonstrations were carried out in a centralized way in which a single computer continuously calculated turning angles for all trackers in the plant and transmitted them using a field data network. The advent of inexpensive microprocessors and embedded electronic systems enabled the development of specific open-loop tracking controllers at feasible unit prices, which enabled the autonomous control of every tracker in a plant. Autonomous tracking control is not only inherently more reliable due to its distributed approach, but also because of the elimination of the dependency on a complex and expensive field-communication system which, due to its extensive coverage, was frequently reported to be vulnerable to, for example, ground-loop currents. The first patents and publications proposing these specific open-loop controllers can be traced back to the 1980s [14], but it is the SolarTrak controller, developed in the early 1990s by Sandia Labs' Alexander Maish, that was the first serious and well-documented effort carried out in this direction.

An open-loop controller, however, even if operating on the very precise sun-ephemeris equations available to date, is affected – once connected in the field to its appointed concentrator – by many error sources which can highly degrade its final tracking accuracy well below its ephemeris' nominal value, and to the point of even missing the concentrator's specifications. Among these error sources, the most significant have a deterministic nature and result from a defective characterization of the concentrator by the controller, and operate over the transform employed to convert sun-ephemeris coordinates, usually in the azimuth-elevation horizontal topocentric format used in solar applications, into tracking-axis turns. Tolerances of the manufacturing, assembly and installation processes of a concentrator will produce some deviations with respect to specifications and, therefore, also to the assumptions made with regard to the sun coordinates to axes-turning-angles

transform. Drifts in the internal timing required for the computation of the sun ephemeris is the other major error source to be corrected. Second-order error sources, and also to some extent predictable ones, such as gravitational bending in wide-aperture trackers, the effect of mismatch in multi-secondary axis trackers, or even ephemeris inaccuracies due to the effect of local atmospheric refraction, have to be considered as well. Feedback of the tracking errors caused by the referred sources must be integrated into the control strategy in order to suppress them. This open-loop core strategy, blended with the feeding-back closed loop, is sometimes referred to as the "hybrid approach".

We can talk of basically two types of hybrid sun tracking controllers, whether we follow (a) the model-based calibrated approach, or the (b) the model-free predictive approach. The calibrated approach relies on a mathematical error model, able to characterize the set of systematic error sources responsible for degrading tracking accuracy below that provided by the core sun-ephemeris equations. After a full clear day session obtaining tracking-error measurements, these are used to fit the model parameters. Error acquisition is a time-consuming task. Some degree of automation in this process is required when used in large tracker fields, in order to permit the simultaneous setup of them all and avoid the need of personnel to carry out this task. After the calibration session, the error model tuned with these best-fit parameters will be used as the transform converting the sun coordinates supplied by the sun ephemeris to tracker axes' turning angles, and thus will in principle operate from then on, on a purely open-loop basis with no further requirement of tracking-error feedback.

Automatic calibration routines are commonly featured in electronic instrumentation products; moreover, very similar approaches to this type of hybrid sun tracking control are commonly found for the calibration of the pointing control of many telescopes in professional observatories worldwide, such as happens with the widespread TPoint software [15]. Among the early developers of this technique is Nobel Laureate Arno Penzias, the discoverer of the background radiation. When Penzias first joined Bell Laboratories, he was put on the pointing committee of an antenna built to communicate with the Telstar satellite. Aiming errors occurred because the steel antenna bent under gravity, wind load and temperature changes, and the antenna's gears were not perfect, and also its foundation was not perfectly horizontal. Penzias' solution was to calibrate it using an error model fitted by pointing to a known and precisely located radio galaxy [16].

On the other hand, the predictive approach to hybrid sun tracking [17] helps to avoid getting into any error modelling and its subsequent fitting. It intends instead to obviate initial assumptions regarding the tracking errors that will be encountered, thus seeking a general concept able to cope with any sort of tracking errors whatever the tracker design; however, to achieve this requires the integration of permanent tracking-error surveillance, implying,

as in the case of a calibration session, some scanning scheme to determine correct sun position. So, in this case, corrections to sun position provided by computed ephemeris will result from an estimation based on some set of past tracking-error measurements and estimations, and for this purpose the wide mathematical toolbox for time series forecasting is at hand. The more general form of this approach is presented in Fig. 11.8, in which everything begins with the computation of the sun ephemeris to provide a first set of sun coordinates. As represented, these ephemeres have to be corrected, due to whichever error sources or simply because the type of sun orientation coordinates employed are not matched with the real tracking axes employed, such as, for example, would happen if providing horizontal azimuth-elevation coordinates to a two-axis tilt-roll tracker. Some scanning scheme is used by the tracking axes to obtain precise sun pointing and the correct axes turning angles from which to obtain tracking-error measurements, which are then to enter the box labelled 'error forecasting' which produces corrections to be added to the next 'raw' sun-ephemeris coordinates.

The first implementation of this tracking-control approach is that developed by Inspira for the EUCLIDES CPV technology (see 'The EUCLIDES System' in this book), called *EPS-Tenerife* (Fig. 11.9), and in which its error-correction estimates are computed using one of the most simple and widely used time-series forecasting methods, as is exponential smoothing, however, in this case, with an adaptive scheme for the variation of its parameter. The required gathering of tracking-error measurements to feed the estimator is highly simplified whenever EUCLIDES is a single-axis linear trough and accurate sun-pointing measurements each time can be acquired by exploring with back-and-forth turns [18, 19]. Other model free hybrid approaches have been proposed by us such as the one which uses a discrete version of a classical proportional-integral (PI) controller as the error-forecasting method [17]. Correction estimation makes sense when precise sun pointing is a costly task, such as can happen when this is obtained through power-output maximiza-

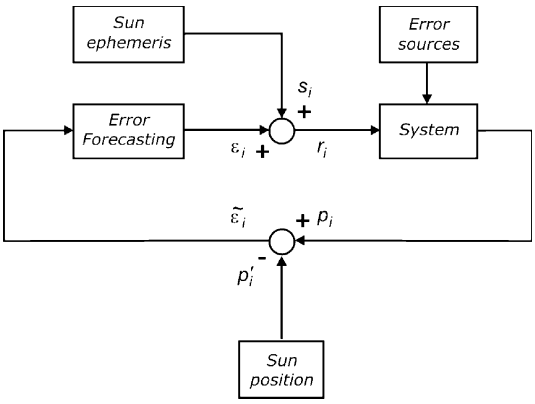

Fig. 11.8. Error-model free hybrid sun tracking control relying on error scanning and iterative forecasting

Fig. 11.9. View of the string of 14 *EPS–Tenerife* tracking controllers designed and produced by Inspira for the EUCLIDES 480 kWp CPV plant in Tenerife

tion, so that in this case prediction will, to some extent, reduce scanning time and increase mean tracking accuracy; however, as stated, some present concentrator tracking controllers work on a two-stage basis, first coarsely aiming based on sun-ephemeris computed coordinates, followed by fine pointing using a sun sensor. Leaving aside the discussed reliability of a sun-pointing sensor, and provided that it is always kept well aligned with maximum power output, this is a feasible method when pointing a sensor is simpler than seeking maximum power orientation, and can be classified with the hybrid model free approaches as the simplest case involving no forecasting at all.

11.4.2 Inspira's SunDog Sun Tracking Control Unit

Inspira's *EPS-Tenerife* tracking control unit made the correction estimates dependent on the tracking angle of the EUCLIDES single-axis tracker, and these estimates are kept in a memory-stored search table, one per each 1° tracking sector, being permanently updated based on the referred adaptive forecasting process. Even if these forecast estimates together with the tracking errors measured for their generation happen to vary continuously during the year, this variation is basically seasonal because it is mostly caused by the above-mentioned systematic characterization errors, which we can attempt to model and correct from the start, in this way making the scheme of permanent scanning movements unnecessary and thus reducing motor fatigue and increasing tracking accuracy. This is even more advantageous in the case of two-axis trackers which require more complex scanning routines, which further subtracts from the accurate tracking operating time.

The error model developed by Inspira, which could also be termed calibration model, assumes that the tracker's axes and their reference orientations have the same reference system as the horizontal azimuth-elevation coordinate system used by the ephemeris. This means that the axis connected to the foundation, also called by us the primary axis, points to the local zenith with its reference orientation pointing south, and the secondary axis, the one

which is fixed to the primary, always remains at right angles with it, and has its reference orientation pointing to the horizon – in other words, the ideal azimuth-elevation pedestal tracker.

The error model is based on a six-parameter kernel that characterizes the departure of the real tracker under control from the ideally assumed:

1. *Primary axis azimuth (φ) and zenith angle (θ)* These two parameters are the azimuth- and zenith-angle coordinates that determine the real orientation of the primary axis, which, regardless of the axes configuration, is always defined as the axis which is fixed to the ground. This is mainly an installation error due to the imprecise foundation of the tracker.
2. *Primary axis offset (β)* This parameter determines the location of the reference orientation of the primary axis. Reference orientation is usually determined by a specific sensor, or the index mark when working with incremental optical encoders directly installed in the primary axis. Misplacement of this sensor during manufacturing or its incorrect alignment at installation may cause this error. When $\varphi = \theta = 0$, β simply becomes the angular offset to the south.

   These first three parameters are in the referred order, the nutation, precession, and spin Euler angles, which relate any two reference systems with a common origin, and only these are required if our tracker has only one axis, the primary axis, such as in present polar, azimuthal, or EW or NS horizontal-axis trackers. When a secondary axis is attached to the primary axis, three more parameters are required, and the pointing vector is defined as that which is oriented by the joint action of the two tracking axes, and if aligned with the sun vector, it produces the maximum power output of the concentrator array.
3. *Non-orthogonality of axes (λ)* This parameter takes the value of the difference to the right angle between the primary and secondary axes. This is mainly a manufacturing error source, and a non-zero value for this angle implies the two-axis tracker is no longer ideal, and a cone of orientations around the primary axis will remain out of reach.
4. *Pointing vector axial tilt (δ)* The pointing vector is assumed to be normal to the secondary axis and is contained in the horizontal plane when this axis rotation is zero. The axial tilt of the pointing vector is the difference angle to a plane normal to the secondary axis. This error can have its origin in the defective assembly of the tracker's aperture frame, but also in the misalignment of the concentrator optics.
5. *Secondary axis offset (η)* The secondary-axis offset accounts not only for the difference angle between the plane normal to the primary axis and the reference orientation of the secondary axis, but also for the difference angle between this reference orientation and the plane containing the pointing vector and the secondary axis, i.e. a radial tilt which is the second value characterizing pointing-vector departure from assumptions. This error therefore derives from both the misplacement of the secondary

axis reference sensor or, again, the improper assembly of aperture frame or optics.

These six parameters appear in a $\mathbb{R}^2 \rightarrow \mathbb{R}^2$ function that consists of the composition of five partial transforms, which convert the ephemeris horizontal coordinates into pairs of angular rotations for both axes. For single-axis trackers only the first three parameters enter into play and it is the primary axis turning angle that is the valid output. Behaviour of this calibration function can be visualized through the usual grid transform representation in complex variable analysis (Fig. 11.10).

The fact that the assumed reference system for the tracker under control is that of an ideal pedestal tracker is just a convention, and the model is able to correct horizontal ephemeris coordinates to any one- or two-axis configuration, including others frequently used, such as, for example, the tilt-roll assembly (ideally $\varphi = \theta = \pi/2$). In order to maintain this generality of the model, no simplifying assumptions have been made regarding the transform parameters, which otherwise would restrain its application range.

As stated, the parameters characterizing a specific tracker and its in-field installation have to be fitted to a set of tracking-error observations, and due to the non-linear nature of the model, it is by means of numerical optimization techniques. The target has to integrate this numerical procedure in a low-cost embedded system, and therefore programming efficiency is required, as well as accuracy of the maximum likelihood estimation (MLE) function. The least-squares (LS) method was the MLE chosen which, even if there are other more robust estimators, this is by far the one that presents the most effective non-linear minimization techniques. The existence of local minima obliged to resort to the global optimization toolbox, and finally a clustered multi-start

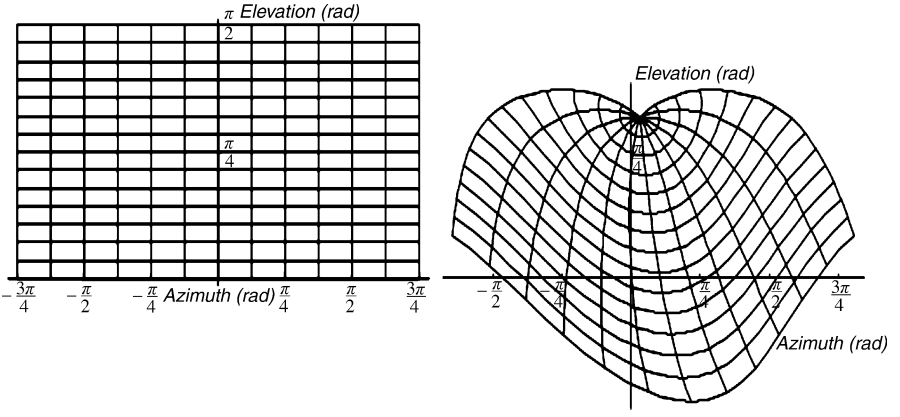

Fig. 11.10. Error-model transform of a rectangular grid in the Azimuth-Elevation coordinates plane into the two axes-turning-angles plane with parameter values $\theta = 30°$, $\lambda = 20°$, $\delta = -20°$

with Levenberg-Marquardt (LM)-based local searching [20, 21], was implemented. These local minima sometimes depend on the day of the year on which the tracking-error measurements are made, e.g. in NS-oriented single-axis trackers especially strong local minima appear when calibrating on the eve of the equinoxes. Fit robustness is further conferred by means of a pre-fit outlier filter discarding clearly defective tracking-error measurements.

The least-squares (LS) fitting routines integrated in the SunDog have been thoroughly tested, first on LS functions of the error model with different simulated error measurement collections produced by different vectors of error sources, and also more generally using the Moré [22] set of standard test functions, the common benchmark for optimization problems. In most practical cases model fitting for these simulated cases required convergence times in the 1-min range, time only surpassed in some unusual cases which, however, were solved in no more than 5 min. In order to verify the physical grounds of the error model, tests were carried out in one of Inspira's laboratory trackers in which several CPV modules were mounted in different ways (e.g. tilted mounts), which allowed the direct measurement of some of the error-model parameters, and after gathering a set of tracking-error measurements, the best-fit parameters obtained closely matched their measured counterparts.

Even if first-development prototypes relied on manual collection of tracking errors, this proved to be a tiresome and error-prone task which had to be automated in order to prevent outliers, and thus increased the accuracy of the corrected ephemeris. An automatic error-collection scheme was developed in which direct search of the alignment of pointing and sun vector to obtain each tracking-error measurement required the maximization of the concentrator's power output; however, in first instance and in order to avoid interaction with the inverter's MPPT, or to be obliged to dissipate a high power, an approximately equivalent variable, such as the CPV array's short-circuit current, was employed as feedback signal.

Sun-precise alignment proceeds in three stages: first, a coarse approach by maximizing the irradiance in a PV cell mounted parallel to the concentrator's aperture. Beyond this point, search proceeds blindly scanning by means of spiral search [23] until the sun enters the concentrator's acceptance angle and then a two-dimensional short-circuit current maximization is carried out [24], the complexity of which depends largely on whether the power output vs off-track angle function exhibits rotational symmetry or not.

The above-described capacities have been implemented in an electronic embedded system, based on an 8-bit microprocessor, along with the required chipset and sensors, to carry out the described algorithms and perform the analogue measurements, and also to provide motor-driving capacities (Fig. 11.11) [25, 26]. Remarkable hardware elements which further enhance performance are the temperature-compensation circuit devised to restrain drifts in the quartz oscillator responsible for internal timing, as well as its encoder decoding and interpolation subsystem which increases the axis-turn-

measurement accuracy. Named *SunDog* (from the notion that it 'always follows his master, the sun') it is supplied with *SunDog Monitor*, a Windows-based application to run in a locally or remotely connected PC as a virtual user interface. It also integrates an interchangeable modem for PSTN, RF, and Ethernet or GSM/GPRS Internet connectivity, which enables E-mail reporting and Web-based control and monitoring. Prepared for operation in harsh environments, it has been tested in electronic certification labs attaining CE labelling covering the corresponding EMC and electrical safety standards, and has also successfully passed climatic tests (temperature cycling, humid and high-salinity environments, water and dust tightness, etc.).

New features are now being implemented in the upcoming versions of the SunDog Sun Tracking Control Unit, features which partly involve the introduction of extensions in the error model accounting for the above-referred second-order error sources such as flexure effects on the pointing vector position, which are usually specific to the tracker concept employed. On the other hand, regarding the very important adjustment of internal-clock drifts, even if Internet connectivity or GPS might provide atomic time synchronicity, and this may be implemented in a cost-efficient manner in networked CPV tracker fields, the availability of high-accuracy ephemeredes provides an immediate and autonomous alternative to precise time-keeping. A time-drift parameter has been included in the model in such a way that it can be fitted with a tracking error set either, jointly with the rest of the parameters or individually within periodic time-adjustment procedures.

Finally, a new alternative to calibration has been devised based on the fact that the tracking error set is not necessarily obtained from the sun, as in principle any other light source with precise analytic kinematics, and with enough emitting power to extract a measurable output from the concentrator,

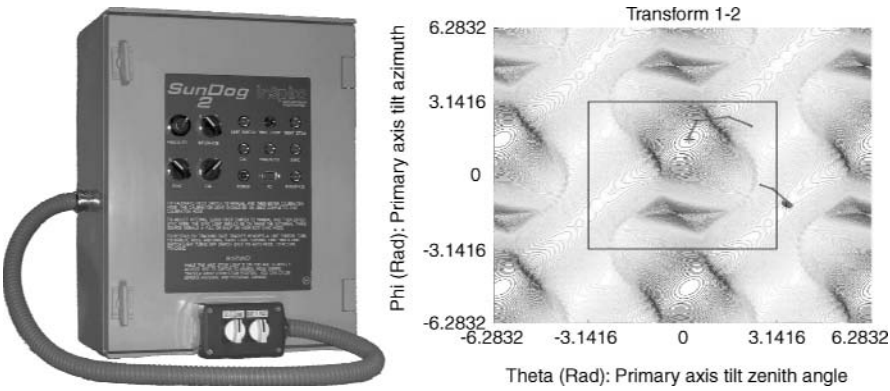

Fig. 11.11. SunDog STCU (*left*) and Levenberg-Marquardt local searches (*right*) in the least-squares function used to fit a simulated error-model transform using for visualization purposes only its two first parameters (φ, θ)

will suffice. In this respect, the full moon proves to be a good candidate, as far as it will enable night calibrations not interfering with concentrator's daily production, and furthermore, it will also permit these calibrations to be done with a maximum power-point bias but at much lower power levels than nominal, thus highly facilitating its ease of handling. As is well known, its 0.49° apparent diameter is very similar to the sun's diameter, whereas its irradiance is six orders of magnitude smaller than that of the sun, so its photo-generated current is still within reach of cheap current-sensing devices. On the other hand, the full-moon irradiance is three orders of magnitude above that of the most brilliant planets and stars, so it will be easily distinguishable by the concentrator when searching the night sky. For this purpose moon ephemeris and lunar-phase equations have been encoded in the calibration routines.

11.5 Sun Tracking Accuracy Monitoring

Assessment of sun tracking accuracy should not be overlooked during the development of CPV technologies, and even more by so those players raising very high-concentration concepts over the $100\times$ frontier. Some analyses point out that the acceptance angle of present designs in concentration optics may be overestimated even from a theoretical point of view, which, added to the still uncertain acceptance-angle losses inflicted on the overall system by mass assembly processes, may finally shrink the allowable tolerance and divert the entire burden to the tracking accuracy. Instrumentation for the monitoring of sun tracking operative performance, providing enough sensitivity to gauge the sub-degree accuracy ranges required by high-concentration systems, is therefore needed, and in this direction a Tracking Accuracy Sensor (TAS), based on a state-of-the-art solid-state image sensor, has been developed at Inspira [27]. This TAS, commercially named *SunSpear*, is essentially based on the so-called position sensitive device (PSD), a monolithic optoelectronic sensor, which is housed along with the signal conditioning, digitizing and transmission electronics, inside a-watertight enclosure which, in addition, integrates a sunlight-collimating tube placed right over the PSD's surface. The TAS is then installed on the aperture of the tracker to be monitored, and whenever the direct sunlight is received within its acceptance angle, the collimated sunbeam will impinge on the PSD surface with the sensor, then producing, in voltage form, the Cartesian coordinates of this sunspot, which can be further converted to an off-track angle with respect to the TAS' axis. The TAS is then linked by means of a serial connection to a PC which is to process the in-streaming sampling of sunspot coordinates, both displaying time series for significant variables and also producing its statistics for a specified time frame.

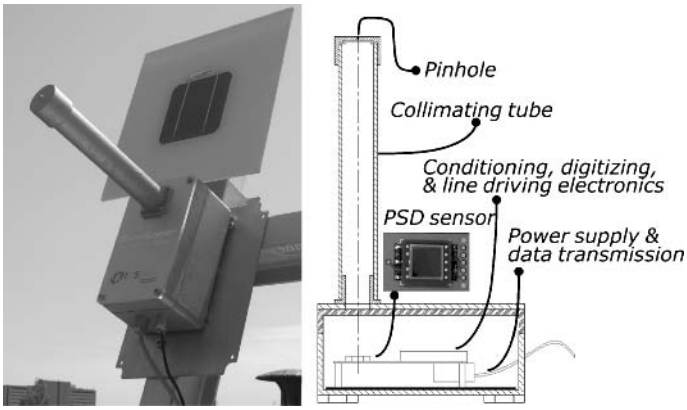

Fig. 11.12. The SunSpear Tracking Accuracy Sensor

11.5.1 Inspira's SunSpear Tracking Accuracy Sensor

There are very few past experiences on which to base the development of a sensor able to measure the incidence angle of direct sun radiation with respect to some built-in axis, at least in the PV field [28]; however, quite recently fairly accurate devices of this kind can be found in the aerospace sector which, based on CCD and CMOS arrays, contributes to satellite-attitude control [29]. These devices usually feature hemispheric acceptance angles which preclude the extraction of higher accuracies from their very high-resolution image sensors, nonetheless attaining the $0.05 - 0.01^\circ$ range. These devices are produced at very high cost due to their required compliance with spacecraft specifications, and usually on a custom-made basis without an explicit commercial intention; thus, even if they could serve our means, it is still worthwhile to develop a specific sensor.

The PSD sensor chosen for the *SunSpear* TAS has no discrete elements such as in CCDs, and provides continuous data of a light spot on its surface by making use of the surface resistance of a planar PIN photodiode. Due to its analogue nature, these sensors feature excellent position resolution in the micron range and very high speed; moreover, they detect the "centre of gravity" position of the light spot and are very reliable. As usual, placing a light collimator on top of this sensor will produce the required light spot and enable the measurement of the angle of the incoming light beam with respect to the sensor's axis, where the acceptance angle and also the angular resolution of this measurement is basically determined by the height of the collimator's pinhole over the sensor's surface. With *SunSpear*'s present design we can achieve resolutions in the 1/1,000th$^\circ$ range at a $\pm 1^\circ$ acceptance angle (Fig. 11.12).

Being concerned about the precision requirements in the TAS assembly, mostly regarding PSD and the collimator's pinhole alignment, we modelled

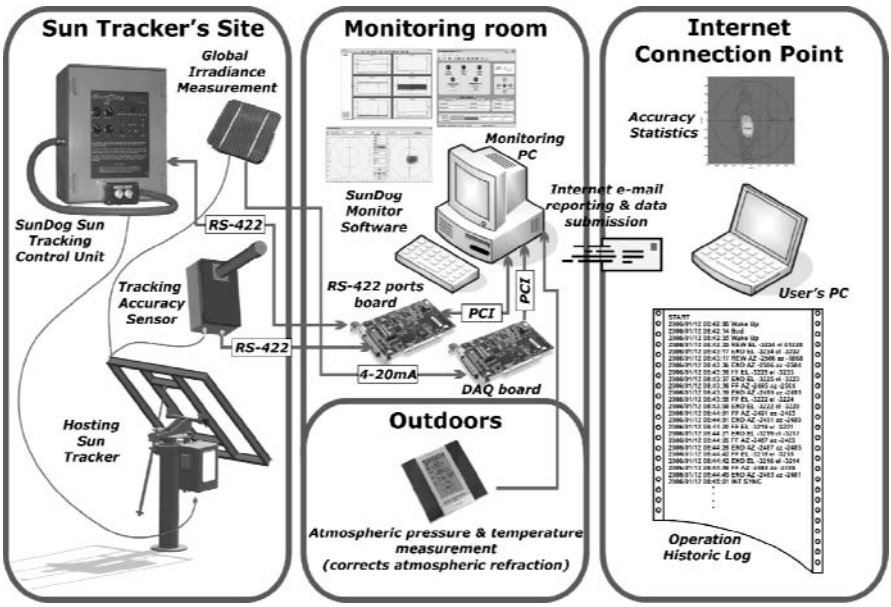

Fig. 11.13. Tracking accuracy monitoring system

the setup and were able to prove its very low sensitivity to misalignment, thus enabling a tolerant fabrication; however, in order to take advantage of future resolution improvements in PSD technology, which may become hampered by a lack of misalignment characterization, a calibration procedure has been developed that requires only the processing of PSD readings when mounted on a rotating axis.

Along with the off-track angle-measurement system, the TAS is completed by a custom-made electronic system that provides signal conditioning to the PSD's output, AD conversion and driving a RS-232 serial output. It is this electronic system that hosts the PSD sensor in its PCB and is contained in a watertight enclosure which also provides a fixture point for the machined collimator tube.

11.5.2 The Monitoring System

The sampled position data generated by the TAS is sent through a serial link to a PC which runs a software application able to store it and also displays it in real time. It also converts sunspot Cartesian coordinates to off-tracking angles, generates plots and statistics of selected tracking periods, and periodically E-mails tracking data and reports. All of these features have been integrated as add-ons in its *SunDog Monitor* interface software (Fig. 11.13).

The first application given to the tracking-error monitor was to enable the assessment of the tracking accuracy of all hybrid tracking routines, which,

even if they are based on an error model or on error-forecasting schemes, all have in common the requirement of obtaining power output feedback, or some equivalent of this, from the CPV array in order to get precise sun-position measurements. The method used to test these strategies, without having to mount a CPV array and its power-output-measurement electronics, relies on using the TAS as a virtual power output, i.e. perfect alignment of the TAS built-in axis with the solar vector is assumed as peak power output. Aside from the simplicity, an added advantage of this setup is that in principle it allows for very precise measurements at a faster rate than real power output maximization, whenever the MPPT stage is involved. In this way this method exposes the specific weaknesses of a certain tracking strategy, when almost not affected by errors in the sun-position measurements whether these are used to feed calibration model fitting or error-forecasting schemes. As stated, due to the positioning resolution limitations inherent in the mechanical drive of any solar tracker, it is impractical to try to precisely position the tracker to obtain maximum power output or equivalently perfect TAS pointing. In the case of calibration against TAS, this procedure is much simplified, and very precise positioning coordinates for perfect TAS sun alignment are obtained from the precisely timed crossings of the sunspot centroid in the PSD surface with the Cartesian reference system axes.

Once these calibration measurements are completed, some selection of them will be fed into the error model of Levenberg-Marquardt LS fitting routine, the basic parameters of which, regarding, for example, the clustered multi-start optimization routine or the stopping criteria, can also be fixed within *SunDog Monitor*. Depending on the selection of error observations, we will get some variation in the best-fit parameters obtained, and *SunDog Monitor* offers the possibility to periodically change the parameters being used by its connected *SunDog* unit for sun-ephemeris correction, in order to jointly obtain the tracking accuracy statistics of an assortment of varying sets of parameters, and thus helps to estimate those measurement schemes that obtain the best performance. In addition, the *SunDog Monitor* version implements these tracking-accuracy-assessment tools when using the TAS as virtual power output for calibration, and features additional resources to further restrict tracking-error margins by integrating the connection with an outdoor thermometer and a barometer. Temperature and atmospheric pressure readings are employed in the computation of atmospheric refraction corrections to the sun-ephemeris elevation coordinate, based on Bennet's model [30]. Measured values of these corrections have been reported to amount to a mean of 0.6° for near the horizon elevations [31], and as is seen in the next section, they can have a measurable impact on a tracking-accuracy-monitoring campaign. These corrections are applied to computed sun ephemeris both in the error-model-fitting stage and also afterwards, during real-time tracking, in which the corrections are periodically transmitted to the *SunDog* controller. Finally, and also contributing to tracking-accuracy enhancement, *SunDog*

Monitor can use top-quality arc-second precise ephemeris during the error-model-fitting data thanks to a built-in direct connection to the USNO MICA software [32].

The second and more general application of the tracking-error monitoring system consists of directly measuring the real tracking accuracy of a concentrator. The system has to be initially calibrated against the peak power output of the CPV array, i.e. recording the sunspot coordinates on the PSD surface when maximum power is delivered, and taking these as the TAS' reference system origin when converting its readings to off-track angle. Provided that the effect of the tracker's self-weight and its CPV array payload upon the bending of the concentrator's structure varies with its orientation, the calibration is carried out at different positions and the reference points to use in off-track angle conversion at each orientation are interpolated from them. This second function is independent of the tracking-control means employed; however, during calibration it requires combined automatic readings both from the TAS and array's power in order to precisely locate the sunspot coordinates on the PSD when power output is maximum. In both of its operation regimes the tracking-error monitor completes its performance by computing and displaying configurable probability density plots of the sunspot over the PSD surface, time series representations of the off-track angle and related variables, and overall statistics for selected time periods.

11.5.3 Accuracy Assessment Example of the SunDog's STCU Strategy

Following the procedure described above, we present here a long-term monitoring performed with the tracking-error monitor devoted to the assessment of the tracking accuracy performance of a *SunDog STCU*, when controlling one of Inspira's small-aperture ($4\,m^2$) laboratory sun trackers. The calibration was made upon an error-measurement session carried out on 31 January 2006 that included 368 points. Four different model-based hybrid routines were set to compete:

- *Case no. 1*: The six core parameters of the SunDog STCU proprietary error model where fitted directly in the *SunDog* processor using all the error measurements. This case represents the normal *SunDog* performance.
- *Case no. 2*: Same as case no 1, but the best-fit values for the six parameters were calculated by the *SunDog Monitor* SW running on a PC, with its added float-point accuracy, and also using the superior performance of the MICA ephemeris when compared with the analytic ones computed by SunDog (0.03° mean accuracy taking MICA as reference). This case works with more precise fit than that being attained by the LM embedded implementation in *SunDog*; however, as in case no. 1, once fitting is completed tracking control relies solely on SunDog and its less accurate built-in ephemeris. It represents an operative alternative in which SunDog

units operating a CPV plant are networked and send their tracking-error measurement sets for fitting to a more powerful central computer.

- *Case no. 3*: Same as case no. 2, but temperature and atmospheric pressure measurements are activated, and atmospheric refraction correction in the ephemeris' elevation is integrated both during the tracking-error acquisition session and also later providing the *SunDog STCU* real-time measurement pairs every 30 s for it to internally calculate the corrections. This case is, in principle, the one which should present the highest performance and is useful to assess the possibility of integrating a thermometer and barometer in the *SunDog STCU* hardware.
- *Case no. 4*: A simple two parameter linear model is used to fit the error measurement set essentially obtaining the mean offsets in both tracking axes. This is the most straightforward tracking-error model which requires no numerical fitting algorithm, and in the same way that the nominal *SunDog* performance of case no. 1 should rank below the enhanced no. 3, this case serves as a low-performance benchmark to rate the benefit of using the *SunDog* non-linear model along with its fitting procedures.

The monitoring ran uninterruptedly till 30 April 2006. Every day tracking control of the lab tracker was assumed by a different case, following a fixed sequence. Every TAS sample includes, along with the Cartesian coordinates of the sunspot on the PSD surface, the incidence light level. This incidence light-level measurement is to be above a certain threshold to ensure the minimum required resolution, and in order to accept a monitoring daily session 90% of its samples were to have its light level above this threshold. This basically means that only full clear-sky days were considered for the analysis in order to compare the performance of the different cases on identical grounds. This means that at the end of the monitoring period some cases had more valid days than others, but nevertheless all had enough to draw some interesting conclusions. For every day the tracking accuracy statistics where calculated: mean; standard deviation; and the daily probabilities of accuracies below 0.1 and 0.05°. Probability density and distribution functions where plotted, and also the probability density of the sunspot point over the PSD surface was obtained.

In Fig. 11.14 daily probability density plots of the collimated sunspot over the PSD surface are included for all four cases, both for the first valid day and the last one comprised in the monitoring period. The 0.1° and 0.2° tracking accuracy rings are displayed in these plots. The purpose of presenting plots for the two ends of the monitoring period is to see how tracking accuracy may drift with time. In Fig. 11.15 (right) a tracking-accuracy statistics sample is shown. This is representative of the best ratings obtained with the case no. 3 setup in this monitoring period, showing a mean daily tracking error of 0.05°, with standard deviation 0.02°, and having accuracy better than 0.1° with 98% probability and better than 0.05° with 50%. Also shown is the sunspot trace over the PSD's surface from which all statistics are obtained. Also on the

left side of Fig. 11.15 the daily plot of the tracking error is presented and, as is seen, this may also prove to be useful in detecting positioning resolution defects in a certain tracking drive, such as occur in the two error peaks which appear symmetrically with respect to solar noon, and which involve a momentary unleashing of the drive's backlash at that precise elevation in which push-and-pull loads equate in the tracker's aperture.

Figure 11.16 plots the evolution of daily mean-tracking error for the four cases during the monitoring period. The most obvious result, as can also be inferred from density plots in Fig. 11.2, is the superiority of the complete six-parameter error model (cases 1 – 3) over the simplified mean offsets model benchmark (case 4); moreover, when the former drifts further apart during monitoring period, and as is seen in its last recorded density plot of 11 April 2006, it is finally incapable of entering the 0.1° ring with its mean accuracy rising over 0.2°. In addition, a more subtle drift is found in the tracking errors of cases 1 and 2 which disregard the atmospheric refraction effect. Even if the accuracy of case 3 was already slightly better than that of cases 1 or 2 from the start, just after the calibration day, case 3 maintains the same ratings over the entire reported monitoring period, whereas cases 1 and 2 suffer a slight decrease in accuracy clearly noticeable when entering the second monitoring month. The main reason for this effect is that calibration is done in winter when sun elevations are lower, and therefore the atmospheric refraction correction is relatively more important during the day. In cases 1 or 2 the effect of atmospheric refraction is erroneously taken for an elevation-axis-offset effect and absorbed by the corresponding error-

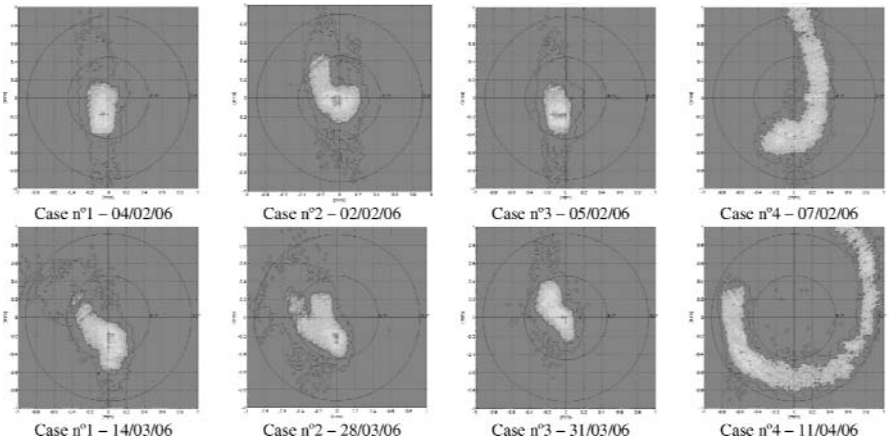

Fig. 11.14. Daily probability density of the sunspot over the PSD surface for the first and last monitoring day in each of the four calibration cases. The 0.1° and 0.2° off-tracking circles are represented. Mean value approaches zero with increasing precision of calibrated ephemeris, and standard deviation relates to positioning resolution

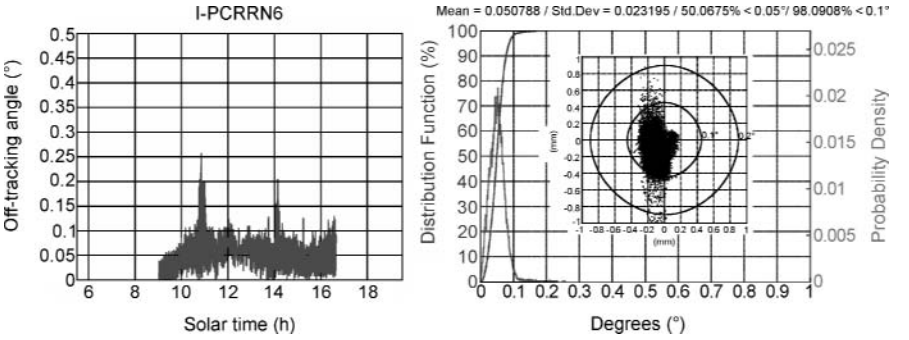

Fig. 11.15. Off-tracking angle during a day remains below 0.1°, except for two symmetric points with respect to noon, at which aperture elevation has equal push and pull forces, thus releasing backlash (*right*). A typical daily off-track angle probability density and distribution functions with 0.05° mean and 0.02° standard deviation, with superimposed sunspot trace over the PSD

model parameter (secondary axis offset above). This defective identification is exposed when approaching summer, and low elevations requiring atmospheric refraction correction become relatively less important. Mean tracking error slightly increases as seen in Fig. 11.4, and with regard to the probability distribution, first 93 – 95% probabilities for errors below 0.1° decrease to 83 – 85%. Also remarkable is the fact that cases 1 and 2 have a similar behaviour and no significant advantage seems to derive from using the PC's higher accuracy float-point arithmetic for the model parameter fitting, or the very accurate MICA ephemeris which, based on the interpolation of tabu-

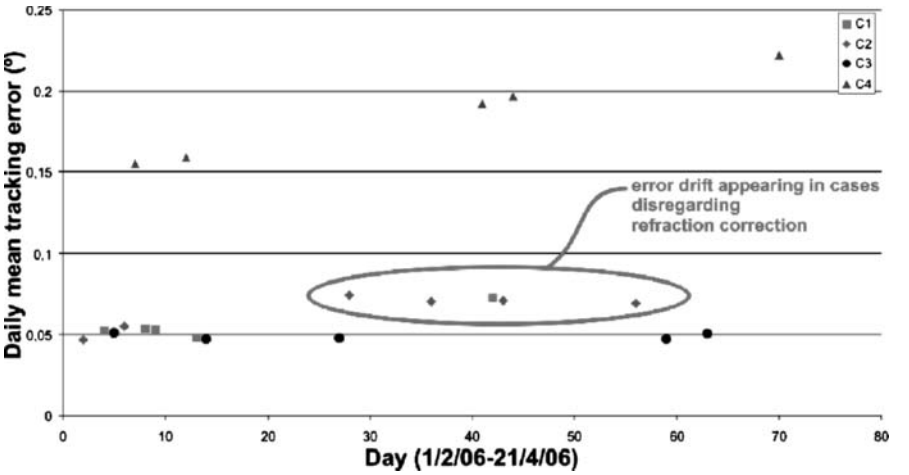

Fig. 11.16. Daily mean tracking error for the fully clear days during the 3-month monitoring period

lated numerically integrated solutions of the equations of celestial motion, are not feasible for a low-cost embedded integration.

References

1. Schmela M. Concentration Please! Photon Int 1, pp. 26–28, 2000
2. Lepley T, Hammond B, Harris A. Evaluation of tracking flat plate and concentrator PV systems. Proc 26th IEEE PV Specialist Conference, Anaheim, 1997
3. Swanson RM. Photovoltaic concentration. In: Handbook of photovoltaic science and engineering, eds. Luque A. and Hegedus S. Wiley, 2003
4. Hering G. Lords of the desert. Photon Int July 7, pp. 50–60, 2005
5. Welford WT, Winston R. The optics of nonimaging concentrators. Academic Press, New York, 1978
6. Randall DE, Grandjean NR. Correlation of insolation and wind data for SOLMET stations. SAND82-0094, Sandia National Laboratories, 1982
7. Luque-Heredia I et al. A subdegree precision sun tracker for 1000× microconcentrator modules. Pro 3rd World Conference on Photovoltaic Energy Conversion, Osaka, 2003
8. Luque-Heredia I et al. Modelling structural flexure effects in CPV sun trackers for a SunDog STCU implementation. Proc 21st European Photovoltaic Solar Energy Conference, Dresden, 2006
9. Welzl E. Smallest enclosing disks (balls and ellipsoids) New results and new trends in computer science (H. Maurer, ed.) Lecture Notes Comput Sci 555, pp. 359–370, 1991
10. McCay TE. Sun tracking control apparatus. United States Patent no. 3,917,942 1975
11. Luque A et al. Project of the Ramón Areces Concentrated Photovoltaic Power Station. Proc 13th IEEE PV Specialist Conference, Washington, 1978
12. Maish A. The SolarTrak Solar Array Tracking Controller. SAND90-1471, Sandia National Laboratories, 1991
13. Quero JM et al. Light source position microsensor. Proc IEEE International on Circuits and Systems, Sidney, 2001
14. Weslow JH, Rodrian JA. Solar tracker. United States Patent no. 4,215,410 1980
15. Software Bisque, http://www.bisque.com/Products/TPoint/TPoint.asp, 2004
16. Bernstein J. Three degrees above zero: Bell Labs in the Information Age. Scribner and Sons, New York, 1984
17. Luque-Heredia I, Gordillo F, Rodríguez F. A PI based hybrid sun tracking algorithm for photovoltaic concentration. Proc 19th European Photovoltaic Solar Energy Conference, Paris, 2004
18. Arboiro JC, Sala G. Self-learning tracking: a new control strategy for PV concentrators. Progr Photovoltaics, 5, pp. 213–226, 1997
19. Luque-Heredia I et al. CPV sun tracking at Inspira. Proc 3rd International Conference on Solar Electric Concentrators for the Production of Electricity or Hydrogen, Scottsdale, 2005
20. Marquardt DW. An algorithm for least-squares estimation of non-linear parameters. J Soc Industrial Appl Math 11, pp. 431–441, 1963

21. Törn AA. Clustering methods in global optimization. Preprints of the 2nd IFAC Symposium on Stochastic Control, Vilnius, 2, pp. 138–143, 1986
22. Moré JJ, Garbow BS, Hillstrom KE. Fortran subroutines for testing unconstratined optimization software. ACM Trans Math Software, 7, 1, pp. 17–41, 1981
23. Baeza-Yates RA, Culberson JB, Rawlins GJE. Searching in the Plane. Inf Comput 106, 234, 1993
24. Brent RP. Algorithms for finding zeros and extrema of functions without calculating derivatives. PhD thesis, Department of Computer Science, Stanford University, 1971
25. Luque-Heredia I et al. SunDog STCU: a generic sun tracking control unit for concentration technologies. Proc 20th European Photovoltaic Solar Energy Conference, Barcelona, 2005
26. Luque-Heredia I et al. Spanish patent no. 200501330, 2005
27. Luque-Heredia I, Cervantes R, Quéméré G. A sun tracking error monitor for photovoltaic concentrators. Proc 3rd World Conference on Photovoltaic Energy Conversion, Hawaii, 2006
28. Galbraith G. Development and evaluation of a tracking error monitor for solar trackers. SAND88-7025, Sandia National Laboratories, 1988
29. Zabiyakin AS et al. Sun sensor orientation and navigation systems of the spacecraft. Proc SPIE International Society for Optical Engineering, 3901, 1999
30. Bennett GG. The calculation of atmospheric refraction in marine navigation. J Inst Navigation 35, 255, 1982
31. Schaefer BE, Liller W. Refraction near the horizon. Publications of the Astronomical Society of the Pacific, 10, 1990
32. U.S. Naval Observatory. Multiyear interactive computer almanac 1800-2050. Willmann-Bell, 2005

12 The Amonix High-Concentration Photovoltaic System

V. Garboushian, K.W. Stone, and A. Slade

12.1 Introduction

Amonix Incorporated (Torrance, Calif.) was established in 1989 to develop and commercialize a solar high-concentration photovoltaic (HCPV) system based upon a custom silicon cell developed by Amonix in collaboration with the Electrical Power Research Institute (Palo Alto, California). By optically concentrating large areas of sunlight onto small-area solar cells, HCPV systems provide a primary benefit of semiconductor material cost reduction. The HCPV systems, however, do require additional components to those needed by fixed flat-plate PV systems. The additional components required are:

1. An efficient optical concentration system (lenses and/or mirrors)
2. A structural system that can support the solar cells and the optical components and maintain their respective orientations.
3. A tracking control and drive system that establishes and maintains, throughout the day, accurate optical alignment between the sun, optical components and solar cells.

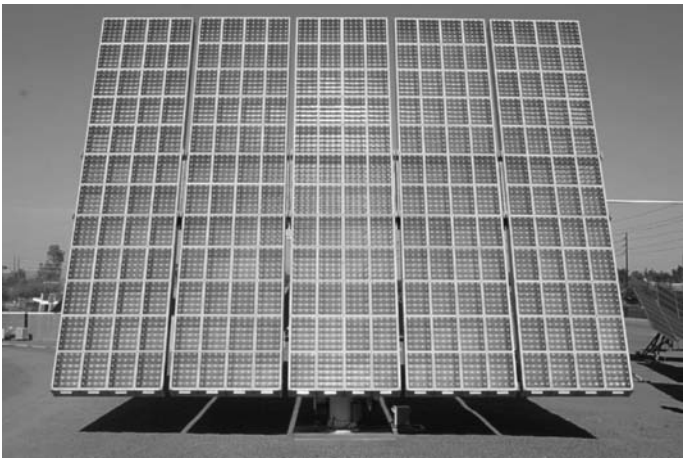

Fig. 12.1. An Amonix 25-kW unit in operation at the Arizona Public Service STAR facility in Phoenix, Arizona

Amonix has focused on utility-scale applications for solar electricity generation, such as the one shown in Fig. 12.1. This chapter describes the development, fabrication, installation and performance of the Amonix HCPV system.

12.2 Why Solar-Concentrating Photovoltaics?

Before photovoltaic systems can provide a substantial part of the world's need for electrical energy, there needs to be a large reduction in the cost. Studies conducted by the Department of Energy (DOE) [1], Electrical Power Research Institute (EPRI) [2], and others [3] concluded that concentrating solar energy systems can eventually achieve lower cost than conventional flat-plate PV power systems. The lower cost results from the following:

1. Lower material expense. The semiconductor material for solar cells is a major cost element of all photovoltaic systems; therefore, reducing the amount of required solar cell material is an effective approach to lowering PV system cost. Amonix has pursued this approach by using low-cost Fresnel lenses to focus large areas of sunlight onto small solar cells, which reduces the required cell area/material by over 500×. A 6-in. wafer used in a flat-plate PV system produces about 2.5 W, but it produces the equivalent of 1000 watts under concentrated sunlight in the Amonix system, as illustrated in Fig. 12.2.
2. Higher cell efficiency. Concentrating PV cells achieve higher efficiencies than do non-concentration PV cells. Flat-plate PV silicon cells have efficiencies in the range of 8 – 15%, whereas the Amonix concentrating silicon cell has an efficiency of over 27%. Multijunction concentrating cells are still in the developmental stage but have achieved efficiency greater than 37%.
3. Increased annual energy production. Increased annual energy production is achieved by the incorporation of two-axis sun tracking which is an inherent requirement in any concentrating system. All high-concentration systems require a sun-tracking control system. This improves the annual energy generated per installed kilowatt by reducing cosine losses,

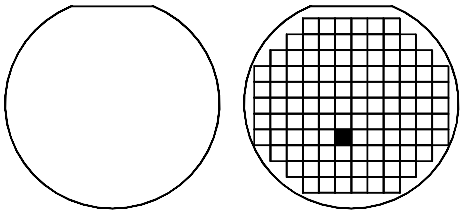

Fig. 12.2. Concentrating reduces the material cost per watt

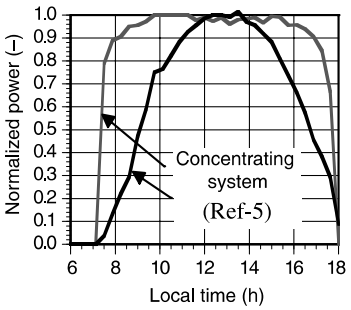

Fig. 12.3. Daily power produced

as shown in Fig. 12.3. Data on the annual energy generated by existing flat-plate PV systems illustrate this point: the average annual energy produced by 19 different fixed flat-plate installations in California ranged from 1000 kWh per rated kilowatt to 1500 kWh per rated kilowatt. As is shown later, the Amonix system generates in excess of 2000 – 2200 kWh per rated kilowatt in the Phoenix, Arizona, and Las Vegas, Nevada plants.

12.3 Solar Cell Development

The inherent very-high-efficiency point contact, rear-junction solar cells that are used in the Amonix system were first published by R.J. Schwartz and M.D. Lammert at Purdue University in the 1970s (Fig. 12.4). The structure proposed then is quite similar to that currently fabricated by Amonix. The high efficiency is derived from the combination of zero metal shadowing, efficient light trapping (textured top side and reflective bottom) and point-contact design for reduced recombination. The initial device design utilized

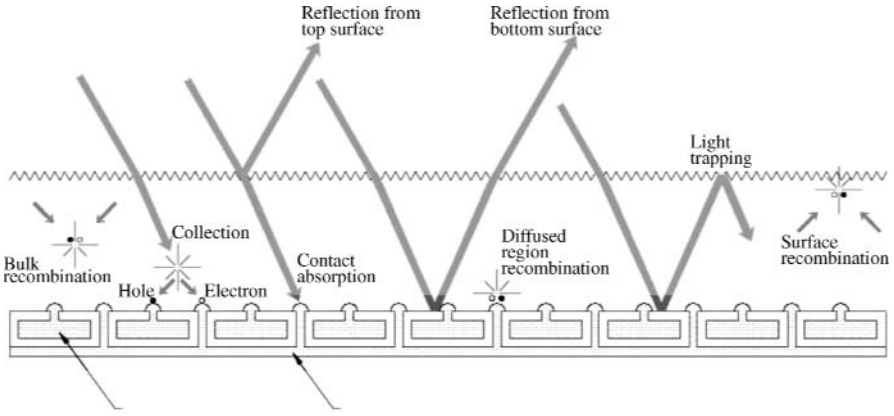

Fig. 12.4. Cross section of the Amonix point-contact, rear-junction solar cell

100-μm-thick silicon with the n and p (negative and positive) contacts on the rear of the cell, on a pitch of about 200 μm. Amonix still uses thin silicon (between 100 and 125 μm), although the pitch of the n and p regions has been reduced below 100 μm. A significant body of work was produced at Stanford University on the science of this device's operation, such as the effect of front-surface recombination velocity, Auger recombination and determination of the recombination due to heavily diffused regions. These contributions to semiconductor science were very applicable to the point-contact, rear-junction solar cell, as was evident by the device efficiency improvements that were achieved by the Stanford group. By the mid- to late 1980s, the foundation had been laid for the design of an efficient concentrator silicon solar cell, and the next challenge was to manufacture this cell; however, various design hurdles remained, such as how to overcome the solar cell's efficiency degradation when exposed to UV radiation. These design problems led EPRI (Electrical Power Research Institute), which was funding the solar cell's development, to contact MA/COM of Torrance, California. MA/COM, a company with experience in radiation protection of silicon microelectronic devices, was able to achieve UV stability in the concentrator solar cells. The effort then moved towards manufacturing. A company called Acrian was involved in this work, but they soon discontinued their efforts due to consistently low electronic yields. Although the concentrator cell design had achieved high sunlight-to-electricity conversion efficiency, the rigors of industry and manufacturability had not yet been effectively addressed.

In the 1990s, both Amonix and SunPower developed concentrator cell manufacturing processes with increased yield rates, although the cells were of lower efficiency than Stanford's demonstration cells. These acceptable-yield manufacturing methods produced enough cells for large-sample field installation and performance characterization. Many companies were initially involved in this, and field testing showed that the devices were indeed stable under various environments. The availability of concentrator solar cells also allowed various concentrator PV companies to test their sunlight concentrating/tracking systems using solar cells that were actually suitable for high-concentration sunlight. Amonix has almost single-handedly demonstrated long-term reliability of its point-focus, refractive-concentrator system. Solar System of Australia has carried out long-term field experience with its reflective-concentrator system – both companies using the silicon point-contact rear-junction concentrator cell to gain such experience.

SunPower, however, discontinued manufacturing their concentrator cell. This placed the system-based concentrator PV companies in a precarious position: From where would they obtain silicon concentrator cells, when Amonix was the only other company that can produce the cell, but Amonix was not selling the cell to anyone? The only alternative, viable or otherwise, was for system-based concentrator PV companies to start trial of the multijunction concentrator cells. Due to the now limited supply (outside of Amonix) of sil-

icon concentrator cells, most of the research community has become devoted to the development of multijunction cell technology.

Although the research community has thus largely abandoned the silicon concentrator cell, the impact on Amonix has been negligible. The next stage of development for the silicon concentrator cell is of cost reduction and mass production – disciplines primarily conducted internally in a company and thus without the input of university researchers. What is Amonix's current status of cell development and production? In the early 2000s the semiconductor industry went from boom to bust, thus enabling Amonix to work more closely with semiconductor factories to develop a simplified, though robust, process for producing these cells in what was then newly-found capacity. The simplified process was first run in September 2002 and has been run various times since (without change) to produce the (approximately) 1 MW of concentrator cells that Amonix required for field testing its fifth-generation system. During this time Amonix also tested some production cells at Fraunhofer Institute in Germany and claimed the world record for silicon solar cell efficiency at 27.6% – almost double the efficiency of the standard silicon solar cells produced for flat panels. Since then, Amonix's cell size has been reduced by 40%, with sunlight concentration increased in proportion, further reducing cost.

Current challenges being undertaken are to manufacture the cell in consistently high volumes and to reduce the process cost through experience and process control stability. This work is being done in a low-tech manufacturing environment so that the overhead cost of production can be substantially reduced.

12.4 HCPV Development

Amonix knew that the development of the HCPV system would meet many challenges towards achieving market cost and performance requirements. The market cost goals would place demands on the manufacturing cost, the installation cost and the operating cost. In order to achieve these goals, the system designers gave consideration to:

1. System manufacturability. The system design (a) should minimize the amount of required material, (b) should not require precise structural tolerances, (c) should minimize the quantity of manufacturing steps and processes, and (d) should be automation-manufacturable, in order to reduce labour cost.
2. Transportation. Components must be transported to the factory, and completed systems must be transported to the installation site. The amount of transportation, and therefore transportation costs, should be minimized. Consideration must be given to the highway transportation limitations of different states.

3. Installation time and procedures. Due to the typically remote desert siting of many large-scale PV installations, and due to the associated vulnerability to weather conditions, consideration should be given to (a) minimizing site installation time, and (b) choice of appropriate installation equipment.
4. System reliability. Since the costs of field retrofits and field maintenance are very high, the system design should be intrinsically reliable. The system should incorporate remotely accessible, diagnostic information acquisition that can be used for monitoring system performance and for planning necessary maintenance.
5. Operation requirements. The system operation should be fully automatic, to eliminate the requirement for an operator.

The performance specifications should consider:

1. The performance life of the system, subsystems and components.
2. The environment that the system will encounter in the intended market region. Although the market region might be limited to the 'solar belt' around the world, the operating specification should include the temperature, wind, snow, humidity, etc., extremes of these regions.

In order to minimize commercial risk, Amonix's development plan included the fabrication and complete field testing of its prospective designs, as illustrated in Fig. 12.5. The lessons learned from this field testing, as well as from the manufacturing and installation processes, were incorporated back into the system design. The systems were installed at different sites in the southwest, including Texas, Georgia, California, Nevada and Arizona.

During its first few years of operation (1989–1992), Amonix was focused upon the development of a stable, high-concentration back-junction silicon cell, and upon establishing manufacturing capability with semiconductor foundries. In late 1991, the efficiency of the Amonix cell was measured at 26.5%. In 1992, once the solar cell's performance and stability were well on their way to being established, Amonix began investigating system designs for integration with its back-junction silicon cell. A Fresnel lens system was selected for sunlight concentration. An enclosed support structure was designed

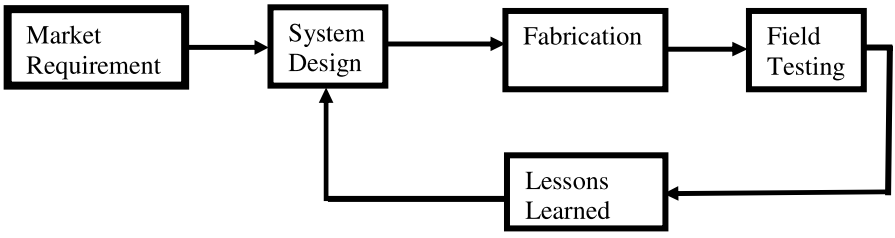

Fig. 12.5. The Amonix development plan depended upon lessons learned from field verification testing

to house, and to establish relative alignment between, the Fresnel lenses and solar cells. This support structure would be mounted onto a single pedestal equipped with elevation and azimuth drive systems.

The first prototype 20-kW system was deployed at Arizona Public Service (APS) Solar Test and Research (STAR) facility in Tempe, Arizona, in October 1994. A second prototype system was installed at the PVUSA facility in Davis, California, in September 1995 as part of the Emerging Technical Program (EMT-3). In late 1996, 20-kW systems were installed for both Nevada Power Company (NPC) and West Texas Utilities.

These prototype installations of the Amonix HCPV system were limited to single-site systems, primarily for demonstration and utility evaluations. In 1999 Amonix contracted with Arizona Public Service (APS) to install 300 kW of the HCPV system within APS's service area. This project represents the largest deployment of high-concentration PV in the world at this time.

In May 2000, three 20-kW systems were installed, and began producing power, at the APS STAR facility. Four 25-kW systems were installed at an APS site in Glendale, Arizona. Amonix's first 35-kW system was installed at the APS STAR facility in July 2001. Two more 25-kW systems were installed later that same year. Five more 25-kW systems were installed in 2002 at the APS STAR facility. Five 35-kW systems were installed at an APS site in Prescott, Arizona, starting from January 2003.

In late 2003, a project began to install an Amonix High Concentration Photovoltaic (HCPV) system at the Centre for Energy Research, located on the campus of University of Nevada, Las Vegas. This project is a joint effort by UNLV, Amonix and Arizona Public Service under the direction of the National Renewable Energy Laboratory (NREL) and funded by Nevada Southwest Energy Partnership. The primary purpose of the project is to generate a database on the performance and reliability of the system.

In 2006, three 25-kW systems were installed at the Clark Generating Station of the Nevada Power Company in Las Vegas.

12.5 Application

Amonix's HCPV system has been designed to serve a variety of power needs and applications. The HCPV system can be sized for generation capacities of 5, 10, 15, 20, 25 or 35 kW. Early in the development, 15- and 20-kW systems were fabricated and field tested. Since 2001, only 25- and 35-kW systems have been fabricated and field tested. Some of the designed applications of the HCPV system are:

1. Utility-scale, grid-connected power. Amonix's MegaModule Generating Systems can be combined to form multi-megawatt power farms that deliver power directly into a utility's electrical grid system. Such applications allow utilities to diversify their fuel mix and become less reliant upon

traditional coal- or natural gas-fired generators. Energy generated by the HCPV systems is clean and environmentally benign. The HCPV system can be used to reduce the utility's peaking load during the hot summer months. The modular design of a multi-megawatt HCPV system allows its generating capacity to be incrementally brought online, following the daily peak power curve. The modular design also allows decentralized siting of generating capacity, helping to relieve overloaded transmission lines and defray the high cost of installing new grid transmission lines. Unlike most conventional power stations, on which construction must be completed before power production can begin, an HCPV system will begin producing power when its first array is installed and field-wired. Figure 12.6 shows five 35-kW HCPV systems connected to Arizona Public Service Company's electrical grid.

2. Village/rural electrification. Amonix's HCPV system has been designed for automatic stand-alone operation and high reliability. Its daily sun-tracking is self-directed, requiring no external or operator input. It has also been designed such that, if a solar cell (or multiple cells) fails, the rest of the HCPV system will continue to produce power. The HCPV system can also operate in locations that have no access to the electrical grid, either due to their remote location or due to the economic constraints of the region. A very large part of the world population does not have access to electrical power. The HCPV system can be installed to provide power for these communities, as illustrated in Fig. 12.7. As their needs grow, additional systems can be installed. The HCPV can provide 24-h power by the addition of an electrical storage system.
3. Water pumping. Much of the developing world needs electrical power to pump water for home use and farming. The Amonix HCPV system's automatic operation and high reliability makes it ideally suited for this

Fig. 12.6. Five HCPV systems generating power for the APS grid

purpose (Fig. 12.8). Because the HCPV system tracks the sun, it will provide 30% more daily generated energy than fixed flat-plate photovoltaic systems.

Fig. 12.7. The Amonix HCPV system can supply power to remote villages

Fig. 12.8. The HCPV system can provide electrical power for water pumping

Fig. 12.9. The HCPV system can provide electrical power directly to desalinization plants

4. Industrial electrical power. Many industrial plants pay high per-kilowatt-hour electricity rates, because they use large quantities of utility-sourced electricity during the utility's daily peak-use period. An HCPV system, located at a plant facility, can reduce that plant's demand for expensive, peak-use period electricity. The HCPV system will also, of course, reduce the plant's total demand for utility-sourced power. The HCPV system can also supply electrical power for water desalinization and purification projects, as illustrated in Fig. 12.9.

12.6 System Description

The MegaModule system shown in Fig. 12.10 is composed of five major subsystems. The major subsystems of the HCPV system are:

1. MegaModule: structure that houses and supports the system's solar cells, concentrating optics and electrical connections. There can be from five to seven MegaModules in a system.
2. drive subsystem: allows the MegaModules to be rotated and positioned directly towards the sun. This subsystem is composed of a pedestal, drive head, hydraulic actuators and torque tube.
3. Tracking control electronics: determines the position of the sun, and controls the hydraulic actuators that position the MegaModules directly towards the sun. The tracking control also senses wind speed and directs the MegaModules to assume a wind-stow position in response to excessive wind speeds.
4. Hydraulic subsystem: activates and deactivates the hydraulic valves that serve the hydraulic actuators of the drive subsystem.
5. Power conditioning subsystem: converts the MegaModules' DC power into AC power, and interfaces the HCPV system with the grid.

Fig. 12.10. Major subsystems and components of the Amonix HCPV system

12.6.1 MegaModule

The Amonix HCPV system uses square Fresnel lenses, with circular facets, to concentrate the sun's irradiance onto the solar cells, as illustrated in Fig. 12.11. The angle of each lens facet varies as a function of that facet's distance from the centre of the lens, such that all the sun's rays will converge at the location of the small solar cell. The Amonix system uses Fresnel lens 'parquets', each consisting of a number of these square Fresnel lenses, rectangularly arrayed within a single sheet. The solar cells are mounted onto modular plates, arrayed and spaced to match the positions of the lens array. The lens parquets and solar cell plates are mounted to the MegaModule structure, as shown in Fig. 12.12.

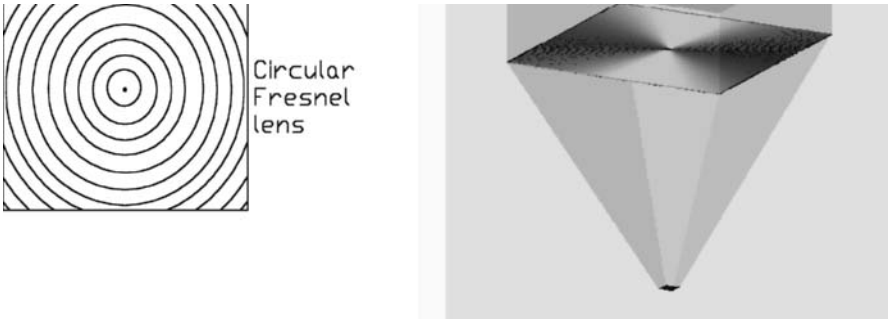

Fig. 12.11. Fresnel lens concentrates the sun's irradiance onto the solar cell

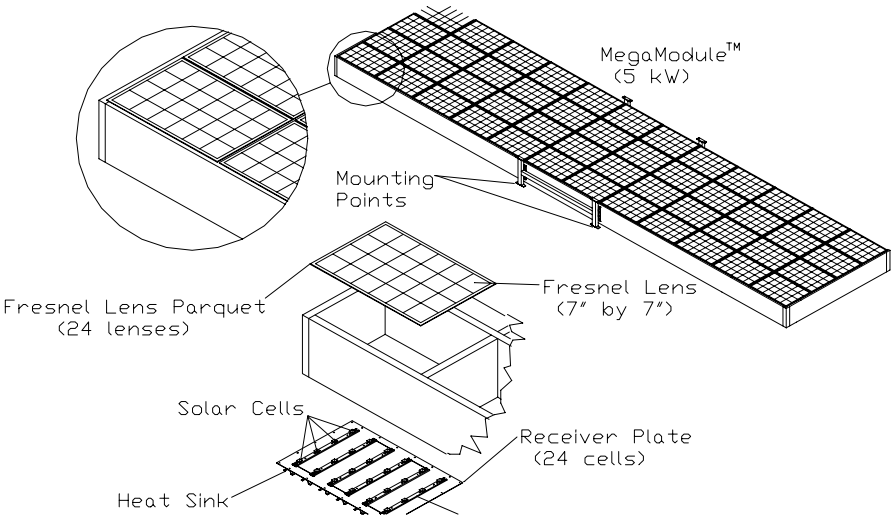

Fig. 12.12. A MegaModule is composed of lenses, solar cell receiver plates and the support structure

12.6.2 Drive Subsystem

The patented Amonix mechanical drive system incorporates three linear hydraulic actuators. One actuator is employed for elevation-axis movement, and two actuators are employed for azimuth-axis movement.

The elevation drive system can operate at two speeds: high speed (for quickly moving the MegaModules into their face-up, high-wind stow position); and low speed (for normal sun tracking movement). The system can move from any position into a face-up wind stow position in less than 15 s. It also has a fail-safe wind stow function: if there is an interruption of power to the control system, the elevation drive will automatically move the MegaModules into wind-stow position, using stored hydraulic pressure from an accumulator.

The two azimuth-drive actuators, by their coordinated extension or retraction, are capable of moving the MegaModules through a full 360° of azimuth rotation.

The drive system is designed to survive a 90-mph wind, and to track the sun up to an average wind speed of 29-mph.

12.6.3 Tracking Control Electronics

The Amonix IHCPV tracking control electronics uses open-loop control algorithms, with modifying inputs from a sun-position detector. Position encoders are linked directly to the elevation and azimuth final drive stages. The open-loop control algorithms calculate the sun's position based upon time-of-day and geographic location data obtained by the system's onboard GPS unit. Information on the MegaModules' current position is inputted to the control electronics by the position encoders. Based on these data, the control electronics calculates the drive movement increment necessary to bring the MegaModules into alignment with the sun. Input from the sun position detector allows the control electronics to quantify and make adjustments for any small tracking errors.

The electronic controller is completely autonomous but can be monitored and controlled remotely. At night, the control system positions the MegaModules in a face-up position. In the morning, when the sun rises to a selected minimum angle above the horizon, the controller moves the MegaModules to face the sun's position. When the sun's irradiance is sufficient for power production, the inverter will automatically establish connection to the grid and start producing power automatically. The controller maintains the array pointing at the sun over the day. In the event of heavy cloud cover, the inverter will automatically disconnect from the grid, but the system will continue to track the sun. When the cloud cover dissipates sufficiently, the inverter will reconnect to the grid and start producing power, within minutes. At the end of the day, when the sun's elevation angle falls below the selected minimum, the system will moved to its night stow position.

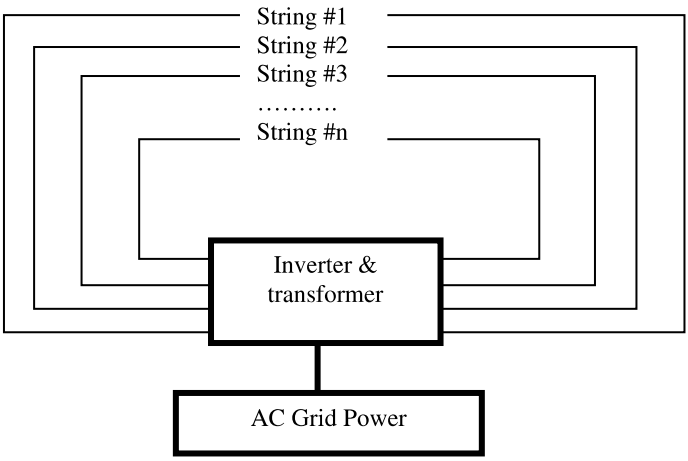

Fig. 12.13. Power output wiring configuration of the HCPV system

An anemometer is mounted onto each array. If the wind speed exceeds a selected maximum, the controller moves the array to a face-up stow position. It will stay in the wind stow position until the wind speed falls below, and stays below, a selected maximum for a pre-selected time period. The system then returns to tracking the sun and generating power.

The power output wiring configuration for the Amonix IHCPV system is shown in Fig. 12.13. Each MegaModule is divided into two power output wiring strings. Each string is composed of 576 series-connected solar cells. For the sake of reliability, the strings of each array are, in turn, wired together in parallel. If a problem occurs with an individual string, the power from that string may be lost, but the power generation of the other strings is not affected. For further reliability, each individual solar cell has a parallel-connected bypass diode, which prevents a bad cell from interrupting the power production of the rest of the string. If a solar cell does fail, only the power of that cell and the drop across the bypass diode are lost, approximately 10 W total. Collectively, these features greatly increase system reliability by reducing the number of single-point failures that could reduce power output to zero. Failures of the inverter, transformer or drive control system are the only major single-point failures that would take the array off-line. Other failures only result in reduced power production.

12.7 System Installation

The support pedestal of the HCPV system is mounted within a concrete-poured hole, which is drilled 3 ft. (ca. 1 m) in diameter and 18 ft. (ca. 5.5 m)

Fig. 12.14. A drilling rig drills the foundation hole

Fig. 12.15. Installing the pedestal

Fig. 12.16. Installation of the drive/torque tube assembly

deep into the ground. A drilling rig (Fig. 12.14) suitable for the drilling operation is pictured left. The finished foundation hole is pictured right.

The pedestal is inserted in the foundation hole and concrete is poured around it. The completed pedestal installation is shown in Fig. 12.15. Next, the drive/torque tube structure is lifted and positioned onto the pedestal by means of a crane equipped with lifting straps, as shown in Fig. 12.16.

MegaModules are delivered to the site by truck, with up to three MegaModules per truckload. A crane is positioned as shown in Fig. 12.17, such

Fig. 12.17. A crane lifts the first module from the truck to the torque tube

Fig. 12.18. The final module is installed on the torque tube

that it can lift the MegaModules directly from the truck and onto the drive subsystem. The first module is installed in the centre position of the torque tube. The next two modules are mounted on either side of the centre module, and then the two outside modules are added to complete the module assembly, as shown in Fig. 12.18.

12.8 System Operation

The Amonix HCPV system is designed for unattended operation for either grid-connected or non-grid applications. When the sun reaches a given elevation angle in the morning, the system moves automatically from a night stow position to sun-tracking position. When the sun's insolation reaches a certain

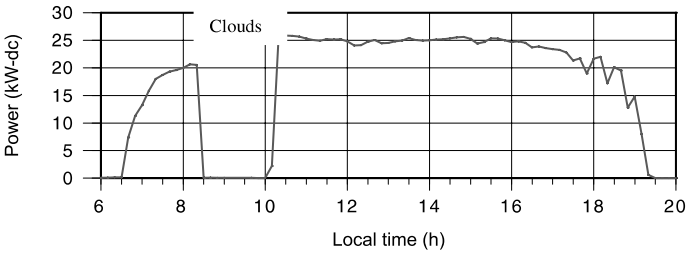

Fig. 12.19. Power output of an HCPV system, over the course of a day

level, the inverter will automatically connect to the grid and start outputting electrical power. It tracks the sun throughout the day, generating electrical power whenever the direct normal irradiance (DNI) is above 400 W/m^2, until the sun sets in the evening time.

An example of daily generated power output is shown in Fig. 12.19. On this particular day, in the late morning, a dense cloud occluded the sun and reduced power output to zero. Later, after the cloud passed, power output resumed and reached 26 kW. A thin cloud layer then decreased power output to 25 kW for most of the day, until late afternoon when small cloud clusters caused the power to fluctuate.

Throughout the day, the electronic control subsystem monitors the sun's position with respect to the MegaModule array's position, and adjusts the array's position if required to maintain the required pointing accuracy. If clouds occur during the day, such that the sun position sensor receives no input, then mathematical sun algorithms are used to maintain the array's alignment with the sun's calculated position, until the clouds dissipate.

12.9 Description of Plant Sites

Over 600 kW of the fifth-generation Amonix HCPV system have been manufactured and installed over the past 6 years. The first three 20-kW units started operating in May 2000. Since that time, additional units have been manufactured and installed for Arizona Public Service (APS), University of Nevada at Las Vegas (UNLV), and Nevada Power Company, Las Vegas. During this time, the units have produced over 3.8 GWh of grid energy.

12.9.1 APS STAR Center, West Field Site

There are currently 145 kW in operation in the West field at the APS STAR facility in Tempe, Arizona. The field now consists of three 25-kW units and two 35-kW units. Initially, there were three 20-kW units and three 25-kW units as shown in Fig. 12.20. The MegaModules from the three 20-kW units were moved to a new 35-kW drive system. These units were installed during

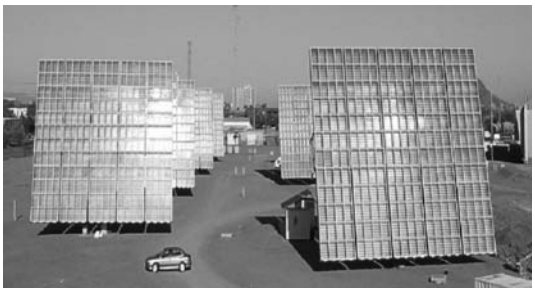

Fig. 12.20. The APS west field

the period from 2000 to 2003 and represent different versions and configurations of the maturing design. The 35-kW units, incorporating seven MegaModules each, are the latest design to be manufactured and installed at this site. The units in the west field have produced over 1185 MWh of grid energy since the start of operation.

12.9.2 APS STAR Center, East Field Site

A second field of Amonix units is located on the east side of the APS STAR facility (see Fig. 12.21). There are five 25-kW units, for a total of 125 kW, at this location. These units were installed during 2002 and have generated over 832 MWh of grid energy.

Fig. 12.21. East field at the APS STAR Facility

Fig. 12.22. The APS Glendale Airport site

12.9.3 Glendale Arizona APS Site

The Glendale Arizona APS site, installed in 2001, is located at the southwest corner of the Glendale airport (see Fig. 12.22). It consists of four 25-kW units, for a total of 100 kW. Since installation, this site has produced over 626 MWh of grid energy. There are no operation or maintenance personnel located at this site. The system's daily performance is remotely monitored from the APS STAR facility. If information from the monitoring system indicates a maintenance need, then personnel are deployed from the STAR facility.

12.9.4 Prescott Arizona APS Site

The APS is currently constructing a concentrating PV plant near Prescott, Arizona. There are currently five 35-kW units in operation at this site. The first 35-kW unit began operating in late 2002. Four additional 35-kW units were installed in 2003, for a present total of 140 kW. Figure 12.23 shows the five systems in operation. These five Amonix units have generated over 590 MWh of grid energy.

12.9.5 University of Nevada in Las Vegas Site

One Amonix 25-kW unit is installed at the Center for Energy Research at the University of Nevada at Las Vegas. This project is a joint effort by UNLV, Amonix and Arizona Public Service, under the direction of Mary Jane Hale of the National Renewable Energy Laboratory (NREL) and funded by the Nevada Southwest Energy Partnership.

This unit, shown in Fig. 12.24, is being operated by UNLV students to obtain performance and reliability data. Simultaneously, the students are learning about solar generating technology. This system started operating in late March 2004 and has generated over 105 MWh since that time.

Fig. 12.23. APS Prescott site

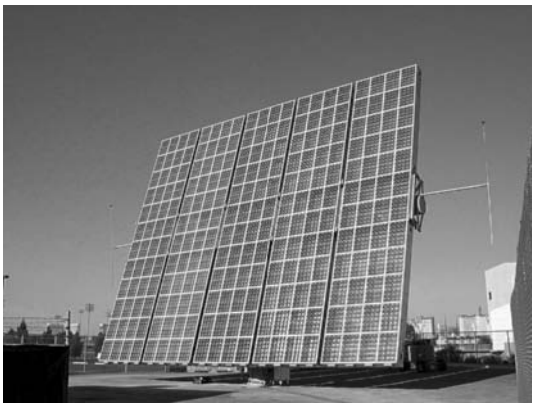

Fig. 12.24. Unit operating at the UNLV site

Fig. 12.25. Nevada Power site

12.9.6 Nevada Power Company Site in Las Vegas

Three 25-kW HCPV systems are operating at Nevada Power Corporation's Clark Generating Station, located in southeast Las Vegas. These MegaModules incorporate a new solar cell receiver plate design. This installation shown in Fig. 12.25 was completed in March 2006, and the system has generated approximately 40 MWh so far.

12.10 System Performance

Part of the Amonix development plan was to deploy multiple systems at different solar sites in order to test the hardware under various environmental conditions. Systems have been deployed in southern California, Nevada, Arizona, Texas and Georgia. Different lessons have been learned at each site. Some of the systems have been in field operation for 6 years. The accumulated grid energy generated, as shown in Fig. 12.26, is nearly 3.8 GWh.

A total of 132 MegaModules have been manufactured and installed in the field. These MegaModules incorporate a total of 6336 receiver plates and

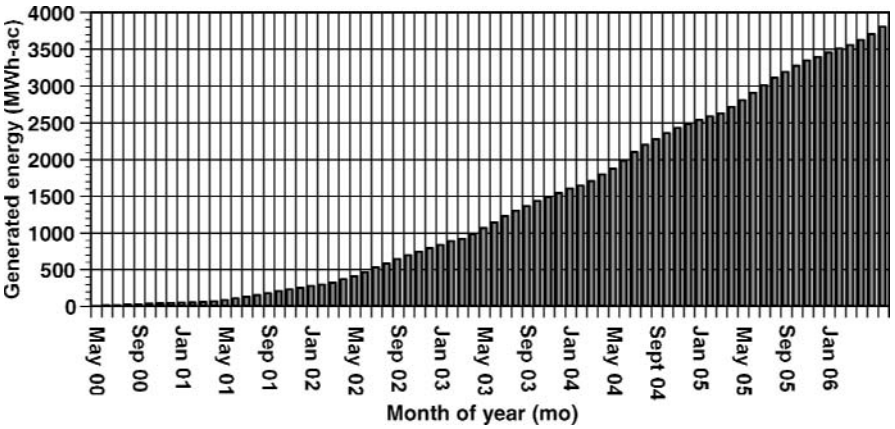

Fig. 12.26. Accumulated grid energy generated by the fifth-generation Amonix HCPV systems

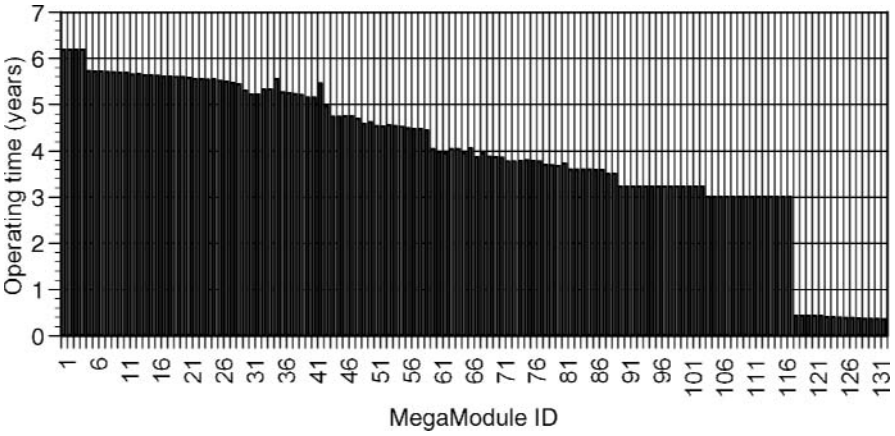

Fig. 12.27. MegaModule field operating time

152,054 solar cells. The total on-sun field operating time is over 510 years, as shown in Fig. 12.27. As lessons were learned from both manufacturing and field-testing, design changes were made to increase performance, increase system reliability and improve manufacturability of the system.

One of the main goals of the field-testing has been to assess long-term performance of the system. The electrical power production of each field unit has been recorded since its time of installation. One of the first units installed was the W3 unit at the APS STAR facility. The total net monthly generated electrical energy for the W3 unit is shown in Fig. 12.28. The performance was low in the first couple of months as issues were being resolved with the new design. The operation of this unit was paused in late 2004, and

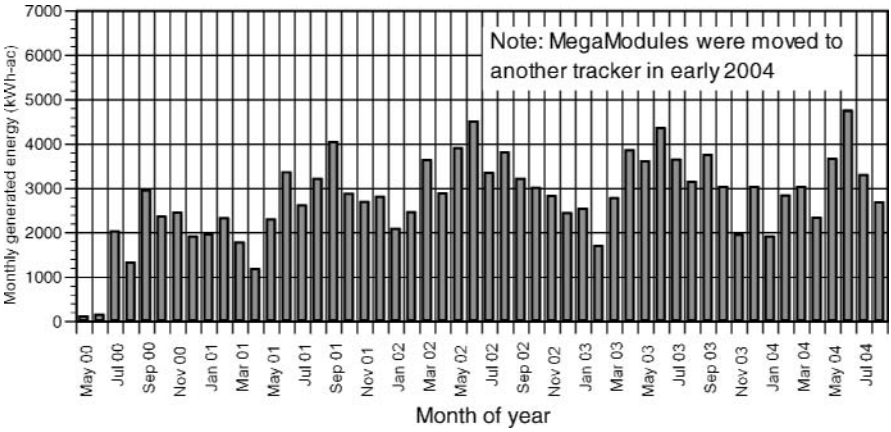

Fig. 12.28. Energy performance of HCPV system W3 at athe APS STAR facility

the unit's MegaModules were moved over to a new drive system that was under development at the time. Because of the seasonal monthly and year-to-year variation in the incident sun irradiance and other factors, such as dust-deposition on the lenses, temperature, wind, system-outage time, etc., it is difficult to determine from these data whether the performance changed over this time period, at least without further analysis.

A better estimate of the trend in the HCPV system performance can be obtained by dividing the (monthly generated energy) by the (total direct-incident sun irradiance energy for the month). Since it is desirable to be able to compare the performance trend of differently-sized arrays (25 and 35 kW, for instance), this mathematical ratio is also divided by the rated power level. The resulting number is referred to as the monthly performance energy factor (MPEF), as shown in Eq. (12.1):

$$MPEF = \frac{Monthly\ energy\ generated\ by\ the\ system}{(Total\ direct\text{-}incident\ sun\ irradiance\ energy) \times (Power\ rating\ of\ the\ system)} \tag{12.1}$$

The MPEF for unit W3 is shown in Fig. 12.29. The MPEF values are not shown for the year 2000, because data on the local direct normal irradiance were not available for that time period. The chart's data stop in mid-2004, when unit W3's MegaModules were removed and then separately installed on different drives (these MegaModules are still in operation). Although the data presented in Fig. 12.29 do not indicate any general degradation, there is still significant variation in the data points. As discussed above, this variation is the result of ambient-temperature variation, wind-speed variation affecting wind-stow events, different rates of dust accumulation on the lenses, outage time, etc. The low MPEF values seen in May 2001 (month 5) and April 2004 (month 4) were the result of extended outages during those months.

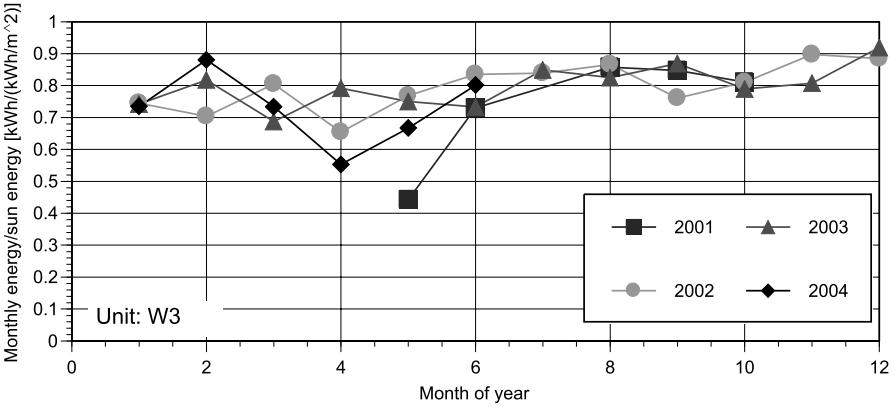

Fig. 12.29. Monthly energy performance factor MPEF of unit W3

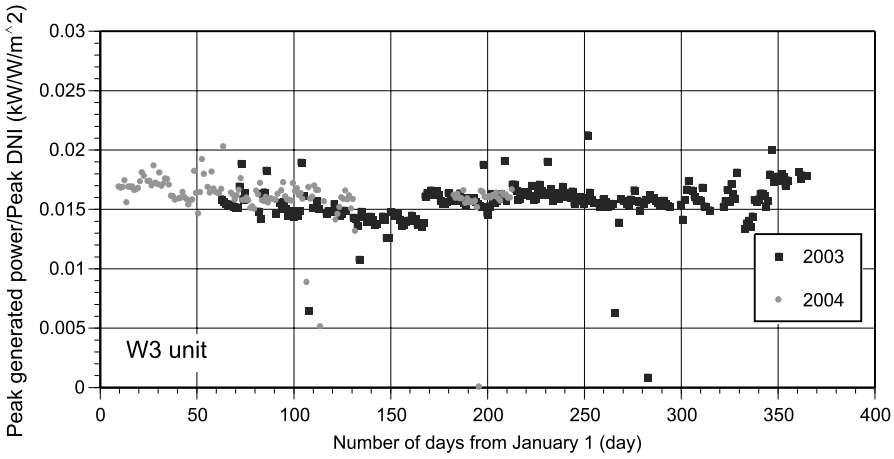

Fig. 12.30. Daily peak power normalized by the DNI

Amonix is also monitoring the peak-power performance of its installed systems. The peak power output divided by the DNI is shown in Fig. 12.30 for unit W3. Calculated values are not available before 2003, due to unavailability of DNI power data. Calculated values stop at year 2004, when unit W3's MegaModules were removed and installed on different drives.

12.11 Maintenance Operation

The Amonix HCPV system has not only been designed for high reliability, but also for low-field-maintenance requirements. Each MegaModule is itself modular, incorporating 48 removable solar cell plates, wired as two series-strings of 24 plates each. In the event of performance degradation or failure,

each solar cell plate can be quickly tested by measuring its open-circuit voltage. Safe execution of this testing does not require that the system be shaded or moved completely away from the sun – the system need only be rotated approximately 10° from the sun, such that the focused sunbeams are no longer focused onto the solar cells. Once the malfunctioned solar cell plate is identified, it can be removed and replaced in situ, without disturbing any adjacent components. The malfunctioned solar cell plate can then be factory repaired, as its structure is also modular, incorporating replaceable solar cell assemblies.

The HCPV system uses a gearless hydraulic drive, and the majority of its components can be replaced without major disassembly of the system. The hydraulic actuators, valves, mechanical linkages and all of the bearings (except for the main azimuth rotational bearing) can be replaced without removing the MegaModule/torque tube structure. Only if there is a problem with the main drive structure would a crane be required for repair.

The control electronics, control valves, inverter, grid interface and transformer are modules that are all located at ground level for easy servicing. They are all separate modules that can be replaced with a minimum of interference with the other modules, minimizing the number of connection and disconnection operations.

Periodic maintenance tasks include washing the Fresnel lenses, greasing the drive bearings, and changing the hydraulic fluid and filter. Periodic washing of the lenses will help to maintain optimum system performance. The frequency of lens washing will depend upon the dustiness and rainfall frequency of the particular site. Greasing of the azimuth and elevation drive bearings should be done every 1–2 years. Amonix's field experience has shown that hydraulic fluid leaks are rare for its drive system, and are detected by the electronic control system. Fluid replacement has been required only every 1–2 years. The hydraulic fluid filter should be replaced once per year.

The UNLV HCPV system program includes the detailed recording of incidents and failures, and of operation and maintenance time spent on the system. The recorded O&M time for the UNLV system does not include the time for washing the lenses, nor does it include travel time (only on-site labour time is included). If the on-site O&M personnel had to call for assistance, only the time of the on-site personnel is included. A plot of the accumulated incident and failure labour time is shown in Fig. 12.31. The total incident and failure labour time per day is shown in Fig. 12.32.

12.12 System Cost

The current installed cost of the Amonix system at a production rate of 500 kW per year is in the $8/watt range. As the annual production rate increases, the estimated installed cost of the system will greatly decrease, as shown in Fig. 12.33.

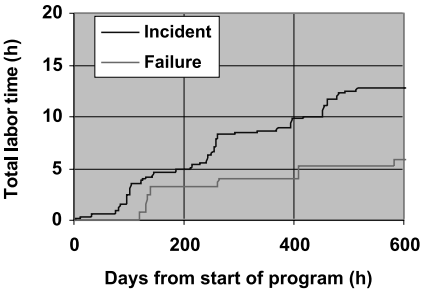

Fig. 12.31. Incident and failure time

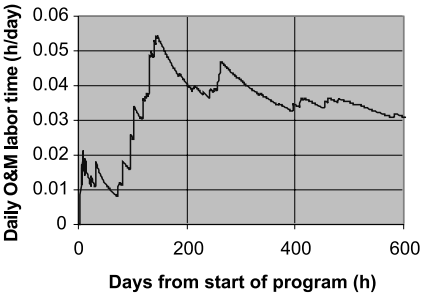

Fig. 12.32. The O&M per day

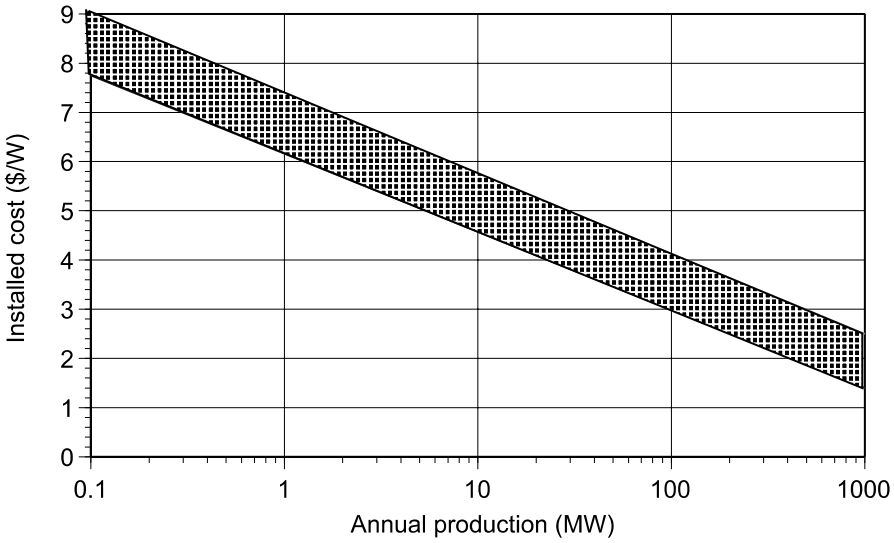

Fig. 12.33. Estimated cost of the installed system

References

1. SunLab–NREL/Sandia, http://www.energylan.sandia.gov/sunlab/overview.htm
2. Stolte WJ, Engineering and economic evaluation of central-station photovoltaic power plants, Electrical Power Research Institute, TR-101255, Research Projects 3166-01: 3273–03, December 1992
3. McDonnell FL, High power density photovoltaics, Renewable Energy World, September to October 2002

13 The EUCLIDES Concentrator

I. Antón and G. Sala

13.1 History

EUCLIDES is a reflective parabolic trough concentrator (PTC) that consists of a linear array tracking around a horizontal N/S axis. The system was conceived in the mid-1990s, sustained on two fundamental pillars. Firstly, the background and wide-ranging experience with linear thermal concentrators, such as the projects carried out in the mid-1980s in California [1], suggested the possibility of transferring the concept to a PV concentrator. Of course, a complete redesign of the system was necessary to fulfil the requirements imposed by a photovotaic system. The most important change was in the receiver, which needed cost-effective PV solar cells able to work at medium concentration levels within the range of 20 – 40 suns.

The second pillar was the entry into the PV market of buried grid laser groove (BGLG) cells, designed by M. Green et al. [2] and commercialized by BP Solar as SATURN technology. In 1995 this technology demonstrated its suitability to produce cells in the conventional 1-sun production line able to operate under $3\,\mathrm{W/cm^2}$ at 18% efficiency [3]. The *Instituto de Energía Solar*, as designer and developer of the idea, and BP Solar, as cell supplier and promoter, later came together to make the concept feasible.

A prototype was designed and installed in Madrid in 1995 with the aim of trialling the concept (see Fig. 13.1). The structure was 24 m long, consisting of 40 mirrors that cast the light onto encapsulated linear modules made of 12 BP Solar concentrator cells at 33× geometric concentration. The first series of BP Solar concentrating modules were installed and tested by December 1995. An efficiency of 10.75% in operating conditions ($T_{\mathrm{cel}} = 75.2\,^{\circ}\mathrm{C}$, $\mathrm{B} = 696\,\mathrm{W/m^2}$) and 14.4% when corrected to standard conditions ($T_{\mathrm{cel}} = 25\,^{\circ}\mathrm{C}$, $\mathrm{B} = 800\,\mathrm{W/m^2}$) was achieved for the small array, including the optical mismatch [4].

The good results provided by the prototype led to the installation of a 480-kWp power plant in Tenerife based on EUCLIDES technology. The EUCLIDES-THERMIE Demonstration Project, developed in the JOULE Programme, was the first to use concentrators subsidized in Europe. This has been a significant step in the development of concentrator technology, in order to initiate and promote the industrial participation. The light and the

shadows of this experience are discussed throughout this chapter since they offer an insight into the very interesting lessons learned.

After the Tenerife experience, and as a consequence of its results, a number of sub-systems were redesigned. Particularly, the cell receiver and mirrors, whose long-term reliability did not perform as expected, have been changed. The third generation of the EUCLIDES concentrator relies on the lessons learned from the power plant, particularly those sub-systems providing good long-term reliability, the cost analysis provided by an industrial scale experience, as well as new materials and manufacturing process developed in the past few years; therefore, a profound analysis of the capability of competing in the present PV market can be carried out based on reliable data, taking into account the current feed-in tariffs in many countries, and can be compared with the new concentrator concepts developed in the past years.

13.2 Description of the System

The EUCLIDES concentrator is shown in Fig.13.1. Although there have been several evolutions and changes in the system over time, the overall concept has changed very little, as listed:

1. Two wings of reflective parabolic mirrors are laid out symmetrically on both sides of the axis of the system.

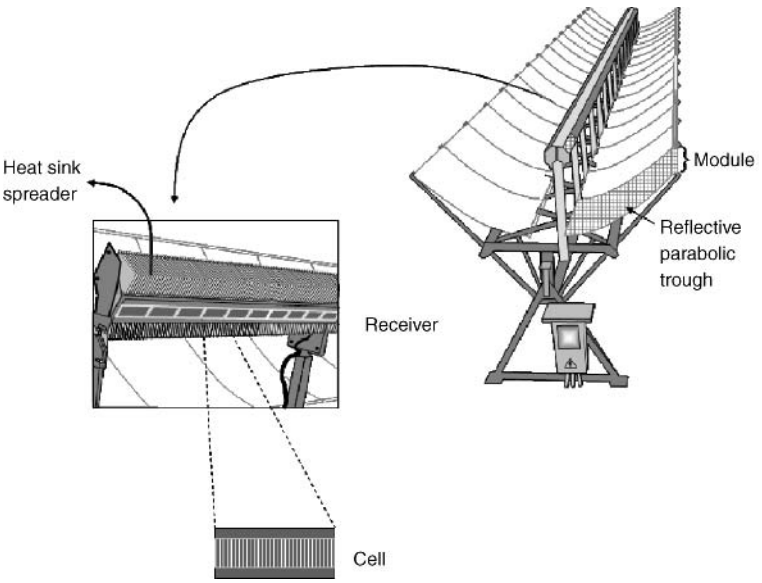

Fig. 13.1. Drawing of the EUCLIDES concentrator, a linear focus PV concentrator

2. The iron structure, north-south oriented, is supported at three points, the central being the tracking driver. The system tracks the sun during the day from east to west. The sun-tracking unit, fixed on one of the supports, is based on a 'self-learning' strategy, i.e. an optimum mixing of closed- and open-loop operation.
3. The concentrator receiver consists of LGBG cells and by-pass diodes, assembled and encapsulated for operation at 30 suns. The aluminium heat sink acts as passive cooling system and fixing support, which is attached to the structure. The receiver includes a reflective secondary stage, which protects the buses from the concentrated beam and widens the angular transmission of the optical system, thus increasing the acceptance angle.

13.3 Optical Design Based on Parabolic Troughs

The sun is an extended light source, with an angular size of $\pm 0.275°$ as seen from the Earth on a clear day. The size of the source, seen by a PV cell through an optical system, is spread by any source of optical error, misalignment or tracking error [5]; therefore, it is necessary to define a lower limit for the acceptance angle of a concentration optical system according to the final size of the sun provided by the concentrator.

Figure 13.2 shows the receiver inscribed in a circumference that subtends the receiver with an angle $\pm\alpha_{\min}$. The acceptance angle of the mirror is different at each point of the parabolic profile. Consequently, if the primary collector is inside this circumference, it would have a minimum semi-acceptance angle of $\alpha_{\min}$. This limit is reached at the edges of the reflector and depends on the concentration ratio. In addition, any point of the reflector profile inside the circle would have a semi-acceptance angle greater than $\alpha_{\min}$.

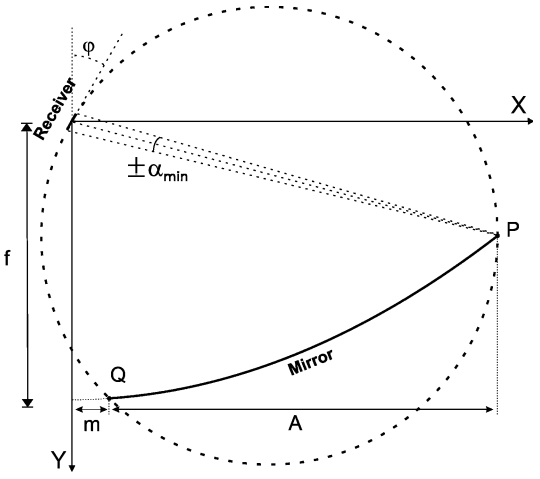

Fig. 13.2. Design of the parabolic profile by maximizing the minimum acceptance angle

The first approach design is based on a procedure proposed by Luque [6], which maximizes the minimum acceptance angle for a given concentration ratio. To maximize the concentration ratio for a given $\alpha_{\min}$, the aperture of the reflector A must be maximum, which happens if the parabolic profile crosses the circumference at its diameter (point P). The distance m must be left between the horizontal projection of the receiver and the starting point of the mirror (point Q in the drawing), where all elements of the receiver, mainly the heat sink, would cast a shadow. In practice, the width of the cells is determined by technological factors, so A is defined by the geometrical concentration ratio; therefore, the optimization process would consist of finding the tilt angle φ of the receiver that provides the greatest acceptance angle for a given concentration ratio. This optimum tilt leads to a focal length f that defines the parabolic profile.

In practice, the aim of the design process should not be to maximize the acceptance angle but the energy collected by the optical system. We evaluate the latter by means of the interception factor, a function of the focal distance f and the tilt angle φ, which is defined as:

$$\gamma(f,\varphi) = \int_{-\infty}^{\infty} H_N(\theta) \cdot T(\theta, f, \varphi)\,\mathrm{d}\theta \;,$$

where $H_N(\theta)$ is the corrected sunshape [5], i.e. the sun spread by the optical errors and seen by the receiver; and $T(\theta, f, \varphi)$is the angular transmission of the parabolic profile, i.e. the ratio of rays that reaches the receiver to the incoming rays, as a function of the angle θ between the incoming rays and that normal to the aperture area.

The corrected sunshape happens to be the convolution of many terms with zero mean, this being the reason why it can be described very accurately as a Gaussian distribution. The imperfections of the system produce a defocusing at the focal plane. Examples of these imperfections are the angular spread of the solar disc when projected over a cross plane normal to the N-S axis of the system, the misaiming resulting from imperfect accurate tracking, contour errors on the surface of the mirrors, scattering on reflective surfaces, torsion in the structure caused by wind or weigh loads, etc.

The sun is commonly modelled with a standard deviation (rms) of the gaussian distribution $\sigma_{\text{sun}} = 0.229°$. The corrected sunshape is the result of the convolution of the sun distribution (σ_{sun}) and the optical errors (σ_{opt}), which leads to a distribution whose a standard deviation is widened by the optical errors according to the expression $\sigma_T^2 = \mathrm{g}\sigma_{\text{sun}}^2 + \sigma_{\text{opt}}^2$.

In Fig. 13.3 the graph on the left shows an f-parameter set of curves that represents the interception factor for different focal lengths in a system with a geometrical concentration ratio of 32×. As stated above, the corrected sunshape has a σ_T greater than the perfect sun ($\sigma_{\text{sun}} = 0.229°$). The focal distance that maximizes the energy collected depends on that value. The ideal

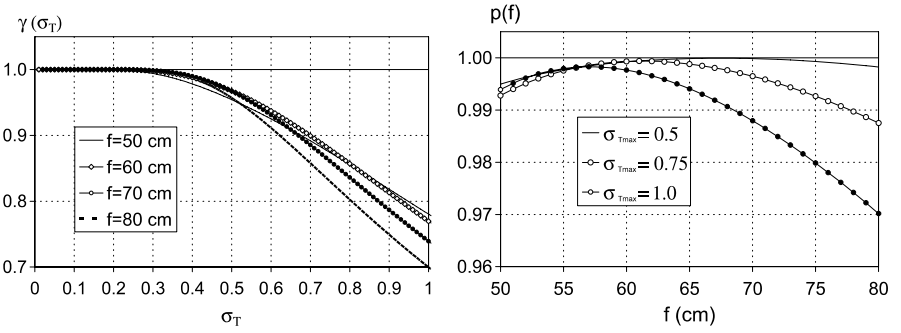

Fig. 13.3. Optical design of a parabolic mirror for a 32× system; *Left:* the interception factor γ as a function of the size of the corrected sun σ_T, for different focal distances; *right:* the loss of efficiency for different focal distances and a maximum size of the corrected sun $\sigma_{T\,\max}$

case, for any value of σ_T, would correspond to an envelope of the f-parameter set $[\sigma_{\rm env}(\sigma_T)]$. We define the p(f) function as the loss of collection energy for a given maximum size of the source ($\sigma_{T\,\max}$), compared to the envelope $\sigma_{\rm env}(\sigma_T)$:

$$p(f) = \frac{1}{\sigma_{T\,\max}} \int_0^{\sigma_{T\,\max}} \frac{\gamma(f,\sigma_T)}{\gamma_{\rm env}(\sigma_T)}\,{\rm d}\sigma \ .$$

The $p(f)$ function is also plotted in the Fig. 13.3 for a 32× system. It shows that, if the quality of the system is very high ($\sigma_T = 0.5$), the optimum design would lead to large focal distances. But the final size of the corrected sunshape depends on many factors and is difficult to determine a priori; thus, we have selected a focal distance $f = 60\,$cm since that value would provide the best collection of energy independently of the optical errors (final size of the corrected sun between $\sigma_T = 0.5$ and $\sigma_T = 1$).

The price to be paid with this design is that the minimum acceptance angle at the edges of the parabolic profile is asymmetric and slightly lower than that obtained by the first method (see Fig. 13.4), which would lead to a larger focal distance. On the other hand, it has been demonstrated that the energy collected can be significantly higher when the collector, structure or tracking system are not perfect.

The semi-acceptance angles of Fig. 13.4 correspond to a 32× single-stage parabolic mirror. The angular transmission function [7], i.e. the relative power transmission as a function of the incident angle, can be widened by using a secondary reflective secondary stage, as Fig. 13.5 shows for one of the EUCLIDES arrays of the Tenerife plant. The function of the secondary stage is not to increase the concentration ratio but to correct the optical errors, mainly those caused by misalignments throughout the long structure [8].

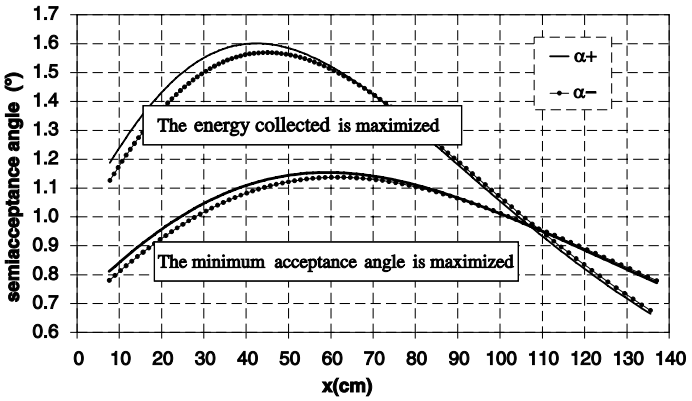

Fig. 13.4. Semi-acceptance angles ($\alpha+$ and $\alpha-$) for the two proposed designs, defined for a 90% transmission. The first design maximizes the minimum acceptance angle at the edges of the parabolic profile, whereas the second one maximizes the energy collected by a system with optical errors

Fig. 13.5. Line of receivers in a EUCLIDES array. The receiver includes a reflective secondary stage to increase the acceptance angle of the optical system

13.4 Technology of the EUCLIDES Mirrors

From the beginning, the ambition was to manufacture the EUCLIDES mirrors with silvered glass because experience with linear thermal concentrator had demonstrated good results and long-term reliability; however, its use in photovoltaics requires higher optical quality and the optical and mechanical design suggested shorter focal distances than those used in a thermal application. In the end, it was not possible to manufacture glass mirrors with these requirements for the prototype since it needed the participation of the glass industry, which was not as motivated at that time.

Alternatively, a new technology based on reflective films was achieved for the prototype. It consisted basically of the lamination of a reflective film, and if necessary, a weather-protective cover, onto an aluminium sheet. The plate is then bent using a parabolic mould and a counter-mould tool, the profile

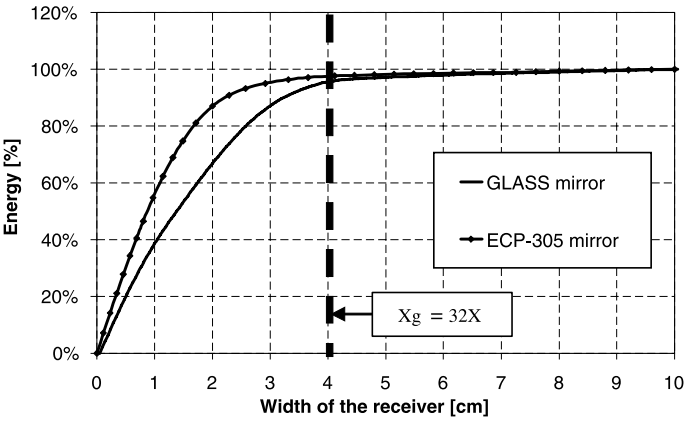

Fig. 13.6. Relative encircled energy, i.e. the percentage of energy impinging on the receiver as a function of its width for the mirror of the prototype (based on ECP-305 reflective film) and silvered glass mirrors

being fixed with ribs and cross-beams. The success of the technology was sustained by the fact that the final shape of the mirror depends only on the mould and not on the accuracy of the rib profile, while the specular surface micro-geometry depends on the reflective film, the transfer adhesive and the surface of the sheet, and not on the surface finish of the mould.

The performance of the parabolic mirrors manufactured for the prototype was impressively good, with optical efficiencies of about 90% for a 32× geometric concentration ratio [9]. The reflective film chosen was the commercial 3M ECP-305, consisting of an acrylic weather-proof film with a coating of silver and an acrylic pressure sensitive adhesive on the rear side. From three year's field experience and the accelerated aging test carried out, a long-term reliability of this technology was suggested.

Nevertheless, this commercial film was no longer available and three alternatives were tried for the Tenerife plant [10]. None of them provided the same optical performance, with optical efficiencies from 70 to 85%. The technology was also very sensitive to the manufacturing process and the care with the mirror during storage and installation. The result is that some of them showed a fast degradation as a consequence of damage to their weather-protective layer.

The poor results obtained from the Tenerife experience have led to the abandonment of reflective films and return to silvered glass in the third generation of EUCLIDES systems [11]. Now, sometime later, the PV market has changed completely and concentrator systems have come on the scene. The new panorama has made it easier to convince industry to get involved in the manufacturing of glass mirrors.

The first generation of glass mirrors has provided sufficiently good results, with an overall reflectance of 85% in the 350- to 1200-nm band and the encircled energy shown in Fig. 13.6. For a geometric concentration ratio of 32×, both the mirror based on the ECP-305 film and the glass mirror deliver more than 95% of the reflected energy to a 40-mm-wide receiver. Nevertheless, the focus line given by the glass mirror is significantly wider, so the aforementioned secondary stage would be necessary to provide a sufficiently high acceptance angle.

13.5 Concentrator Receiver for Operation at 30 Suns

The cornerstone of the EUCLIDES receiver is the laser-grooved buried contact (LGBC) cell [2], which has been in production for more than 10 years at the BP Solar facilities in Madrid. This '1-sun' technology is particularly suitable for the production of concentrator solar cells with very few changes. The key is the low series resistance associated to the front grid. The buried and narrow deep metal fingers that are buried in laser-carved grooves are made of silver-covered electroless copper which provides excellent conductivity.

The grid design and the metallization must be slightly redesigned. Cost-effective concentrator cells able to work up to 10 W/cm^2 can be manufactured with this technology [12]. Of course, better efficiencies (up to 20%) are obtained with FZ wafers, providing higher minority carrier lifetimes. With CZ wafers, the efficiency at 40 suns is about 18%.

The EUCLIDES system takes advantage of these cells, redesigned to work between 20 and 40 suns, with efficiencies exceeding 18% at nominal conditions. The parameters related to the metallization and grid have a very significant influence on the cell performance and have been carefully optimized [13]. The contact depth of the grooves, the finger pitch and metal layer thickness (see Fig. 13.7) have been studied in detail in order to find the processing conditions that optimize cell efficiency.

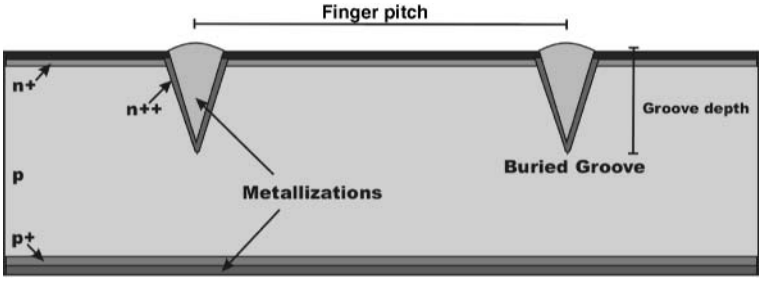

Fig. 13.7. Structure of a laser-grooved buried contact cell. The front grid is formed by laser micromachining fine grooves in the silicon surface, which are later filled with metal

The base of the module consists of an aluminium tray on which the cells are mounted. Cell connections, wires and by-pass diodes complete the module (see Fig. 13.8), which is covered with a front glass and filled with a transparent encapsulant material. The module is thermally stuck to the heat sink [14], which also provides the supports on which to hang the receiver in the line structure. Two linear reflective secondary stages are fixed to the front face of the module, which prevents the concentrated direct irradiation impinging on the soldered tabs and widens the angular transmission of the system.

An electrically insulated material, which provides sufficient heat transfer, is placed between the cells and the modules. This material is the most delicate part of the module and several solutions have been tested. The first attempt was based on pressure-sensitive adhesive thermal tapes [3], which can provide very high dielectric voltage breakdown with only 150 µm thickness. Despite its low thermal conductivity, this thickness leads to very acceptable thermal drops. The modules for both the prototype and the Tenerife plant were manufactured by BP Solar using this type of material. Ten sample modules passed all of the tests carried out in a specifically designed proof of concept test, including humidity and temperature cycling, hi-pot at 2600 V, etc. Nevertheless, the modules in operation at the Tenerife plant have not shown long-term reliability [15], and this solution has been abandoned. This experience showed the need for an international standard for the design qualification of concentrator photovoltaic modules suitable for long-term operation. This standard is currently being approached by the IEC-TC82 [16] and is a key issue to ensure the reliability of concentrator systems.

With the aim of achieving a more sturdy and reliable module, it has been completely redesigned for the third generation of EUCLIDES systems [17]. Aluminium sheets are glued between the cells and modules, providing the necessary heat transfer and electrical insulation. The new design is currently in trial phase in accordance with the IEC 62108 norm [15], which will become an international standard very soon.

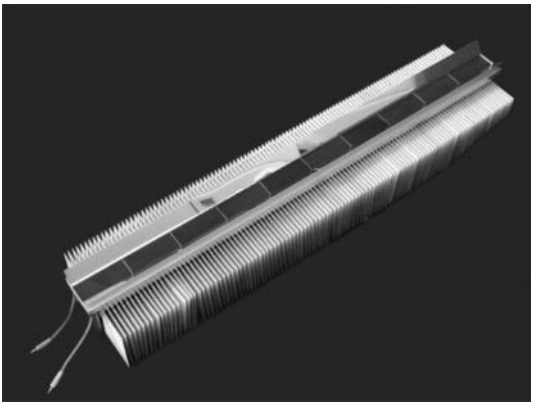

Fig. 13.8. A fully finished EUCLIDES receiver, including the secondary reflective stage and the aluminium passive heat sink

13.6 Structure for Sub-degree Tracking

The system was conceived to have an overall length of between 70 and 90 m to minimize the weight of fixed costs such as the driving system [18]. There are only three supports per structure, thus reducing the assembly and ground preparation costs. Consequently, the structure was designed for a span of 35 – 45 m with no significant deformation, in agreement with the limited acceptance angle of the optical system. The semi-acceptance angle of the primary reflector is about 1°; therefore, misalignments bigger than 0.5° must be prevented throughout the structure to assure that all of the modules are properly illuminated.

The EUCLIDES self-learning tracking system is able to compensate any source of misalignment affecting the whole array, such as ground tilt, N-S axis deviation, zenith position error, etc. They are all sources of tracking errors but need only be corrected once, at the beginning of the system. This relaxes the requirements for orientation accuracy.

On the other hand, the misalignments caused by relative angular displacements between the collectors and receivers, resulting from weight or wind loads, are very critical; therefore, the structure meets strict requirement on torsion stiffness so that the whole line remains aligned within a narrow angular range. This torsion resistance also resulted in a high flexional stiffness, which allows for the aforementioned long span. In spite of its stiffness, the structure is very lightweight, i.e. 145 kg/m including supports.

Fig. 13.9. The driving mechanism and central support of the EUCLIDES structure. A large wheel is supported by two smaller ones, the three being moved by a pair of steel cables pulled by a sliding bar, which is driven by the motor

The structure, which is made of iron, has only three supports: the driving mechanism in the centre, and two bearings at the extremes. The central support (see Fig. 13.9) consists of a wheel which converts the powerful but smooth linear movement of a sliding bar into a circular one by means of a pair of steel cables. The bar is connected to a worm gearing screw which is driven by a motor. The design of the central support permits the linear axis to tilt up to 12° with respect to the ground, which simplifies and reduces the cost of the civil work.

13.7 The EUCLIDES Pointing System

The sun-tracking unit (EPS or EUCLIDES Pointing System) was designed and developed by IES-UPM for the EUCLIDES prototype installed in Madrid. A new tracking strategy, based on self-learning concepts, was implemented with outstanding results [19].

EUCLIDES is a one-axis PV concentrator, so the position of the sun is determined by a single value. The EUCLIDES pointing system (EPS) continuously corrects any misalignment with no regard to its cause. An error table is updated where angular deviations are stored. The table contains a first column with the angle to be aimed at, and a second with the error estimated for each position. We shall call this *error correction table:*

$$[\varepsilon_i] = \left\{\varepsilon_i^{-69}, \varepsilon_i^{-68}, \ldots, \varepsilon_i^{69}, \varepsilon_i^{70}\right\} \ ,$$

where every element of the table represents the *error estimate* associated to the tracking range between k-1 and k degrees. The tracking range is ±70° with a sub-degree step of up to ±0.05°, minimum value determined by the hysteresis of the mechanical components of the tracking structure. Since the table resolution is 1°, higher than the tracking step, sub-degree tracking positions have associated the same error estimate; however, one value per degree is enough to properly characterize the system.

At time t, the *expected sun position* of the array is obtained as

$$\omega = \Omega(t) + \varepsilon_i \ ,$$

where $\Omega(t)$ is the calculated position of the sun and ε_i is the error estimate for that position.

The procedure followed to obtain observations ε_i consists of detecting the optimum sun position while the array is moving, with the output current as an optimizing signal. The array oscillates around the expected sun position ω. Let us assume that ω_i is the *observed angle*, i.e. the angle where the output current is maximum at moment t'. The *observed error estimate* is then

$$\tilde{\varepsilon}_i = \omega_i - \Omega(t') \ .$$

Now the system has to choose between the error estimate ε_i stored in the correction table (open-loop system) and the new *observed estimate* $\tilde{\varepsilon}_i$ (closed-loop system). If the confidence in the estimate is very high, the closed-loop option should be chosen ($\varepsilon_{i+1} = \tilde{\varepsilon}_i$), but on the other hand, the open-loop option ($\varepsilon_{i+1} = \varepsilon_i$) is a better choice. Actually, the new error estimate is calculated as a weighted average of the old one ε_I and the observed one $\tilde{\varepsilon}_i$ following the equation:

$$\varepsilon_{i+1} = \mu_i \varepsilon_{\mathrm{i}} + (1 - \mu_{\mathrm{i}})\tilde{\varepsilon}_i \ .$$

The weight factor, μ_i, is called *certainty* and is a measurement of the confidence in the error estimate. It rules the speed at which any observed error is assimilated by the system, i.e. the speed at which system learns. It takes values of between zero (closed-loop approach) and one (open-loop approach). As the system obtains valid observations, confidence, and therefore certainty value, increases and comes close to one. To obtain a valid observation, the current output should be over a threshold in a clear day. Certainty values are stored in a *certainty table* similar to the *error table* also with a resolution of one degree:

$$[\mu_i] = \left\{ \mu_i^{-69}, \mu_i^{-68}, \ldots, \mu_i^{69}, \mu_i^{70} \right\} \ .$$

When the system is learning, i.e. taking observations, the array oscillates around an expected sun position. Once the array is placed at the 'astronomic' position, an angular range is scanned using the array output current as the optimizing signal. The maximum amplitude of this scanning, δ, varies as a function of certainty from zero to a determined maximum value. When confidence is high, i.e. the system is very confident of the current error table, the scanning amplitude is low, or even zero, and vice versa. After several days without *learning*, i.e. obtaining valid observations, confidence decreases and scanning amplitude increases.

This self-learning strategy had shown very high accuracy in the aiming of the array. The success was based on the fact that the closed-loop sensor was the whole array itself, the output current being the optimizing sensor. The EPS requires a sun-position sensor to work as a closed-loop system. As misalignments are distributed throughout the array and can vary with the position, the use of a specific sensor at a located point of the array can provide error information about the best array aiming. The array output current is an outstanding measurement of the position of the sun and takes into account all errors distributed throughout the array. Nevertheless, the conditions necessary to ensure a correct coexistence with maximum power point (MPP) tracking systems, which also uses the output power of the array as as optimizing signal, needed to be established.

A major characteristic of the EPS is its capability to self-correct any tracking error whatever its cause might be. This capability relaxes the installation

requirements, simplifying the on-site system assembly and contributing to cost reduction.

But some errors affecting the EPS are related to the array installation and remain constant throughout its life. Ground tilt, N-S axis deviation, zenith position error, etc., are sources of tracking errors that would contribute to higher values of the error correction table if they are not considered in the EPS. But they need only be corrected once, at the beginning of its life. The benefit is that, in general, the error estimates will be much lower, and therefore, so will the amplitude of the scanning (δ) required. Although this is not a necessary condition for the EPS, it will contribute to a correct coexistence between EPS and MPPT.

Figure 13.10 shows a sample of the error table from the first learning day after the array installation. Corrections of up to 2°, and consequently larger scanning amplitudes than that value, are required to keep the array pointed. The permanent sources of pointing errors (ground tilt, N-S axis deviation, misalignment caused by weight loads, zenith offset, etc.) are deduced from this table [20] and are included in the equations of the EPS, which reduces the maximum correction in the error tables to values lower than $\pm 0.3°$ for the whole life of the system. This figure is comparable to that of the acceptance angle of the system at the maximum power point [8], i.e. the angle formed by the incident light beam and that normal to the collector aperture plane for which the relative power transmission (at MPP) is 90%. In practice, the quantification of the permanent errors of the array after the installation and its inclusion in the ephemeris could make the open-loop operation in the aiming system feasible for the rest of its life, which is one of the current approaches in modern sun tracking systems [21].

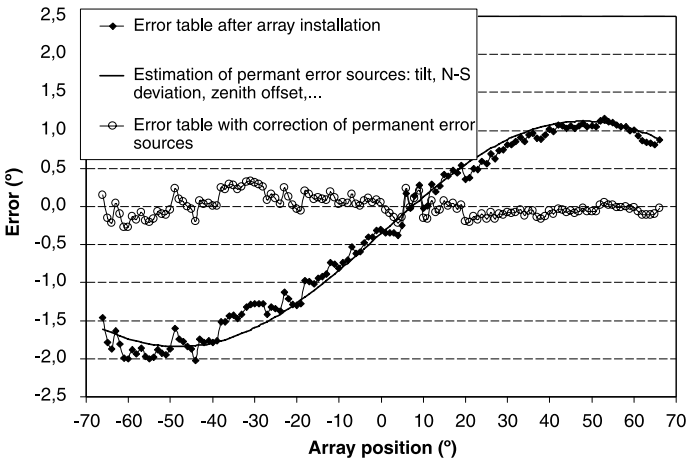

Fig. 13.10. Correction table of a EUCLIDES pointing system (EPS) and estimation of permanent error sources which are later included in the ephemeris

If the angular range explored during the self-learning process is very wide, the light spot may be totally outside the effective area of the receiver. This does not affect the process when short-circuit current is used as optimizing signal, but in operation and with the array biased at MPP, this broad scanning can drastically affect the array bias, and therefore the MPP tracking control.

A second condition to ensure the compatibility between both systems refers to the MPP tracking control, which must keep the bias voltage quasi-constant during the sun scanning carried out by the EPS. If voltage varies drastically, the output current depends not only on sun aiming but also biasing, which would lead to wrong error estimates. The experience of the EULIDES plant showed that quasi-constant voltage MPP tracking was compatible with the self-learning process. The quasi-constant voltage condition is equivalent to saying that the time constant of the feed-back MPP control is much larger than the time constant of the EPS.

Figure 13.11 shows the self-learning process, the array current being the optimizing signal, with the array biased at the maximum power point by the MPP tracking system. The amplitudes of the scanning process are reduced to around maximum through time for each position of the table (the resolution is 1°). At the following position of the table, the process starts again. The graph shows that even for the maximum scanning amplitudes, at the beginning of each 1° step, the array is illuminated, which is a necessary condition for the MPP control.

EULIDES is the first approach to a PV linear concentrator based on parabolic troughs. To test the concept, a prototype of only 60 m^2 (24 m long)

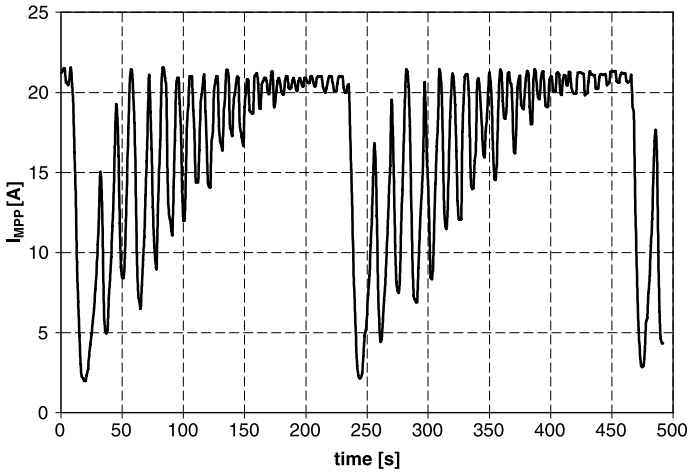

Fig. 13.11. Self-learning process of the pointing system, I_{MPP} being the optimising signal with the array biased at the maximum power point. The MPP control keeps the voltage quasi-constant to avoid interference with the pointing system

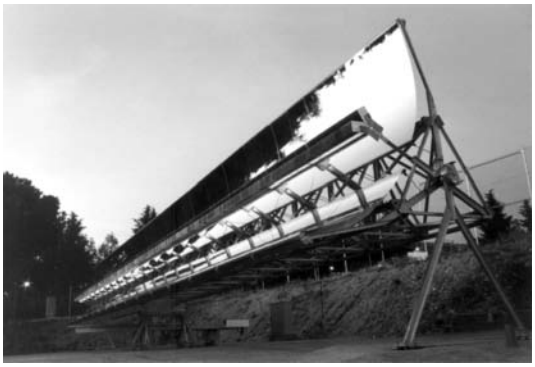

Fig. 13.12. Picture of the EUCLIDES prototype installed in Madrid in 1995

was designed and installed at the IES-UPM facilities in 1996 (see Fig. 13.12). Many new sub-systems were successfully developed at that time, which are described throughout this chapter. Parabolic mirrors based on reflective films, the one-axis tracking structure, the self-learning sun-pointing system, LGBG cells for operating at 30 suns, modules based on those cells and high efficiency but lightweight heat sinks are the highlight of that work. Despite this experience being the first attempt and the many completely new sub-systems involved, very good results have been obtained, which have encouraged BP Solar and IES-UPM to set out on a bigger project where its potential of cost reduction could be proved.

13.8 From the Prototype to an Industrial-Scale Plant

A demonstration power plant [10, 15, 22] was proposed and subsidized by the European Commission in 1996. The aim was to identify the most suitable subcontractors for developing the tooling and manufacturing the components of this technology in order to probe its industrial feasibility. Figures 13.13

Fig. 13.13. EUCLIDES line at the Tenerife plan. Each line is 84m long and has an aperture area of 232 m^2

and 13.14 illustrate the size of the project, the first PV plant with concentrators installed in Europe.

The 480-kWp plant consisted of 14 EUCLIDES lines, each 80 m long. The significant figures of a EUCLIDES line and the whole plant are detailed in Table 13.1. The installation of the systems was finished by the end of 1998 and was connected to the grid at the beginning of 1999.

As this was the first experience based on concentrators in Europe and the largest in the world at that time, this project had to confront many unsolved problems related to concentrator systems. For example, the lack of international standards, especially those referring to system qualification, was a substantial handicap since there was no experience on qualifying concentrator system in order to ensure long-term operation. A proof of concept was designed both for the modules and the mirrors, based on conventional

Fig. 13.14. View of the Tenerife plant, where 14 lines were installed with a nominal power of 480 kWp

Table 13.1. Figures of the Tenerife plant based on EUCLIDES concentrator

Plant figures		
Power peak	480	kWp
Aperture area	3528	M^2
EUCLIDES lines	14	
No. of receivers (module + heat sink)	1932	
No. of mirrors	1960	
No. of inverters	7	
EUCLIDES line figures		
Aperture area	252	M^2
Geometric concentration	38	
No. of receivers (module + heat sink)	138	
No. of mirrors	140	
Nominal power	31.4	kWp
Isc at nominal conditions	45	A
Voc at nominal conditions	940	V

PV and electronic international standards. While the samples passed these tests, the long-term operation of the systems was not as good as expected.

Since the grid connection of the plant, it has been discovered that many of the modules have lost their insulating properties, causing leakages to ground. The nominal operating voltage was 800 V, but the modules had been qualified up to 2600 V in the high-pot test. The task of identifying, disconnecting and replacing these failing modules was extremely hard and very time-consuming. Successive module failures prevented the continuous operation of the plant and required repeated action by the staff to solve the problems.

Regarding the mirrors, the lack of commercial availability of the film used for the prototype forced alternatives to be found. This involved not only the search for new materials but also a new manufacturing processes. None of the three technologies used in the plant showed the same results as the prototype with regard to optical efficiency and long-term reliability [10]. Many problems were related to the quality control in the manufacturing and storage of the mirrors, which were carried out on site. Some of them showed sealing defects which contributed to a fast degradation in especially hard weather conditions such as those of Tenerife. The continuous maintenance actions on the arrays, resulting from module failures, also caused a lot of damage to the mirrors. The technology based on reflective film lamination has now been abandoned and replaced by glass mirrors as explained above.

Despite these technical problems, which obviously restricted a good performance of the plant, there are many contributions of this project to be highlighted. The performance of the rest of the sub-systems, such as the tracking structure, the pointing system, and the heat sinks was excellent, and all they reached the required industrialization for a commercial exploitation.

The project contributed to a significant advance in the knowledge acquired by the partners. The performance prediction of concentrator cells and modules from their dark characteristic [23] allowed equipment for the classification of the more than 20,000 concentrator cells to be developed as well as the 2000 modules manufactured for the plant. The losses caused by optical dispersion and misalignments, a particular characteristic of concentrator systems, and their implications on the angular transmission and acceptance angle at the maximum power point, could be studied first [8].

But the most significant result of the plant is the demonstration of the envisaged cost with the prototype. A figure of 4.45 €/Wp was achieved for the plant (in 1998), which proved that the projection figure of 3.84 €/Wp for a 10 MW/year production was very possible. Nevertheless, the technical problems of the plant and changes within BP Solar, owner of the exploitation license, meant a halt in the EUCLIDES technology. With a little more effort, those problems could have been solved and the EUCLIDES technology, with that cost figure, could now be a commercial alternative to conventional PV plants, such as those arising in many countries due to the existing feed-in tariffs.

The third generation of EUCLIDES technology has stressed the redesign of the manufacturing process of both the modules and mirrors, whose new concepts have been described throughout this chapter. The technology being ready, the cost analysis and the new panorama of the PV business are discussed below in order to determine the real possibilities of this concept to enter the PV market.

13.9 Cost Analysis

Large PV power stations, also called 'solar farms', are currently being installed in some countries at multi-megawatt capacity. The reason is that some European countries are promoting clean energy from renewable sources as a consequence of the Kyoto protocol. A feed-in tariff has been established for the energy produced by PV installations, which has excited the market.

Concentrator systems must enter the market in competition with conventional PV plants. We analyze the maximum cost of EUCLIDES-III technology to have a reasonable chance in the current booming of 'solar farms'. The objective, with respect to the EUCLIDES concentrator, is to achieve a system whose cost could be paid off within a period of 10 years under the 'feed-in tariff' Spanish conditions. The tariff for photovoltaic systems are stated in 'ROYAL DECREE 436/2004 of the 12th of March 2004'. The price for the energy produced in installations with an instantaneous power up to 100 kWp is 0.4215 €/kWh by 2005.

13.9.1 Energy Production Calculation and Price per Watt

We have taken the Madrid irradiance data for the energy production calculation. The energy production in Madrid of one EUCLIDES array can be calculated as:

Annual energy (kW h) $= B_a\,(\mathrm{kWh/m^2}) \cdot A_r\,(\mathrm{m^2}) \cdot \eta_{\mathrm{op}} \cdot \mathrm{PR} \cdot \eta_{\mathrm{rec}} = 1570 \cdot A_r \cdot 0.8 \cdot 0.7 \cdot 0.175 = 153.86 \cdot A_r\,(\mathrm{kWh})$, where B_a is the radiation collected by one concentrator with one horizontal axis oriented N-S in Madrid ($B_a = 1570\,\mathrm{kWh/m^2}$), A_r is the collector surface area, η_{op} is the optical efficiency ($\eta_{\mathrm{op}} = 80\%$), PR is the performance ratio ($\mathrm{PR} = 0.7$) and η_{rec} is the receiver efficiency at nominal operating conditions and the cell temperature of 25 °C ($\eta_{\mathrm{rec}} = 17.5\%$).

The net income obtained, taking into account taxes and maintenance expenses is:

$$\mathrm{Netincome} = 0.8 \cdot 153.86 \cdot A_r \cdot 0.4215 = 51.88 \cdot A_r\,(\mathrm{e})\ .$$

For an array of 250 $\mathrm{m^2}$ of aperture area, with a peak power of 33.25 kWp at STC (Irradiance = 1000 $\mathrm{W/m^2}$; $T_{\mathrm{cell}} = 25\,^{\circ}\mathrm{C}$; Wind = 1 m/s), the cost per Wp should be less than 3.89 €/Wp for a payback period of 10 years.

Table 13.2. Projected cost of a 33.25-kW peak EUCLIDES array, at STC, for installations of 2 MW. Based on the cost of materials and projecting the labor cost in automated manufacturing plants, we obtained a cost projection for the first megawatts of this technology (Total 1) and long-term cost (Total 2). Installation costs are also taken into account

Components	No. of parts	Unit	Unit price	Units	Total 1	Total 2
Mirrors	250	m^2	70	€/m^2	17,500	17,500
Heat sink	33.250	Watt	0.4		13,300	11,600
Array structure					18,000	10,000
Driver					13,000	9000
Transportation					12,000	11,000
Painting					5000	5000
Field mounting					6000	5000
Land preparation					6000	6000
Modules (without cells)					13,500	9500
Inverter	26.000	Wp	0.3	€/Wp	7800	7800
Total without cells					112,100	92,400
Cell price (€/cell)					11.2	
Cost of cells					17,150	16,690
System cost					129,250	109,090
Cost per Wpeak (STC conditions)					3.9 €	3.30 €
Cost per Wpeak ($B = 800\,W/m^2$; $T_{cell} = 50\,°C$)					5.4 €	4.56 €

13.9.2 Calculation of Component and System Cost

The expected cost of the new EUCLIDES-III technology are described in the Table 13.2. All figures are updated from those obtained from the experience of the Tenerife EUCLIDES power plant of 480 kWp, and the estimated cost provided by industries involved in the third generation of EUCLIDES technology. The costs are based on the current cell efficiency (CZ wafers) of 18%.

13.10 Conclusion

The EUCLIDES concept, i.e. a reflective parabolic trough concentrator (PTC) consisting of a linear array tracking around a horizontal N/S axis was conceived and developed in the mid-1990s. A large PV plant experiment was carried out in Tenerife, which highlighted the lack of maturity of the mirror and module technology, but demonstrated the cost potential of the concept.

The whole system has now been redesigned from the lessons learned from experience, paying special attention to the achievement of long-term reliabil-

ity of both modules and mirrors. The technology being ready, the question now arises as to its capability to compete in the PV market for power plants. The current feed-in markets in some countries together with the present conventional module scarcity offer an excellent opportunity for concentrators. This particular situation can assume prices within the range 5 – 6 €/Wpeak, but this situation will not last much longer and lower prices will be required within next few years.

The cost figures for the EUCLIDES technology (3.9 €/Wp) and the Spanish scenario leads to a payback period of 10 years for an array installed in Madrid; therefore, this concentrator could have been competing in the market since the beginning of the feed-in tariff. Nevertheless, the technical problems in the Tenerife plant and the changes taking place in BP Solar, owner of the exploitation license, meant that the EUCLIDES technology was discontinued after the Tenerife project. With a little more effort, these problems could have been solved and the EUCLIDES technology, with that cost figure, could currently be a commercial alternative to conventional PV plants.

Nevertheless, the cost figure forecasts an uncertain future for this technology, at least at 18% of cell efficiency. With this efficiency level, it is almost impossible to achieve the objective of 3 €/Wp in the short term, which will probably be the market price within the next few years when new concepts of compact high-concentration systems, such as those described in this book, reach the market. In the case of cells with 23% efficiency, the cost becomes 2.85 € under STC conditions and EUCLIDES would become really competitive.

References

1. Larson RW, West RE. Implementation of solar thermal technology. MIT Press, Boston, 1996
2. Wenham SR. Buried-contact silicon solar cells. Prog Photovoltaics Res Appl, 1993; 1:3–10
3. Cunningham DW, Gasson MP, Bruton TM. Development of a solar cell module capable of opertaing under 30× concentration. Proc 13th European Photovoltaic Solar Energy Conference and Exhibition, 1995; 2278–2280
4. Luque A, Sala G, Arboiro JC, Bruton T, Cunningham D, Mason N. Some results of the EUCLIDES photovoltaic concentrator prototype. Progr Photovoltaics Res Appl, 1997; 5:195–212
5. Rabl A. Active solar collectors and their applications. Oxford University Press: New York, 1985
6. Luque A. Quasi-optimum pseudo-Lambertian reflecting concentrators: an analysis. Appl Optics 1980; 19:2398–2402
7. Antón I, Pachon D, Sala G. Characterization of optical collectors for concentration photovoltaic applications. Progr Photovoltaics Res Appl, 2003; 11:387–405
8. Antón I, Sala G. Losses caused by dispersion of optical parameters and misalignments in PV concentrators. Prog Photovoltaics Res Appl, 2005; 13:341–352
9. Arboiro JC, Sala G, Molina JI, Hernando L, Luque A. Parabolic reflector with efficiencies over 90% for the EUCLIDES concentrator. Proc 14th European Photovoltaic Solar Energy Conference and Exhibition, 1997; 1340–1343

10. Sala G, Arboiro JC, Luque A, Antón I, Gasson MP, Mason N, Heasman K. 480 kW peak concentrator power plant using the EUCLIDES parabolic trough technology. Proc 2nd World Conference and Exhibition on Photovoltaic Solar Energy Conversion, 1998; 1963–1968
11. Sala G, Pachón D, Antón I, Vivar M, Mohring HD, Klotz FH, Morilla C, Fernández JM, Martinelli G, Stefancich M, Malagú C, Eames P, Mallick T, Luque-Heredia I, Cervantes R. IDEOCONTE Project: Searching the Best Si-Cells PV Concentrator. Proc 20th European Photovoltaic Solar Energy Conference and Exhibition, 2005; 2360–2363
12. Bruton TM. Low cost concentrator cells from one sun production cell technology. Proc International Conference on Solar Concentrators for the Generation of Electricity or Hydrogen, 2005; NREL/CD-520-38172, Publ. NREL
13. Morilla MC, Fernández JM, Antón I, Pachón D, Sala G. Buried contact cell design optimisation for concentration systems. Proc 20th European Photovoltaic Solar Energy Conference and Exhibition, 2005; 1149–1151
14. Sala G, Luque A, Zamorano JC, Huergo P, Arboiro JC. Lightweight heat-sinks for the EUCLIDES concentrator array. Proc 13th European Photovoltaic Solar Energy Conference and Exhibition,1995; 2398–2401
15. Sala G, Antón I, Monedero J, Valera P, Friend MP, Cendagorta M, Pérez F, Mera E, Camblor E. The Euclides-Thermie Concentrator Power Plant in continuous operation. Proc 17th Photovoltaic Solar Energy Conference and Exhibition, 2001; 488–491
16. IEC 62108 Draft 8d. Concentrator photovoltaic (CPV) modules and assemblies: design qualification and type approval
17. Vivar M, Sala G, Pachón G, Antón I. Large-area Si-cell encapsulation for concentrator systems: review of critical points and new proposal for the third generation of EUCLIDES. Proc 4th World Conference and Exhibition on Photovoltaic Solar Energy Conversion, 2006
18. Arboiro JC, Sala G, Molina I, Hernando L, Camblor E. The EUCLIDES concentrator: a lightweight 84 m long structure for sub-degree tracking. Proc 2nd World Conference and Exhibition on Photovoltaic Solar Energy Conversion, 1998; 2229–2232
19. Arboiro JC, Sala G. Self-learning tracking: a new control strategy for PV concentrators. Progr Photovoltaics Res Appl, 1997; 5:213–226
20. Antón I, Pérez F, Luque I, Sala G. Interaction between sun tracking deviations and inverter MPP strategy in concentrators connected to grid. Proc 29th IEEE Photovoltaic Specialist Conference, 2002; 1592–1595
21. Luque-Heredia I, Moreno JM, Quéméré G, Cervantes R, Magalhaes PH. SunDog^{TM} STCU: a generic sun tracking control unit for concentration technologies. Proc 20th European Photovoltaic Solar Energy Conference and Exhibition, 200; 2047–2050
22. Sala G, Antón I, Arboiro JC, Luque A, Camblor E, Mera E, Gasson MP, Cendagorta M, Valera P, Friend MP, Monedero J, González S, Dobón F. The 480 kWp EUCLIDES-THERMIE Power plant: installation, set-up and first results. Proc 16th European Photovoltaic Solar Energy Conference and Exhibition, 2000; 2072–2077
23. Antón I, Sala G, Heasman K, Kern R, Bruton TM. The performance prediction of concentrator solar cells and modules from dark I-V characteristics. Progr Photovoltaics Res Appl, 2003; 11:165–178

14 The FLATCON System from Concentrix Solar

A.W. Bett and H. Lerchenmüller

14.1 Introduction and History of the Development

Concentrix Solar GmbH (Freiburg, Germany) is a company that was founded with the aim of launching an innovative technology based on high-concentration photovoltaic (PV) cells. The technology is based on development work at Fraunhofer ISE in Freiburg, Germany. Some of the essential features of this technology go back to 1993 when Fraunhofer ISE published the results obtained for a concentrator test module using single-junction GaAs solar cells made by liquid-phase epitaxy (LPE) [1–3].

Figure 14.1 shows the concentrator module as constructed. Twenty-four Fresnel lenses made of PMMA with an area of $4.5 \times 4.5\,\mathrm{cm}^2$ and a focal length of 53 mm were used to concentrate the sunlight by a factor of ~ 130 onto the GaAs solar cells. The cells had a diameter of 4 mm and used a prismatic cover to reduce the shading losses by the metal fingers of the front grid design. The measured module efficiency was as high as 20.1% under operating conditions in Freiburg [3]. This was a very promising and encouraging result. In the module, single-junction GaAs solar cells with an efficiency of 24% at 100×AM1.5d were used [2]. The cells were manufactured by a fairly simple LPE process using the etchback regrowth technique [4–6]. In order to manufacture high-concentration solar cells, special tools have been developed at Fraunhofer ISE. For example, computer codes were generated to optimize the grid design [1]. In this context, it is noteworthy that there is not 'the concentrator solar cell'. The cell must always be adapted to the requirements of the concentrating optics, or vice versa. This is essential in order to optimize a concentrator PV system with respect to the output power.

Since the results of the first concentrator module were very promising, the next target was to demonstrate higher efficiencies. This can be achieved by increasing the number of p-n junctions in a solar cell. The easiest way is to stack single cells made of different semiconductor materials on top of each other [7,8]. Considering a dual-junction solar cell, the GaAs-GaSb combination has been shown theoretically to be nearly optimal [9]. Moreover, it was feasible to fabricate high-quality GaSb solar cells using a simple Zn vapour-diffusion process [10–12]. Consequently, in 1997 Fraunhofer ISE constructed a module using mechanically stacked GaAs and GaSb cells. In this case, 24 Fresnel lenses with an area of $4.5 \times 4.5\,\mathrm{cm}^2$ were used again to con-

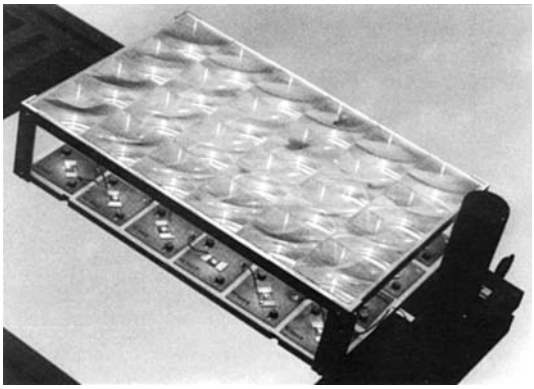

Fig. 14.1. A concentrator module fabricated at Fraunhofer ISE in the mid-1990s. Fresnel lenses with a focal length of 53 mm were used to concentrate the sunlight by a geometrical factor of 160 onto GaAs single-junction solar cells. This corresponds to an electrical concentration factor of ∼130

centrate the sunlight by a factor of ∼ 130. The measured outdoor module efficiency increased to 23% [13]. However, the mechanically stacked approach needs two separate cells and sophisticated interconnection of the single cells at the module level [14]. In this respect, another approach, the monolithically grown multijunction solar cell structure (see the chapter 'Multijunction Concentrator Solar Cells') is preferable.

In 1997 Fraunhofer ISE installed an AIX26000G3 MOVPE (metal organic vapour-phase epitaxy) reactor. Three years later, a dual-junction concentrator solar cell made of $Ga_{0.35}In_{0.65}P/Ga_{0.83}In_{0.17}As$ achieved a record efficiency of 31.3% at a concentration level of 300 suns [15,16]. These monolithic cells were mounted in a test module with an aperture area of 192 cm^2. In this case, 4 × 4-cm^2 Fresnel lenses with a focal length of 76 mm were used. The Fresnel lens structure was made in silicone using an embossing process developed together with the Ioffe Institute in St. Petersburg [17, 18]. This high-efficiency Fresnel lens module was measured during 3 days in August, September and October 2001. The average module efficiency was 23.8% and the maximum module efficiency was 24.8% [8, 19]. This was the highest reported module efficiency at that time.

All these results were important milestones for the further path to develop concentrator modules for long-term operation and market introduction. They demonstrated the principles to achieve high efficiency; however, as is shown in Fig. 14.1, these modules were not suitable for long-term operation. The cells are not protected, so the modules had to be dismounted from the tracking unit if it started to rain. Nevertheless, these early test modules already included essential features which are still characteristic for the FLATCON module fabricated by Concentrix Solar today. These main features are:

1. The use of a small cell area.
   This allows passive heat removal (see also Fig. 14.2) because the heat is generated over a tiny area and is then distributed very effectively by a simple copper plate in two dimensions; thus, the copper plate acting as a heat sink has nearly the same area as the lens aperture. This concept

allows passive cooling even for very-high-concentration ratios of up to 1000.
The small cell facilitates extraction of the generated current. The resistive losses are proportional to the square of the current; thus, smaller cell areas produce less current, and therefore the shading factor introduced by the metal fingers can be lower.
The industrial manufacturing processes of the cells and the packaging are similar to light-emitting diodes; thus, existing packaging equipment may be used in large-scale production, which lowers the investment costs.

2. Selection of a 'short' focal length.
A short focal length of around 75mm allows easy handling. This is important for the transport of the module and the mounting procedure on a tracking system.
The flat Fresnel structures can be fabricated easily.

After the technological principles had been demonstrated, cost issues were considered more seriously; therefore, an initial cost estimate was made [15]. These cost estimates showed that, when using III-V solar cells, the concentration ratio of 100× might be too low to achieve cost advantages compared with flat-plate silicon solar modules. The III-V solar cells are known to operate reliably up to concentration levels of 5800× [20]; thus, in principle, there is no limitation on increasing the concentration ratio. For practical manufacturing reasons, a concentration ratio of 500× was chosen. This concentration ratio allows the module to be cost competitive. In the future, the concentration ratio can be easily increased to 1000× by including secondary optics in the module. This is currently under investigation at Fraunhofer ISE. The higher concentration ratio of 500 was easily achieved by reducing the cell diameter from 4mm to 2mm and modifying the Fresnel lens structure slightly [19, 21].

Another important step in the development was started in 1999 when the all-glass housing concept was introduced [17, 18]. This was done in cooperation with the Ioffe Institute of St. Petersburg, Russia. Based on the optical concept already used at Fraunhofer ISE, the housing was made completely of glass. This required the development of a technology to fabricate the Fresnel structure on glass plates. This challenge was solved by the development of an embossing process into a thin silicone film [17]. Optical efficiencies as high as 91% for a 4-mm-diameter cell were achieved with this technique [18]. The copper heat sink together with the concentrator solar cell (see Figs. 14.2, 14.3) were attached to a glass sheet with an adhesive. Subsequently, the Fresnel lens plate and the solar cell plate were cemented to the glass side walls to complete the construction of the glass frame (see Fig. 14.3). The characteristics of this module design led to the registered trade name FLATCON (Fresnel lens all-glass tandem cell concentrator). In these first approaches, the modules were hermetically sealed with structural silicone [17]. However, long-term and accelerated indoor ageing tests showed penetration of moisture.

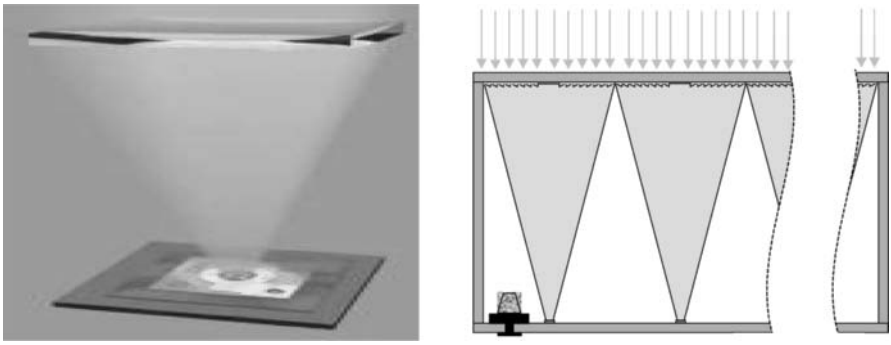

Fig. 14.2. Operating principle of the FLATCON technology. The light is concentrated on a tiny cell. The cell is mounted on a copper heat sink which facilitates passive cooling. It is noteworthy that the copper area is similar to the lens area. This guarantees similar thermal behaviour to a flat-plate module, even though highly concentrated light is used

Fig. 14.3. The main components of a FLATCON module: the Fresnel lens plate, the glass frame and the lower glass plate with the solar cell assemblies

Thus, in a later stage of the development, filters were introduced to the modules, allowing the module to breathe. The first hermetically sealed, all-glass modules used GaAs single-junction cells and achieved an efficiency of 19%. Modules equipped with monolithic dual-junction cells made of $Ga_{0.35}In_{0.65}P/Ga_{0.83}In_{0.17}As$ and applying a concentration ratio of 500× showed efficiency as high as 22.7% [21, 22]. Based on these experimental results, further research efforts were made to increase the efficiency of the modules, for example, by introducing triple-junction solar cells and improving the optical efficiency of the Fresnel lenses. Accelerated ageing and reliability tests and the manufacturing on automatic packaging equipment led to some modification of the module concept. In addition, a more detailed cost analysis was performed.

The good technical results concerning module efficiency and the promising economic perspectives for this technology led to the foundation of Concentrix Solar in February 2005, taking advantage of more than 10 years of experience gained at Fraunhofer ISE. Concentrix Solar will bring the FLATCON technol-

Fig. 14.4. Concentrator PV power plants in the MW range will be installed by Concentrix Solar using the FLATCON module technology

ogy onto the market and offers complete concentrator PV systems and solar power plants as visualized in Fig. 14.4. The current status of the FLATCON technology as well as cost issues are described in the following sections.

14.2 The FLATCON Concentrator Systems

14.2.1 Optics

Concentrator photovoltaic (CPV) systems require highly efficient optics in order to reach high system efficiencies. On the other hand, the optics need to be inexpensive and durable. The FLATCON system uses Fresnel lenses to focus the sunlight onto the cell. Like a burning glass, they direct the sunlight onto a focal point, the solar cell; however, the use of Fresnel lenses without secondary optics produces a quasi-Gaussian profile with 2500× concentration in the centre of the 2-mm-diameter solar cell (see Fig. 14.5). This demands a specially adapted grid design for the solar cell.

The production process of the lenses is based on a simple embossing process in a silicone film as described in [17]. A complete Fresnel lens panel, as illustrated in Fig. 14.3, can be produced in one process. However, the cells

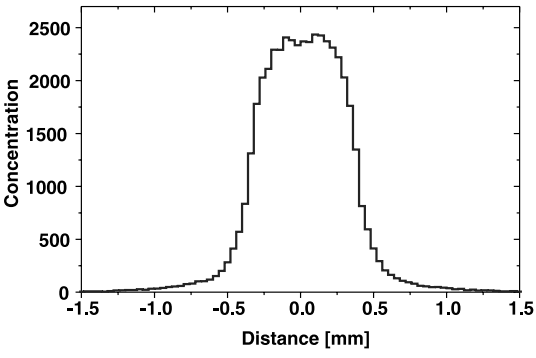

Fig. 14.5. Calculated intensity profile of a Fresnel lens used in the FLATCON module. Whereas the average geometrical concentration factor is 500, the concentration factor is 2500 at the centre of the cell with a diameter of 2mm

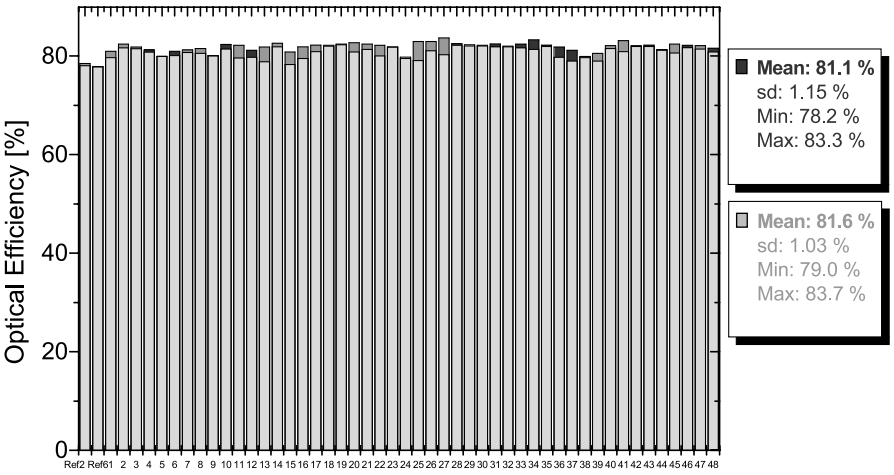

Fig. 14.6. Distribution of the measured optical efficiencies for two Fresnel lens panels consisting of 48 Fresnel lenses $4 \times 4\,\mathrm{cm}^2$. The measured mean values are above 81% and the measured minimum value is 78.2%

in the module are series-connected, so it is very important that each individual Fresnel lens show the same high optical efficiency; otherwise, the module efficiency drops. Therefore, the main emphasis of the process development was to obtain a homogeneous efficiency distribution over the panel and to improve the reproducibility of the process. Figure 14.6 shows the measured optical efficiency distribution for two Fresnel lens panels. After process optimization, satisfying results with a minimum optical lens efficiency of 78.2% and an average value of $> 81\%$ for the Fresnel lens panels were obtained. The advantages of this method are the high UV resistance and the process reliability. The optical design of the FLATCON modules leads to an acceptance angle of $\pm 0.6^\circ$ [22].

14.2.2 Cell Development

The FLATCON modules use tandem cells based on III-V semiconductors. Until the end of 2005, lattice-mismatched $Ga_{0.35}In_{0.65}P/Ga_{0.83}In_{0.17}As$ dual-junction solar cells with an inner diameter of 2 mm were applied in the test modules fabricated at Fraunhofer ISE. They achieve efficiency of up to 31.3% at 300 suns (AM1.5d spectrum) [23] and, on average, 29% at 400 suns (AM1.5d spectrum with low aerosol optical density value). The cell proved to be very robust when tested under accelerated ageing conditions. An example of one testing sequence is shown in Fig. 14.7, which illustrates the experimental results of exposing a bare cell at 95 °C to an environment saturated with water vapour (damp-heat test) [24, 25].

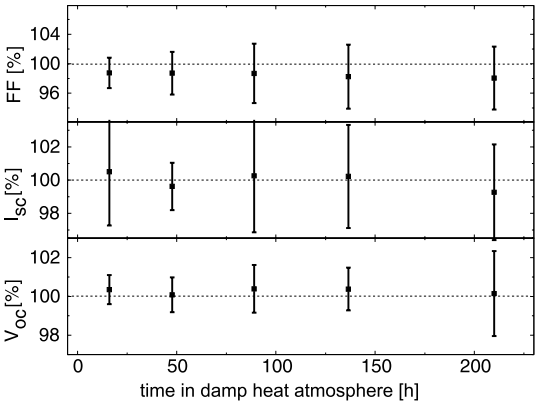

Fig. 14.7. Dependence of dual-junction cell parameters on the exposure time of bare cells to an environment saturated with water vapour at 95 °C. (From [25])

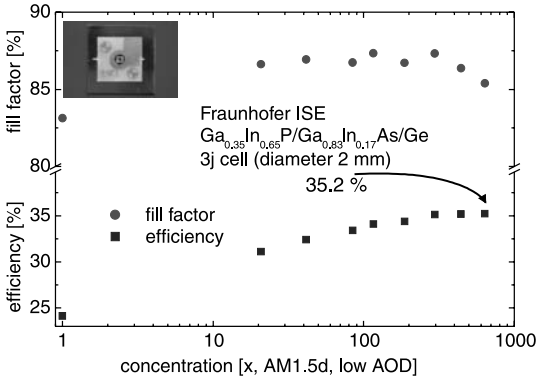

Fig. 14.8. Fill factor and efficiency vs concentration ratio of a lattice-mismatched triple-junction concentrator solar cell

The tunnel diode of the dual-junction cell has been shown to be extremely robust and able to work at concentration ratios as high as 10,000 suns. So, even at the centre of the cell, where concentration up to 2500× may occur during operation in a real module (see Fig. 14.5), no problems are expected.

Since the end of 2005, lattice-mismatched triple-junction cells have been used instead of the dual-junction cell. They consist of $Ga_{0.35}In_{0.65}P/Ga_{0.83}In_{0.17}As/Ge$. The first European triple-junction concentrator solar cell achieved an efficiency of 35.2% at 600 suns (AM1.5d spectrum, low AOD value; see Fig. 14.8) [26]. The cell was designed such that all three subcells generate the same current under the AM1.5d spectrum, low AOD value. This was proven by integration of the external quantum efficiency and the AM1.5d spectrum. It is noteworthy that in the more commonly used $Ga_{0.50}In_{0.50}P/Ga_{0.99}In_{0.01}As/Ge$ lattice-matched triple-junction cells, Ge always generates a higher current than the upper cells. Consequently, the lattice-mismatched approach has the higher-efficiency potential; however, lattice-mismatched structures require growth of a suitable buffer to prevent threading dislocations which harm the active solar cell material [27].

Fig. 14.9. Pilot production line for FLATCON module production up to 1 MW_p

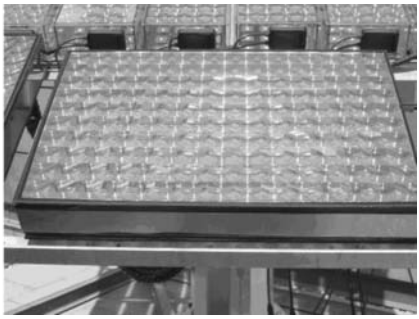

Fig. 14.10. *Left:* First-generation modules, where the housing is made completely of glass. *Right:* Recent FLATCON modules, where the frame is made of metal and the area of the modules has been increased

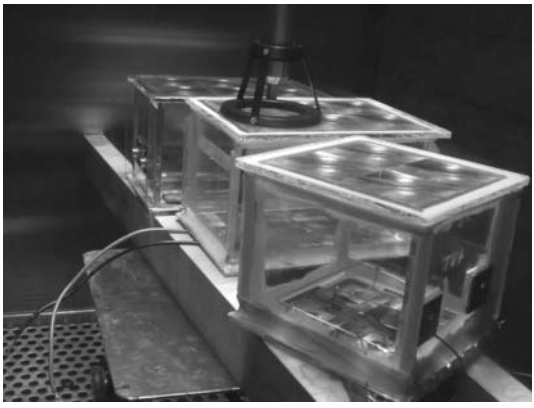

Fig. 14.11. Test modules in the climatic chamber. This is an example of our extensive indoor testing activity to develop a reliable product

14.2.3 FLATCON Module Fabrication

Early in 2006, a pilot production line with a nominal production capacity of 1 MW_p was installed in Freiburg in close co-operation between Concentrix

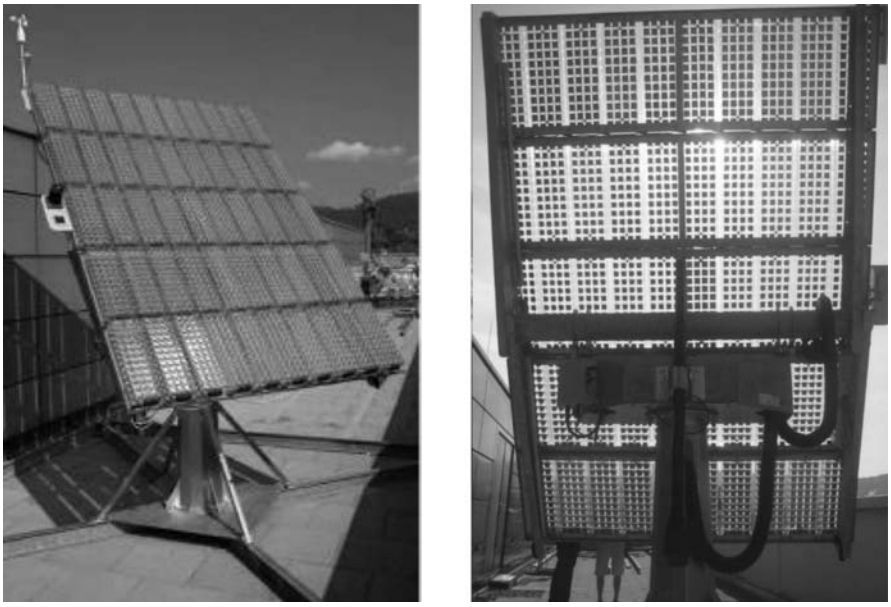

Fig. 14.12. A 1-kW FLATCON demonstration system on the roof of Fraunhofer ISE in Freiburg

and Fraunhofer ISE. Using electronic production equipment, such as a die-bonder and a pick-and-place machine, FLATCON modules can be produced in a semi-automated line. Figure 14.9 shows a photo of the production line.

For the first test modules, the housing was made completely of glass (see Fig. 14.10). Presently, FLATCON modules are larger in size and are made with a metal frame which mechanically connects the top glass plate with the lenses to the bottom glass plate with the mounted cells (see Fig. 14.10). Whereas at the beginning of development the very first modules were hermetically sealed, these were shown by indoor tests, in climatic chambers, to be insufficiently reliable. Over time, moisture penetrated the seal and accumulated in the module without a chance to escape. Figure 14.11 shows an example of the work performed in order to develop a durable product: test modules are shown during testing in a climatic chamber [26]. Consequently, a new filter was introduced which allows the module to 'breathe'. Humidity freeze tests were performed which demonstrated the value of this new concept. In addition, long-term outdoor measurements were performed with the test facility of Fraunhofer ISE in Freiburg and NREL USA [28].

14.2.4 The Tracking System

The first demonstration system of Concentrix was set up on top of the roof of Fraunhofer ISE in June 2005 (see Fig. 14.12). These first demonstration

systems use a Pairan Pesos SF18 tracker. The gearbox was modified by Pairan to reduce backlash. For the first systems, the tracking system was controlled with a separate control system developed at Fraunhofer ISE. The tracking is controlled by astronomic calculation of the sun's position in combination with four-quadrant sensor signals, in order to achieve an optimum system output.

The 1-kW systems are demonstration projects at different sites in Europe in order to gain experience with the operating systems. Currently, Concentrix is shifting to a system size of 5 kW. These systems will have the same size as the planned concentrator units in the power plants (see Fig. 14.4).

In large FLATCON concentrator power plants, a specialized inverter will be used which will also serve simultaneously as the tracking control (see Fig. 14.13). The inverters are connected via a communication interface with a central computer of the power plant. This central computer has access to the Internet. This access enables remote monitoring of each tracking system. Figure 14.14 shows a schematic diagram of a FLATCON power plant.

14.3 Performance of the FLATCON Systems

14.3.1 Experimental Results

The first demonstration system was equipped with modules using dual-junction solar cells. Since December 2005, the demonstration system has been equipped with triple-junction solar cells. The first results are very satisfactory. The system is reliable and the results of the grid-connected system are as expected. Figure 14.15 shows the measurement for 1 day in June 2006.

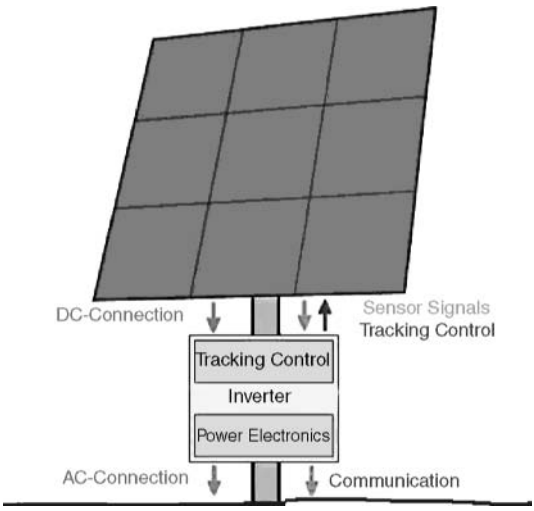

Fig. 14.13. System concept of a FLATCON tracker

The direct normal irradiance (DNI) as well as the global irradiance on a 45° tilted fixed plate is displayed together with the DC power output and the efficiency of the demonstration system. The maximum measured system efficiency during the course of the day was 23.5%.

14.3.2 Optimization of the FLATCON Modules

With the present technology status, module efficiencies up to 26.8% were measured [29]. Nevertheless, the technology is being constantly improved, mainly by improving production accuracy, by increasing the optical efficiency and by increasing the efficiency of the solar cells. In the near future triple-junction cells with minimum efficiencies of 35% will be used in module production; therefore, the averaged operating module efficiency will be well above 25% with peak efficiencies of up to 29%.

Triple-junction solar cells with different structures are currently under development at Fraunhofer ISE. Figure 14.8 shows the highest efficiency obtained so far; however, this cell suffers tunnel-diode problems for concentration factors higher than 650×. Thus, the cell cannot be applied successfully in FLATCON-type modules (see also Fig. 14.5); however, lattice-matched solar cells with an efficiency of 33% are also under development at Fraunhofer ISE. These cells operate well also at high concentration levels [30]. In order to explore the frontiers for the module efficiency, we used six selected triple-junction cells showing a calibrated cell efficiency of 33.0% at 300 – 500 suns and mounted these in a test module. This module has been operated and monitored since July 2005. The best module efficiency of 26.8% was recorded

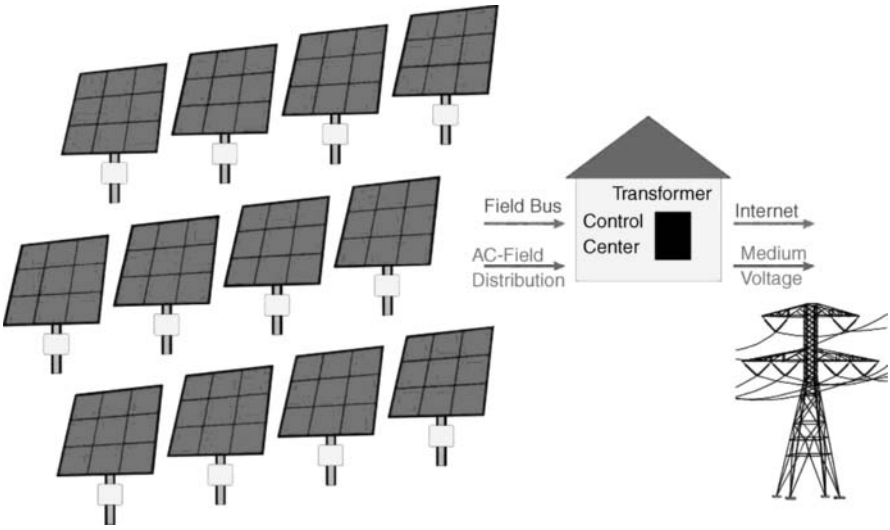

Fig. 14.14. Schematic diagram of a FLATCON power plant

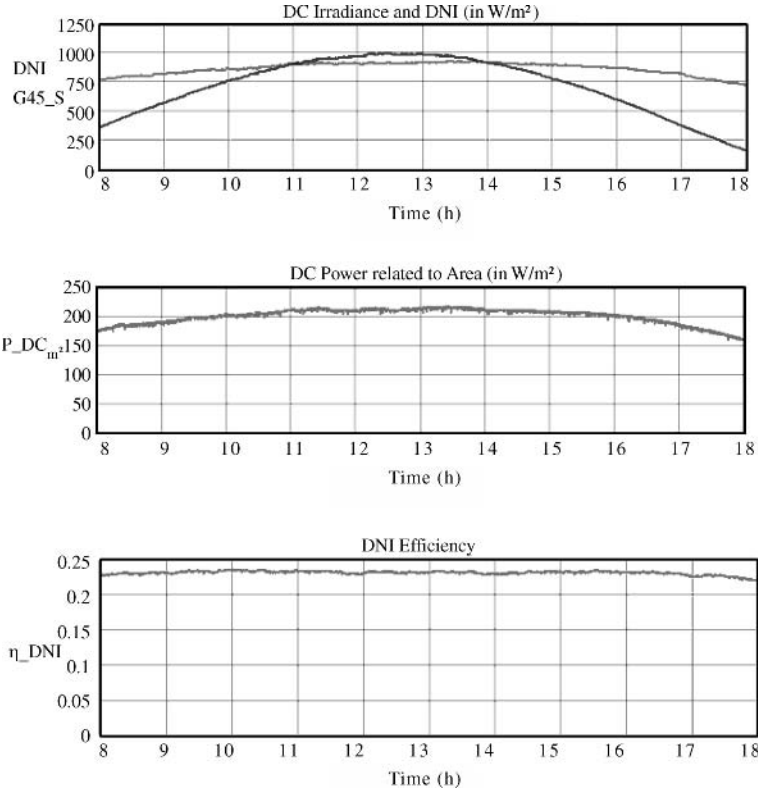

Fig. 14.15. Experimental results for the CPV system using FLATCON modules equipped with triple-junction solar cells. *Top*: measured direct normal irradiance (*DNI*) and global irradiance on a south-oriented plane tilted at 45°; *centre*: DC power output of the CPV system; *bottom*: Efficiency of the system during the course of the day

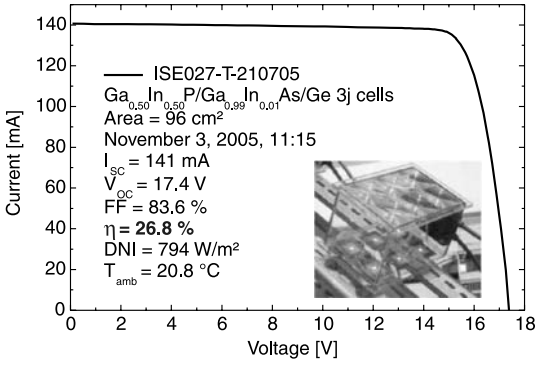

Fig. 14.16. A IV curve of a test module equipped with six triple-junction cells with a standard test condition efficiency of 33.0% at 300–500 suns. The maximum operating module efficiency is 26.8%

in November 2005 (see Fig. 14.16). A temperature correction to 25 °C would provide a module efficiency of 27.3% [29]. Figure 14.17 shows the efficiency distribution of the test module during its operation period. Clearly, many measurements show efficiencies well above 20%.

14.4 Projected Costs and Market for the FLATCON System

14.4.1 Engineering Approach for Cost Prediction

Flat-plate silicon PV, the present leading PV technology, is rapidly becoming less expensive generally due to improvements in technology and the effect of market growth. For any new PV technology, in general, low production cost can only be reached at high production volumes, whereas high sales volumes can only be reached with competitive prices. This 'chicken-and-egg' problem can be overcome by the concentrator technology since it can take advantage of the fact that the production technologies needed for concentrating PV are well established in other applications: concentrator cells are very similar to III-V space solar cells and production technology for positioning and electrical connection of the cells can apply the standard pick-and-place machines used for the assembly of printed circuit boards. This is why cost assessments for III-V concentrator systems are very promising, even for relatively low production capacities. Table 14.1 shows the results of a cost assessment for the

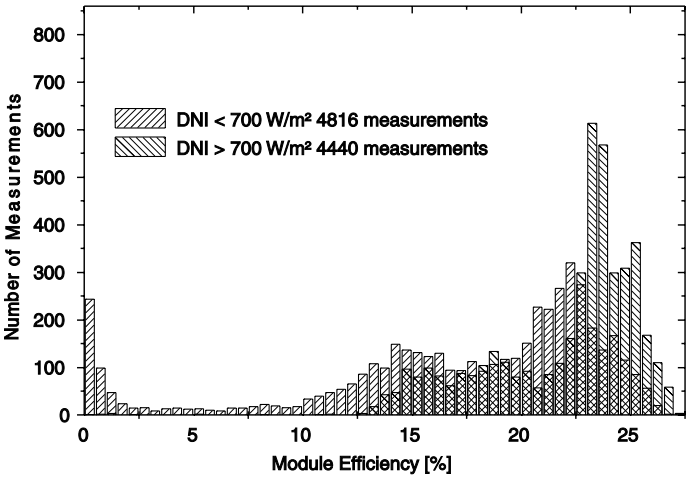

Fig. 14.17. Efficiency distribution for the test module from 27 July 2005 to April 2006. Half of the measurements are obtained for a DNI below 700 W/m^2, where a broad distribution is observed. This is a result of tracking errors in the test system at Fraunhofer ISE. The measurements at DNI above 700 W/m^2 clearly show a narrower distribution, with most of the measurement values above 20%

Table 14.1. Result of the cost analysis (only direct costs) based on annual production capacities of 20 and 200 MW

Production item	20 MW (€/W)	200 MW (€/W)
Solar cells	0.46	0.17
Solar cell assembly	0.41	0.20
Lens	0.16	0.07
Module assembly	0.24	0.14
Tracker	0.45	0.29
Module costs and tracker	1.72	0.87
Power inverter	0.33	0.15
Installation	0.07	0.05
Electronics/BOS	0.40	0.20

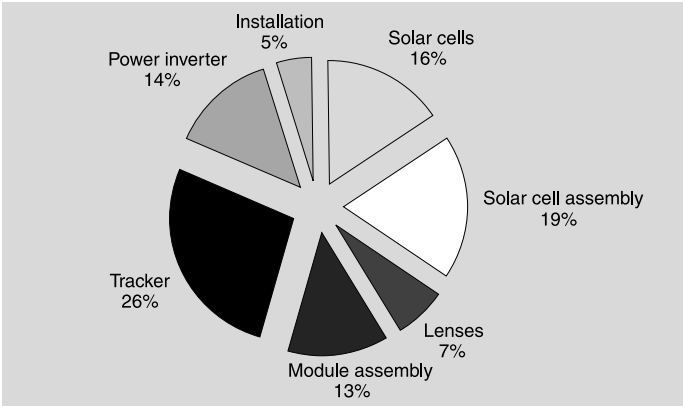

Fig. 14.18. Relative production costs for an annual production capacity of 200 MW

FLATCON technology carried out by Fraunhofer ISE and Concentrix Solar for the direct costs of concentrator systems [31, 32].

The central outcome of the cost analysis is that in a production line with 20-MW annual production capacity, the module cost can be 1.27 €/W. For a production capacity of 200 MW, the module production costs can be 0.58 €/W. The cost distribution for the 200-MW cost projection is shown in Fig. 14.18.

14.4.2 Comparison between Flat-Plate-PV-Levelized Electricity Cost for Different Sites

If the cost for the tracking is added to the cost for the concentrator module, this value can be compared to that of silicon flat-plate modules. Costs of 1.72 €/W were determined for 20-MW production capacity, whereas for 200-MW production, the costs were calculated to be 0.87 €/W (see Table 14.1).

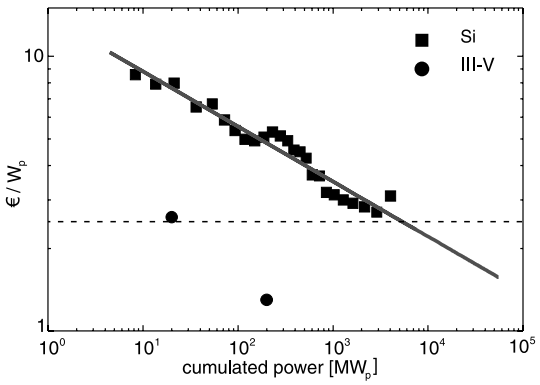

Fig. 14.19. Price curves for flat-plate silicon PV modules and for concentrator modules including the tracking. The *dashed line* indicates costs of $2.5\,€/\mathrm{W_p}$

For comparison of these values to the well-known price curve of flat-plate silicon PV displayed in Fig. 14.18, the following assumption was made: a 50% mark-up was assumed for profit and indirect costs such as management costs and expenses for R&D to calculate prices from the costs derived in Table 14.1.

Each new technology has its own price curve and starts with low shipment values (see Fig. 14.19). Provided that concentrator PV can achieve high growth rates, this technology is very interesting from an economic point of view; hence, concentrators may have a bright future in the utility-scale PV market in countries with high solar radiation levels. To assess the potential of the technology, a cost comparison between flat-plate PV and the FLAT-

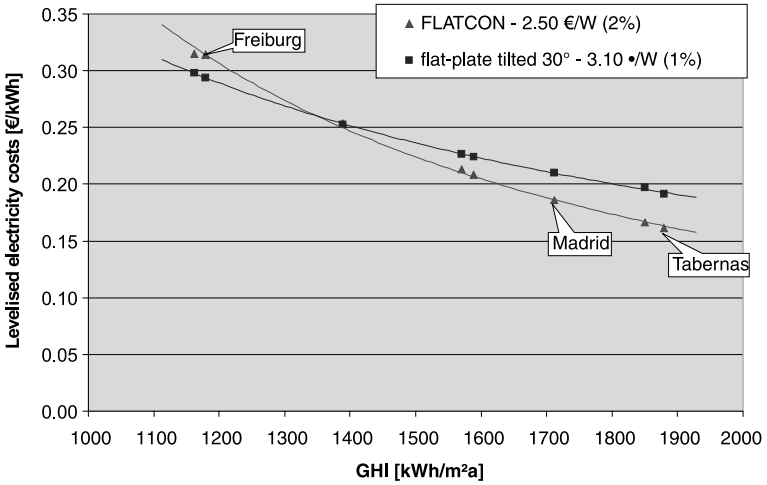

Fig. 14.20. Comparison of LEC's for flat-plate PV systems with a fixed tilt angle of 30° and FLATCON systems. Different sites in Europe have been considered. *GHI* means global horizontal irradiation. The cost calculations have been carried out for the year 2010

CON concentrator system was carried out also with respect to the levelized electricity cost (LEC). This comparison is also affected by the assumptions regarding annual depreciation of the initial investment in the PV power plant, the operating and maintenance costs (O&M) and the annual energy output. As a fully automated production line is not presently available, the comparison was made with assumptions for the year 2010, calculating 2.5 €/W_p as the system price of the FLATCON system. By then, the system price for flat-plate PV will be around 3.1 €/W_p. Since the concentrator system has to be a moving system, normal flat-plate O&M costs were doubled for the FLATCON system. For flat-plate PV, 1% of the initial investment was considered to cover the O&M costs and 2% was used for the concentrator system. The results of these calculations are shown in Fig. 14.20. The LEC calculations show that for sites with moderate solar resources such as Munich, Freiburg and Paris, the flat-plate system is superior, whereas the FLATCON technology is expected to have an advantage over flat-plate systems at sites with high direct solar radiation: 15% lower LEC for good sites in Spain and 20% for sites in Arizona and northern Africa are expected.

14.4.3 Market Perspectives for CPV Systems

The major driving force for the growth of concentrator technology is related to the progress in multijunction solar cells for highly concentrating applications; however, significant progress has also been made in optics and its production technology. Last but not least, the window of opportunity for concentrators has been opened by favourable feed-in tariffs in suitable regions such as Spain, and the rush towards renewable energies in the U.S.

Due to the fact that highly concentrating systems can use only direct sunlight, the main target market is in sunny regions with more than 1500 kW h/m^2 of direct normal irradiation (DNI). With the FLATCON CPV system, Concentrix is not aiming for the roof-top market but will address the market for large installations between 100 kW and 10 MW.

14.5 Conclusion

This chapter gives a short introduction to the FLATCON system and its stage of development at Fraunhofer ISE and Concentrix Solar. Concentrix Solar has installed several demonstration systems of 1 kW at different sites in Europe. The peak power of a single CPV system will be 5 kW. These systems will be installed in 100-kW and 10-MW solar power plants. The pilot production is running and it is expected that the first solar power plants will be installed by the middle of 2007. Results of demonstration systems are very promising and in line with the predictions; however, further analysis of the measured data still has to be performed. In order to reduce the cost for concentrator technology, it will be essential to fabricate the modules in a highly automated

process. Real cost competition to silicon flat-plate PV is expected when the production volume reaches at least 20 MW per year. Then, at sites with high direct solar radiation, the FLATCON technology is expected to have a clear competitive advantage over flat-plate silicon-based PV. It is noteworthy that the cost analysis was carried out for a 20-MW production line, a plant size which is small compared with current and future silicon-based wafer and module factories; thus, further cost reduction for large-scale production was analysed. Since production capacity for concentrator systems can be increased very rapidly, the learning curve for concentrator modules can be followed in a very short time, resulting in a fast cost reduction.

In summary, Concentrix Solar sees a bright future for the FLATCON CPV technology. With the strong financial and strategic backing of Good Energies, which joined Concentrix as an investor early in 2006, Concentrix will be able to grow as rapidly as planned.

Acknowledgement. The authors thank the many people who have contributed to the success of Concentrix Solar. They cannot all be named personally; however, we specifically want to thank Prof. Luther as the former head of Fraunhofer ISE for his continuous support for the III-V concentrator technology, and B. Burger from Fraunhofer ISE who contributed greatly to the successful grid connection of the first demonstration system.

References

1. U. Blieske, A. Baldus, A.W. Bett, F. Lutz, T. Nguyen, C. Schetter, K. Schitterer, O.V. Sulima, W. Wettling, Concentrator module based on LPE-grown GaAs solar cells, Proc 23rd IEEE Photovoltaic Specialists Conference, Louisville, Kentucky, 1993, pp. 735–739
2. U. Blieske, A.W. Bett, T. Duong, C. Schetter, O.V. Sulima, Optimization of GaAs solar cells for application in concentrator modules, Proc 12th European Photovoltaic Solar Energy Conference, Amsterdam, Netherlands, 1994, pp. 1409–1412
3. U. Blieske, A. Wegener, A.W. Bett, W. Wettling, Stand-alone, accurate tracker for concentrator module measurements, Proc 13th European Photovoltaic Solar Energy Conference, Nice, France, 1995, pp. 2362–2365
4. A. Bett, S. Cardona, A. Ehrhardt, F. Lutz, H. Welter, W. Wettling, Optimization of LPE-grown high efficiency GaAs solar cells, Proc 22nd IEEE Photovoltaic Specialists Conference, Las Vegas, 1991, pp. 137–141
5. A. Baldus, A.W. Bett, U. Blieske, T. Duong, F. Lutz, C. Schetter, W. Wettling, GaAs one-sun and concentrator solar cells based on LPE-ER grown structures, Proc 1st World Conference on Photovoltaic Energy Conversion, Waikoloa, Hawaii, 1994, pp. 1697–1700
6. A. Blug, A. Baldus, A.W. Bett, U. Blieske, G. Stollwerck, O.V. Sulima, W. Wettling, Zn-post diffusion for GaAs LPE-ER concentrator solar cells, Proc 13th European Photovoltaic Solar Energy Conference, Nice, France, 1995, pp 910–913

7. A.W. Bett, F. Dimroth, G. Stollwerk, O.V. Sulima, III-V compounds for solar cell applications, Appl Phys A 69, 1999, pp. 119–129
8. A.W. Bett (2004) Tandem cells for very high concentration, In: Next generation photovoltaics, Editors: A. Marti and A. Luque. Bristol and Philadelphia, Institute of Physics Publishing, pp. 64–88
9. A.W. Bett, F. Dimroth, S. Keser, G. Stollwerck, O.V. Sulima W. Wettling, A concept for 30% efficiency: tandem-concentrator solar cells, Proc Eurosun 1996, Freiburg, Germany, 1996, pp. 572–577
10. A.W. Bett, A.M. Mintairov, A. Namazov, O.V. Sulima, G. Stollwerck, Optimization of low-temperature Zn diffusion for GaSb solar cell structures fabrication, Proc 13th European Photovoltaic Solar Energy Conference, Nice, France, 1995, pp. 137–140
11. A.W. Bett, S. Keser, G. Stollwerck, O.V. Sulima, W. Wettling, GaSb-based (thermo)photovoltaic cells with Zn diffused emitters, Proc 25th IEEE Photovoltaic Specialists Conference, Washington, DC, 1996, pp. 133–136
12. O.V. Sulima, A.W. Bett, Fabrication and simulation of GaSb thermophotovoltaic cells, Technical digest of the 11th International Photovoltaic Science and Engineering Conference, Sapporo, Japan, 1999, pp. 441–442
13. A.W. Bett, S. Keser, G. Stollwerck, O.V. Sulima, W. Wettling, Over 31%-efficient GaAs/GaSb tandem concentrator solar cells, Proc 26th IEEE Photovoltaic Specialists Conference, Anaheim, California, 1997, pp. 931–934
14. A.W. Bett, G. Stollwerck, O.V. Sulima, W. Wettling, Highest efficiency GaAs/GaSb tandem concentrator module, Proc 2nd World Conference on Photovoltaic Energy Conversion, Vienna, 1998, pp. 268–272
15. A.W. Bett, F. Dimroth, G. Lange, M. Meusel, R. Beckert, M. Hein, S. van Riesen, U. Schubert, 30% monolithic tandem concentrator solar cells for concentrations exceeding 1000 Suns, Proc 28th IEEE Photovoltaic Specialists Conference, Anchorage, Alaska, 2000, pp. 961–964
16. F. Dimroth, R. Beckert, M. Meusel, U. Schubert, A.W. Bett, Metamorphic $Ga_yIn_{1-y}P/Ga_{1-x}In_xAs$ tandem solar cells for space and for terrestrial concentrator applications at C > 1000 suns, Progr Photovoltaics Res Appl 9(3), 2001, pp. 165–178
17. V.D. Rumyantsev, M. Hein, V.M. Andreev, A.W. Bett, F. Dimroth, G. Lange, G. Letay, M.Z. Shvarts, O.V. Sulima, Concentrator array based on GaAs cells and Fresnel lens concentrators, Proc 19th European Photovoltaic Solar Energy Conference, Glasgow, 2000, pp. 2312–2315
18. V.D. Rumyantsev, V.M. Andreev, A.W. Bett, F. Dimroth, M. Hein, G. Lange, M.Z. Shvarts, O.V. Sulima, Progress in development of all-glass terrestrial concentrator modules based on composite Fresnel lenses and III-V solar cells, 28th IEEE Photovoltaic Specialists Conference, Anchorage, Alaska, 2000, pp. 1169–1172
19. A.W. Bett, F. Dimroth, M. Hein, G. Lange, M. Meusel, U. Schubert, G. Siefer, Development of III-V-based concentrator solar cells and their application in PV-modules, Proc 29th IEEE Photovoltaic Specialists Conference, New Orleans, 2002, pp. 844–847
20. V.M. Andreev, V.P. Khvostikov, V.R. Larionov, V.D. Rumyantsev, E.V. Paleeva, M.Z. Shvarts, C. Algora, 5800 suns AlGaAs/GaAs concentrator solar cells, Technical Digest of the 11th International Photovoltaic Science and Engineering Conference, Sapporo, Japan, 1999, pp. 147–148

21. A.W. Bett, C. Baur, F. Dimroth, G. Lange, M. Meusel, S. van Riesen, G. Siefer, V.M. Andreev, V.D. Rumyantsev, N.A. Sadchikov, FLATCON-modules: technology and characterisation, Proc 3rd World Conference on Photovoltaic Energy Conversion, Osaka, 2003, pp. 634–637
22. A.W. Bett, F. Dimroth, S.W. Glunz, A. Mohr, G. Siefer, G. Willeke, FLATCON and FLASHCON concepts for high concentration PV, Proc 19th European Photovoltaic Solar Energy Conference, Paris, 2004, pp. 2488–2491
23. F. Dimroth, P. Lanyi, M. Meusel, U. Schubert, A.W. Bett, New lattice mismatched GaInP/GaInAs tandem solar cell concepts for high efficiency space and terrestrial concentrator solar cells, Proc 16th European Photovoltaic Solar Energy Conference, Glasgow, 2000, pp. 106–109
24. S. van Riesen, A.W. Bett, G.P. Willeke, Accelerated ageing tests on III-V solar cells, Proc 3rd World Conference on Photovoltaic Energy Conversion, Osaka, 2003, pp. 837–840
25. S. van Riesen, A.W. Bett, Degradation study of III-V solar cells for concentrator applications, Progr Photovoltaics Res Appl 13(5), 2005, pp. 369–380
26. A.W. Bett, G. Siefer, C. Baur, S. van Riesen, G. Peharz, H. Lerchenmüller, F. Dimroth, FLATCON concentrator PV-technology ready for the market, Proc 20th European Photovoltaic Solar Energy Conference, Barcelona, 2005, pp. 114–117
27. A.W. Bett, C. Baur, F. Dimroth, J. Schöne, Metamorphic GaInP-GaInAs layers for photovoltaic applications, Materials Research Society Symposium Proceedings 836, 2005, pp. 223–233
28. G. Siefer, A.W. Bett, K. Emery, One year outdoor evaluation of a FLATCON concentrator module, Proc 19th European Photovoltaic Solar Energy Conference, Paris, 2004, pp. 2078–2081
29. A.W. Bett, B. Burger, F. Dimroth, G. Siefer, H. Lerchenmüller, High-concentration PV using III-V solar cells, Proc 4th World Conference on Photovoltaic Energy Conversion, Waikoloa, Hawaii, 2006, pp. 745–748
30. C. Baur, A.W. Bett, F. Dimroth, G. Siefer, M. Meusel, W. Bentsch, K. Köstler, G. Strobl, Triple-junction III-V based concentrator solar cells: perspectives and challenges, J Solar Energy Eng (in press)
31. H. Lerchenmüller, A.W. Bett, J. Jaus, G. Willeke, Cost and market perspectives for FLATCON systems, 3rd International Conference on Solar Concentrators for the Generation of Electricity and Hydrogen, Scottsdale, Arizona, 2005, NREL-CD 520-38172
32. J. Luther, A. Luque, A.W. Bett, F. Dimroth, H. Lerchenmüller, G. Sala, C. Algora, Concentration photovoltaics for highest efficiencies and cost reduction, Proc 20th European Photovoltaic Solar Energy Conference, Barcelona, 2005, pp. 1953–1957

15 Concentrator Solar Cell Modules and Systems Developed in Japan

M. Yamaguchi, K. Araki, and T. Takamoto

15.1 Introduction

Dissemination of photovoltaic (PV) systems has advanced, and solar cell module production has also significantly increased in Japan as a result of R&D programs such as the New Sunshine Project under the Ministry of Economy, Trade and Industry (METI), Residential PV System Dissemination Program, as well as others. Figure 15.1 shows Japanese cumulative installed capacity of PV systems. The total installed capacity of PV systems in 2004 reached 268.8 MW and the cumulative installed capacity recorded 1128.2 MW (over 1-GW level). The PV market in Japan is working toward a target of 4.82 GW by 2010. As a result of discussion at the Committee for the 2030 PV Road Map in Japan organized by the New Energy and Industrial Technology Development Organization (NEDO) and METI, we also expect about 100-GW cumulative installed capacity [1], about 10% of Japanese electricity consumption, by 2030. The rapid growth in the PV market in recent years has been driven by the rooftop installations in the range 3 – 5 kWp; however, a market for larger PV systems is beginning to emerge, and in 2003 more than 20 systems of over 450 kWp in size were commissioned in Europe and the U.S., with an installed capacity of 26 MWp [2]. In addition, large-scale PV systems are necessary to develop in order to realize installation targets of PV systems shown in PV road maps. These facts suggest that concentrating PV systems can play a very important role for a growing PV market and a large-scale productions of PV systems when cost-effectiveness against flat-plate arrays is demonstrated. According to the Japanese PV2030 road map as shown Table 15.1, by 2030 we will have to realize super high-efficiency multijunction (MJ) solar cells and modules with efficiencies of 50 and 40%, respectively.

Since the solar spectrum is broad, conversion efficiency of single-junction solar cells is limited to less than about 30%. The solution to this problem is, in principle, to divide the spectrum into several spectral regions and to convert each with a cell whose band gap is tuned for the region. The greater the number of spectral regions allowed, the higher potential conversion efficiency. The III-V compound semiconductor MJ (Tandem) solar cells have great potential for achieving high conversion efficiency of over 50% [3] because of wide photo response and are promising for space and terrestrial applications. Although AlGaAs/GaAs tandem cells, including tunnel junctions and

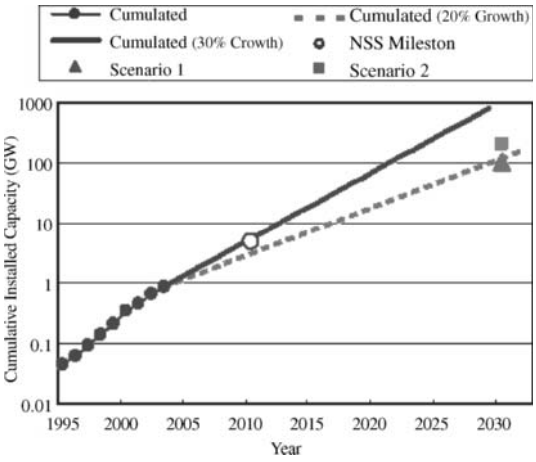

Fig. 15.1. Cumulated installed capacity of PV systems in Japan (by year)

Table 15.1. Module efficiency target (% cell efficiency) in the 2030 PV Road Map in Japan

Cell type	2010	2020	2030
Thin-bulk multi-c-Si	16 (20)	19 (25)	22 (25)
Thin-film Si	12 (15)	14 (18)	18 (20)
CIS type	13 (19)	18 (25)	22 (25)
Super-high η	28 (40)	35 (45)	40 (50)
Dye-sensitized	6 (10)	10 (15)	15 (18)

metal interconnectors, were developed in the early years, a high efficiency (close to 20%) was not obtained [4]. This is because of difficulties in making high-performance and stable tunnel junctions, and the defects related to the oxygen in the AlGaAs materials [5]. A double-hetero (DH) structure tunnel junction was found to be useful for preventing diffusion from the tunnel junction and improving the tunnel junction performance [6]. An InGaP material for the top cell was proposed by Olson et al. [7]. As a result of performance improvements in tunnel junction and top cell, over 30% efficiency has been obtained with InGaP/GaAs tandem cells, as reported by Takamoto et al. [8].

Concentrator operation is very effective for cost reduction of solar cell modules and, thus, that of PV systems [9]. Concentrator operation of the MJ cells is essential for their terrestrial applications. Since the concentrator PV systems using MJ solar cells have great potential of cost reduction, R&D on concentrator technologies, including MJ cells, has started in Japan.

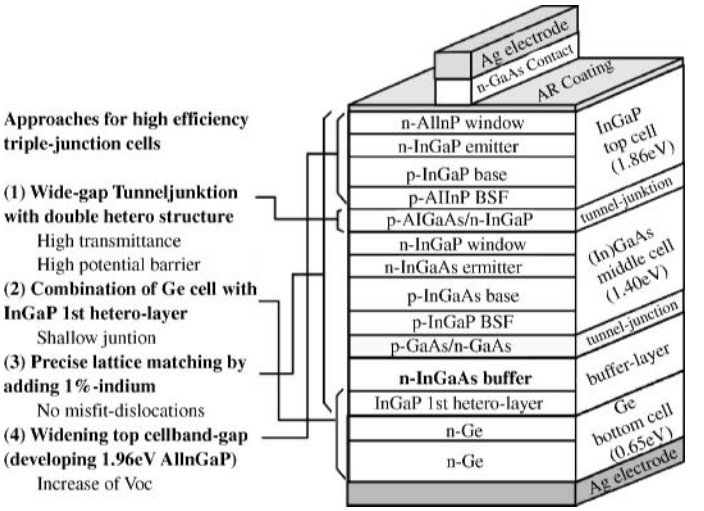

Fig. 15.2. A triple-junction cell and approaches for improving efficiency of the cell

15.2 Development of High-Efficiency MJ Solar Cells

As one of the Sunshine Programs in Japan, an R&D project for super high-efficiency MJ solar cells was started in 1990. Conversion efficiency of InGaP/GaAs-based multijunction solar cells has been improved by subsequent technologies. Illustration of the InGaP/(In)GaAs/Ge triple-junction solar cell and key technologies for improving conversion efficiency are shown in Fig. 15.2.0

15.2.1 Wide Band-gap Tunnel Junction

A wide band-gap tunnel junction, which consists of double-hetero-structure p – Al(Ga)InP/p – AlGaAs/n – (Al)InGaP/n – Al(Ga)InP, increases incident light into the (In)GaAs middle cell and produces effective potential barriers for both minority carriers generated in the top and middle cells. Both Voc and Isc of the cells are improved by the wide band-gap tunnel junction without absorption and recombination losses [8]. It is difficult to obtain high tunneling peak current with a wide-gap tunnel junction, so thinning the depletion-layer width with highly doped junctions is necessary. Since impurity diffusion occurs during growth of the top cell [6], carbon and silicon, which have low diffusion coefficients, are used for p-type AlGaAs and n-type (Al)InGaP, respectively. Furthermore, the double-hetero structure is presumed to suppress impurity diffusion from the highly doped tunnel junction [10]. The second tunnel junction, between the middle and bottom cells, consists of p – InGaP/p – (In)GaAs/n – (In)GaAs/n – InGaP, which has a wider band gap than middle-cell materials.

15.2.2 Combination of Ge Bottom Cell

InGaP/GaAs cell layers are grown on a p-type Ge substrate. The p-n junction is formed automatically during MOCVD growth by diffusion of V-group atom from the first layer grown on the Ge substrate; thus, the material of the first heterolayer is important for the performance of the Ge bottom cell. An InGaP layer is thought to be suitable material for the first heterolayer, because phosphor has a lower diffusion coefficient in Ge than arsenic, and indium has lower solubility in Ge than gallium. Figure 15.3 shows the change in spectral response of the triple-junction cell by changing the first hetero-growth layer on Ge from GaAs to InGaP. Quantum efficiency of the Ge bottom cell was improved by the InGaP hetero-growth layer. In the case of GaAs hetero-growth layer, junction depth was approximately 1 μm. On the other hand, thickness of n-type layer produced by phosphor from the InGaP layer was 0.1 μm. An increase in Ge quantum efficiency was confirmed to be due to a reduction in junction depth.

It was found that the absorption edge of the InGaP top cell shifted to the longer wavelength region, by using the InGaP first heterolayer. Figure 15.4 shows the change in band-gap energy determined by PL measurement for

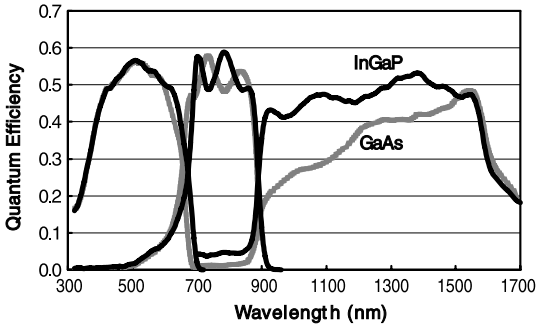

Fig. 15.3. Change in the spectral response due to modification of the first heterolayer from GaAs to InGaP (without ARC)

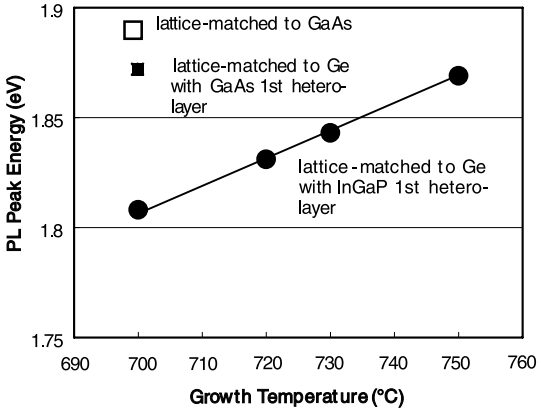

Fig. 15.4. Change in PL peak energy for InGaP layer lattice-matched to Ge with GaAs or InGaP

InGaP-layer grown under various conditions. Band gap of the InGaP top cell decreased from 1.86 to 1.81 eV by changing the hetero-growth layer from GaAs to InGaP. The fact that the band gap increased with the growth temperature increase indicated that this phenomenon was due to the ordering effect in the InGaP material [11]. Since the band-gap narrowing of the top cell decreases Voc of the triple-junction cell, an approach for growth of less-ordering InGaP is necessary. In fact, conversion efficiency has been improved up to 30% (AM0) by increasing top-cell bang gap up to 1.89 eV [12].

15.2.3 Precise Lattice-Matching to Ge Substrate

Although 0.08% lattice mismatch between GaAs and Ge was thought to be negligible, misfit dislocations were generated in thick GaAs layers and deteriorated cell performance. By adding about 1% indium to the InGaP/GaAs cell layers, all cell layers are lattice matched precisely to the Ge substrate. As a result, cross-hatch pattern caused by misfit dislocations due to lattice mismatch disappeared in the surface morphology of the cell with 1% indium, as shown in Fig. 15.5. The misfit dislocations were found to influence not the Isc but the Voc of the cell. The Voc was improved by eliminating misfit dislocations for the cell with 1% indium. In addition, wavelength of the absorption edge became longer and Isc of both top and middle cells increased, by adding 1% indium.

15.2.4 Widening of Top-Cell Band Gap by AlInGaP

We are presently developing AlInGaP top cells in order to improve Voc of the triple-junction cells. Current matching between top and middle cells should be done by controlling the top-cell band gap instead of thinning the top cell. In this case, Voc of the cell can be increased with keeping the maximum current.

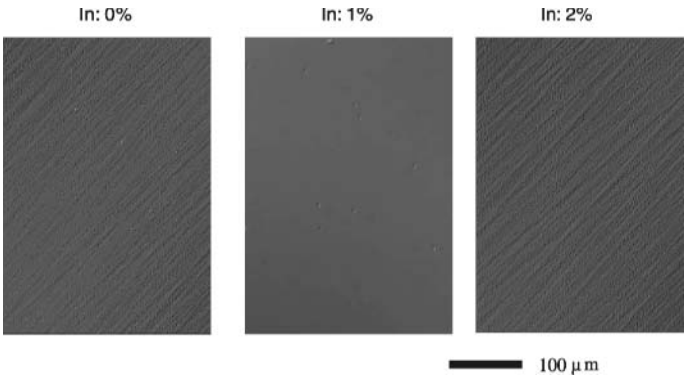

Fig. 15.5. Surface morphology of InGaAs, with various indium composition grown on Ge

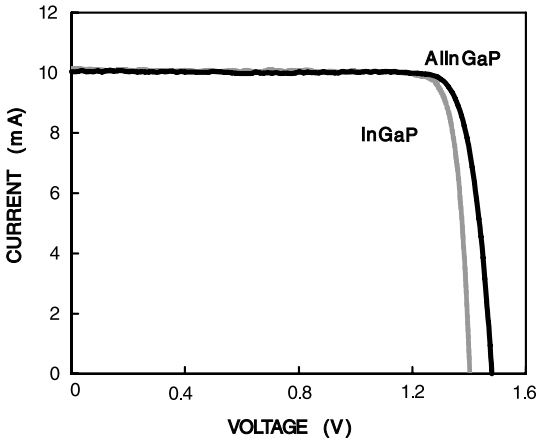

Fig. 15.6. Light IV curves of the single-junction AlInGaP and InGaP cells (AM1.5G, without ARC)

Table 15.2. Characteristics of the triple-junction cells

Voc (mV)	Jsc (mA/cm^2)	FF	Eff. (%)	Condition
2567	14.1	0.87	31.5	AM1.5G,25 °C
2568	17.9	0.86	29.2	AM0, 28 °C

An AlInGaP cell with 1.96-eV band gap and 2.5 µm thickness was found to attain high Voc of 1.5 V while keeping the same Isc as the conventional InGaP top cells under AM1.5G conditions.

Figure 15.6 shows comparison of light IV curve under AM1.5G conditions. For AM0 conditions, further increase in band gap to about 2.0 – 2.03 eV is required for the AlInGaP cells, although it depends on the current matching requirement from the beginning of life (BOL) to the end of life (EOL).

The best data of the triple-junction cells in our laboratory are summarized in Table 15.2. Technologies described previously were applied to fabrication of the triple-junction cells. Band gap of the InGaP top cell of about 1.82 eV is still low. By using AlInGaP top cell with 1.96 eV, higher Voc (close to 2.72 V) is predicted. Conversion efficiencies over 33% (AM1.5G) and close to 31% (AM0) are expected for the (Al)InGaP/InGaAs/Ge triple-junction cells.

15.3 Development of High-Efficiency Concentrator MJ Solar Cells

The R&D project for super-high-efficiency concentrator MJ solar cells and modules was initiated in Japan in 2001. In order to apply a high-efficiency MJ cell developed for 1-sun conditions to a concentrator cell operating under $\sim$ 500-sun conditions, reduction in energy loss due to series resistance is the

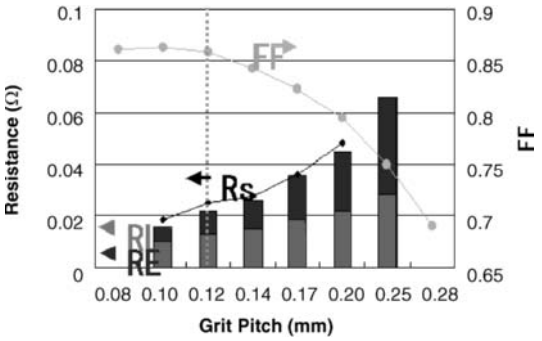

Fig. 15.7. FF of the concentrator cells with various grid pitching under 250-sun light. Series resistance (Rs), lateral resistance (RL) and total electrodes resistance (RE) are also shown

most important issue. Cell size was determined to be 7×7 mm considering total current flow. Grid electrode pitching, height and width were designed in order to reduce series resistance. Figure 15.7 shows FF of the cell with various grid pitching under 250 suns. Grid electrode with 5-μm height and 5-μm width was made of Ag. Grid pitching influences lateral resistance between two grids (RL) and total electrodes resistance (RE). Series resistance of the cell (RS), RE and RL are also shown in Fig. 15.7. The RE was measured directly after removing the electrode from the cell by chemical etching. The RL was calculated by using sheet resistance of window and emitter layers. Based on

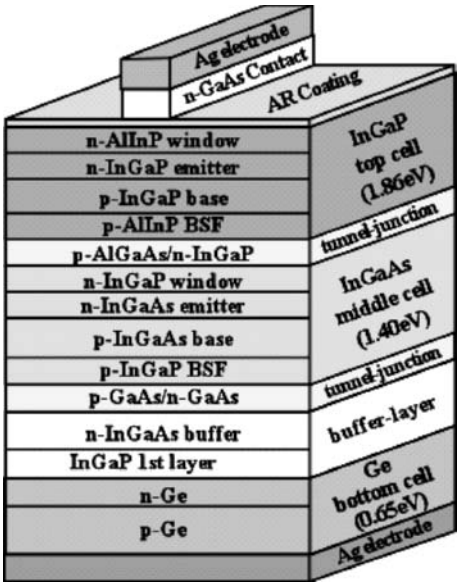

Fig. 15.8. A structure of a high-efficiency InGaP/InGaAs/Ge triple-junction concentrator solar cell

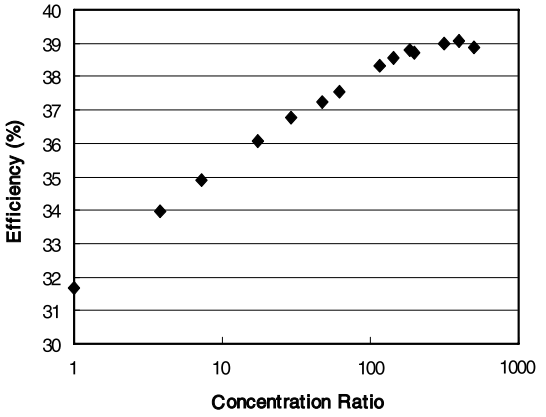

Fig. 15.9. Efficiency of a high-efficiency InGaP/InGaAs/Ge triple-junction cell vs number of suns

the data in Fig. 15.6, the grid pitching is determined to be 0.12 mm at this time. In order to reduce series resistance down to 0.01 Ω and obtain high FF under 500 suns, grid height should be increased twofold. High efficiency under < 500 suns is thought to be obtained by the optimal grid design without modification of the cell-layer structure such as emitter thickness and tunnel junction thickness from the cell developed for 1-sun conditions.

For concentrator applications, the grid structure has been designed in order to reduce the energy loss due to series resistance as shown in Fig. 15.7. Most recently, we have successfully fabricated high-efficiency concentrator InGaP/InGaAs/Ge triple-junction solar cells designed for 500-sun application. Figure 15.8 shows a structure of a high-efficiency InGaP/InGaAs/Ge triple-junction concentrator solar cell. The efficiencies by in-house measurement are 39.2% at 200 suns and 38.9% at 489 suns, as shown in Fig. 15.9 [12]. The solar simulator was equipped with both Xe lamp and halogen lamp and adjusted AM1.5G spectrum.

15.4 Development of High-Efficiency, Low-Cost Concentrator Triple-Junction Cell Modules

The concentrator InGaP/InGaAs/Ge triple-junction solar cell modules were developed using the new technologies described below [13–15].

15.4.1 Concentrator Optics

A new concentrator optics has been introduced that consists of a non-imaging dome-shaped Fresnel lens and a kaleidoscope homogenizer. The non-imaging Fresnel lens allows wide-acceptance half angle while keeping the same optical efficiency with minimum chromatic aberration. The homogenizer reshapes

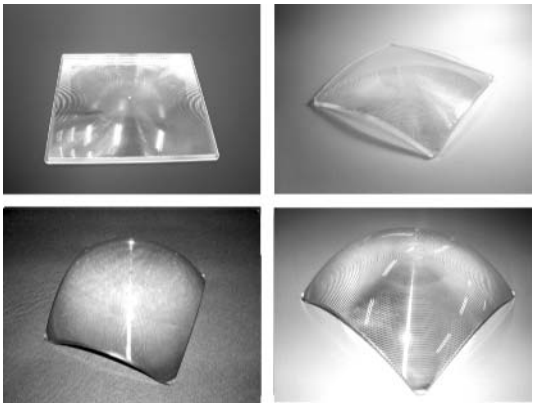

Fig. 15.10. Generations of injection-molded Fresnel lenses. *Top left*: First-generation flat design (400×, 77.3% of peak efficiency, 2001). *Top right*: Second-generation half-dome design (400×, 81.5% of peak efficiency, 2002). *Bottom left*: Third-generation full-dome design made by collapsible molding die (400×, 85.4% of peak efficiency). *Bottom right*: Fourth-generation full-dome design made by collapsible molding die (556×, 91% of theoretical efficiency)

the concentrated into square solar cell aperture, mixed rays to uniform flux (see Fig. 15.10).

Injection molding is capable of manufacturing thousands of lenses in a single day and by a single machine. The drawback of this method is difficulty in creating precise prism angles and flat facets. The maximum efficiency was slightly above 80% and overall efficiency was 73%. After improvement of the process conditions, the average efficiency increased to 85.4%.

15.4.2 Module and Packaging Technology

A new packaging structure for III-V concentrator solar cells has been developed, applicable mainly to Fresnel lens concentrator modules but also of utility in dish concentrator systems. The solar cell used in the new receiver package is III-V 3J concentrator solar cell. It is grown on a fragile Ge sub-

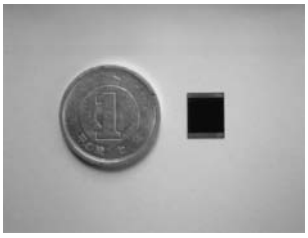

Fig. 15.11. Bare InGaP/InGaAs/Ge triple-junction concentrator chip

strate with thickness of only 150 um. The overall size is 7×9 mm with 7 mm^2 aperture area (see Fig. 15.11).

In addition, the following technologies have been developed:

1. Super-high-pressure and vacuum-free lamination of the solar cell that suppresses the temperature increase to 20° under 550× geometrical concentration illumination of sun beam
2. Direct and voids-free soldering technologies of the fat metal ribbon to the solar cell, suppressing hot spots and reducing the resistance, thereby allowing a current 400 times higher than normal non-concentration operation to be passed with negligible voltage loss
3. A new encapsulating polymer that survives exposure to high-concentration UV and heat cycles
4. Beam-shaping technologies that illuminate the square aperture of the solar cell, from a round concentration spot
5. Homogenizer technologies that give a uniform flux and prevent the conversion losses that stem from chromatic aberration and flux intensity distribution

Figure 15.12 shows an inverted pyramid kaleidoscope used in this project. Figure 15.13 shows effectiveness of the inverted pyramid homogenizer to correct chromatic aberration. The inverted pyramid homogenizers are found to have many functions to boost efficiencies, including beam shaping, uniform illumination, chromatic aberration correction, enlarging assemble tolerance and so forth.

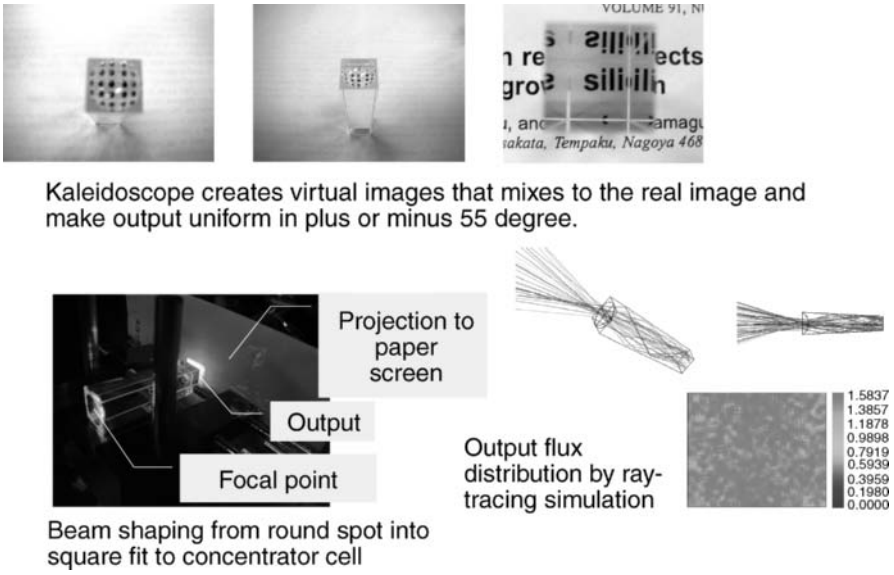

Fig. 15.12. An inverted pyramid kaleidoscope used in this project

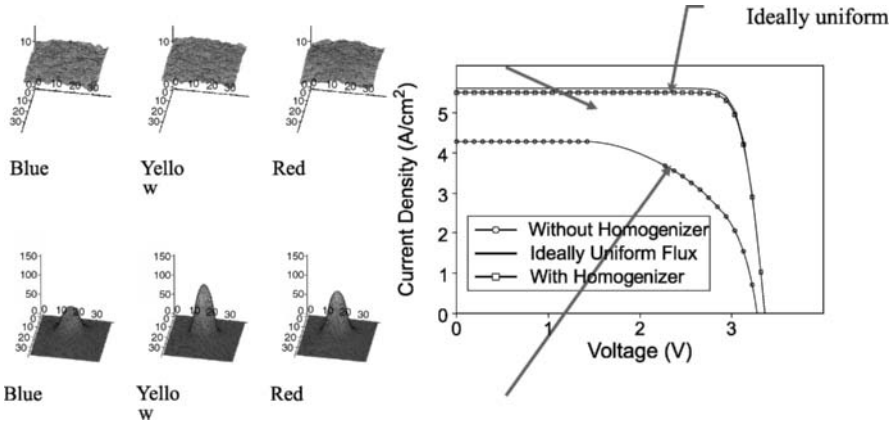

Fig. 15.13. Effectiveness of the inverted pyramid homogenizer to correct chromatic aberration

The concentrator module is designed with ease of assembly in mind. All the technologically complex components are packaged into a receiver so that a series of receivers and lenses can be assembled with standard tools, using local materials and workforce. The concept is similar to the computer and automobile assembly industries, where key components are imported but the product is assembled locally. It is anticipated that this approach will reduce the manufacturing cost of the module (see Fig. 15.14).

15.4.3 Reliability and Fail-safe

Fail-safe

One of the concerns for the reliability of concentrator modules is safety against some accidents. For example, the concentrated solar beam may burn

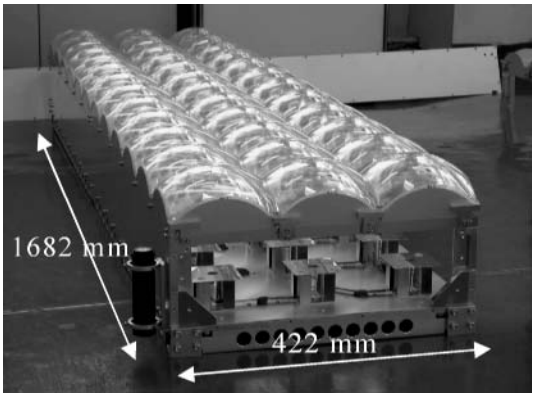

Fig. 15.14. Inside of the 400× concentrator module with 36 receivers connected in series

the interior of the module components including internal cables, if the solar tracker has some problems and the off-axis beam hits outside the solar cell. This was sometimes the case in the early development of the concentrators [18]. The current non-imaging concentrator Fresnel lens maintains beam intensity within $\pm 0.9^\circ$ of tracking error, but the beam intensity substantially drops out of that acceptance angle [19, 20]. These characteristics help to reduce the thermal flux from off-axis beam to unwanted components. The homogenizer glass rod shifts the focal surface from the cell area and thus reduces intensity of the off-axis beam. The temperature increase by off-axis beam from $850\,\mathrm{W/m^2}$ direct normal irradiance was typically 15 K [21].

Robustness

The hail-impact test has been conducted on the Fresnel lens. It was shown that the lens thickness was significant in survival against 90-km/h hail impact. Some thin-film surface coatings partly helped to raise robustness against impact in thin lens design.

Static load test was conducted to see robustness against wind. We experienced heavy snow (20 cm thick in Inuyama site) in this year. We found that snow did not stay on the module (or lenses), possibly because of tracking; therefore, it is safe to say that the test load can be decided exclusively by wind.

Lifetime of Sealing Polymer

Since III-V solar cells are more reactive against environment than silicon solar cells, they need complete sealing from environment; however, the transparent sealing polymer on the solar cell is exposed by concentrated sunlight and may be damaged by UV rays [22]. Even though the sealing polymer keeps transparency, the mechanical strength would usually be degraded, and there is a chance of the seal breaking. The typical environmental-chamber test, including hot-wet test, thermal-cycle test and freezing-cycle test, were not sufficient to unveil the potential damage, because the degradation mechanism was different.

A good method is to expose concentrated UV in a wet environment while the receiver is cooled and collects water condensation by a water-cooled Fe-Metalhalide lamp [22]. The acceleration ratio was examined by the comparison with outdoor exposure test of 400× module (see Fig. 15.15).

Various kinds of polymers were examined. Most of the polymers did not survive in 20 years of accumulated concentrated UV light, but we found one polymer that exhibited more than 20 years of lifetime (see Fig. 15.16).

Cost

Various aspects, including capital cost, labour and material cost, determine the cost of the PV module. With the effort of PV industries as well as the

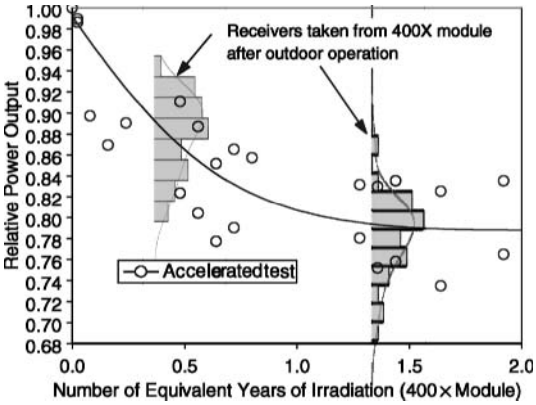

Fig. 15.15. Comparison between the acceleration test and outside exposure test

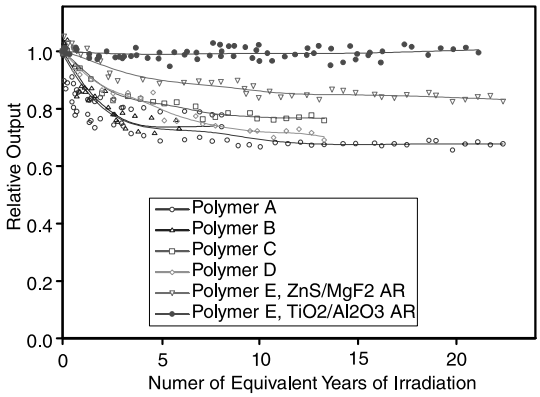

Fig. 15.16. Acceleration test by simultaneous concentrated UV irradiation and water condensation

expansion of the scale of the management, the ratio of capital cost and labour cost are decreasing. The final effort is to be devoted to reducing the material cost. The material cost will be an indication of the potential for lowering the module cost with manufacturing growth.

The concentrator modules of the past were believed to be massive metal structures. It was true that they used big heat sinks or water-cooling systems. Many present concentrator modules successfully spread concentrated heat to the back body and do not rely on heat sinks. Our module succeeded in reducing the weight to a level comparable to that of a typical thin-film solar module. The concentrator module is expected to overwhelm the typical multicrystalline silicon module after some technical innovations.

15.4.4 Outdoor Evaluation

Both 400 and 550× modules, as shown in Fig. 15.17, were evaluated by four test sites. Three sites were operated by independent organizations. All the results were 'uncorrected'. In contrast to flat-plate modules, the corrected procedure is not agreed internationally.

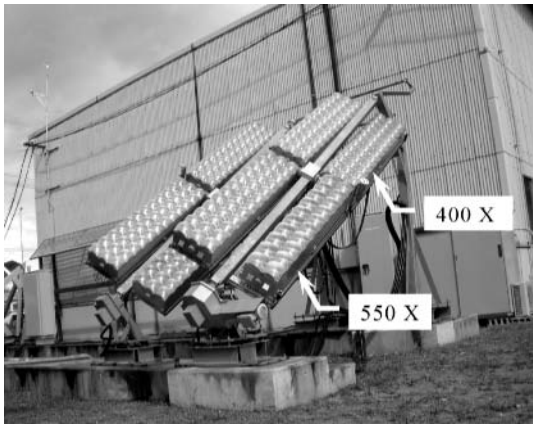

Fig. 15.17. Shown are 550× and 400× modules on two-axis trackers using open-loop control. The bottom-right module with two lines of lenses is a 550× 150-W module; the others are 400× 200-W modules. The overall system rating is 1550 W

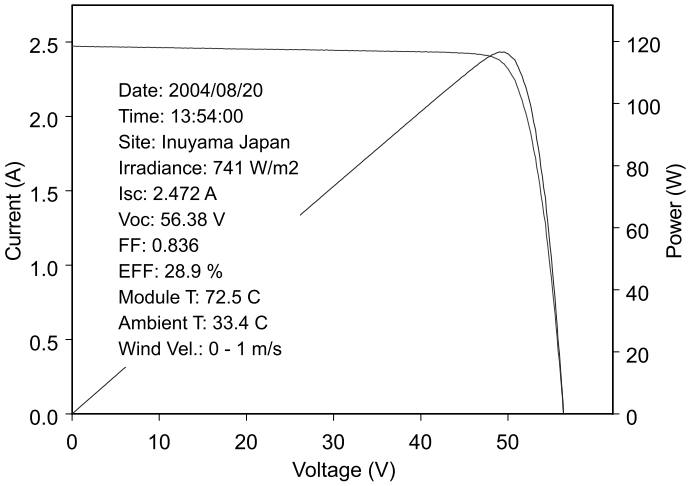

Fig. 15.18. Typical outdoor I-V curve of the 550× module

Figure 15.18 shows a typical outdoor I-V curve for the 550× modules. All 20 cells were connected in series and each cell was protected using a by-pass diode. Since the receivers had sufficient margin for assembly and the variation among lenses was small, the step in the I-V curve, due to cells becoming shunted by by-pass diodes as a result of current mismatching, was rarely observed. The peak uncorrected efficiency for the 5445-cm^2 550× module was 28.9%.

The peak uncorrected efficiency for the 7056-cm^2 400× module with 36 solar cells connected in series was 26.6%, measured in-house. The peak uncor-

rected efficiencies for the same type of module with six solar cells connected in series and 1176-cm^2 area measured by Fraunhofer ISE and NREL were 27.4 and 24.9%, respectively.

Table 15.3 summarizes the measured efficiency in three different sites.

15.4.5 Efficiency Comparison of Concentrator Modules Output with that of Flat-Plate Modules

Power-generation trend was compared with the commercial flat-plate crystalline silicon module (see Fig. 15.19). The newly developed concentrator module produced 2.9 times more power per area.

Table 15.3. Uncorrected peak efficiency measurement

Concentration	Area (cm^2)	Site	Ambient (°C)	Uncorrected efficiency (%)	DNI (W/m^2)
400×	7056	Inuyama, Japan (manufacturer)	29	27.6	810
400×	7056	Toyohashi, Japan (independent)	7	25.9	645
400×	1176	Fraunhofer ISE, Germany (independent)	19	27.4	839
400×	1176	NREL, USA (independent)	29	24.9	940
550×	5445	Inuyama, Japan (manufacturer)	33	28.9	741
550×	5445	Toyohashi, Japan (independent)	28	27	777

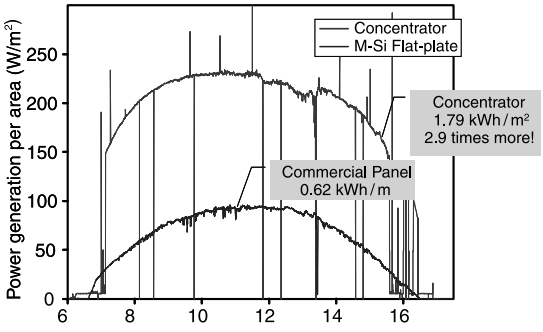

Fig. 15.19. Comparison with a commercial flat-plate crystalline silicon module

A concentrator module utilizes only the direct beam irradiance. It has been stated for a long time that concentrator PV was *not* suitable for the climate in Japan. In order to disprove this misunderstanding, a long-term field test was started to see if the high efficiency of concentrator PV overcomes the reduction in irradiation. A typical flat-plate module was installed at the Inuyama site, composed of 14.06% rated efficiency multi-crystalline silicon solar cells mounted on a 30° sloped fixture. The amount of the energy relative to the flat-plate module depended on the relative sunshine duration, defined as the probability when DNI exceeds more than 120 W/m^2 from sunrise to sunset.

Figure 15.20 indicates the ratio of the energy production from 15 July to 15 October 2004. For the period with a lower percentage of sunshine, such as September, the concentrator module only produced the same amount of energy as the flat-plate module with the same area; however, over a period with a lot of sunny days, the energy per unit area from the concentrator module was more than 2.5 times that of the flat-plate system. Applying the normal value of the sunshine duration, defined as the averaged sunshine duration from 1960 to 1990, the concentrator module would produce roughly 1.7 – 2.6 times more energy per area per annum than the 14% multi-crystalline silicon module in most cities in Japan.

The sunshine duration data was collected in many cities. The comparison with sunshine duration is convenient to anticipate the energy production by the concentrator PV; however, it is admitted that the analysis is crude and will lead to some inaccuracy in the result. In the future, a more rigorous estimate will be made and compared against long-term data.

15.4.6 Applications

One of the possible applications in Japan is a rooftop on the apartment houses. A new lightweight open-loop tracker (see Fig. 15.21) and lightweight module is being developed. This is a two-axis tracker moving as an astronomical globe. The hour-angle axis points to the polar star and seasonal change is performed by another slope axis. The weight is 0.3 kg/W including modules. The weight does not include the base structure. It is also impor-

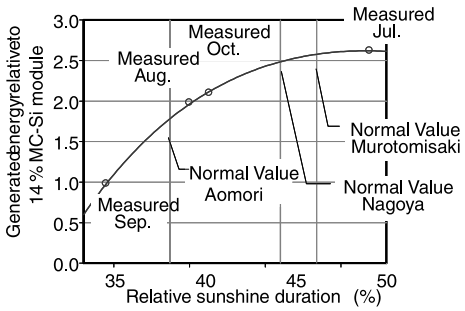

Fig. 15.20. Comparison against the MC-Si flat-plate module with a 14.06% rated efficiency

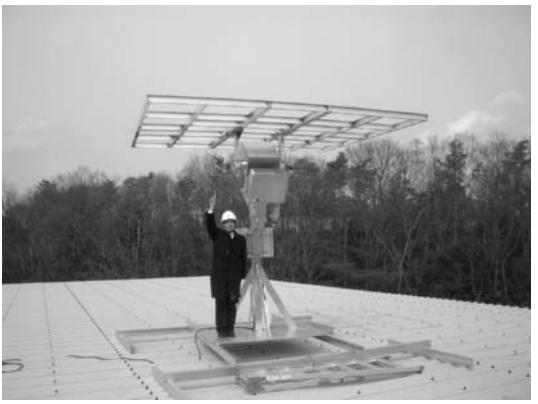

Fig. 15.21. A new 3-kW tracker for rooftop application

Fig. 15.22. A CPV for 'breeding plants' that collects direct beam and provides diffused sunlight to the plant underneath

tant to develop a low-weight module. We are now developing a 0.08 kg/W lightweight module for this rooftop application. The challenge is to realize robust structure against 60 m/s wind load by standard metal works.

Another interesting application is what we call the tree-planting PV (Fig. 15.22). The CPV utilizes only direct beam in the sunlight, which is often harmful for tree planting. The CPV system without the back cover is transparent to the diffused sunlight. The CPV module shades the strong direct beam and provides rich diffused sunlight to plants. With this transparent module, the area under the module is no longer the dead area. Different from 'see-through' flat-plate modules, the power generation is not compromised at all.

15.5 Conclusion

The conversion efficiency of InGaP/(In)GaAs/Ge triple-junction solar cells has been improved to 31.5% (AM1.5G) using technologies such as double-

hetero wide-band-gap tunnel junctions, combination of Ge bottom cell with InGaP first heterolayer, and precise lattice matching to Ge substrate by adding 1% indium into the cells; however, the band gap of the top cell is not high enough. Using an AlInGaP top cell with 1.95 eV should further improve efficiency. For concentrator applications, the grid structure has been designed in order to reduce the energy loss due to series resistance, and 38% (AM1.5G, 100–500 suns) efficiency has been demonstrated.

There are three hurdles: performance; reliability; and cost that concentrator solar electricity technology must clear for long-term growth and success in the market place.

15.5.1 Performance

A $31.5 \pm 1.7\%$ (peak) module efficiency was achieved by the module after correction to 25 °C cell temperature under Japanese direct beam spectrum. The expected annual power generation per area derived from a side-by-side comparison in Inuyama site from July to October suggested 1.7 – 2.6 times greater annual energy production over a 14% efficient multicrystalline silicon module. This is true even in the Japanese climate, which was thought to be unsuitable for concentrator applications due to insufficient direct beam irradiation.

15.5.2 Reliability

Most of the problems have been solved. The environmental chamber tests and other standard tests have been completed, and good durability has been exhibited. A 20-year lifetime against concentrated UV flux has been proven by the UV acceleration test. That test showed a good correlation to the outdoor exposure test. The fail-safe characteristics against off-axis concentrator beam and water invasion have also been confirmed.

15.5.3 Cost

A substantial reduction is anticipated but not yet proven. The reduction of module weight has already caught up with the thin-film module and will exceed the crystalline silicon module. Considering that most of the material in the concentrator module is inexpensive plastic and metal, it is expected to replace both crystalline silicon and thin-film modules in the near future. The highest-efficiency module with many new technologies has been developed as a NEDO project. It is a combination of III-V semiconductor technology, optics, mechanical engineering, etc. The project was carried out mainly by three private companies, Sharp, Daido Steel and Daido Metal, with five universities, including Nara-AIST, Fukui University, Toyota Technological Institute, Tokyo University of Agriculture and Technology, Toyohashi University of

Technology, and one organization, PVTEC. The R&D was done from 2001 to 2003. The evaluation study was done in 2004. Now, the NEDO project is over, but three companies continue development by themselves. We are moving towards product development.

Finally, although we have succeeded in developing the highest-efficiency module, our odyssey is not over. We are moving towards higher-concentration application while maintaining high performance. We are doing research for higher efficiency and III-V concentrator cells. We are doing research to unveil myths about the strange behaviours of MJ and concentrator PV cells as well as systems under realistic operation conditions.

References

1. K. Kurokawa, F. Aratani, Proc 19th European Photovoltaic Solar Energy Conference and Exhibition, Paris, France, 7–11 June 2004, (WIP, 2004) p. 2731
2. T. Bruton, S. Roberts, N. Mason and K. Heasman, Proc 31st IEEE Photovoltaic Specialists Conference, Florida, 3–7 January (IEEE, New York, 2005) p. 647
3. J.C.C. Fan, B-Y. Tsaur, B.J. Palm, Proc 16th IEEE Photovoltaic Specialists Conference, (IEEE, New York, 1982) p. 692
4. J.A. Hutchby, R.J. Markunas, S.M. Bedair, Proc SPIE, Photovoltaics, S.K. Ded Ed., Vol. 543, (1985) p. 543
5. K. Ando, C. Amano, H. Sugiura, M. Yamaguchi, A. Salates, Jpn J Appl Phys 26, L266 (1987)
6. C. Amano, H. Sugiura, A. Yamamoto, M. Yamaguchi, Appl Phys Lett 51, 1998 (1987)
7. J.M. Olson, S.R. Kurtz, K.E. Kibbler, Appl Phys Lett 56, 623 (1990)
8. T. Takamoto, E. Ikeda, H. Kurita, M. Ohmori, M. Yamaguchi, Jpn J Appl Phys 36, 6215 (1997)
9. M. Yamaguchi, A. Luque, IEEE Trans. Electron Devices, 46, 2139 (1999)
10. T. Takamoto, M. Yamaguchi, E. Ikeda, T. Agui, H. Kurita, and M. Al-Jassim, J Appl Phys, 85, 1481 (1999)
11. A. Gomyo, T. Suzuki, K. Kobayashi, S. Kawata, I. Hino, T. Yuasa, Appl Phys Lett, 50, 673 (1987)
12. R. King, C. Fetzer, P. Colter, K. Edmondson, J. Ermer, H. Cotal, H. Yoon, A. Stavrides, G. Kinsey, D. Kurzt, N. Karam, Proc 29th IEEE Photovoltaic Specialists Conf, (IEEE, New York, 2002) p. 776
13. M. Yamaguchi, T. Takamoto, T. Agui, M. Kaneiwa, K. Nishimura, Y. Yagi, T. Sasaki, N.J. Ekins-Daukes, H.S. Lee, N. Kojima, Y. Ohshita, Proc 19th European Photovoltaic Solar Energy Conference and Exhibition, Paris, France, 7-11 June 2004, (WIP, 2004) p. 3610
14. T. Takamoto, M. Kaneiwa, M. Imaizumi, M. Yamaguchi, Prog Photovolt Res Appl, 13, 495 (2005)
15. K. Araki et al., Proc 19th European Photovoltaic Solar Energy Conference and Exhibition, Paris, France, 7-11 June 2004, (WIP, 2004) p. 2451, p. 2495
16. K. Araki, H. Uozumi, T. Egami, M. Hiramatsu, Y. Miyazaki, Y. Kemmoku, A. Akisawa, N.J. Ekins-Daukes, H.S. Lee, M. Yamaguchi, Prog Photovolt Res Appl, 13, 495 (2005)

17. M. Hiramatsu, Y. Miyazaki, T. Egami, A. Akisawa, Y. Mizuta, Proc 3rd World Conference on Photovoltaic Energy Conversion, (2003) p. 2383
18. J. Laisch, CDROM, SCC2003, (2003).
19. R. Leutz et al., (2001) Nonimaging Fresnel Lenses: Design and Performance of Solar Concentrators; Springer Verlag, Heidelberg (2009).
20. A. Akisawa et al., J.J. Solar Energy, 29, 157 (2003).
21. IEC 62108 Draft 5
22. K. Araki, M. Kondo, H. Uozumi and M. Yamaguchi, Proceedings of the 3rd World Conference on Photovoltaic Energy Conversion, May 11-18, 2003, Osaka, Japan (WCPEC-3, 2003) pp.805.

Index